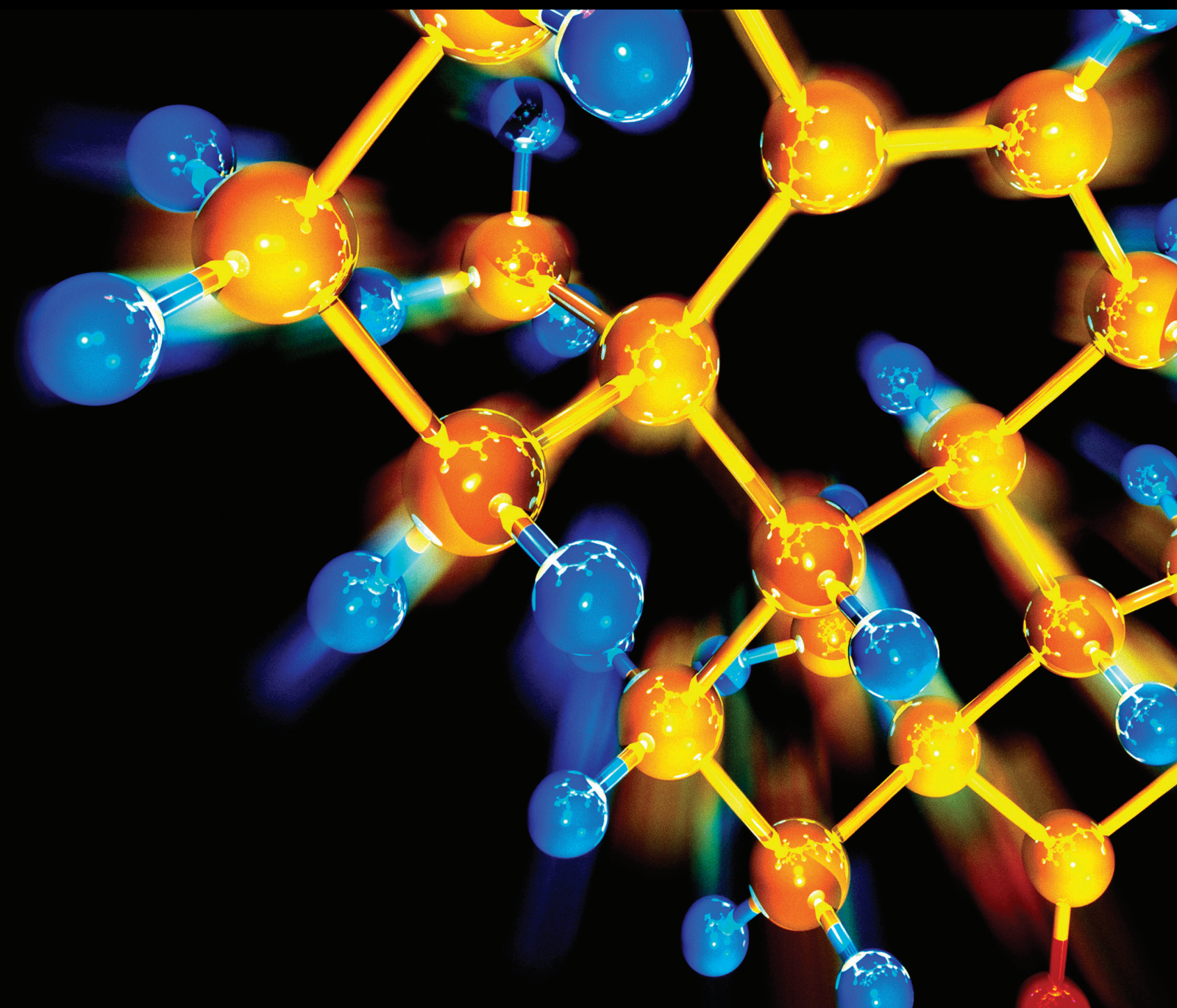


Journal of Chemistry

# Materials Chemistry for Sustainability and Energy

Guest Editors: Fan Dong, Sirilak Sattayasamitsathit, Yu Xin Zhang, and Ying Zhou





---

# **Materials Chemistry for Sustainability and Energy**

Journal of Chemistry

---

## **Materials Chemistry for Sustainability and Energy**

Guest Editors: Fan Dong, Sirilak Sattayasamitsathit,  
Yu Xin Zhang, and Ying Zhou



---

Copyright © 2014 Hindawi Publishing Corporation. All rights reserved.

This is a special issue published in "Journal of Chemistry." All articles are open access articles distributed under the Creative Commons Attribution License, which permits unrestricted use, distribution, and reproduction in any medium, provided the original work is properly cited.

# Contents

**Materials Chemistry for Sustainability and Energy**, Fan Dong, Sirilak Sattayasamitsathit, Yu Xin Zhang, and Ying Zhou

Volume 2014, Article ID 152384, 3 pages

**Synthesis of an Anion-Exchange Membrane Based on Imidazolium-Type Ionic Liquids for a Capacitive Energy Extraction Donnan Potential Device**, Young-Seok Kim and Seong-Ho Choi

Volume 2014, Article ID 858541, 7 pages

**Development of Low Energy Gap and Fully Regioregular Polythiénylenevinylene Derivative**,

Tanya M. S. David, Cheng Zhang, and Sam-Shajing Sun

Volume 2014, Article ID 379372, 7 pages

**Structural and Electrochemical Properties of Lithium Nickel Oxide Thin Films**, Gyu-bong Cho, Tae-hoon Kwon, Tae-hyun Nam, Sun-chul Huh, Byeong-keun Choi, Hyo-min Jeong, and Jung-pil Noh

Volume 2014, Article ID 824083, 5 pages

**Preparation of Mesoporous SnO<sub>2</sub> by Electrostatic Self-Assembly**, Yang Jing, Wang Yan, and Xu Xiaowen

Volume 2014, Article ID 713573, 7 pages

**Synthesis and Application of One-Dimensional La(OH)<sub>3</sub> Nanostructures: An Overview**, Xiang Xiao, Yu Huang, and Fan Dong

Volume 2014, Article ID 305986, 9 pages

**Investigations of the Montmorillonite and Aluminium Trihydrate Addition Effects on the Ignitability and Thermal Stability of Asphalt**, Kai Zhu, Ke Wu, Bin Wu, and Zhiyi Huang

Volume 2014, Article ID 847435, 8 pages

**A Study on the Morphology of a Dispersed Particle Gel Used as a Profile Control Agent for Improved Oil Recovery**, Qing You, Yongchun Tang, Caili Dai, Mingwei Zhao, and Fulin Zhao

Volume 2014, Article ID 150256, 9 pages

**Catalytic Combustion of Low Concentration Methane over Catalysts Prepared from Co/Mg-Mn Layered Double Hydroxides**, Hongfeng Liu, Xingrui Fu, Xiaole Weng, Yue Liu, Haiqiang Wang, and Zhongbiao Wu

Volume 2014, Article ID 751756, 6 pages

**Inhibition Effect of Glycerol on the Corrosion of Copper in NaCl Solutions at Different pH Values**, Santos Lorenzo Chi-Ucán, Andrea Castillo-Atoche, Pedro Castro Borges, José Antonio Manzanilla-Cano, Gerardo González-García, Rodrigo Patiño, and Luis Díaz-Ballote

Volume 2014, Article ID 396405, 10 pages

**Phthaloylchitosan-Based Gel Polymer Electrolytes for Efficient Dye-Sensitized Solar Cells**, S. N. F. Yusuf, M. F. Aziz, H. C. Hassan, T. M. W. J. Bandara, B.-E. Mellander, M. A. Careem, and A. K. Arof

Volume 2014, Article ID 783023, 8 pages

**Production of Biologically Activated Carbon from Orange Peel and Landfill Leachate Subsequent Treatment Technology**, Zhigang Xie, Wei Guan, Fangying Ji, Zhongrong Song, and Yanling Zhao

Volume 2014, Article ID 491912, 9 pages



---

**Removing and Recovering Phosphate from Poultry Wastewater Using Amorphous Ceramics**, Youhui Xie, Qin Li, Xianzhi Zhao, Yi Luo, Yangming Wang, Xiangwei Peng, Qigui Wang, Jian Su, and Yin Lu  
Volume 2014, Article ID 132582, 7 pages

**A Quaternized Polysulfone Membrane for Zinc-Bromine Redox Flow Battery**, Mingqiang Li, Hang Su, Qinggang Qiu, Guang Zhao, Yu Sun, and Wenjun Song  
Volume 2014, Article ID 321629, 5 pages

## Editorial

# Materials Chemistry for Sustainability and Energy

Fan Dong,<sup>1</sup> Sirilak Sattayasamitsathit,<sup>2</sup> Yu Xin Zhang,<sup>3</sup> and Ying Zhou<sup>4</sup>

<sup>1</sup>Chongqing Key Laboratory of Catalysis and Functional Organic Molecules, College of Environmental and Biological Engineering, Chongqing Technology and Business University, Chongqing 400067, China

<sup>2</sup>Department of Nanoengineering, University of California, San Diego (UCSD), La Jolla, CA 92093, USA

<sup>3</sup>Department of Materials Science and Engineering, Chongqing University, Chongqing 400044, China

<sup>4</sup>School of Materials Science and Engineering, State Key Laboratory of Oil and Gas Reservoir Geology and Exploitation, Southwest Petroleum University, Chengdu 610500, China

Correspondence should be addressed to Fan Dong; [dfctbu@126.com](mailto:dfctbu@126.com)

Received 22 September 2014; Accepted 22 September 2014; Published 22 December 2014

Copyright © 2014 Fan Dong et al. This is an open access article distributed under the Creative Commons Attribution License, which permits unrestricted use, distribution, and reproduction in any medium, provided the original work is properly cited.

Environmental pollution and energy storage are two global menaces and the magnitude of them is ever-increasing due to rapid pace of urbanization and industrialization. Thus, providing clean environment and renewable energy for people is a great challenge. The nano/microstructured materials with intriguing physical and chemical properties have given immense scope and opportunities to address the key issues of environmental sustainability and clean energy development. In the past two decades, great progress has been made on design, synthesis, and utilization of artificial materials for sustainability and energy. These nano/microstructured materials in various fashions are stimulating various practical applications in environmental and energy sector. The rapid development in materials chemistry has led to significant advances in understanding the controlled synthesis, chemical properties, and structure-activity relationship of materials.

This special issue contains 13 papers, which are mainly related to energy development and pollutant removal utilizing newly artificial materials. Among them, 5 papers are related to pollutants removal, 3 papers are about batteries development, and 2 papers are for solar cell. In addition, 1 paper is related to investigations of the montmorillonite and aluminium trihydrate addition effects on the ignitability and thermal stability of asphalt and 1 paper is exploring the effects of concentration, temperature, torque value, roughness, and washer shape on crevice corrosion for 254 SMO alloys. Furthermore, 1 paper is about newly polymeric anion-exchange membranes (AEMs) fabrication. Additionally, there is 1

review that systematically introduces the synthesis and application of one-dimensional  $\text{La}(\text{OH})_3$  nanostructures. We would like to express our sincere thanks to all the authors for submitting their interesting and meaningful works to this special issue. A brief summary of all 13 papers is provided below.

The paper entitled “A quaternized polysulfone membrane for zinc-bromine redox flow battery” reported that a quaternized polysulfone (QNPSU) composite membrane was synthesized for zinc-bromine redox flow battery. The conductivity of the membrane was tested by electrochemical analyzer. It was found that the conductivity of the membrane was about 0.01 S/cm in 25°C with 100 RH%. Furthermore, the discharge voltage was 0.9672 V and the power density was 6 mW/cm<sup>2</sup> at a current of 0.1 A, which demonstrated that the novel composite membrane was a promising material for the flow battery.

In “A study on the morphology of a dispersed particle gel used as a profile control agent for improved oil recovery,” a new profile control agent termed dispersed particle gel (DPG) has been fabricated and reported, which was used to control the injection water and improve oil recovery. The AFM studies showed that DPG was composed of small pseudospherical particles and that their sizes can be controlled by adjusting the initial polymer mass concentration, the shearing rate, and the salinity. Furthermore, the effects of the initial polymer mass concentration, the shearing rate, the salinity, and the high-temperature aging on the particle size of DPG were studied

by dynamic light scattering (DLS). This work paves the way for the formula design of DPG and its application in the oil and gas field.

The paper “*Catalytic combustion of low concentration methane over catalysts prepared from Co/Mg-Mn layered double hydroxides*” described that a series of Co/Mg-Mn mixed oxides were synthesized through thermal decomposition of layered double hydroxides (LDHs) precursors. The resulted catalysts were then subjected for catalytic combustion of methane and it was revealed that the  $\text{Co}_{4.5}\text{Mg}_{1.5}\text{Mn}_2\text{LDO}$  catalyst possessed the best performance with the  $T_{90} = 485^\circ\text{C}$ . The redox ability of the catalysts can be significantly improved by the addition of cobalt. Besides, certain amount of magnesium was essential to guarantee the catalytic activity, which was helpful to enhance the oxygen mobility and improve the dispersion of Co and Mn oxides, preventing the surface area loss after calcination.

The paper entitled “*Development of low energy gap and fully regioregular polythienylenevinylene derivative*” introduced that low energy gap and fully regioregular conjugated polymers were widely used in solar energy conversion applications. This paper reported the synthesis and characterization of a new polymer, a low energy gap, fully regioregular, terminal functionalized, and processable conjugated polymer poly-(3-dodecyloxy-2,5-thienylene vinylene) or PDDTV. The UV-vis-NIR absorption spectrum demonstrated that the polymer exhibited an optical energy gap of 1.46 eV. The highest occupied molecular orbital (HOMO) level is  $-4.79$  eV based on electrochemical measurement, while the lowest unoccupied molecular orbital (LUMO) level is  $-3.33$  eV based on optical energy gap. The polymer is thermally stable up to about  $300^\circ\text{C}$ , which demonstrated that this polymer is beneficial for effective solar cell applications.

The paper “*Inhibition effect of glycerol on the corrosion of copper in NaCl solutions at different pH values*” investigated the inhibition effect of glycerol against copper corrosion in aerated NaCl (0.5 M) solution at various pH values. The inhibition efficiency was assessed by conventional electrochemical techniques: open circuit potential, potentiodynamic polarization, and electrochemical impedance analysis. It was found that glycerol is capable of reducing the corrosion rate of copper in NaCl solutions. Moreover, glycerol was more efficient for use in alkaline chloride media where the best inhibition effect was obtained ( $\eta \approx 83\%$ ). The inhibition efficiency in alkaline media was ascribed to an increase in viscosity and the presence of copper-glycerol complexes.

The paper entitled “*Investigations of the montmorillonite and aluminium trihydrate addition effects on the ignitability and thermal stability of asphalt*” investigated the effects of unmodified montmorillonite (MMT), organically modified montmorillonite (OMMT), and aluminium trihydrate (ATH) additions on the flame retardancy for asphalt combustion by means of limiting oxygen index (LOI), cone calorimeter, and TG-DSC tests. Experimental results revealed that adding a small amount of montmorillonite did not significantly increase the oxygen index of the asphalt. Besides, TGA measurements showed that the montmorillonite (MMT, OMMT) could suppress the release of flammable volatiles and

form more asphaltenes, which hence postponed the burnout time of asphalt. In addition, the combining montmorillonite (MMT, OMMT) and ATH exerted a synergistic effect, which further reduced the heat release rate and increased the oxygen index of asphalt simultaneously.

In “*Phthaloylchitosan-based gel polymer electrolytes for efficient dye-sensitized solar cells*,” phthaloylchitosan-based gel polymer electrolytes were fabricated with tetrapropylammonium iodide ( $\text{Pr}_4\text{NI}$ ), a material with decent conductivity. The electrolyte with the composition rate of phthaloylchitosan (15.7 wt.%), ethylene carbonate (EC) (31.7 wt.%), propylene carbonate (PC) (3.17 wt.%),  $\text{Pr}_4\text{NI}$  (19.0 wt.%), and iodine (1.9 wt.%) exhibited the highest room temperature ionic conductivity of  $5.27 \times 10^{-3} \text{ S cm}^{-1}$ . The dye-sensitized solar cell (DSSC) fabricated with this electrolyte exhibited an efficiency of 3.5% with JSC of  $7.38 \text{ mA cm}^{-2}$ , VOC of 0.72 V, and fill factor of 0.66. The overall conductivity was observed to decrease as various amounts of lithium iodide (LiI) were added to the optimized gel electrolyte.

The paper entitled “*Preparation of mesoporous  $\text{SnO}_2$  by electrostatic self-assembly*” described that mesoporous  $\text{SnO}_2$  nanoparticles with diameters of 5-6 nm crystalline walls and 3-4 nm pore diameter were successfully obtained with the assistance of templating agent,  $\text{Mo}_7\text{O}_{24}^{6-}$ , at room temperature. XRD, TEM, UV-DRS, XPS, and BET characterization were used to measure the samples. The product has a moderately high surface area of  $132 \text{ m}^2 \text{ g}^{-1}$  and a narrow mesoporous structure with an average pore diameter of 3.5 nm. The methyl orange (MO) aqueous solution was used to evaluate the photocatalytic capability of the mesoporous  $\text{SnO}_2$  under UV light irradiation.

In “*Production of biologically activated carbon from orange peel and landfill leachate subsequent treatment technology*,” orange peel activated carbon with biophile characteristic has been fabricated by one-step method. The yield of the as-prepared biological activated carbon is 50.9%, accompanied with the BET specific surface area, and pore volume reached  $1477 \text{ m}^2/\text{g}$  and  $2.090 \text{ m}^3/\text{g}$ , respectively. The orange peel active carbon has hydroxyl, carbonyl, methoxy, and lactones hydrophilic functional group. The orange peel active carbon had a well adsorption capability to deal with leachate biochemical tail water, ascribed to small crystallite size and crystallite thickness. The removal rate of  $\text{UV}_{254}$  is 63.0% and TOC is 59.7%, respectively. This research can advance the process of effectively controlling water pollution, improving area water quality, easing orange peel waste pollution, and promoting coordinated development among society, economy, and environment.

The paper “*Removing and recovering phosphate from poultry wastewater using amorphous ceramics*” described that a novel strategy for phosphate from poultry wastewater was developed using amorphous ceramics. Widely available, inexpensive materials such as lime and silica fume were used to synthesize amorphous ceramics, which showed high performance for phosphate removal and recovery from poultry wastewater. Phosphate content on the surface of amorphous ceramics could reach 14.20%. This study may be interesting and promising which can advance the development of

the phosphate removing and recovering from poultry wastewater.

The paper entitled “*Structural and electrochemical properties of lithium nickel oxide thin films*” documented that  $\text{LiNiO}_2$  thin films were fabricated by RF magnetron sputtering. X-ray diffraction and field-emission scanning electron microscopy were used to investigate the microstructure of the films. The electrochemical properties were investigated with a battery cycler using coin-type half-cells. Surface carbonate existed when the  $\text{LiNiO}_2$  thin films were annealed below  $500^\circ\text{C}$ . The results reflected that surface carbonate interrupted the Li intercalation and deintercalation during charge/discharge. The capacity did not enhance; nevertheless the annealing process enhanced the crystallization of  $\text{LiNiO}_2$ . The  $\text{ZrO}_2$ -coated  $\text{LiNiO}_2$  thin film showed an enhanced discharge capacity compared to prine  $\text{LiNiO}_2$  thin film. Hence, the enhancement in electrochemical characteristics can be attributed to the inhibition of surface carbonate by the  $\text{ZrO}_2$  coating layer.

The paper entitled “*Synthesis of an anion-exchange membrane based on imidazolium-type ionic liquids for a capacitive energy extraction Donnan potential device*” described that polymeric anion-exchange membranes (AEMs) were synthesized via the photocopolymerization of a vinyl imidazolium ionic liquid, with 1-butyl-3-(4-vinylbenzyl)imidazolium chloride ( $[\text{BVBI}][\text{Cl}]$ ) as the anion-exchange group and styrene, acrylonitrile, and divinylbenzene as cross-linked agents. The mechanical, physical, and electrochemical properties of the fabricated AEMs such as swelling degree (%), water uptake (%), ion-exchange capacity (mmol/g), thermal stability, tensile strength (Mpa), tensile modulus (Mpa), elongation (%), and ionic conductivity (S/cm) were evaluated. The obtained AEMs were demonstrated to have good mechanical, physical, and electrochemical properties for application of a capacitive energy extraction Donnan potential (CDP) device membrane. The CDP device was obtained by using the synthesized AEM, and the specific capacitance of the CDP device with AEM was determined as 2.53 F/g and 3.44 F/g by galvanostatic charge/discharge and cyclic voltammetry, respectively. The synthesized AEM with imidazolium ionic liquid can be beneficial for the development of the CDP device membrane.

The review article “*Synthesis and application of one-dimensional  $\text{La}(\text{OH})_3$  nanostructures: an overview*” is aimed at describing and summarizing current status on the application of 1D  $\text{La}(\text{OH})_3$  nanostructures including nanowires, nanoneedles, nanobelts, and nanorods. Various strategies utilized to synthesize the 1D  $\text{La}(\text{OH})_3$  nanostructures are discussed, such as precipitation, composite-hydroxide-mediated, hydrothermal, and solvothermal methods, as well as the introduction of the corresponding growth mechanisms. Then, the unique properties of 1D  $\text{La}(\text{OH})_3$  nanostructures are assigned to their unique electronic structures and numerous transition modes involving the 4f shells of these ions are represented. Furthermore, the wide applications in photocatalyst, capacitors, and photoluminescence based on the unique properties are discussed. Finally, the article ends with a summary and some perspectives on the challenges and new directions in this emerging area.

## Acknowledgment

We wish to express our sincere thanks to all the authors for submitting interesting contributions to this special issue.

Fan Dong  
Sirilak Sattayasamitsathit  
Yu Xin Zhang  
Ying Zhou

## Research Article

# Synthesis of an Anion-Exchange Membrane Based on Imidazolium-Type Ionic Liquids for a Capacitive Energy Extraction Donnan Potential Device

Young-Seok Kim and Seong-Ho Choi

Department of Chemistry, Hannam University, Daejeon 305-811, Republic of Korea

Correspondence should be addressed to Seong-Ho Choi; [shchoi@hannam.ac.kr](mailto:shchoi@hannam.ac.kr)

Received 19 June 2014; Accepted 31 July 2014; Published 18 September 2014

Academic Editor: Ying Zhou

Copyright © 2014 Y.-S. Kim and S.-H. Choi. This is an open access article distributed under the Creative Commons Attribution License, which permits unrestricted use, distribution, and reproduction in any medium, provided the original work is properly cited.

Polymeric anion-exchange membranes (AEMs) were synthesized via the photocopolymerization of a vinyl imidazolium ionic liquid, with 1-butyl-3-(4-vinylbenzyl)imidazolium chloride ([BVBI][Cl]) as the anion-exchange group and styrene, acrylonitrile, and divinylbenzene as cross-linked agents. The physical, mechanical, and electrochemical properties of the prepared AEMs such as water uptake (%), swelling degree (%), ion-exchange capacity (mmol/g), thermal stability, tensile strength (Mpa), tensile modulus (Mpa), elongation (%), and ionic conductivity (S/cm) were evaluated. The synthesized AEMs were shown to have good physical, mechanical, and electrochemical properties for application of a capacitive energy extraction Donnan potential (CDP) device membrane. The CDP device was fabricated by using the synthesized AEM. The specific capacitance of the CDP device with AEM was determined as 2.53 F/g and 3.44 F/g by galvanostatic charge/discharge and cyclic voltammetry, respectively. The synthesized AEM with imidazolium ionic liquid can be applied as the CDP device membrane.

## 1. Introduction

Polymeric anion-exchange membranes (AEMs), which have selective anion permeability, were applied to wide range fields such as clean up and decontamination processes. AEMs have been traditionally investigated intensively because of their current and potential applications such as ion-exchangers [1], biomaterials [2], coating [3], and membranes in electro dialysis devices [4–7]. In the past decade, interest in AEMs has been focused on their application toward more demanding uses such as alkaline fuel cells, redox flow batteries, and electrolyzers because of the low overpotential of many electrochemical reactions at high pH [8–11]. Most of studies that have interest in AEMs have been related to the development of materials based on quaternized polymers that contain quaternary ammonium groups as anion exchangers.

On the other hand, a capacitive energy extraction Donnan potential (CDP) device is a piece of equipment that extracts energy from the salinity gradient difference between

river and sea water. A CDP device was combined with carbon electrodes and ion-exchange membranes in a supercapacitor flow cell, which has been proposed to have desirable advantages [12]. Sales et al. proposed a characterization methodology of a CDP device with AEM via CDP device performance [13].

Ionic liquids (ILs) have been studied extensively in recent years due to their unique properties. These properties of ILs include being liquid at room temperature and possessing thermal and electrochemical stability because they consist of ions. In addition, ILs also possess low volatility, nonflammability, and high ion conductivity. The excellent ion-exchange capabilities of ILs make them very useful in ion-exchange applications. However, generally ILs cannot be polymerized because they possess no vinyl groups in spite of having unique properties. Therefore, ILs cannot be used to prepare anion-exchange membranes.

In this study, vinyl IL monomer was synthesized with a vinyl group named 1-butyl-3-(4-vinylbenzyl)imidazolium

chloride ([BVBI][Cl]) in order to prepare AEMs. After that, photocopolymerization of the [BVBI][Cl] was performed in the presence of acrylonitrile and styrene as comonomers in order to synthesize AEMs. The physical, mechanical, and electrochemical properties of the synthesized AEMs were investigated for application to the CDP device membrane. Finally, the specific capacitance CDP device with the synthesized AEMs was determined by galvanostatic charge/discharge analysis and cyclic voltammetry analysis.

## 2. Materials and Methods

**2.1. Materials.** Styrene, acrylonitrile, 1-butylimidazole, 4-vinylbenzyl chloride, and divinylbenzene were obtained from Sigma-Aldrich, USA. The acetonitrile, sodium chloride, sodium hydroxide, ammonia solution, and hydrochloric acid solution (Samchun, South Korea) and P12 (NEO Special, South Korea) were purchased. Before use, the acrylonitrile was distilled and the styrene and divinylbenzene were made inhibitor-free by passing the liquid through a column filled with  $\text{Al}_2\text{O}_3$  powder.

**2.2. Synthesis and Characterization of the [BVBI][Cl].** The vinylated ILs, [BVBI][Cl], were synthesized by coupling reaction of 1-butylimidazole (0.2 mol, 30 mL) and 4-vinylbenzyl chloride (0.2 mol, 39 mL) in acetonitrile (150 mL) at 70°C for 16 h under nitrogen atmosphere. The resultants were washed using ether three times to remove acetonitrile and then the products were dried in a vacuum oven at room temperature for 6 h to remove ether. The chemical structure of the synthesized [BVBI][Cl] with vinyl groups was confirmed by  $^1\text{H}$  NMR spectroscopy (Inova 600, Varian, USA) and Fourier transform infrared spectroscopy (IS10 FT-IR, Thermo Scientific, USA).

**2.3. Preparation of the AEMs.** The AEMs were synthesized as follows: the mixture solution of the synthesized [BVBI][Cl] (0.015 mmol, 4 g), styrene (0.043 mmol, 4.5 g), acrylonitrile (0.028 mmol, 1.5 g), divinylbenzene (0.003 mmol, 0.5 g), and P12 (2.0 wt% to feed) as a photoinitiator was stirred to obtain a homogeneous solution. The AEMs were prepared by photocopolymerization of the mixture solution on glass plate using irradiation with ultraviolet light of a 250~440 nm wavelength for 30 min at room temperature as shown in Figure 1.

**2.4. Characterization of the AEMs.** The chemical structure of the synthesized AEMs was confirmed by  $^1\text{H}$  NMR spectroscopy (Inova 600, Varian, USA) and Fourier transform infrared (FT-IR) spectroscopy (IS10 FT-IR spectrometer, Thermo Scientific, USA). The morphology of the prepared AEMs was also characterized by using a scanning electron microscope (FE-SEM (S-4800), Hitachi Science System, Japan).

The water uptake  $W(\%)$  for the synthesized AEMs was calculated with the following equation:

$$W(\%) = \frac{W_w - W_d}{W_d} \times 100\%, \quad (1)$$

where  $W_d$  and  $W_w$  are the weight of the dried and wetted AEMs immersed in deionized water at room temperature for 24 h, respectively. Here, the wetted AEMs were treated by removing the excess water on the surface using tissue paper.

The swelling ratio (%) for the AEMs was characterized by a linear expansion ratio, which was determined by the difference between the wet and dry dimensions of a membrane sample. The calculation was conducted with the following equation:

$$\text{Swelling}(\%) = \frac{X_{\text{wet}} - X_{\text{dry}}}{X_{\text{dry}}} \times 100\%, \quad (2)$$

where  $X_{\text{wet}}$  and  $X_{\text{dry}}$  are the lengths of the wet state and dry state AEMs, respectively.

The ion exchange capacity (IEC) of the AEMs was determined via a back-titration method. The AEMs were dried and weighed before immersing them in a 0.01 M NaOH solution (100 mL) for 48 h. The AEMs with hydroxide ions were again immersed in 0.01 M HCl solution for 48 h. After anion exchange, the HCl solution was titrated by a 0.01 M ammonia solution in the presence of phenolphthalein as an indicator. The IEC value was calculated as follows:

$$\text{IEC} = \frac{V_{0,\text{HCl}}C_{\text{HCl}} - V_{\text{X,HCl}}C_{\text{HCl}}}{m_{\text{dry}}}, \quad (3)$$

where  $V_{0,\text{HCl}}$  and  $V_{\text{X,HCl}}$  are the volume of the consumed HCl without AEMs and with AEMs, respectively.  $C_{\text{HCl}}$  is the molar concentration of the HCl, which is titrated by the 0.01 M ammonia solution, and  $m_{\text{dry}}$  is the mass of the dry samples. Titration was performed three times.

The mechanical properties of the samples were measured by using an Instron universal tester (AG-X, Shimadzu, Japan) at room temperature, with 10 mm × 25 mm at a crosshead speed of 25 mm/min. Tensile strength, tensile modulus, and elongation at break values were recorded.

The thermal stabilities of the synthesized samples were recorded by thermogravimetric analyzer (TGA N-1000, SCINCO, South Korea) under a nitrogen flow from 25 to 500°C at a heating rate of 10°C/min  $r$ .

The resistance value of the prepared AEMs was measured by four-point probe alternating current (AC) impedance spectroscopy (IM 6 EX, Zahner, German) with a frequency range of 1 Hz to 1 MHz. The ionic conductivity of the membrane,  $\sigma$  (S/cm), was calculated from the equation:

$$\sigma = \frac{l}{RA}, \quad (4)$$

where  $l$  is the distance between two platinum wire electrodes (cm),  $A$  is the cross-sectional area of sample ( $\text{cm}^2$ ), and  $R$  is the sample resistance value from the AC impedance data ( $\Omega$ ). The samples were fully hydrated in deionized water for 24 h for conductivity measurement. To maintain the relative humidity at 100% during the experiments, conductivity measurements were conducted in a chamber filled with deionized water under fully hydrated conditions.

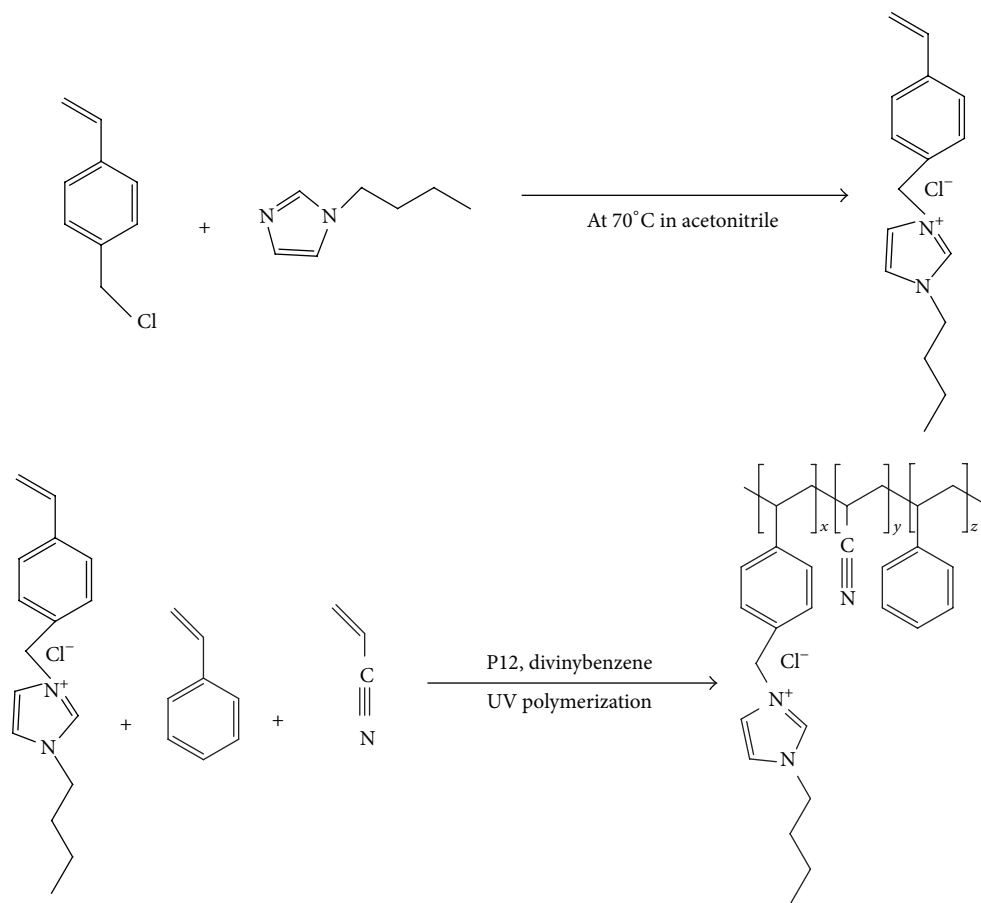


FIGURE 1: Synthesis of anion-exchange vinyl monomer and anion-exchange polymer by UV copolymerization.

**2.5. Fabrication of CDP Device Flow System with AEMs.** The CDP device flow system with a flow channel of  $10\text{ cm} \times 2.2\text{ cm} \times 1.5\text{ cm}$  was fabricated according to a homemade method (see Figure 7(a)). Graphite plates were used as current collectors (unique carbon, South Korea). Here, each current collector was introduced to an activated carbon electrode, which is prepared by coating of the activated carbon slurry with 10% nafion (Sigma-Aldrich, USA) on carbon paper. The surface area of the activated carbon electrode was calculated as  $22\text{ cm}^2$ . In detail, the carbon slurry was prepared by the mixing of the activated carbon powder (2.0 g) and 10% nafion (2.0 mL) in 2-propanol (2.0 mL) by magnetic stirring for 12 h. The carbon slurry was casted by doctor blade on the surface of graphite paper (Wonatech, South Korea) and was then dried for 24 h at room temperature. The 0.5 M NaCl solution and a 0.017 M NaCl solution as an electrolyte were sequentially flowed in the CDP device at a 60 mL/min flow rate.

The capacitance ( $F$ ) was investigated by the cyclic voltammetry and galvanostatic charge-discharge methods (Versa STAT-3, Ametek, USA). In detail, the cyclic voltammetry analysis of the CDP device was performed from 0.4 V to  $-0.4\text{ V}$  with 1 mV/s. The capacitance ( $F$ ) of the CDP device with AEMs was measured as the total integrating current value in a range of 0.0 V~+0.3 V from the obtained cyclic voltammograms.

Galvanostatic charge-discharge with a current density of  $0.45\text{ A/m}^2$  was also performed. The capacitance ( $F$ ) was calculated as in the following equation:

$$C = \frac{Q}{\Delta V}, \quad (5)$$

where  $C$  is the capacitance ( $F$ ),  $Q$  is the amount of charges ( $C$ ), and  $\Delta V$  ( $V$ ) is obtained from Galvanostatic charge-discharge data.

### 3. Results and Discussion

Figure 2 designates the Fourier transform infrared (FT-IR) spectra of the [BVBI][Cl] as ionic liquids and the prepared AEMs. Both [BVBI][Cl] and the AEMs displayed the characteristic peaks at  $3000\sim 3200\text{ cm}^{-1}$  and  $1450\sim 1600\text{ cm}^{-1}$  due to the aromatic ring in vinyl ionic liquids and AEMs. The characteristic peaks at  $\sim 1578\text{ cm}^{-1}$  and  $\sim 861\text{ cm}^{-1}$  were also displayed due to the imidazolium cations stretching band. The peaks of the cyano ( $-\text{C}\equiv\text{N}$ ) group for the vinyl ionic liquids and AEMs were presented at  $2248\text{ cm}^{-1}$  as strong stretching. As for results, the vinyl ionic liquids as vinyl monomers and AEMs were successfully synthesized.

Figure 3 shows the  $^1\text{H}$  NMR spectra of the synthesized vinyl ionic liquids (Figure 3(a)) and AEMs prepared by

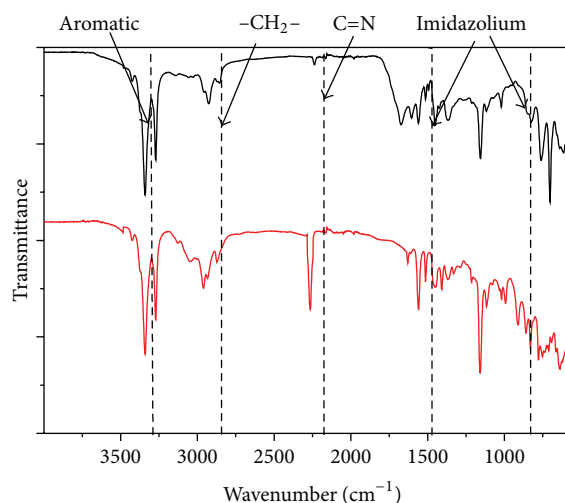


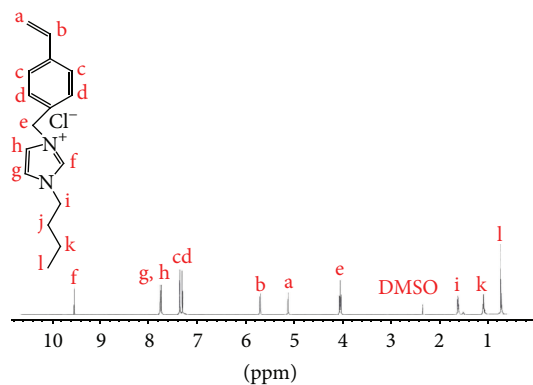
FIGURE 2: FT-IR spectra of [BVBI][Cl] (black line) and anion-exchange membrane (red line).

photocopolymerization (Figure 3(b)). The structures of the [BVBI][Cl] and AEMs were assigned as shown in Figure 3. From these results, it is clear that the AEMs for CDP device were successfully synthesized.

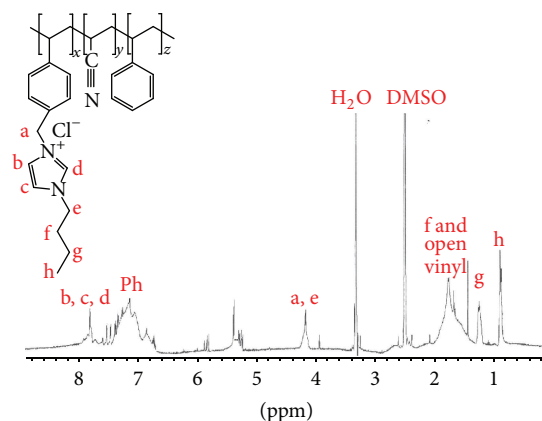
Figure 4 presents photograph (Figure 4(a)), of the surface SEM images (Figure 4(b)), and the cross-section SEM image (Figure 4(c)) for the AEM prepared photocopolymerization. The prepared AEM appeared as a transparent film and displayed uniform surface morphology as shown in Figures 4(a) and 4(b). The thickness of the prepared AEMs was determined to be about  $26.1 \mu\text{m}$  from the cross-section SEM images. In the cross-section SEM image of the AEM, the diversiform voids were presented due to solvent evaporation based on high temperature induced during photocopolymerization. However, visual observation was used to confirm that the prepared AEMs displayed good mechanical properties before they were used as a CDP device membrane.

Figure 5 displays thermogravimetric analysis (TGA) curves (Figure 5(a)) and an impedance plot (Figure 5(b)) of AEM prepared by photocopolymerization. In Figure 5(a), the first weight loss for the AEM was displayed during  $250^\circ\text{C} \sim 450^\circ\text{C}$  due to copolymer main degradation. These results mean the synthesized AEM displayed high thermal stability. The electrical resistance of the SEM was  $9.47 \times 10^3 \Omega$  as shown in Figure 5(b). The ion conductivity of the AEM was calculated to be  $3.05 \times 10^{-3} \text{ S/cm}$ . As for results, the prepared AEM could be applied as an anionic-exchanged membrane in a CDP device flow system.

Table 1 summarizes the physical, mechanical, and electrochemical properties of the synthesized AEM. The water uptake (%) and swelling degree of the AEM were 66.0% and 27.8%, respectively. Tensile strength, tensile modulus, and elongation at the break of the prepared AEM were calculated to be 13.3 Mpa, 330.3 Mpa, and 42.6%, respectively. The ion exchange capacity (IEC) of the prepared AEM can be refracted from the exchangeable properties. The IEC value of the AEM was 0.499 mmol/g, and this value was close to the



(a)



(b)

FIGURE 3:  $^1\text{H}$  NMR spectra of the synthesized vinyl ILs (a) and AEMs prepared by photocopolymerization (b).

theoretical value (0.567 mmol/g). As for results, the prepared AEMs can be used as separators in CDP device flow systems.

Figure 6 displays a photograph of the CDP device flow system with AEMs (Figure 6(a)) and cell potential (mV) and power density ( $\text{mW/m}^2$ ) according to time (Figure 6(b)) for 0.5 M NaCl electrolyte flow as charging and 0.015 M NaCl electrolyte flow as discharging. In CDP flow system performance, the 0.5 M NaCl electrolyte first flowed through the CDP flow device as a charging step related to linear cell potential. In this study, the linear cell potential ( $\sim 18 \text{ mV}$ ) of the CDP device with AEM was reached at time of 1000 s. This means that ions flowed through the anion-exchange membranes to the capacitive electrodes. The Donnan potential occurred in the CDP device with AEM from ion flow to the capacitive electrode as cell potential. In this CDP device with AEM performance, the highest power density obtained was calculated at  $109.0 \text{ mW/m}^2$  as charging step and  $20 \text{ mW/m}^2$  as discharging step, respectively. As for the results, energy extraction from the CDP device flow system with AEM could be obtained according to the salinity gradients.

Figure 7 displays cyclic voltammograms with a  $1.0 \text{ mV/s}$  scan rate (Figure 7(a)) and the galvanostatic charge and discharge (Figure 7(b)) of the CDP device flow system with  $0.45 \text{ A/m}^2$  current density at a  $60 \text{ mL/min}$  flow rate. In

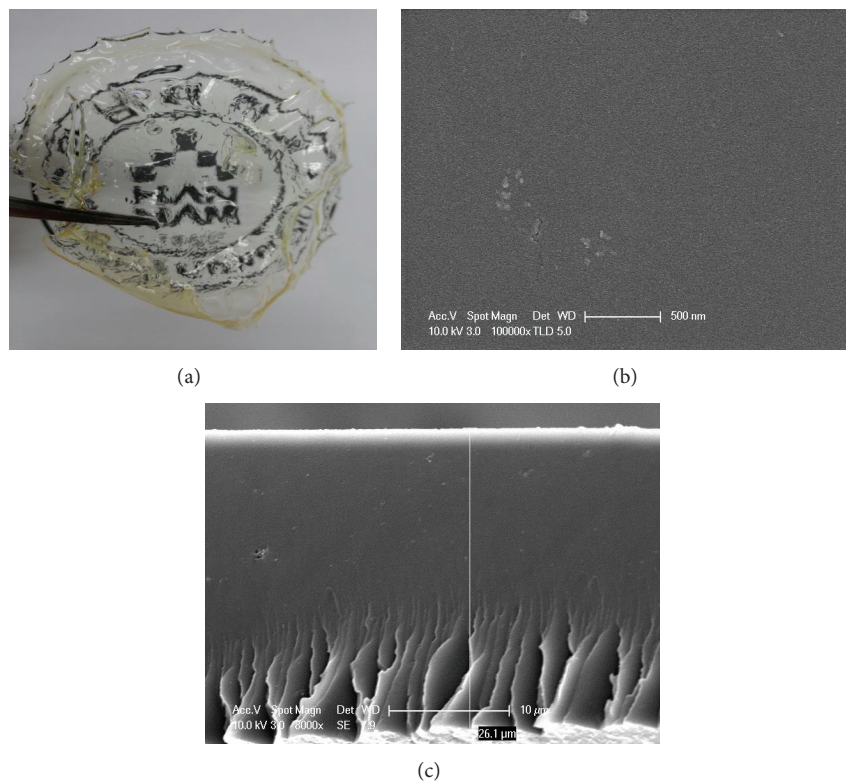


FIGURE 4: Photograph (a), the surface SEM images (b), and cross-section SEM image (c) for the AEM prepared photocopolymerization.

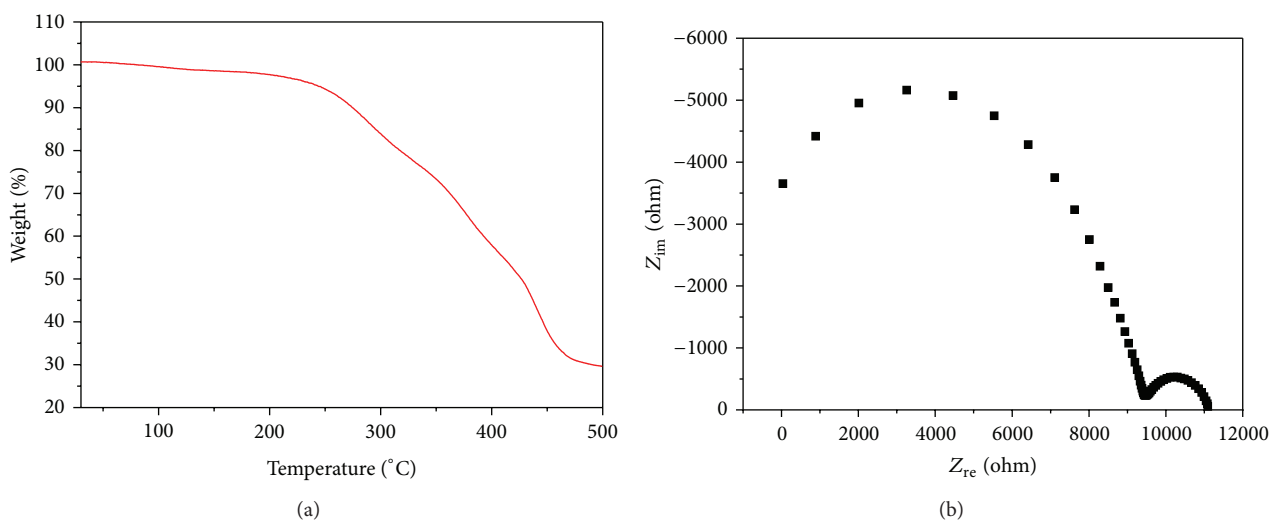


FIGURE 5: Thermogravimetric analysis (TGA) curves (a) and an impedance plot (b) of AEM prepared by photocopolymerization.

TABLE I: Physical, mechanical, and electrochemical properties of the synthesized AEMs.

	Physical properties		Mechanical properties			Electrochemical properties		
	Water uptake (%)	Swelling ratio (%)	Tensile strength (Mpa)	Tensile modulus (Mpa)	Elongation at break (%)	Ion conductivity (S/cm)	Ion exchange capacity (mmol/g)	
							Theoretical	Experimental
AEM	66.0	27.8	13.3 ± 2.1	330.3 ± 24.1	42.6 ± 7.7	3.05 × 10 <sup>-3</sup>	0.567	0.499

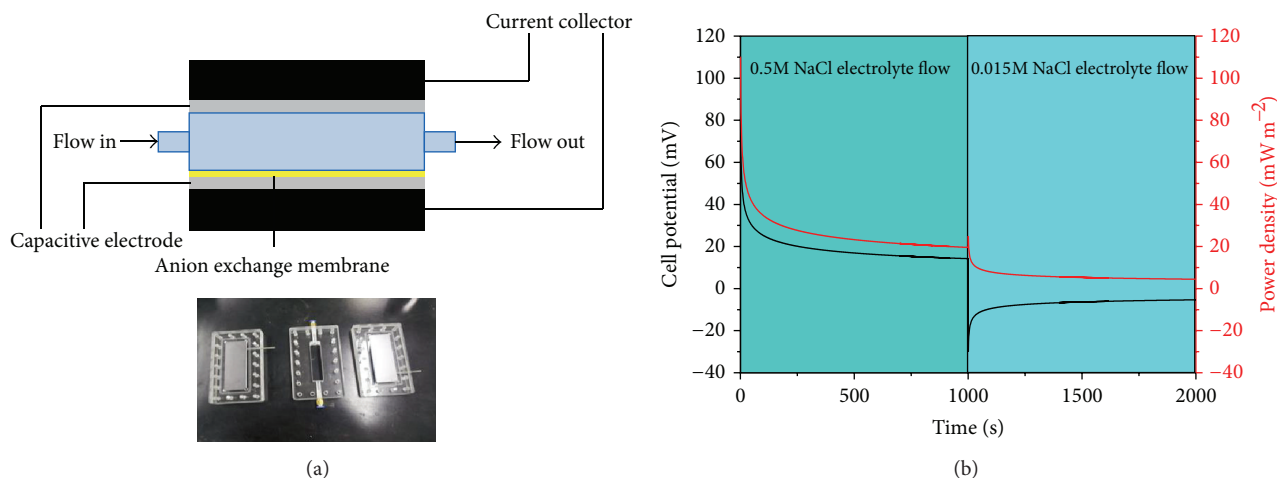


FIGURE 6: Photograph of the CDP device flow system with AEMs (a) and cell potential (mV) and power density ( $\text{mW}/\text{m}^2$ ) according to time (b) for 0.5 M NaCl electrolyte flow as charging and 0.015 M NaCl electrolyte flow as discharging.

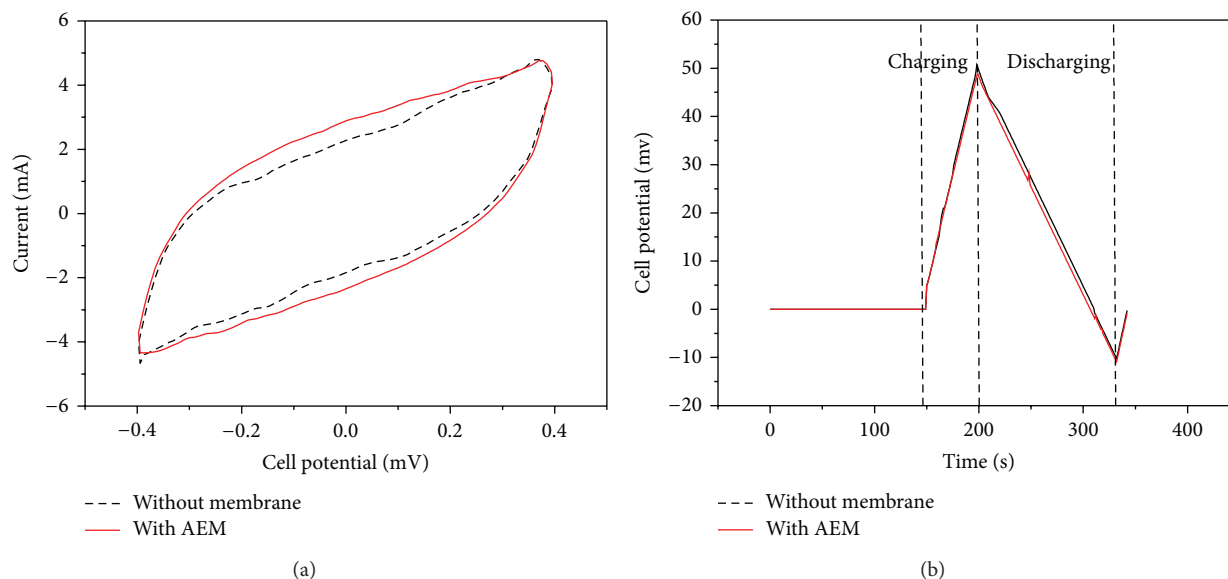


FIGURE 7: Cyclic voltammograms with 1.0 mV/s scan rate (a) and galvanostatic charge and discharge (b) with  $0.45 \text{ A}/\text{m}^2$  current density of CDP device flow system at a 60 mL/min flow rate.

Figure 7(a), the specific capacitances of the CDP device with AEM and without AEM were calculated at 3.44 F/g and 2.93 F/g, respectively. In Figure 7(b), the specific capacitances of the CDP device with AEM were also determined to be at 2.53 F/g and 2.20 F/g as charging and discharging, respectively. The specific capacitances of the CDP device without AEM were also determined to be 2.41 F/g and 2.17 F/g as charging and discharging, respectively. As for the results, the specific capacitance of the CDP device with AEM was higher than that of the CDP device without AEM. The prepared AEMs can be used as a separator in CDP device flow systems.

Table 2 summarizes the specific capacitances (F/g) of a CDP device flow system with a 60 mL/min flow rate in 0.5 M

NaCl electrolyte in the presence and absence of AEM. The specific capacitance of the CDP device flow system with AEM was higher than that of the CDP device flow system without AEM by CV and galvanostatic charge and discharge measurement. From these results, the synthesized AEM can be applied as a separator in CDP device flow systems.

#### 4. Conclusions

The AEMs were synthesized via the photocopolymerization of vinyl imidazolium ionic liquid, [BVBI][Cl] as anion-exchange group, styrene, acrylonitrile, and divinylbenzene as cross-linked agents. The synthesized AEMs were characterized with physical, mechanical, and electrochemical

TABLE 2: Specific capacitances (F/g) of the CDP device flow system with a 60 mL/min flow rate in 0.5 M NaCl electrolyte in the presence and absence of AEM.

	Galvanostatic charge-discharge <sup>a</sup>		Cyclic voltammetry <sup>b</sup>
	Charge (F/g)	Discharge (F/g)	
Without AEM	2.41	2.17	2.41
With AEM	2.53	2.20	3.44

<sup>a</sup>At a 0.45 A/m<sup>2</sup> current density.

<sup>b</sup>At a 1 mV/s scan rate.

properties in order to be used as membranes in CDP devices. As a result, the conclusions are as follows.

- (1) Water uptake (66.0%), swelling degree (27.8%), tensile strength (13.3 Mpa), tensile modulus (330.3 Mpa), elongation at break (42.6%), ion conductivity ( $3.05 \times 10^{-3}$  S/cm), and ion exchange capacity (0.499 mmol/g) for the AEMs were evaluated.
- (2) The specific capacitance of a CDP device flow system with AEMs was calculated at 3.44 F/g by CV analysis and at 2.53 F/g by galvanostatic charge-discharge analysis, respectively.
- (3) That synthesized AEM can be applied as a separator in CDP device flow systems.

## Conflict of Interests

The authors declare that there is no conflict of interests regarding the publication of this paper.

## Acknowledgment

This work was supported by National Research Foundation of Korea Grant funded by the South Korean government (NRF-2013M1A3A3A02041878).

## References

- [1] E. S. Dragan, E. Avram, D. Axente, and C. Marcu, "Ion-exchange resins. III. functionalization-morphology correlations in the synthesis of some macroporous, strong basic anion exchangers and uranium-sorption properties evaluation," *Journal of Polymer Science A: Polymer Chemistry*, vol. 42, no. 10, pp. 2451–2461, 2004.
- [2] A. K. Salem, F. R. A. J. Rose, R. O. C. Oreffo et al., "Porous polymer and cell composites that self-assemble in situ," *Advanced Materials*, vol. 15, no. 3, pp. 210–213, 2003.
- [3] X. Jiang, H. Yu, R. Frayne, O. Unal, and C. M. Strother, "Surface functionalization of polyethylene for magnetic resonance signal-enhancing coating materials," *Chemistry of Materials*, vol. 14, no. 5, pp. 1914–1920, 2002.
- [4] J. R. Varcoe and R. C. T. Slade, "Prospects for alkaline anion-exchange membranes in low temperature fuel cells," *Fuel Cells*, vol. 5, no. 2, pp. 187–200, 2005.
- [5] A. R. Roudman and R. P. Kusy, "UV-visible spectroscopic study of the reaction kinetics of methylpiperazine-modified poly(vinyl chloride)s for use as fixed-state proton carrier membranes," *Polymer*, vol. 39, no. 16, pp. 3641–3649, 1998.
- [6] T. Xu, Z. Liu, and W. Yang, "Fundamental studies of a new series of anion exchange membranes: membrane prepared from poly(2,6-dimethyl-1,4-phenylene oxide) (PPO) and triethylamine," *Journal of Membrane Science*, vol. 249, no. 1-2, pp. 183–191, 2005.
- [7] R. C. T. Slade and J. R. Varcoe, "Investigations of conductivity in FEP-based radiation-grafted alkaline anion-exchange membranes," *Solid State Ionics*, vol. 176, no. 5-6, pp. 585–597, 2005.
- [8] J. Wang, Z. Zhao, F. Gong, S. Li, and S. Zhang, "Synthesis of soluble poly(arylene ether sulfone) ionomers with pendant quaternary ammonium groups for anion exchange membranes," *Macromolecules*, vol. 42, no. 22, pp. 8711–8717, 2009.
- [9] S. Lu, J. Pan, A. Huang, L. Zhuang, and J. Lu, "Alkaline polymer electrolyte fuel cells completely free from noble metal catalysts," *Proceedings of the National Academy of Sciences of the United States of America*, vol. 105, no. 52, pp. 20611–20614, 2008.
- [10] Y. Wang, L. Li, L. Hu, L. Zhuang, J. Lu, and B. Xu, "A feasibility analysis for alkaline membrane direct methanol fuel cell: thermodynamic disadvantages versus kinetic advantages," *Electrochemistry Communications*, vol. 5, no. 8, pp. 662–666, 2003.
- [11] G. F. McLean, T. Niet, S. Prince-Richard, and N. Djilali, "An assessment of alkaline fuel cell technology," *International Journal of Hydrogen Energy*, vol. 27, no. 5, pp. 507–526, 2002.
- [12] D. Brogioli, R. Zhao, and P. M. Biesheuvel, "A prototype cell for extracting energy from a water salinity difference by means of double layer expansion in nanoporous carbon electrodes," *Energy and Environmental Science*, vol. 4, no. 3, pp. 772–777, 2011.
- [13] B. B. Sales, F. Liu, O. Schaetzle, C. J. N. Buisman, and H. V. M. Hamelers, "Electrochemical characterization of a supercapacitor flow cell for power production from salinity gradients," *Electrochimica Acta*, vol. 86, pp. 298–304, 2012.

## Research Article

# Development of Low Energy Gap and Fully Regioregular Polythiénylenevinylene Derivative

Tanya M. S. David,<sup>1</sup> Cheng Zhang,<sup>1,2</sup> and Sam-Shajing Sun<sup>1</sup>

<sup>1</sup> Center for Materials Research, Norfolk State University, 700 Park Avenue, Norfolk, VA 23504, USA

<sup>2</sup> Department of Chemistry and Biochemistry, South Dakota State University, P.O. Box 2202, Brookings, SD 57007, USA

Correspondence should be addressed to Sam-Shajing Sun; [ssun@nsu.edu](mailto:ssun@nsu.edu)

Received 20 June 2014; Accepted 15 August 2014; Published 3 September 2014

Academic Editor: Sirilak Sattayasamitsathit

Copyright © 2014 Tanya M. S. David et al. This is an open access article distributed under the Creative Commons Attribution License, which permits unrestricted use, distribution, and reproduction in any medium, provided the original work is properly cited.

Low energy gap and fully regioregular conjugated polymers find its wide use in solar energy conversion applications. This paper will first briefly review this type of polymers and also report synthesis and characterization of a specific example new polymer, a low energy gap, fully regioregular, terminal functionalized, and processable conjugated polymer poly-(3-dodecyloxy-2,5-thiénylene vinylene) or PDDTV. The polymer exhibited an optical energy gap of 1.46 eV based on the UV-vis-NIR absorption spectrum. The electrochemically measured highest occupied molecular orbital (HOMO) level is  $-4.79$  eV, resulting in the lowest unoccupied molecular orbital (LUMO) level of  $-3.33$  eV based on optical energy gap. The polymer was synthesized via Horner-Emmons condensation and is fairly soluble in common organic solvents such as tetrahydrofuran and chloroform with gentle heating. DSC showed two endothermic peaks at  $67^{\circ}\text{C}$  and  $227^{\circ}\text{C}$  that can be attributed to transitions between crystalline and liquid states. The polymer is thermally stable up to about  $300^{\circ}\text{C}$ . This polymer appears very promising for cost-effective solar cell applications.

## 1. Introduction

Availability of organic conjugated polymers with different frontier orbitals and energy gaps is crucial and vital for the development and optimizations of polymer based optoelectronic devices such as solar cells or photodetectors. Polythiénylene vinylene (PTVs) are one class of conjugated polymers that are very attractive for optoelectronic applications due to its relatively lower energy gaps compared to polyphenylenevinylenes (PPVs) and polythiophenes (PThs), and particularly its capability of forming regioregular polymers with high crystallinity in solid states [1]. PTVs are derivatives of polythiophenes that have vinylene linkages between the aromatic thiophene rings. With the combination of the low resonance energy and good thermal stability of the thiophene ring, incorporation of the vinylene linkage as well as other tailoring methods into the macroscopic structure all contribute to the very promising electronic and photonic properties that have been observed from PTVs [2–4]. The introduction of the vinylene linkage into the polymer main chain lowers band gaps by about 0.3 eV in comparison

to polythiophenes [4]. One of the appealing features about PTVs is that chemical modification for tuning optoelectronic properties can be done with relative ease and gives rise to promising properties.

PTVs have been synthesized using a number of synthetic methods such as Ni-catalyzed Grignard [2, 5, 6], Stille coupling [7–9], Heck coupling [2], Horner-Emmons [1, 10], acyclic diene metathesis (ADMET) [11], dithiocarbamate route [12, 13], sulphanyl route [14], and bis(xanthate) route [14] (Figure 1).

Many of these synthetic methods give regiorandom coupling (head-head and tail-tail) (Figure 2). However, it has been shown that the Ni-catalyzed Grignard method and the Horner-Emmons method can promote 100% regioregular coupling (head-tail).

Alkoxy-substituted PTV (RO-PTV) has been synthesized by many of these methods; however, the resulting polymers have a regiorandom coupling [7, 12]. From our earlier work on the synthesis of a 3-dodecyl-substituted PTV (RR-C<sub>12</sub>-PTV) via Horner-Emmons reaction as well as Stille coupling reaction [1], we learned that PTV from the Stille reaction was

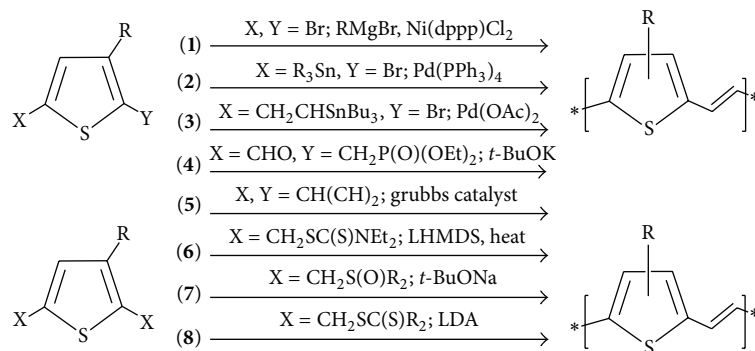


FIGURE 1: Various synthetic routes to synthesize PTV: 1 [2, 5, 6], 2 [7–9], 3 [2], 4 [1, 10], 5 [11], 6 [12, 13], 7 [14], and 8 [14].

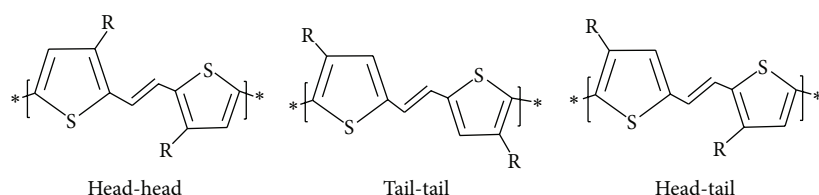


FIGURE 2: Regiorandom and regioregular coupling of PTV polymer.

neither regioregular nor structurally free of defect. On the other hand, Horner-Emmons reaction produced  $C_{12}$ -PTV with 100% head-to-tail regioregularity, which showed much higher crystallinity than the regiorandom  $C_{12}$ -PTV obtained via the Stille coupling reaction [1].

In this work, a 3-dodecyloxy-substituted PTV ( $C_{12}O$ -PTV) or PDDTV, the alkoxy analog of our previously synthesized PTV, was synthesized by Horner-Emmons reaction utilizing asymmetrically functionalized monomers. A different synthetic approach was taken for the synthesis of PDDTV than our previously synthesized RR- $C_{12}$ -PTV, which proved more favorable for the more electron rich alkoxy-substituted thiophene. Compared to PTV, the new PDDTV exhibits the advantage of having a lower band gap due to the electron donating properties of the alkoxy substituent and better for matching photons of similar energy on surface of the earth. The optoelectronic properties of the polymer will also be discussed.

## 2. Experimental Section

All commercially available products were used as received. Proton and carbon NMR spectra were recorded at a 300 MHz NMR spectrometer. Flash column chromatography was performed using Sigma-Aldrich silica gel 60 (200–400 mesh). Electrochemical studies (cyclic voltammetry) were performed on a Bioanalytical (BAS) Epsilon-100w tri-electrode cell system. Three electrodes are a glassy carbon working electrode, an ancillary Pt electrode, and a silver reference electrode (in a  $CH_3CN$  solution of 0.01 M  $AgNO_3$  and 0.1 M TBA-HFP). The polymer samples were dried directly on the electrode and placed a solution of anhydrous  $CH_3CN$  with

0.10 M tetrabutylammonium hexafluorophosphate (TBA-HFP). Ferrocene (2 mM in 0.10 M TBA-HFP/THF solution) was used as an internal reference standard (its HOMO level of  $-4.8$  eV was used in calculations). Before starting a measurement, dry nitrogen gas was bubbled through the solution for at least 10 min to remove any dissolved oxygen. Between the experiments, the surface of the electrodes was cleaned or polished. Scan rate was 100 mV/s.

**2.1. 3-Methoxythiophene (1).** Literature method was followed with minor modifications [15, 16].

Copper bromide (9.629 g, 67 mmol) was weighed in a 500 mL round bottom flask and placed in a nitrogen atmosphere glove box. Within the glove box sodium methoxide (54.067 g, 1000 mmol) and dry NMP (171.476 g, 1729 mmol) were added, and the flask was stoppered and removed from the glove box. With a syringe, 3-bromothiophene (108.130 g, 663.2 mmol) was added, and the solid reagents were allowed to dissolve at  $110^\circ C$  for 15 min. After the addition of anhydrous methanol (100 mL), the reaction was allowed to reflux at  $110^\circ C$  for 3 hours and 15 minutes. Throughout the reaction time a receiving flask collected vaporized methanol. At reaction end, the product was separated by vacuum distillation, followed by washing the organic layer with water (100 mL  $\times$  3) and aqueous layer with pentane (100 mL  $\times$  3). The organic layer was then dried with magnesium sulfate ( $MgSO_4$ ) and filtered, and all the solvent was removed by a rotary evaporator. The product was pale yellow oil with a 78.59% yield. NMR data match with the literature data.

**2.2. 3-Dodecyloxythiophene (2).** The literature method for 3-octylthiophene was followed [17].

3-Methoxythiophene (26.86 g, 235 mmol), p-toluenesulfonic acid monohydrate (0.91 g, 4.78 mmol), and 1-dodecanol (39.21 g, 210.4 mmol) were mixed together in a 1000 mL round bottom flask and refluxed at 92°C at low pressure (220 mTorr–132 mTorr) for 3.5 hours. The reaction was allowed to cool down to room temperature, followed by the addition of a 1:1 molar equivalent of sodium carbonate to p-toluenesulfonic acid in order to quench the acid. The solution was then washed with water (100 mL) and hexane (100 mL). Subsequent washings of the aqueous and organic layer were done with hexane (50 mL × 3) and water (50 mL × 3), respectively. Separation of organic layer was done by low pressure to vacuum distillation, and purification was performed by column chromatography (hexane as eluent). The product was a light green solid with a 91.64% (57.88 g) yield. <sup>1</sup>H NMR (CDCl<sub>3</sub>): δ 0.88 (t, 3H), 1.26 (m, 18H), 1.76 (t, 2H), 3.91 (t, 2H), 6.22 (t, 2H), 6.71 (t, 2H), 7.12 (t, 2H). <sup>13</sup>C NMR: δ 14.1, 22.71, 26.0, 29.6, 31.9, 70.2, 76.6 (CDCl<sub>3</sub>), 96.9, 119.5, 124.4, 158.0. Anal. Calcd: C, 71.58; H, 10.51; S, 11.94. Found: C, 71.41; H, 10.57; S, 11.69.

2.3. *2,5-Dibromo-3-dodecyloxythiophene (3)*. NBS (45 g, 247 mmol/~2.7 mol equiv.) was dissolved in anhydrous DMF (100 mL) and added dropwise to a mixture of 3-dodecyloxythiophene (27.88 g, 103.8 mmol) and anhydrous DMF (120 mL) in a low temperature bath. The addition and the reaction were done with the exclusion of light by covering the flask in a black plastic bag. The reaction was carried out at room temperature for 3–6 hours. The product was extracted with hexane and water (2 mL × 5) and purified by column chromatography (hexane as eluent). The product retrieved was light green oil with a yield 47.97% (18.09 g). <sup>1</sup>H NMR (CDCl<sub>3</sub>): δ 0.88 (t, 3H), 1.26 (m, 18H), 1.73 (t, 2H), 3.98 (t, 2H), 6.75 (s, 2H). <sup>13</sup>C NMR: δ 14.0, 22.6, 25.7, 29.3, 72.5, 76.5 (CDCl<sub>3</sub>), 90.5, 109.3, 120.8, 153.8. Anal. Calcd for C<sub>16</sub>H<sub>26</sub>Br<sub>2</sub>O: S: C, 45.08; H, 6.15; Br, 37.49; S, 7.52. Found: C, 45.18; H, 6.22; Br, 37.27.

2.4. *3-Dodecyloxy-2,5-diformylthiophene (4)*. Anhydrous THF (40 mL) was added to 2,5-dibromo-3-dodecyloxythiophene (12.2 g, 28.6 mmol). This mixture was then added dropwise, by syringe, to a mixture of THF (50 mL) and 1.6 M butyl lithium (53.66 mL/3 mol equiv.) that was in a dry ice/hexane bath. The reagents reacted at ~ -78°C for 5 to 10 minutes and then were removed from the dry ice bath. This solution was slowly added with a syringe to anhydrous DMF (7.09 mL, 3.2 mol eq.) and allowed to react for 5 minutes after addition. The product was extracted by first washing the solution with water (100 mL), hexane (100 mL), and acetic acid (15 mL to 20 mL) (which was monitored using litmus paper as the acid was added) in a separatory funnel. Once the organic and aqueous solution visibly separated, the aqueous layer was discarded, and sodium carbonate was added until the organic solution was basic. The organic layer was further washed with water (50 mL × 4) and aqueous layer with hexane (50 mL × 4). The product was dried with MgSO<sub>4</sub>, solvent removed by rotary evaporator, and the product recrystallized. The filtrate from the recrystallized crystals was

purified using column chromatography (1EtAc:17 hexane used as eluent). The solid yellow product had a 59.5% (5.527 g) yield. <sup>1</sup>H NMR (CDCl<sub>3</sub>): δ 0.87 (t, 3H), 1.26 (m, 18H), 1.85 (t, 2H), 4.21 (t, 2H), 7.25 (s, 1H), 9.89 (s, 1H), 10.1 (s, 1H). <sup>13</sup>C NMR: δ 14.1, 22.6, 25.7, 29.6, 31.9, 72.4, 77.1 (CDCl<sub>3</sub>), 121.7, 127.4, 146.5, 163.2, 182.2, 183.0. Anal. Calcd for C<sub>18</sub>H<sub>28</sub>O<sub>3</sub>S: C, 66.63; H, 8.70; S, 9.88. Found: C, 66.91; H, 8.65; S, 9.81.

2.5. *3-Dodecyloxy-2-formyl-5-methylhydroxyl Thiophene (5)*. A solution of ethyl alcohol (60 mL), 3-dodecyloxy-2,5-diformyl thiophene (3.69 g, 11.3 mmol), and sodium carbonate (4 drops) were allowed to stir at room temperature until all of the starting material dissolved. In a 50 mL Erlenmeyer flask, water (4 g) was added to potassium hydroxide flakes (3.22 g, 3 mol eq.) and the solid was first allowed to dissolve then placed in an ice bath to cool. Once the solution cooled, sodium borohydride (0.2154 g, 0.367 mol eq.) was then added and stirred until it dissolved. After the sodium borohydride dissolved, that solution was added dropwise to the 3-dodecyloxy-2,5-diformyl thiophene solution with vigorous stirring and allowed to react for five minutes. Next, in a warm water bath (40°C) solid sodium bicarbonate (5.82 g, 6.1 mol eq.) was added to the solution, and a light flow of air blew into the flask through a tube to slowly remove the ethanol. The solution was taken out of the warm bath after five minutes once the solution turned dark brown with a precipitate at the bottom of the flask. The product was extracted by first washing the solution with water (7 mL), and diethyl ether, and the aqueous layer was discarded. Then, water (2 mL) and sodium chloride (brine) were added to the organic layer and were discarded along with any inorganic salts. The organic layer was further washed with water (2 mL × 3) and aqueous layer with ether (3 mL × 4). The product was dried with MgSO<sub>4</sub>, and the solvent removed by rotary evaporator. The product was purified by column chromatography (1 EtAc:5 hexane used as eluent). The solid yellowish orange product had a 92.45% (3.43 g) yield. <sup>1</sup>H NMR (CDCl<sub>3</sub>): δ 0.88 (t, 3H), 1.26 (m, 18H), 1.79 (t, 2H), 3.25 (t, 1H), 4.11 (t, 2H), 4.77 (d, 2H), 6.78 (s, 1H), 9.89 (s, 1H). <sup>13</sup>C NMR: δ 14.1, 22.6, 25.8, 29.6, 31.9, 60.7, 72.0, 76.6 (CDCl<sub>3</sub>), 113.3, 119.7, 156.3, 164.9, 181.3. Anal. Calcd for C<sub>18</sub>H<sub>30</sub>O<sub>3</sub>S: C, 66.22; H, 9.26; S, 9.82. Found: C, 66.10; H, 9.26; S, 9.66.

2.6. *5-Chloromethyl-3-dodecyloxy-2-formyl Thiophene (6)*. A solution of 3-dodecyloxy-2-formyl-5-methylhydroxyl thiophene (1.515 g, 4.64 mmol), anhydrous DCM (28 mL), and pyridine (0.734 g, 2 mol eq) were placed in a water bath with no ice (22°C) until the starting material dissolved. Then, 1.2 molar equivalence of thionyl chloride (0.406 mL, 0.662 g) was diluted with anhydrous DCM in a syringe (4 mL) and added dropwise by syringe to the solution. Once the addition was completed, the solution was added to a 2:1 molar ratio of 2 N HCl (4.6 mL) to pyridine and a few cubes of ice to quench the base. Extraction was done with ether and water (2 mL × 3). A small amount of sodium carbonate was added and monitored by litmus paper until reaction was neutral to slightly basic. The product was dried with MgSO<sub>4</sub>, and the solvent removed

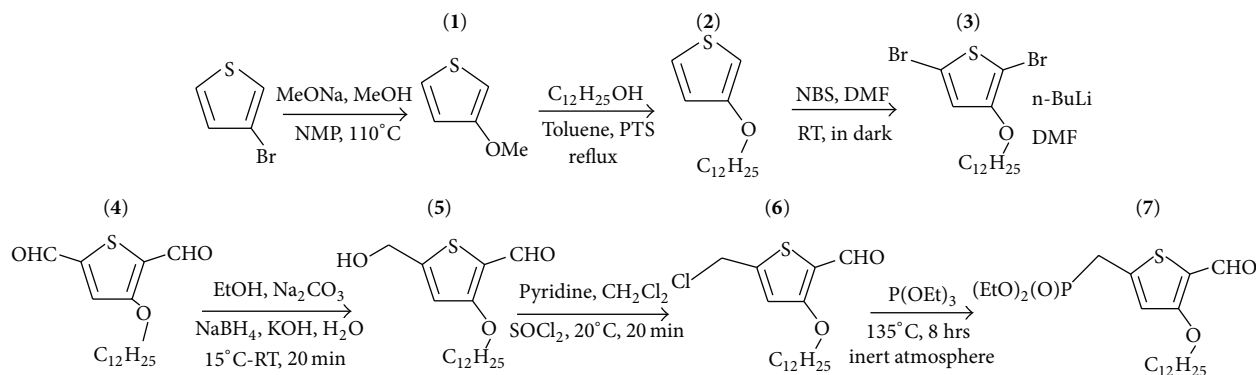


FIGURE 3: Synthetic scheme for asymmetric monomer 7 (3-dodecyloxy-2-formyl-thiophen-5-ylmethyl) phosphonic acid diethyl ester.

by rotary evaporator. No further purification was done on the sample, due to the possibility that it would decompose, so the yellowish orange solid product had a yield of 108% (1.714 g). The sample contained a small amount of impurity.  $^1\text{H NMR}$  ( $\text{CDCl}_3$ ):  $\delta$  0.87 (t, 3H), 1.26 (m, 18H), 1.80 (t, 2H), 4.13 (t, 2H), 4.66 (s, 2H), 6.88 (s, 2H), 9.96 (s, 1H).  $^{13}\text{C NMR}$ :  $\delta$  12.2, 20.8, 27.6, 30.0, 38.5, 70.2, 75.6 ( $\text{CDCl}_3$ ), 114.6, 119.6, 147.4, 161.8, 179.1.

**2.7. (3-Dodecyloxy-2-formyl-thiophen-5-ylmethyl) Phosphonic Acid Diethyl Ester (7).** A solution of 3-dodecyloxy-2-formyl-5-methylhydroxyl thiophene (1.515 g, 4.64 mmol), anhydrous DCM (28 mL), and pyridine (0.734 g, 2 mol eq.) were placed in a water bath with no ice ( $22^\circ\text{C}$ ) until the starting material dissolved. Then, 1.2 molar equivalence of thionyl chloride (0.406 mL, 0.662 g) was diluted with anhydrous DCM in a syringe (4 mL) and added dropwise by syringe to the solution. Once the addition was completed, the solution was added to a 2:1 molar ratio of 2N HCl (4.6 mL) to pyridine and a few cubes of ice to quench the base. Extraction was done with ether and water (2 mL  $\times$  3). A small amount of sodium carbonate was added and monitored by litmus paper until reaction was neutral to slightly basic. The product was dried with  $\text{MgSO}_4$ , and the solvent removed by rotary evaporator. No further purification was done on the sample, due to the possibility that it would decompose, so the yellowish orange solid product had a yield of 108% (1.714 g). The sample contained a small amount of impurity.  $^1\text{H NMR}$  ( $\text{CDCl}_3$ ):  $\delta$  0.87 (t, 3H), 1.26 (m, 18H), 1.80 (t, 2H), 4.13 (t, 2H), 4.66 (s, 2H), 6.88 (s, 2H), 9.96 (s, 1H).  $^{13}\text{C NMR}$ :  $\delta$  12.2, 20.8, 27.6, 30.0, 38.5, 70.2, 75.6 ( $\text{CDCl}_3$ ), 114.6, 119.6, 147.4, 161.8, 179.1.

**2.8. Poly-(3-dodecyloxy-2,5-thienylene Vinylene) (8).** Anhydrous THF (2 mL) and 1.2 molar equivalent of potassium t-butoxide (0.0959 g, 0.854 mmol) were added to (3-dodecyloxy-2-formyl-thiophen-5-ylmethyl) phosphonic acid diethyl ester (0.318 g, .712 mmol), in a nitrogen atmosphere glove box. After 3.5 hours of reacting at  $78^\circ\text{C}$ , the polymer was dissolved with THF and washed with methanol. The polymer was purified by filtration after washing with methanol. The bluish purple solid had a yield of 45.2% (0.094 mg).  $^1\text{H NMR}$  ( $\text{CDCl}_3$ ):  $\delta$  0.87(t, (3H) $_n$ ), 1.25 (m,

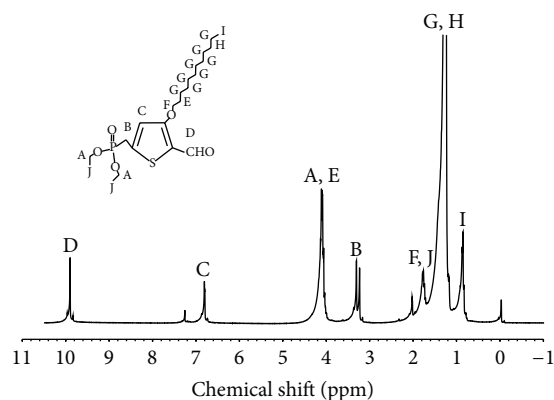


FIGURE 4:  $^1\text{H NMR}$  spectrum of (3-dodecyloxy-2-formyl-thiophen-5-ylmethyl) phosphonic acid diethyl ester.

(18H) $_n$ ), 1.66 (t, (2H) $_n$ ), 4.05 (t, (2H) $_n$ ), 6.66, 6.74, 7.02, 7.07 ( $-\text{C}=\text{C}-$ , aromatic3), 9.90, 10.0 ( $-\text{CHO}$ ).

### 3. Results and Discussion

**3.1. Synthesis.** In order to promote 100% regioselectivity in the polymer, a monomer was designed and synthesized to be monoaldehyde monophosphonate functionalized (asymmetric), as to eliminate any possibility of regiorandomness as seen in polymers of difunctionalized monomers [12, 14, 18]. The asymmetric PTV monomer, (3-dodecyloxy-2-formyl-thiophen-5-ylmethyl) phosphonic acid diethyl ester (7), was synthesized using a seven-step synthetic process (Figure 3). In order to form the asymmetric functional groups on the thiophene ring, the alkoxy thiophene underwent bromination to form the dibromo groups (3), followed by formylation to form dialdehyde (4). Then, one of the dialdehydes was selectively reduced to a hydroxyl group (5), which was in the proceeding reaction chlorinated (6). The phosphonate functional group was formed successfully using Michaelis-Arbusov reaction (7). The  $^1\text{H NMR}$  of the monomer (7) is shown in Figure 4.

The Horner-Emmons reactivity of the monomer 7 with potassium tert-butoxide (a nucleophile) is much lower than

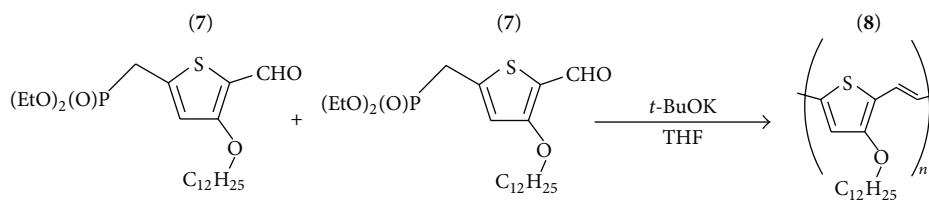
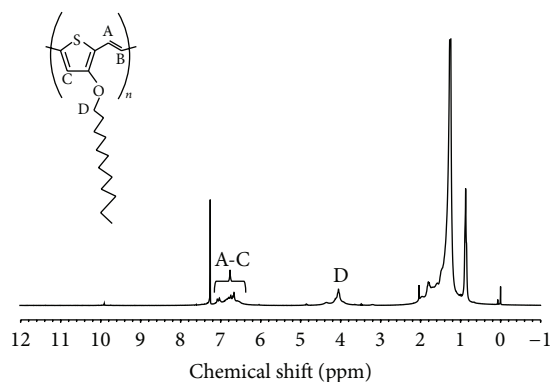
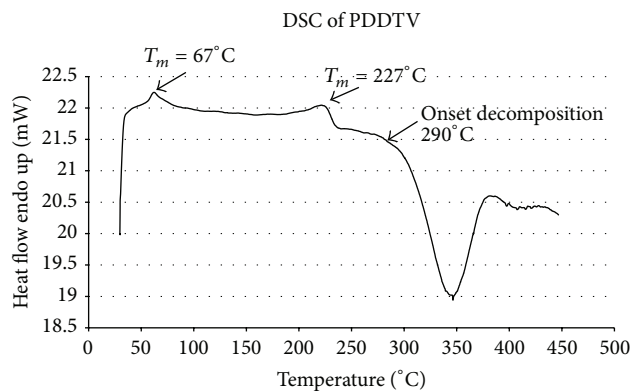


FIGURE 5: Polymerization of asymmetric monomer 7.

FIGURE 6:  $^1\text{H}$  NMR spectrum of poly(3-dodecyloxy-2,5-thiophene vinylene).

its alkyl version [1] possibly due to the lack of electron deficiency of the aldehyde group resulting in low reactivity. In the first trial and second trial, THF and *t*-BuOK were added to the monomer and allowed to react at room temperature for 10–20 minutes. In the first trial, the color of the reaction changed from reddish amber to green. However, the  $^1\text{H}$  NMR spectrum of the reaction mixture extract showed that there was only monomer in the solution; no polymer had formed. In the second trial the solution contained only 8% of the polymer. Since the first and second trials were not fully successful the solvent was changed from THF (a weakly polar aprotic solvent) to dimethylformamide (DMF) (stronger polar aprotic solvent) and allowed to react for 20 hrs. The change in solvent was to determine if the reaction environment to polymerize was polar enough. The  $^1\text{H}$  NMR showed no reaction occurred, and only starting material remained. After it was concluded from the third trial that THF was a sufficient enough solvent for the reaction, the reaction conditions from the second trial were repeated with the exception of duration and temperature. The reaction was boiled for 10 minutes, and the  $^1\text{H}$  NMR showed that only 15% of the monomer remained. Most of the polymer had formed. Once the reaction condition was determined, the remaining monomer reaction mixture was allowed to react for 3.5 hours at  $78^\circ\text{C}$  (Figure 5). The  $^1\text{H}$  NMR shown in Figure 6 indicate the formation of polymer (8) as evidenced from the loss of  $-\text{CH}_2$  doublet peak of  $-\text{CH}_2\text{P}(\text{O})(\text{OCH}_2\text{CH}_3)_2$  (position 5) and the  $-\text{CHO}$  peak (position 2) on the monomer (Figure 4).  $-\text{OCH}_2$  peaks from the dodecyloxy substituent on the monomer (position 3, D) appeared at 4.0 ppm on the  $^1\text{H}$  NMR (Figure 6). Peaks from the phosphonate group also

FIGURE 7: DSC plot of the PDDTV with a heating rate of  $10^\circ\text{C}/\text{min}$  under nitrogen atmosphere.

disappeared. The broadening of the other peaks, especially those in the aromatic region (A–C), is another indication of the polymer formation.

**3.2. Thermal Properties.** Thermal properties of the PDDTV (polymer 8) were studied using TGA and DSC under Nitrogen atmosphere. The DSC thermogram (Figure 7) shows two endothermic peaks at  $67^\circ\text{C}$  and  $227^\circ\text{C}$ . These data could indicate that this polymer exhibits polymorphic behavior similar to the reported comparable poly(3-alkyl thiophene)s [19, 20]. The peak at  $67^\circ\text{C}$  could be attributed to the transition from crystalline state to liquid crystal (mesophase). The second peak at  $227^\circ\text{C}$  could be due to the transition from liquid crystal (mesophase) to an isotropic liquid [19, 20]. The exothermic peak with an onset at  $290^\circ\text{C}$  is due to decomposition by reactions involving C=C bonds. Figure 8 shows the TGA graph of the polymer. A weight loss of 5% starts at  $\sim 330^\circ\text{C}$ .

**3.3. Optoelectronic Properties.** UV-vis absorption spectrum was used to determine the  $\pi-\pi^*$  transition and the excitation energy gap of the polymer 8 backbone. The optical excitation energy gap was measured at 1.46 eV from the onset of the UV-vis absorption peak in chloroform. A UV-vis spectrum of P3HT in chloroform was also measured to compare the absorption shift of polymer (8) with that of P3HT. As shown in Figure 9, there is a red shift of polymer (8) absorption peak in comparison with P3HT, with a  $\lambda_{\text{max}}$  at 662 nm and a shoulder peak at 723 nm (P3HT has a  $\lambda_{\text{max}}$  absorption at 450 nm). The shoulder at 723 nm could

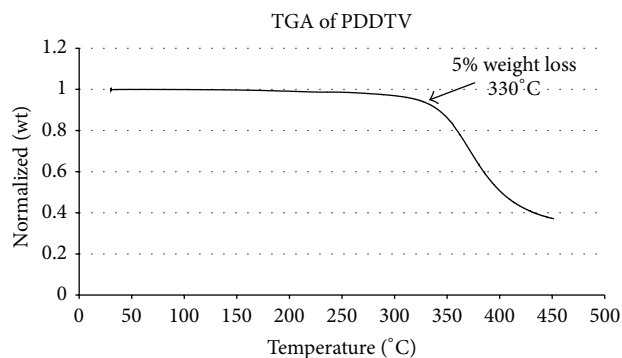


FIGURE 8: TGA plot of the PDDTV with a heating rate of  $10^{\circ}\text{C}/\text{min}$  under nitrogen atmosphere.

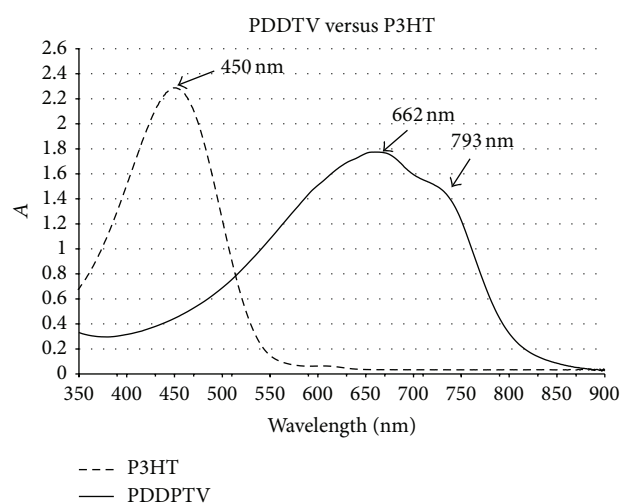


FIGURE 9: Absorption spectra of PDDTV versus P3HT.

be attributed to the vibronic fine structure seen in fully regioregular PTVs [19]. Photoluminescence measurements were conducted; however, there was no observable emission. This is in agreement with previous observations that PTVs have little or no luminescence due to the forbidden transition from the lowest energy excited state ( $2A_g$ ) to the ground state ( $1A_g$ ) [9].

**3.4. Electrochemical Properties.** The electrochemical properties of the polymer (**8**) were studied using cyclic voltammetry (CV). The first onset of oxidation potential was used to determine the HOMO level. The LUMO level was calculated from the optical excitation energy gap combined with the measured HOMO ( $E_{\text{LUMO}} = \text{Optical Eg} + E_{\text{HOMO}}$ ). The identification of the HOMO level position was based on the correlation between oxidation potentials and the HOMO orbitals were referenced to ferrocene. The CV graph of the polymer **8** is shown in Figure 10, and the results of the calculations are given in Table 1. The calculated HOMO level was  $-4.79\text{ eV}$  and the calculated LUMO using the above equation was  $-3.33\text{ eV}$ . Since the oxidation is reversible, this polymer (**8**) is very stable for a variety of optoelectronic

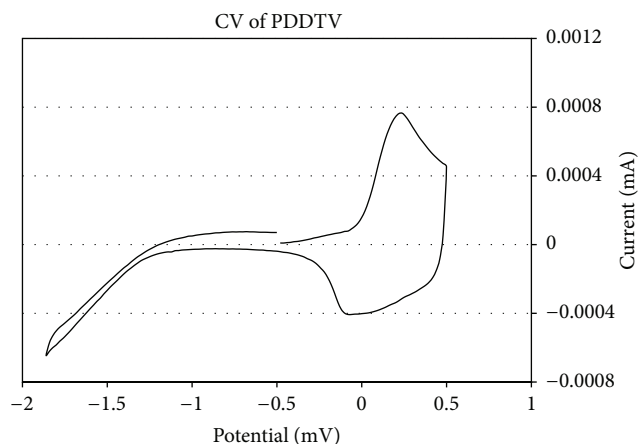


FIGURE 10: Cyclic voltamogram of the PDDTV dried on a platinum electrode immersed in a solution of  $\text{AgNO}_3$  and  $\text{Bu}_4\text{NPF}_6$  in  $\text{CH}_3\text{CN}$ .

TABLE 1: Electrochemical onset potential and electronic energy levels of the polymer.

$\phi_{\text{ox}}$ (eV)	HOMO (eV)	LUMO (eV)
0.049	$-4.789$	$-3.329$

applications as a donor or p-type material. The reduction is not reversible on the other hand, but that is not a major concern as this material will not be used as an N-type or acceptor material. For a donor material, a photovoltaic process is similar to an electrochemical redox process with the removal and recovery of electrons during the oxidation process.

## 4. Conclusions

Fully regioregular and terminally functionalized poly(3-dodecyloxy-2,5-thienylene vinylene) or PDDTV has been successfully synthesized via Horner-Emmons reaction. Regioregularity coupling was ensured by the design and polymerization of an asymmetrically functionalized monomer (monoaldehyde monophosphonate). Monomer and polymer formation were confirmed by NMR. The synthetic method utilized in this research allows for an alternative approach for the synthesis of alkoxy-substituted PTV, while ensuring regioregularity. The method also provides facile approaches to synthesizing difunctionalized symmetric and asymmetric intermediate alkoxy-substituted thiophene compounds.

Optical characterization of the polymer showed a distinct red shift in the absorption spectra when compared to P3HT with a  $\lambda_{\text{max}}$  at 662 nm and a shoulder peak at 723 nm. The measured optical energy gap is at 1.46 eV, which is an acceptable energy to capture photons in the highest irradiation range on the Earth's surface of 1 to 2 eV. This band gap is also as much as  $\sim 0.3\text{ eV}$  less than other reported PTVs [1–3, 7]. Electrochemical characterization of the polymer indicated

that the electrooxidation process is reversible but the electroreduction process was nonreversible. The CV measured HOMO level is at  $-4.79$  eV. The polymer is partially soluble in common organic solvents such as tetrahydrofuran and chloroform, and solubility increases at elevated temperatures. The TGA and DSC showed that the polymer has good thermal stability with onsets of decomposition at  $330^{\circ}\text{C}$  and  $290^{\circ}\text{C}$ , respectively.

This polymer shows great promise as a p-type material for photovoltaic application with its low optical energy gap and good thermal stability. Further optoelectronic studies including morphological studies and device fabrications will be studied and reported separately.

## Conflict of Interests

The authors declare that there is no conflict of interests regarding the publication of this paper.

## Acknowledgments

This material is based upon work supported, in part, from ARO award no. W911NF-11-1-0158, NSF award no. 1036494, and DOE award no. DE-EE-0004002. Lab assistance from Mrs. Rui Li and Mrs. Nicole Miller is greatly appreciated.

## References

- [1] C. Zhang, T. Matos, R. Li et al., "Poly(3-dodecyl-2,5-thienylenevinylene)s from the Stille coupling and the Horner-Emmons reaction," *Polymer Chemistry*, vol. 1, no. 5, pp. 663–669, 2010.
- [2] R. S. Loewe and R. D. McCullough, "Effects of structural regularity on the properties of poly(3-alkylthienylenevinylene)s," *Chemistry of Materials*, vol. 12, no. 10, pp. 3214–3221, 2000.
- [3] C. Zhang, T. H. Nguyen, J. Sun et al., "Design, synthesis, characterization, and modeling of a series of S,S-dioxothiolenylenevinylene-based conjugated polymers with evolving frontier orbitals," *Macromolecules*, vol. 42, no. 3, pp. 663–670, 2009.
- [4] R. Kroon, M. Lenes, J. C. Hummelen, P. W. M. Blom, and B. de Boer, "Small bandgap polymers for organic solar cells (polymer material development in the last 5 years)," *Polymer Reviews*, vol. 48, no. 3, pp. 531–582, 2008.
- [5] M. L. Blohm, J. E. Pickett, and P. C. Van Dort, "Synthesis, characterization, and stability of poly(3,4-dibutoxythiophenevinylene) copolymers," *Macromolecules*, vol. 26, no. 11, pp. 2704–2710, 1993.
- [6] C. Shi, Y. Yao, Y. Yang, and Q. Pei, "Regioregular copolymers of 3-alkoxythiophene and their photovoltaic application," *Journal of the American Chemical Society*, vol. 128, no. 27, pp. 8980–8986, 2006.
- [7] E. E. Havinga, C. M. J. Mutsaers, and L. W. Jenneskens, "Absorption properties of alkoxy-substituted thienylenevinylene oligomers as a function of the doping level," *Chemistry of Materials*, vol. 8, no. 3, pp. 769–776, 1996.
- [8] A. Iraqi, G. W. Barker, and D. F. Pickup, "Synthesis and characterisation of functionalised thiophene copolymers with electron donor and acceptor substituents," *Reactive and Functional Polymers*, vol. 66, no. 1, pp. 195–200, 2006.
- [9] J. Hou, Z. Tan, Y. He, C. Yang, and Y. Li, "Branched poly(thienylene vinylene)s with absorption spectra covering the whole visible region," *Macromolecules*, vol. 39, no. 14, pp. 4657–4662, 2006.
- [10] K. van de Wetering, C. Brochon, C. Ngov, and G. Hadziioannou, "Design and synthesis of a low band gap conjugated macroinitiator: toward rod-coil donor-acceptor block copolymers," *Macromolecules*, vol. 39, no. 13, pp. 4289–4297, 2006.
- [11] J. C. Speros, B. D. Paulsen, S. P. White et al., "An ADMET route to low-band-gap poly(3-hexadecylthienylene vinylene): a systematic study of molecular weight on photovoltaic performance," *Macromolecules*, vol. 45, no. 5, pp. 2190–2199, 2012.
- [12] H. Diliën, A. Palmaerts, M. Lenes et al., "A deeper insight into the dithiocarbamate precursor route: synthesis of soluble poly(thienylene vinylene) derivatives for photovoltaic applications," *Macromolecules*, vol. 43, no. 24, pp. 10231–10240, 2010.
- [13] F. Banishoeib, P. Adriaensens, S. Berson et al., "The synthesis of regio-regular poly(3-alkyl-2,5-thienylene vinylene) derivatives using lithium bis(trimethylsilyl)amide (LHMDS) in the dithiocarbamate precursor route," *Solar Energy Materials and Solar Cells*, vol. 91, no. 11, pp. 1026–1034, 2007.
- [14] S. Gillissen, A. Henckens, L. Lutsen, D. Vanderzande, and J. Gelan, "Synthesis of a processible high molecular weight poly(thienylene vinylene). polymerisation and thin-film transistor properties," *Synthetic Metals*, vol. 135-136, pp. 255–256, 2003.
- [15] M. A. Keegstra, T. H. A. Peters, and L. Brandsma, "Efficient procedures for the Cu(I)-catalyzed methoxylation of 2- and 3-bromothiophene," *Synthetic Communications*, vol. 20, pp. 213–216, 1990.
- [16] K. Fäid, R. Cloutier, and M. Leclerc, "Design of novel electroactive polybithiophene derivatives," *Macromolecules*, vol. 26, no. 10, pp. 2501–2507, 1993.
- [17] N. Agarwal, S. P. Mishra, A. Kumar, C.-H. Hung, and M. Ravikanth, "Synthesis and crystal structure of 2,3,12,13-tetraalkoxy-21, 23-dithiaporphyrins," *Chemical Communications*, no. 22, pp. 2642–2643, 2002.
- [18] C. Giroto, D. Cheyons, T. Aernouts et al., "Bulk heterojunction organic solar cells based on soluble poly(thienylene vinylene) derivatives," *Organic Electronics: Physics, Materials, Applications*, vol. 9, no. 5, pp. 740–746, 2008.
- [19] C. Zhang, J. Sun, R. Li, S.-S. Sun, E. Lafalce, and X. Jiang, "Poly(3-dodecylthienylenevinylene)s: regioregularity and crystallinity," *Macromolecules*, vol. 44, no. 16, pp. 6389–6396, 2011.
- [20] V. Causin, C. Marega, A. Marigo, L. Valentini, and J. M. Kenny, "Crystallization and melting behavior of poly(3-butylthiophene), poly(3-octylthiophene), and poly(3-dodecylthiophene)," *Macromolecules*, vol. 38, no. 2, pp. 409–415, 2005.

## Research Article

# Structural and Electrochemical Properties of Lithium Nickel Oxide Thin Films

Gyu-bong Cho,<sup>1</sup> Tae-hoon Kwon,<sup>1</sup> Tae-hyun Nam,<sup>1</sup> Sun-chul Huh,<sup>2</sup> Byeong-keun Choi,<sup>2</sup> Hyo-min Jeong,<sup>2</sup> and Jung-pil Noh<sup>2</sup>

<sup>1</sup> School of Materials Science and Engineering and RIGECT, Gyeongsang National University, No. 501, Jinju-daero, Jinju, Gyeongnam 660-701, Republic of Korea

<sup>2</sup> Department of Energy and Mechanical Engineering and Institute of Marine Industry, Gyeongsang National University, No. 38, Cheondaegukchi-gil, Tongyeong, Gyeonnam 650-160, Republic of Korea

Correspondence should be addressed to Jung-pil Noh; nohjp@gnu.ac.kr

Received 19 June 2014; Revised 28 July 2014; Accepted 28 July 2014; Published 27 August 2014

Academic Editor: Yu Xin Zhang

Copyright © 2014 Gyu-bong Cho et al. This is an open access article distributed under the Creative Commons Attribution License, which permits unrestricted use, distribution, and reproduction in any medium, provided the original work is properly cited.

LiNiO<sub>2</sub> thin films were fabricated by RF magnetron sputtering. The microstructure of the films was determined by X-ray diffraction and field-emission scanning electron microscopy. The electrochemical properties were investigated with a battery cycler using coin-type half-cells. The LiNiO<sub>2</sub> thin films annealed below 500°C had the surface carbonate. The results suggest that surface carbonate interrupted the Li intercalation and deintercalation during charge/discharge. Although the annealing process enhanced the crystallization of LiNiO<sub>2</sub>, the capacity did not increase. When the annealing temperature was increased to 600°C, the FeCrNiO<sub>4</sub> oxide phase was generated and the discharge capacity decreased due to an oxygen deficiency in the LiNiO<sub>2</sub> thin film. The ZrO<sub>2</sub>-coated LiNiO<sub>2</sub> thin film provided an improved discharge capacity compared to bare LiNiO<sub>2</sub> thin film suggesting that the improved electrochemical characteristic may be attributed to the inhibition of surface carbonate by ZrO<sub>2</sub> coating layer.

## 1. Introduction

In an attempt to miniaturize high performance portable electronic equipment, batteries with high power and energy density are required. Thin film batteries have been developed in an attempt to satisfy this requirement [1–3]; however, improving the performance of the cathode films is critical for advancing the use of electrochemical thin film batteries. Among the possible materials that could be used for a cathode film, LiCoO<sub>2</sub>, owing to its high theoretical specific capacity and ease of preparation, is a promising candidate [4–6]. However, the high cost and toxicity of cobalt limit the use of LiCoO<sub>2</sub> in thin film batteries. Therefore, it is necessary to develop less expensive cathode materials for thin film battery applications. LiNiO<sub>2</sub> has emerged as a useful cathode material owing to its low cost and high energy density [7–10].

In the current study, LiNiO<sub>2</sub> thin films were deposited by using RF magnetron sputtering. The microstructure of the films was measured by X-ray diffraction and field-emission scanning electron microscopy. Finally, the electrochemical

properties were investigated with a battery cycler using coin-type half-cells, in the potential range of 3.0 V–4.2 V.

## 2. Experimental

Bare and ZrO<sub>2</sub>-coated LiNiO<sub>2</sub> thin films have been deposited onto stainless steel (STS 304) foil substrates held at a distance of 6 cm away from the target. The STS304 substrate was ultrasonically cleaned with acetone, alcohol, and distilled water in that order. The LiNiO<sub>2</sub> and ZrO<sub>2</sub> targets were made by Pascal Co. (Japan). A base vacuum of  $5 \times 10^{-6}$  Torr was obtained with a cryopump. Gas flow rate of Ar/O<sub>2</sub> was 4/1 with a total gas flow amount of 150 sccm. Deposition pressure was maintained at  $2 \times 10^{-3}$  Torr during deposition. The LiNiO<sub>2</sub> target was presputtered for 30 min and the deposition time was 360 min at 100 W RF power. ZrO<sub>2</sub> coating layer was deposited for 10 min at 100 W RF power. Figures 1(a) and 1(b) show the surface and cross-section images of bare LiNiO<sub>2</sub> thin film deposited on Si wafer substrate. As seen in Figure 1(a),

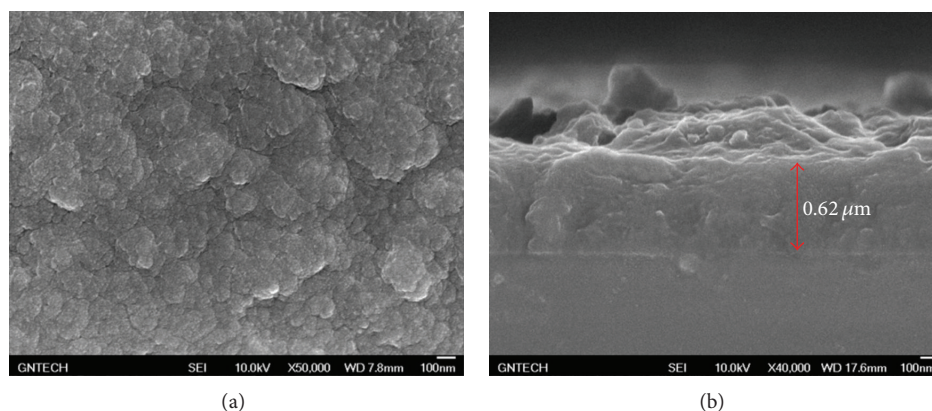


FIGURE 1: FE-SEM images of (a) surface and (b) cross-section images of  $\text{LiNiO}_2$  thin film deposited on Si wafer substrate.

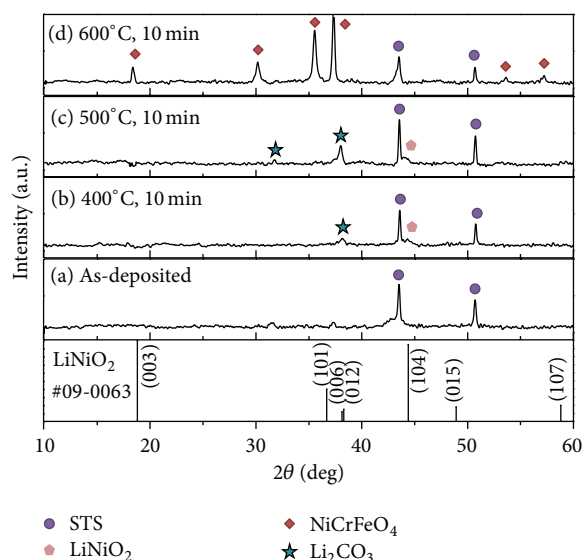


FIGURE 2: XRD patterns of (a) as-deposited, (b) 400°C, (c) 500°C, and (d) 600°C annealed  $\text{LiNiO}_2$  thin films. The annealing time was 10 minutes.

a uniform distribution of clusters of  $\sim 50$  nm was seen. The calculated deposition rates of  $\text{LiNiO}_2$  were approximately 1.7 nm/min. The deposited thin films were annealed from 400°C to 600°C in air to obtain the crystalline film.

The structure of the  $\text{LiNiO}_2$  thin films was investigated by X-ray diffractometry (XRD, Rigaku, Miniflex). The XRD measurements were performed using  $\text{Cu K}\alpha$  radiation ( $\lambda = 1.5406 \text{ \AA}$ ) and phase identification was made by comparing the diffraction patterns with the JCPDS references. The morphology of the deposited films was studied by field-emission scanning electron microscopy (FE-SEM, Jeol, JSM-6701F).

In order to examine the electrochemical properties of cathode thin films, coin-type cells were assembled with lithium foils as the counter and reference electrode and 1M  $\text{LiPF}_6$  in ethylene carbonate (EC):diethyl carbonate (DEC) (1:1, vol.%) electrolytic solution. The charge-discharge test was carried out with a battery cyler (Won A Tech,

WDCS3000s) at a constant current density of  $5 \mu\text{A}/\text{cm}^2$  in the potential range of 3.0–4.2 V.

### 3. Results and Discussion

Figure 2 shows the XRD patterns of as-deposited and annealed  $\text{LiNiO}_2$  thin films at various temperatures at 10 min. Crystallization peaks of  $\text{LiNiO}_2$  were not seen in the as-deposited films. However, the XRD pattern of the 400°C annealed film exhibited broad (104)  $\text{LiNiO}_2$  and lithium carbonate ( $\text{Li}_2\text{CO}_3$ ) reflection peaks. The degree of crystallization of  $\text{LiNiO}_2$  was enhanced at 500°C because the (104) reflection became stronger as the annealing temperature was increased. The intensity of the  $\text{Li}_2\text{CO}_3$  peak also increased. However, after annealing at 600°C, the reflection peaks of  $\text{LiNiO}_2$  and  $\text{Li}_2\text{CO}_3$  disappeared and impurity peaks of  $\text{NiCrFeO}_4$ , which was considered an oxide layer of the STS304 substrate, were observed (Figure 2(d)).

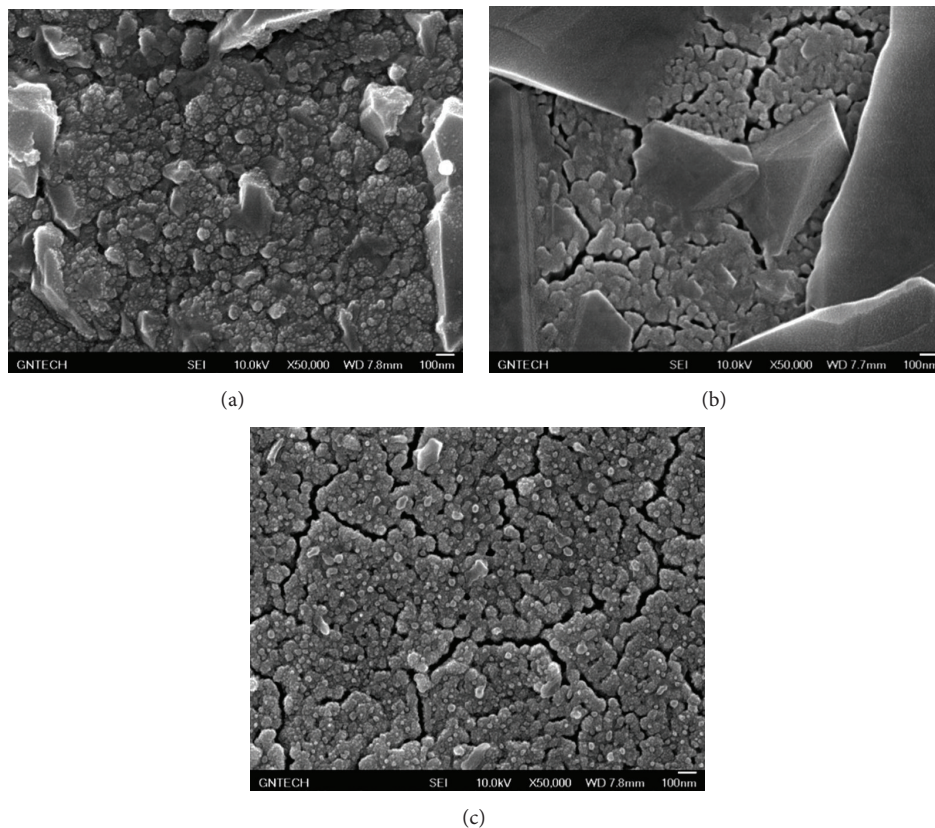


FIGURE 3: FE-SEM images of  $\text{LiNiO}_2$  thin film with various annealing temperatures at (a)  $400^\circ\text{C}$ , (b)  $500^\circ\text{C}$ , and (c)  $600^\circ\text{C}$ , respectively. The annealing time was 10 minutes.

Surface images of the annealed  $\text{LiNiO}_2$  thin films are shown in Figure 3. The  $400^\circ\text{C}$  annealed film had a rough surface with no cracks and some surface impurities (Figure 3(a)). When the annealing temperature was increased to  $500^\circ\text{C}$ , the size of the surface impurities grew and became angular. After annealing at  $600^\circ\text{C}$ , complete removal of the surface impurities was achieved and the surface had a smooth morphology compared with that of the  $400^\circ\text{C}$  annealed film. The XRD (Figure 2) and FE-SEM (Figure 3) results suggest that the angulated surface impurity, which disappeared at an annealing temperature of  $600^\circ\text{C}$ , was lithium carbonate ( $\text{Li}_2\text{CO}_3$ ).

Figure 4 shows the initial discharge curves of the as-deposited and annealed  $\text{LiNiO}_2$  thin films. All of these films were tested at a current density of  $5 \mu\text{A}/\text{cm}^2$  between 3.0 V and 4.2 V and a plateau was observed in the  $400^\circ\text{C}$  annealed films. When the annealing temperature was increased to  $500^\circ\text{C}$ , the plateau was more clearly exhibited and indicated a phase transition of crystalline  $\text{LiNiO}_2$  [11, 12]; the discharge capacity, however, did not increase. These results suggest that the surface carbonate interrupts the lithium intercalation and deintercalation during charge/discharge, affecting the discharge capacity. The  $600^\circ\text{C}$  annealed films exhibited a lower initial discharge capacity compared with the other annealed films. This may be attributed to the formation of an intermediate oxide layer between the substrate and

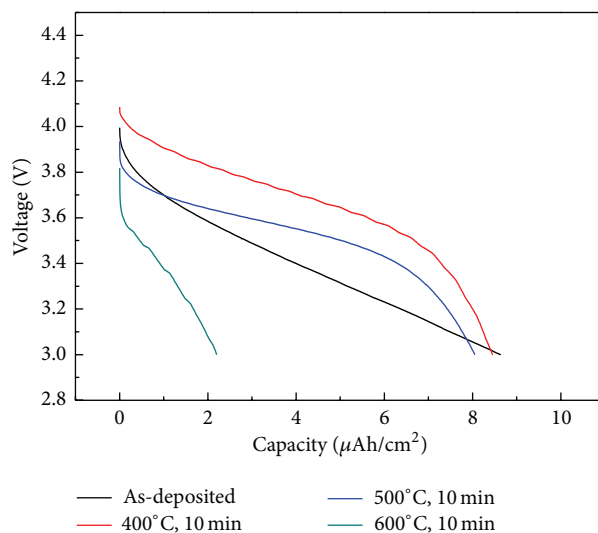


FIGURE 4: Initial discharge curves of  $\text{LiNiO}_2$  thin film with various annealing temperatures. The annealing time was 10 minutes.

active material film. The intermediate oxide layer that formed may lead to an oxygen deficiency in the annealed  $\text{LiNiO}_2$  thin films. In order for the  $\text{LiNiO}_2$  film to obtain good electrochemical characteristics, the deposited  $\text{LiNiO}_2$  thin

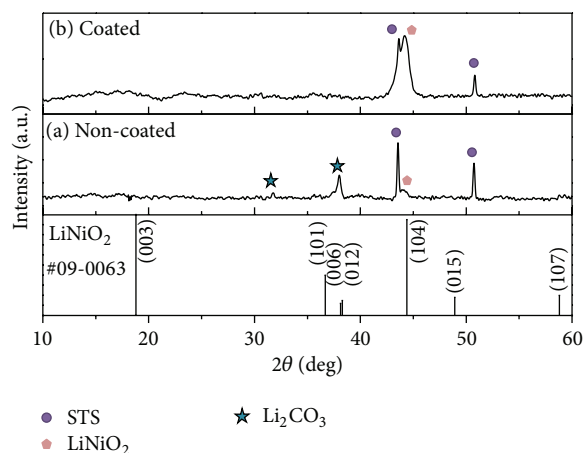


FIGURE 5: XRD patterns of (a) noncoated and (b)  $\text{ZrO}_2$ -coated  $\text{LiNiO}_2$  thin films. The films were annealed in 10 min at  $500^\circ\text{C}$ .

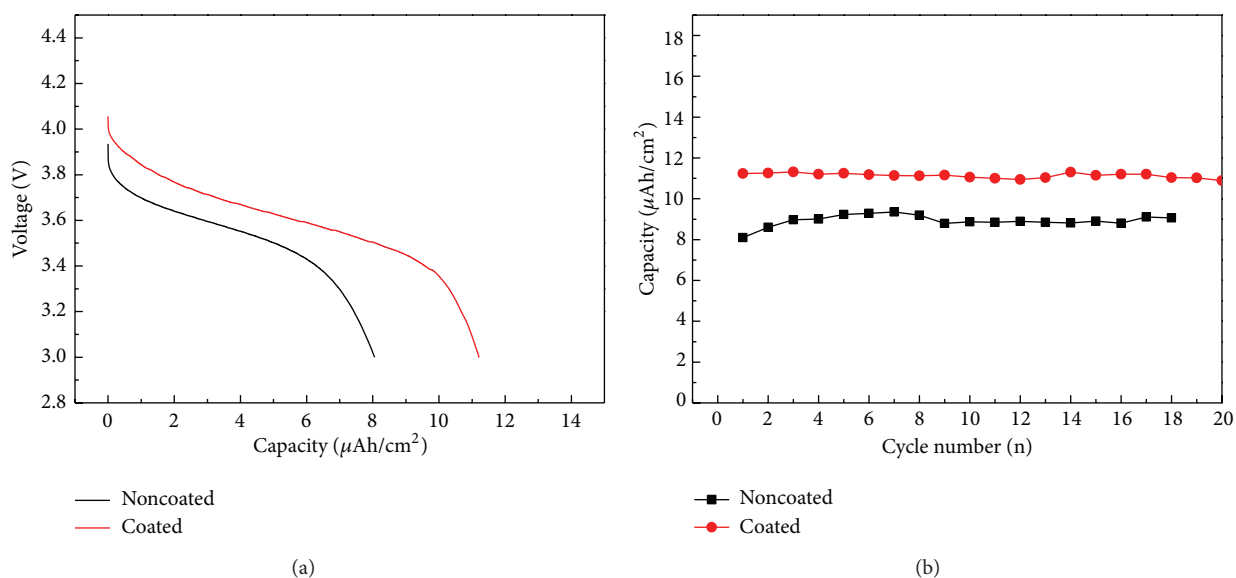


FIGURE 6: (a) Initial discharge behavior and (b) cyclic performance of  $\text{LiNiO}_2$  thin films. The films were annealed in 10 min at  $500^\circ\text{C}$ .

films should be annealed at a temperature that prevents the formation of an intermediate oxide layer. In addition, it is necessary to remove the surface carbonate. It has been previously reported that surface coatings enhance the electrochemical properties of cathode materials without sacrificing the specific capacity of the respective cathode [13].

Figure 5 shows the XRD patterns of bare and  $\text{ZrO}_2$ -coated  $\text{LiNiO}_2$  thin films annealed at  $500^\circ\text{C}$  for 10 min. As seen in Figure 5(a), the diffraction peak of the surface carbonate disappeared in the coated thin film, suggesting that the  $\text{ZrO}_2$  coating prevents the formation of surface carbonate during the annealing process.

Figure 6 shows the first discharge curves and cycle stability of bare and  $\text{ZrO}_2$ -coated  $\text{LiNiO}_2$  thin films. As seen in Figures 6(a) and 6(b), a single plateau was observed in both of the films, corresponding to the phase transition of crystalline  $\text{LiNiO}_2$ . Therefore, this would indicate that both films are crystallized. However, the first discharge capacity

is slightly different such that the first discharge capacity of  $\text{ZrO}_2$ -coated film is higher than that of the bare  $\text{LiNiO}_2$  thin film. The capacity retention rate is similar in both thin films as seen in Figure 6(b).

#### 4. Summary

$\text{LiNiO}_2$  thin films were fabricated by RF magnetron sputtering. Crystallization began at annealing temperatures above  $400^\circ\text{C}$ ; however, the films that were annealed below  $500^\circ\text{C}$  exhibited surface carbonate (in the form of  $\text{Li}_2\text{CO}_3$ ) identified by XRD. Surface carbonate interrupts the Li intercalation and deintercalation during charge/discharge and therefore the capacity did not increase, although the degree of  $\text{LiNiO}_2$  crystallization was enhanced. When the annealing temperature was increased to  $600^\circ\text{C}$ , the  $\text{FeCrNiO}_4$  oxide phase was generated and the discharge capacity decreased due to

the oxygen deficiency in the  $\text{LiNiO}_2$  thin film. The  $\text{ZrO}_2$ -coated  $\text{LiNiO}_2$  thin film provided an improved discharge capacity compared to the bare  $\text{LiNiO}_2$  thin film at an annealing temperature of  $500^\circ\text{C}$ . Therefore, the improvement in electrochemical characteristics can be attributed to the inhibition of surface carbonate by the  $\text{ZrO}_2$  coating layer.

### Conflict of Interests

The authors declare that there is no conflict of interests regarding the publication of this paper.

### Acknowledgment

This research was supported by the Science Research Program through the National Research Foundation of Korea (NRF) funded by the Ministry of Education, Science and Technology (2012-RIA1A2008821 and 2012-RIA2A1A01006546).

### References

- [1] Y. Iriyama, C. Yada, T. Abe, Z. Ogumi, and K. Kikuchi, "A new kind of all-solid-state thin-film-type lithium-ion battery developed by applying a D.C. high voltage," *Electrochemistry Communications*, vol. 8, no. 8, pp. 1287–1291, 2006.
- [2] S. J. Lee, H. K. Baik, and S. M. Lee, "An all-solid-state thin film battery using LISIPON electrolyte and Si-V negative electrode films," *Electrochemistry Communications*, vol. 5, no. 1, pp. 32–35, 2003.
- [3] Y. J. Kim, H. Kim, B. Kim et al., "Electrochemical stability of thin-film  $\text{LiCoO}_2$  cathodes by aluminum-oxide coating," *Chemistry of Materials*, vol. 15, no. 7, pp. 1505–1511, 2003.
- [4] G. G. Amatucci, J. M. Tarascon, and L. C. Klein, " $\text{CoO}_2$ , the end member of the  $\text{Li}_x\text{CoO}_2$  solid solution," *Journal of The Electrochemical Society*, vol. 143, no. 3, pp. 1114–1123, 1996.
- [5] K. Edstrom, T. Gustafsson, and J. O. Thomas, "The cathode-electrolyte interface in the Li-ion battery," *Electrochimica Acta*, vol. 50, no. 2-3, pp. 397–403, 2004.
- [6] J. H. Kim, M. Y. Eom, S. W. Noh, and D. W. Shin, "Performance optimization of all-solid-state lithium ion batteries using a  $\text{Li}_2\text{S-P}_2\text{S}_5$  solid electrolyte and  $\text{LiCoO}_2$  cathode," *Electronic Materials Letters*, vol. 8, pp. 209–213, 2012.
- [7] H. Arai, S. Okada, H. Ohtsuka, M. Ichimura, and J. Yamaki, "Characterization and cathode performance of  $\text{Li}_{1-x}\text{Ni}_{1+x}\text{O}_2$  prepared with the excess lithium method," *Solid State Ionics*, vol. 80, pp. 261–269, 1995.
- [8] S. H. Ju, J. H. Kim, and Y. C. Kang, "Electrochemical properties of  $\text{LiNi}_{0.8}\text{Co}_{0.2-x}\text{Al}_x\text{O}_2$  ( $0 \leq x \leq 0.1$ ) cathode particles prepared by spray pyrolysis from the spray solutions with and without organic additives," *Metals and Materials International*, vol. 16, no. 2, pp. 299–303, 2010.
- [9] S. N. Kwon, J. Song, and D. R. Mumm, "Effects of cathode fabrication conditions and cycling on the electrochemical performance of  $\text{LiNiO}_2$  synthesized by combustion and calcination," *Ceramics International*, vol. 37, no. 5, pp. 1543–1548, 2011.
- [10] M. Y. Song, C. K. Park, H. R. Park, and D. R. Mumm, "Variations in the electrochemical properties of metallic elements-substituted  $\text{LiNiO}_2$  cathodes with preparation and cathode fabrication conditions," *Electronic Materials Letters*, vol. 8, no. 1, pp. 37–42, 2012.
- [11] J. Cho, T. Kim, Y. J. Kim, and B. Park, "High-performance  $\text{ZrO}_2$ -coated  $\text{LiNiO}_2$  cathode material," *Electrochemical and Solid-State Letters*, vol. 4, no. 10, pp. A159–A161, 2001.
- [12] E. Endo, T. Yasuda, K. Yamaura, A. Kita, and K. Sekai, " $\text{LiNiO}_2$  electrode modified by plasma chemical vapor deposition for higher voltage performance," *Journal of Power Sources*, vol. 93, no. 1-2, pp. 87–92, 2001.
- [13] J. Kim, C. S. Johnson, J. T. Vaughey et al., "The electrochemical stability of spinel electrodes coated with  $\text{ZrO}_2$ ,  $\text{Al}_2\text{O}_3$ , and  $\text{SiO}_2$  from colloidal suspensions," *Journal of the Electrochemical Society*, vol. 151, no. 10, pp. A1755–A1761, 2004.

## Research Article

# Preparation of Mesoporous SnO<sub>2</sub> by Electrostatic Self-Assembly

Yang Jing, Wang Yan, and Xu Xiaowen

School of Chemistry and Biology Engineering, Jiangsu Key Laboratory for Environment Functional Materials, University of Science and Technology of Suzhou, Suzhou 215009, China

Correspondence should be addressed to Xu Xiaowen; xwxu@mail.usts.edu.cn

Received 12 June 2014; Revised 7 August 2014; Accepted 7 August 2014; Published 21 August 2014

Academic Editor: Fan Dong

Copyright © 2014 Yang Jing et al. This is an open access article distributed under the Creative Commons Attribution License, which permits unrestricted use, distribution, and reproduction in any medium, provided the original work is properly cited.

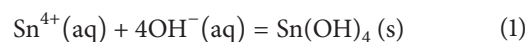
We report a simple and scalable strategy to synthesize mesoporous SnO<sub>2</sub> with tin dioxide nanoparticles of 5–6 nm crystalline walls and 3–4 nm pore diameter with the assistance of Mo<sub>7</sub>O<sub>24</sub><sup>6-</sup> as templating agent at room temperature. The samples were characterized by XRD, TEM, UV-DRS, XPS, and BET. The product has a moderately high surface area of 132 m<sup>2</sup> g<sup>-1</sup> and a narrow mesoporous structure with an average pore diameter of 3.5 nm. The photocatalytic activities of the mesoporous SnO<sub>2</sub> were evaluated by the degradation of methyl orange (MO) in aqueous solution under UV light irradiation.

## 1. Introduction

Porous SnO<sub>2</sub> has received great attention because of its wide-ranging applications, in areas such as in lithium-ion batteries [1], gas sensors [2], catalysis [3–5], solar cells [6, 7], and supercapacitor electrodes [8] due to its abundance, low cost, and high surface area. Recently, the extensions of soft or/and hard templating procedures to prepare porous SnO<sub>2</sub> with huge specific surface areas have been reported [3]. In order to obtain mesoporous SnO<sub>2</sub>, the reported general approach is to use a templating agent, usually a surfactant, which is removed by calcination or chemical extraction after the SnO<sub>2</sub> network is formed. However, the posttreatment, such as high-temperature calcination, may affect the properties of the SnO<sub>2</sub> particles and may reduce the surface areas and pore volume. Therefore, avoiding the use of surfactants is highly desirable and would be beneficial in terms of cost, environmental impact, and scale-up potential. For instance, Mancin and coworkers constructed mesoporous silica through a surfactant-free approach. The templating agent that they used is a hydrolytically unstable inorganic phase and the template could be removed by solvent exchange with water at room temperature [9], but the surface area and pore structure of mesoporous silica had remained unclear.

In this work, we developed a novel, facile, and controllable technique to synthesize mesoporous SnO<sub>2</sub>. The technique of electrostatic self-assembly of charged colloidal particles

was exploited to prepare mesoporous SnO<sub>2</sub>. In our previous works, mesoporous NiO has been fabricated with the assistance of MoO<sub>4</sub><sup>2-</sup> [10]. Our concept is that two kinds of soluble salt in acidic solution do not hydrolyze. The formation of the homogeneous assemblies is initiated with the generation of a large number of nucleuses after the mixing of the acidic precursor with basic solutions. It is well known that the solubility of Sn(OH)<sub>4</sub> in aqueous solution is determined by the pH and the Sn<sup>4+</sup> concentration. When the pH was adjusted to around 4, the Sn<sup>4+</sup> ions are almost transformed to colloidal Sn(OH)<sub>4</sub>



However, the isoelectric point of colloidal Sn(OH)<sub>4</sub> solutions is 4.5 [11]. The pH value that we used (4) was below the isoelectric point of Sn(OH)<sub>4</sub>; hence the surfaces of Sn(OH)<sub>4</sub> colloid are positively charged because of the presence of abundant protonated hydroxyl groups. MoO<sub>4</sub><sup>2-</sup> ions could be condensed in acid solution, and the extent of condensation depended on the pH level. The dominant species are MoO<sub>4</sub><sup>2-</sup> ions in pH range of 7–12, and the protonated species were those of Mo<sub>7</sub>O<sub>24</sub><sup>6-</sup> ions and of Mo<sub>8</sub>O<sub>26</sub><sup>4-</sup> ions in pH ranges 3–5 and at pH below 2, respectively [12]. Therefore, the positively charged Sn(OH)<sub>4</sub> and the negatively charged Mo<sub>7</sub>O<sub>24</sub><sup>6-</sup>

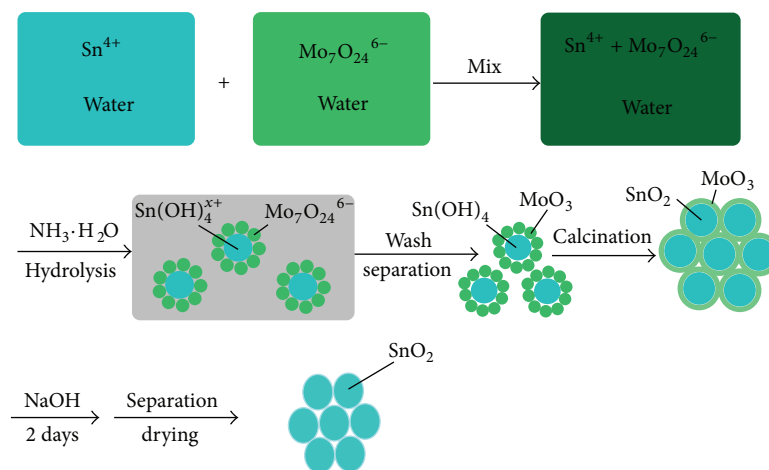
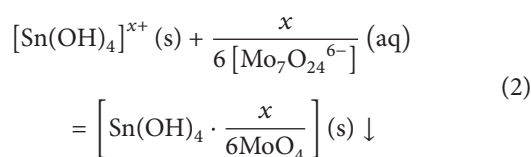


FIGURE 1: Schematic illustration of the preparation of mesoporous SnO<sub>2</sub>.

ions began to coprecipitate (2) when Mo<sub>7</sub>O<sub>24</sub><sup>6-</sup> ions were added to colloidal solutions of Sn(OH)<sub>4</sub> at a pH value of 4



Systems of nanoparticles (NPs) interacting through electrostatic forces have been reported. For example, Grzybowski and coworkers reported that large 3D crystals could be prepared by the electrostatic self-assembly of oppositely charged metallic nanoparticles [13]. Crystal growth requires advancing of grain boundaries. Grain boundaries can be “pinned” and hence their motion is restricted by introducing tiny secondary-phase particles along the grain boundaries. The growth of NPs is generally inhibited by surface modification with organic molecules, such as surfactants and ligands [14]. In our system, Mo<sub>7</sub>O<sub>24</sub><sup>6-</sup> ions play the role of traditional organic passivating ligands that anchor onto the surface of colloidal Sn(OH)<sub>4</sub> particles and form the “pins” at grain boundaries, inhibiting the growth of the particles. Then SnO<sub>2</sub>/MoO<sub>3</sub> is formed following the process of separation and calcination. Mesoporous SnO<sub>2</sub> was prepared by dissolving SnO<sub>2</sub>/MoO<sub>3</sub> with NaOH solution. Figure 1 illustrates the preparation procedure of mesoporous SnO<sub>2</sub>.

## 2. Experimental Section

**2.1. Synthesis.** Chemicals: all of the chemicals (analytic reagent, AR) were used as received without further purification.

In a typical experiment, SnCl<sub>4</sub>·5H<sub>2</sub>O (0.02 M) was dissolved in deionized water (50 mL) and produced a clear precursor solution after stirring for 1 h. (NH<sub>4</sub>)<sub>6</sub>Mo<sub>7</sub>O<sub>24</sub>·4H<sub>2</sub>O (0.0029 M) was dissolved in deionized water (50 mL) to obtain the solution of (NH<sub>4</sub>)<sub>6</sub>Mo<sub>7</sub>O<sub>24</sub>, which was added to the solution of SnCl<sub>4</sub> dropwise. After stirring for 30 min, the pH of the solution was adjusted to 4 by dropwise

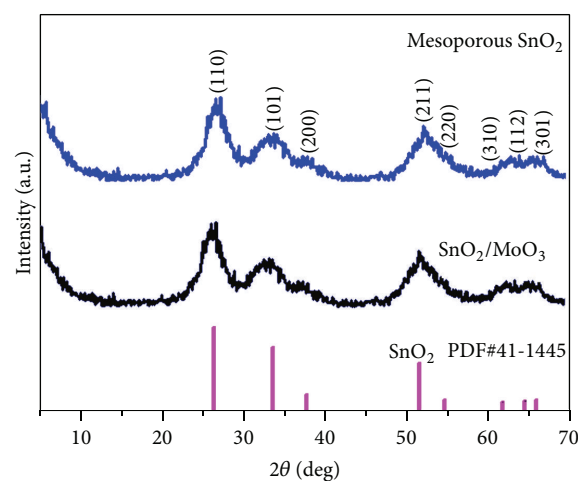


FIGURE 2: XRD patterns of SnO<sub>2</sub>@MoO<sub>3</sub> and mesoporous SnO<sub>2</sub>.

addition of NH<sub>3</sub>·H<sub>2</sub>O solution (2 M). The resulting mixture was stirred for an additional 3 h. Then the precipitate was centrifuged and thoroughly washed with deionized water to remove remaining Cl<sup>-</sup> and NH<sub>4</sub><sup>+</sup> to obtain the precursor. The precursor was calcined at 400°C in an oven for 3 h with a heating rate of 10°C min<sup>-1</sup> and then cooled to ambient temperature to obtain SnO<sub>2</sub>@MoO<sub>3</sub>. The SnO<sub>2</sub>/MoO<sub>3</sub> was dissolved in NaOH solution (2 M) for 2 days under magnetic stirring, was collected by filtration with a membrane filter, and was dried at 110°C to obtain mesoporous SnO<sub>2</sub>.

**2.2. Characterizations.** The phase structures of as-prepared products were characterized by X-ray diffraction (XRD) (Bruker D8 advance) with Cu-Kα radiation (λ = 1.5418 Å) over a 2θ range between 5° and 70° and the scanning speed of 4° min<sup>-1</sup> with a step of 0.02°. The sample morphology was examined by transmission electron microscope (TEM) with the accelerating voltage of the electron beam of 200 kV (JEOL JEM-3930EX). Diffuse reflectance spectra (DRS) were obtained for the dry-pressed disk samples using a scan

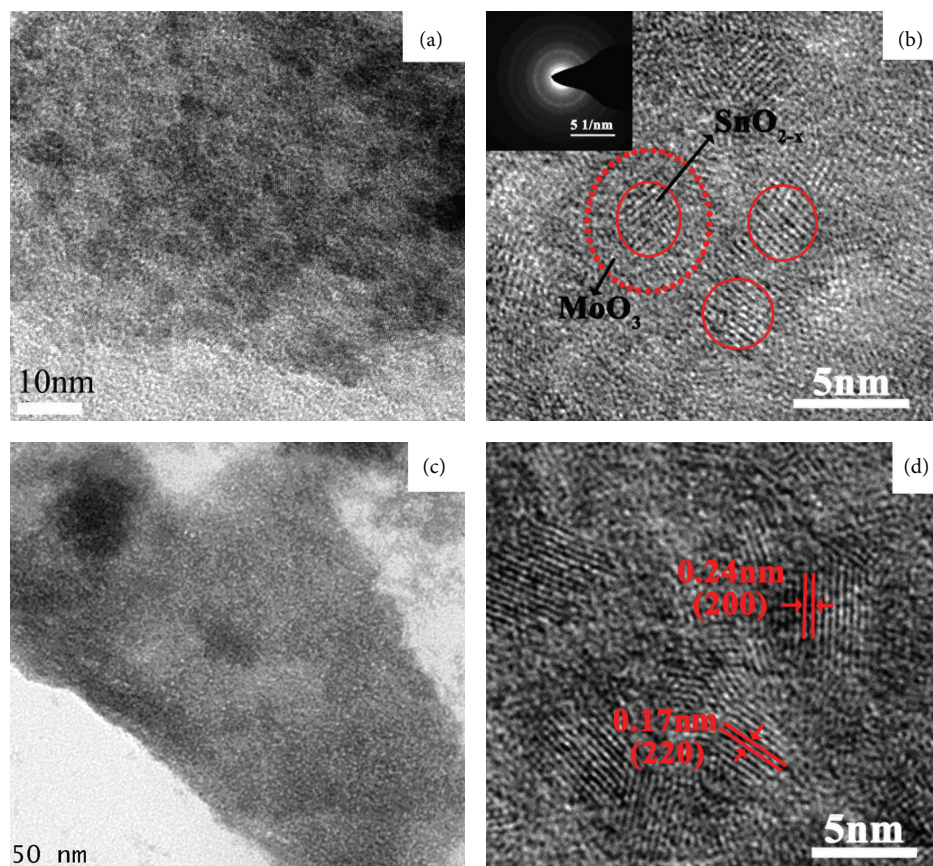


FIGURE 3: (a) TEM image of  $\text{SnO}_2@\text{MoO}_3$ ; (b) HRTEM image of  $\text{SnO}_2@\text{MoO}_3$ ; (c) TEM image of mesoporous  $\text{SnO}_2$ ; (d) HRTEM images of image of mesoporous  $\text{SnO}_2$ . Inset shows the corresponding SAED patterns.

UV-vis spectrophotometer (Hitachi U-3010) equipped with an integrating sphere assembly, using  $\text{BaSO}_4$  as reflectance sample. The spectra were recorded at room temperature in air, in the range of 200–800 nm. Specific surface area and pore diameter of samples were measured by the BET method using  $\text{N}_2$  adsorption measurement (ASAP 2020 V3.01H) on nitrogen adsorption at 77 K after the pretreatment at 393 K for 2 h. The specific surface area was calculated by the Brunauer-Emmett-Teller (BET) method, and pore size distribution was obtained from desorption plots by a Barrett-Joyner-Halenda (BJH) analysis. X-ray photoelectron spectroscopy (XPS) spectra were acquired with a Kratos Axis Ultra DLD spectrometer (Kratos Analytical-A Shimadzu group company) using a monochromatic Al  $K\alpha$  source (1486.6 eV). The analyzer uses hybrid magnification mode (both electrostatic and magnetic) and take-off angle is  $90^\circ$ . Under slot mode, the analysis area is  $700 \times 300 \mu\text{m}$ . Analysis chamber pressure is less than  $5 \times 10^{-9}$  Torr. Pass energy of 160 eV and 40 eV is normally used for survey spectra and narrow scan spectra, respectively. The BE scale was calibrated according to the C 1s peak (284.8 eV) of adventitious carbon on the analyzed sample surface.

**2.3. Measurements of Photocatalytic Activity.** The photocatalytic activity of samples was evaluated in terms of the

degradation of methyl orange (MO, 10 mg/L). The photocatalyst (0.05 g) was added into a 100 ml quartz photoreactor containing 50 ml of a MO solution. The mixture was stirred for 0.5 h in the dark in order to reach the adsorption-desorption equilibrium. Ultraviolet light was obtained by a 200 W high-pressure mercury lamp with main emission wavelength 313 nm as light source and the distance between the light and the reaction tube is 20 cm. After a given irradiation time, the samples were withdrawn for subsequent analysis with a UV-vis spectrophotometer (Shanghai 760).

### 3. Results and Discussion

The XRD pattern of the mesoporous  $\text{SnO}_2$  is illustrated in Figure 2 to confirm the constitution of the product. It shows eight characteristic diffraction peaks at  $26.6^\circ$ ,  $33.9^\circ$ ,  $37.9^\circ$ ,  $51.8^\circ$ ,  $54.8^\circ$ ,  $61.9^\circ$ ,  $64.7^\circ$ , and  $65.9^\circ$ , corresponding to the (110), (101), (200), (211), (220), (310), (112), and (301) crystalline planes of  $\text{SnO}_2$  (JCPDS card number 41-1445). No diffraction peaks of other impurities were detected, indicating that  $\text{MoO}_3$  exists in the product in amorphous form. The crystallite size calculated from the widened (110) diffraction peak at  $2\theta = 26.6^\circ$  according to the Scherrer equation is 5.1 nm, which is in good accord with the thickness observed on HRTEM (Figure 3).

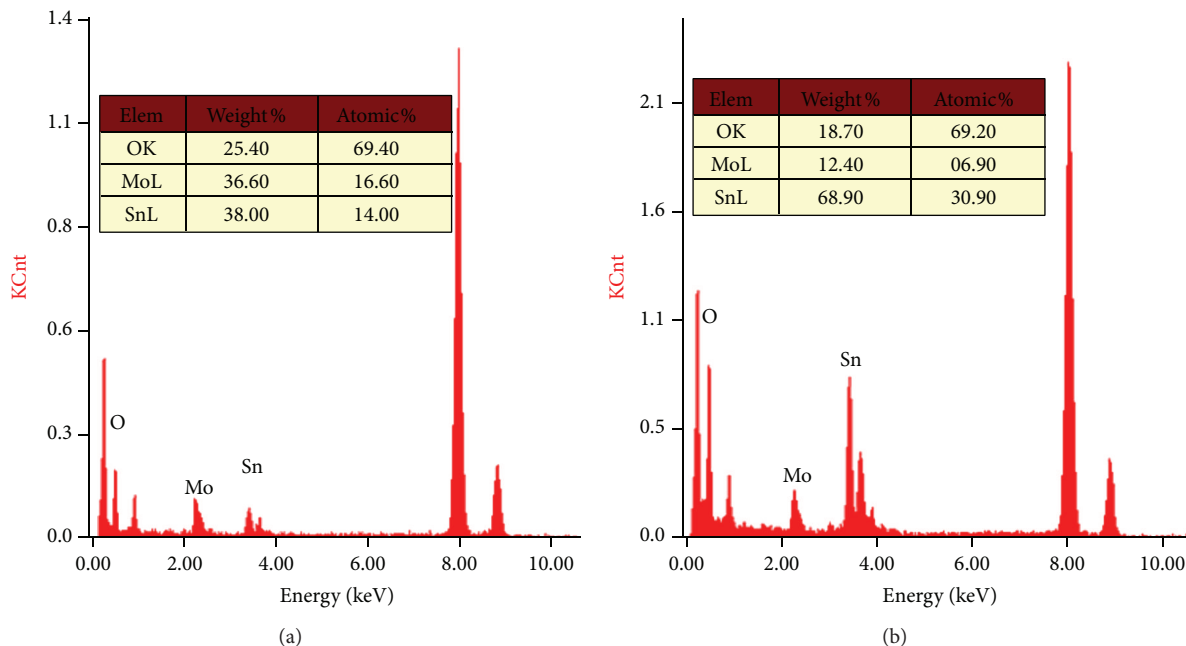


FIGURE 4: The EDX patterns of the content of Mo atoms in SnO<sub>2</sub>@MoO<sub>3</sub> (a) and mesoporous SnO<sub>2</sub> (b).

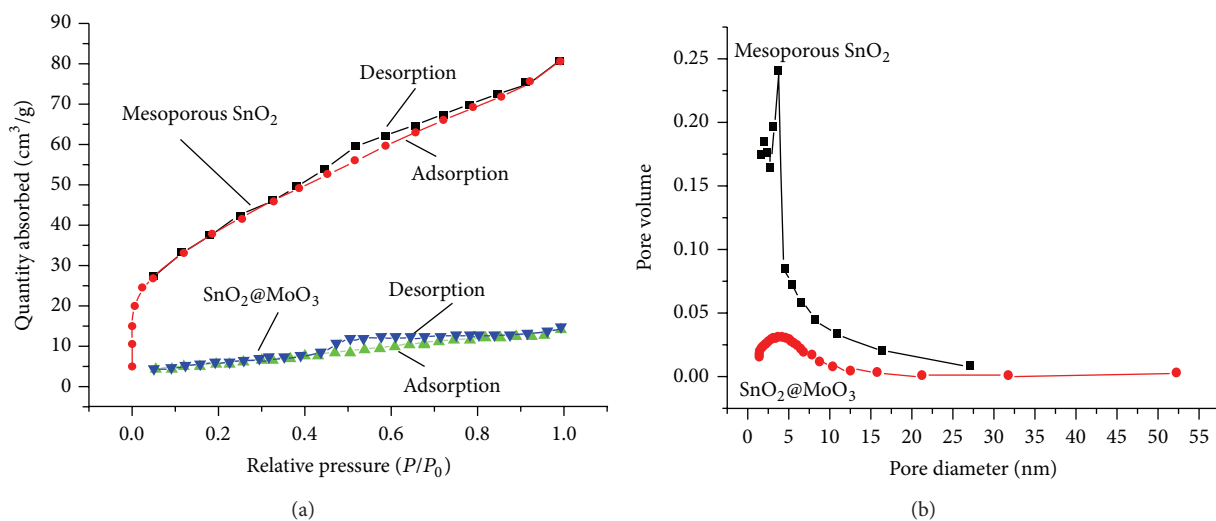
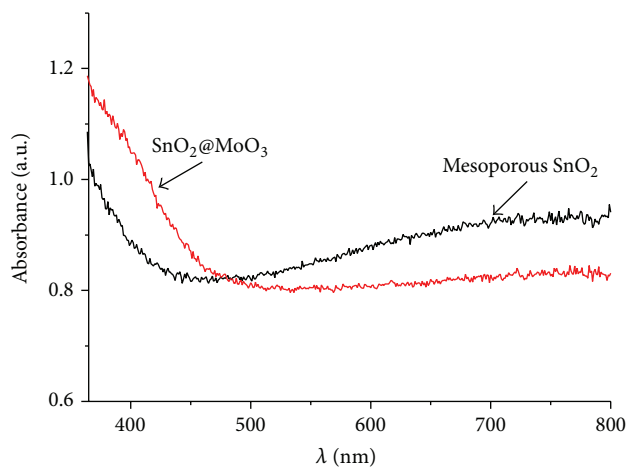
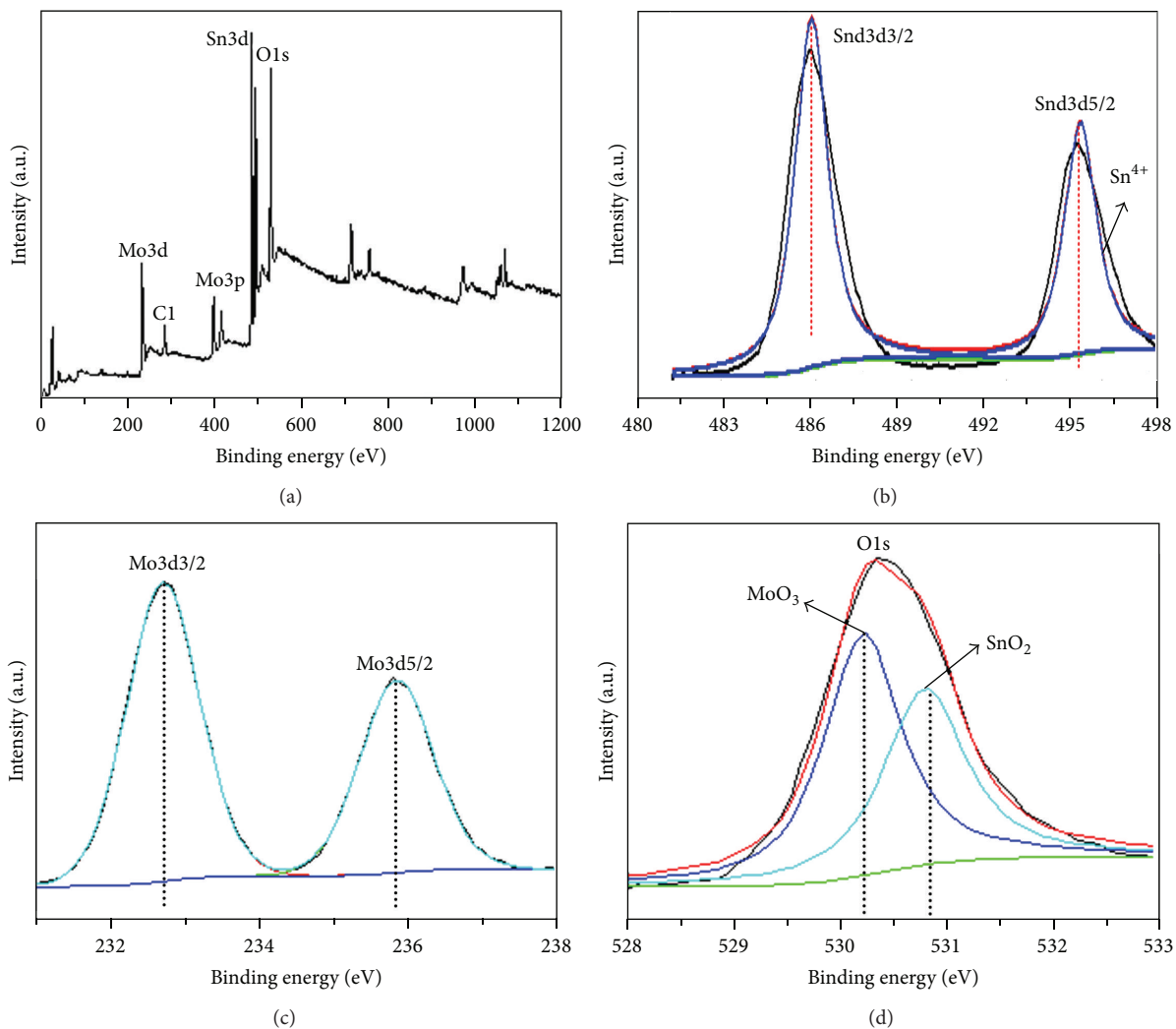


FIGURE 5: Nitrogen adsorption-desorption isotherm (a) and pore size distribution (b).

The morphology and microstructure of the prepared SnO<sub>2</sub>@MoO<sub>3</sub> and mesoporous SnO<sub>2</sub> were examined by TEM measurements. Figures 3(a) and 3(b) show representative SnO<sub>2</sub>@MoO<sub>3</sub> samples and Figures 3(c) and 3(d) show representative mesoporous SnO<sub>2</sub>, which aggregated from ultrafine nanoparticles with a typical diameter of 6 nm. It can be clearly seen that amorphous MoO<sub>3</sub> layer was coated onto SnO<sub>2</sub> nanoparticles in SnO<sub>2</sub>@MoO<sub>3</sub> in Figure 3(b), confirming that the formation mechanism of SnO<sub>2</sub>/MoO<sub>3</sub> is exactly as described in Figure 1. The SnO<sub>2</sub> nanoparticles with a size of about 5-6 nm can be identified. The SAED (inset of Figure 3(b)) image presents the polycrystalline behavior of the materials due to the spot and ring patterns. The spacing

between two adjacent lattice fringes are 0.24 nm and 0.17 nm, corresponding well to the spacing of the (200) and (220) plane of SnO<sub>2</sub> (Figure 3(d)), respectively. This is perfectly in agreement with the XRD analytical results. Since SnO<sub>2</sub> is insoluble and MoO<sub>3</sub> is highly soluble in NaOH solution, the content of Mo atoms in SnO<sub>2</sub>@MoO<sub>3</sub> is reduced from 16.6% before dissolution to 6.9% after dissolution in NaOH solution (Figure 4), which suggests that Mo<sub>7</sub>O<sub>24</sub><sup>6-</sup> plays the role of the protective and stabilizing agent coated onto SnO<sub>2</sub> to inhibit the growth of the particles during calcination.

The nitrogen adsorption-desorption isotherm (a) and BJH-derived pore size distributions (b) of the sample are shown in Figure 5. Its micro/mesoporous properties are

FIGURE 6: Diffuse reflectance spectra of  $\text{SnO}_2/\text{MoO}_3$  and mesoporous  $\text{SnO}_2$ .FIGURE 7: (a) XPS survey spectra of mesoporous  $\text{SnO}_2$ , High-resolution XPS of (b) Sn3d, (c) Mo3d, and (d) O1s spectra.

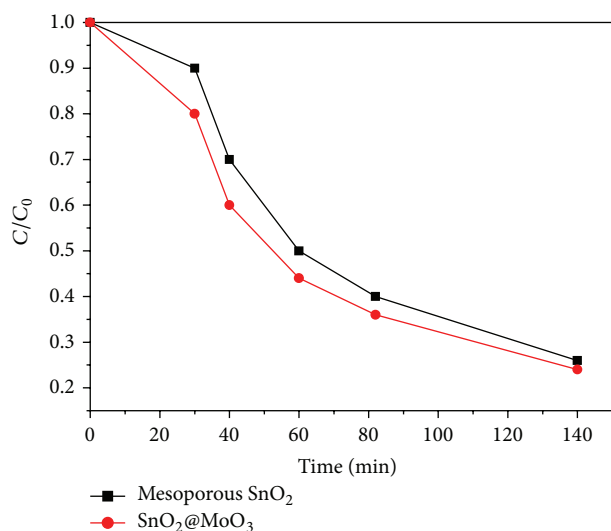


FIGURE 8: Photodegradation of MO under ultraviolet light irradiation by SnO<sub>2</sub>@MoO<sub>3</sub> and mesoporous SnO<sub>2</sub>.

indicated by the hybrid isotherm (I + IV) type in Figure 5(a). The sample has a BET surface area of 132 m<sup>2</sup> g<sup>-1</sup>, a narrow mesoporous structure with an average pore diameter (Figure 3(b)) of 3.5 nm, and a pore volume of 0.12 cm<sup>3</sup> g<sup>-1</sup>. The BET surface area of samples increased to 132 m<sup>2</sup> g<sup>-1</sup> from 21 m<sup>2</sup> g<sup>-1</sup>, and the average pore diameter reduced from 4.2 nm to 3.5 nm after dissolution with NaOH, which suggests that MoO<sub>3</sub> plays the role of the protective and stabilizing agent coated onto SnO<sub>2</sub> to inhibit the growth of the particles during calcinations.

The diffuse reflectance spectra of the samples show photoresponse in visible light region (Figure 6). The absorption edge of mesoporous SnO<sub>2</sub> is estimated to be 420 nm with a band gap of 3.0 eV, which is less than the bulk band gap (3.6 eV). Meanwhile, it can be clearly observed that SnO<sub>2</sub>@MoO<sub>3</sub> exhibits a higher absorbance in the visible light range than mesoporous SnO<sub>2</sub>. This may be caused by the fact that MoO<sub>3</sub> shell can serve as a component in the composites and the interfacial coupling effect between MoO<sub>3</sub> and SnO<sub>2</sub> particles is possibly for the red-shift of the band gap. Such an enhancement in the visible light harvesting, including absorbance and scattering, can increase the number of photogenerated electrons and holes to participate in the photocatalytic reaction and enhance the photocatalytic performance [15].

The surface chemical composition and chemical states of mesoporous SnO<sub>2</sub> were further confirmed by X-ray photoelectron spectroscopy (XPS). Only Sn, Mo, C, and O species were detected (Figure 7(a)). In Figure 7(b), the Sn3d5 binding energy peaks are observed at ~486.7 and ~495.1 eV, corresponding to the spin orbit of Sn3d5/2 and Sn3d3/2, which suggests that Sn in the samples exists in a tetravalent-oxidation state [16]. The Mo 3d core level spectrum of the MoO<sub>3</sub> consists of a spin orbit doublet with peaks at 232.6 and 235.8 eV, associated with Mo cations in the higher oxidation

state (Mo<sup>6+</sup>) (Figure 7(c)) [17]. Additionally, the peak with an O1s binding energy around 530.8 eV is attributed to oxygen in the SnO<sub>2</sub> crystal lattice, which corresponds to the Sn–O–Sn bonds [18], while the other peak positioned at 530.4 eV should be ascribed to the typical Mo–O bond [19].

The photocatalytic activities of the investigated samples were evaluated by measuring the time-dependent degradation of MO in an aqueous catalyst suspension. Figure 8 illustrates the relative concentration  $C/C_0$  of MO as a function of time under ultraviolet light irradiation in the presence of the catalysts. Prior to irradiation, the suspension of the catalyst and dye solution was stirred in the dark for 0.5 hours to reach the equilibrium adsorption. It was noteworthy that the adsorption of MO was found to gradually increase with the increase of Mo content and MO could be completely decolorized after 2.5 hours.

In order to evaluate the photocatalytic activity of the synthesized mesoporous SnO<sub>2</sub>, photocatalytic degradation of methylene blue (MB) was also studied under ultraviolet light irradiation. Mesoporous SnO<sub>2</sub> also performed on photocatalytic activity of degradation of MO. The effect of the pH value of the MO solution on the photocatalytic activity of mesoporous SnO<sub>2</sub> was tested. It can be observed that the pH value can significantly affect the photocatalytic activity. The degradation rates are 60% and 100% under the conditions of pH = 4 and pH = 7, respectively, while it is only 10% when the pH value is further increased to 9.

## 4. Conclusion

In summary, we have synthesized SnO<sub>2</sub> nanoparticles 5-6 nm in size with the assistance of Mo<sub>7</sub>O<sub>24</sub><sup>6-</sup> in aqueous solution at room temperature and assembled them into mesoporous materials. Mesoporous SnO<sub>2</sub> shows photocatalytic activities by the degradation of MO in aqueous solution under UV light irradiation.

## Conflict of Interests

The authors declare that there is no conflict of interests regarding the publication of this paper.

## References

- [1] L. Y. Jiang, X. L. Wu, Y. G. Guo, and L. J. Wan, "SnO<sub>2</sub>-based hierarchical nanomicrostructures: facile synthesis and their applications in gas sensors and lithium-ion batteries," *The Journal of Physical Chemistry C*, vol. 113, no. 2, pp. 14213–14219, 2009.
- [2] P. Manjula, R. Boppella, and S. V. Manorama, "A facile and green approach for the controlled synthesis of porous SnO<sub>2</sub> nanospheres: application as an efficient photocatalyst and an excellent gas sensing material," *ACS Applied Materials & Interfaces*, vol. 4, no. 11, pp. 6252–6260, 2012.
- [3] Q. Q. Wang, B. Z. Lin, B. H. Xu, X. L. Li, Z. J. Chen, and X. T. Pian, "Preparation and photocatalytic properties of mesoporous SnO<sub>2</sub>-hexaniobate layered nanocomposite," *Microporous and Mesoporous Materials*, vol. 130, no. 1–3, pp. 344–351, 2010.

- [4] X. Wang, H. Q. Fan, and P. R. Ren, "Electrospinning derived hollow SnO<sub>2</sub> microtubes with highly photocatalytic property," *Catalysis Communications*, vol. 31, pp. 37–41, 2013.
- [5] X. J. Liu, L. K. Pan, T. Q. Chen et al., "Visible light photocatalytic degradation of methylene blue by SnO<sub>2</sub> quantum dots prepared via microwave-assisted method," *Catalysis Science & Technology*, vol. 3, no. 7, pp. 1805–1809, 2013.
- [6] M. A. Hossain, G. Yang, M. Parameswaran, J. R. Jennings, and Q. Wang, "Mesoporous SnO<sub>2</sub> spheres synthesized by electrochemical anodization and their application in CdSe-sensitized solar cells," *Journal of Physical Chemistry C*, vol. 114, no. 49, pp. 21878–21884, 2010.
- [7] G. L. Shang, J. H. Wu, M. L. Huang et al., "Facile synthesis of mesoporous tin oxide spheres and their applications in dye-sensitized solar cells," *Journal of Physical Chemistry C*, vol. 116, no. 38, pp. 20140–20145, 2012.
- [8] J. Yan, E. Khoo, A. Sumboja, and P. S. Lee, "Facile coating of manganese oxide on tin oxide nanowires with high-performance capacitive behavior," *ACS Nano*, vol. 4, no. 7, pp. 4247–4255, 2010.
- [9] L. Bau, B. Bartova, M. Arduini, and F. Mancin, "Surfactant-free synthesis of mesoporous and hollow silica nanoparticles with an inorganic template," *Chemical Communications*, no. 48, pp. 7584–7586, 2009.
- [10] H. Chen, J. L. Xu, X. W. Xu, and Q. L. Zhang, "Preparation of mesoporous NiO with excellent pseudocapacitive behavior," *European Journal of Inorganic Chemistry*, vol. 2013, no. 7, pp. 1105–1108, 2013.
- [11] G. A. Parks, "The isoelectric points of solid oxides, solid hydroxides, and aqueous hydroxo complex systems," *Chemical Reviews*, vol. 65, pp. 177–198, 1965.
- [12] C. V. Krishnan, M. Garnett, B. Hsiao, and B. Chu, "Electrochemical measurements of isopolyoxomolybdates: 1. pH dependent behavior of sodium molybdate," *International Journal of Electrochemical Science*, vol. 2, pp. 29–51, 2007.
- [13] A. M. Kalsin, M. Fialkowski, M. Paszewski, S. K. Smoukov, K. J. M. Bishop, and B. A. Grzybowski, "Electrostatic self-assembly of binary nanoparticle crystals with a diamond-like lattice," *Science*, vol. 312, no. 5772, pp. 420–424, 2006.
- [14] Y. Oaki, K. Nakamura, and H. Imai, "Homogeneous and disordered assembly of densely packed titanium oxide nanocrystals: an approach to coupled synthesis and assembly in aqueous solution," *Chemistry—A European Journal*, vol. 18, no. 10, pp. 2825–2831, 2012.
- [15] T. G. Xu, L. W. Zhang, H. Y. Cheng, and Y. F. Zhu, "Significantly enhanced photocatalytic performance of ZnO via graphene hybridization and the mechanism study," *Applied Catalysis B: Environmental*, vol. 101, pp. 382–387, 2011.
- [16] H. J. Ahn, H. C. Choi, K. W. Park, S. B. Kim, and Y. E. Sung, "Investigation of the structural and electrochemical properties of size-controlled SnO<sub>2</sub> nanoparticles," *The Journal of Physical Chemistry B*, vol. 108, no. 28, pp. 9815–9820, 2004.
- [17] W. Grünert, A. Y. Stakheev, R. Feldhaus, K. Anders, E. S. Shpiro, and K. M. Minachev, "Analysis of Mo(3d) XPS spectra of supported Mo catalysts: an alternative approach," *Journal of Physical Chemistry*, vol. 95, no. 3, pp. 1323–1328, 1991.
- [18] S. Wu, S. Yuan, L. Y. Shi, Y. Zhao, and J. H. Fang, "Preparation, characterization and electrical properties of fluorine-doped tin dioxide nanocrystals," *Journal of Colloid and Interface Science*, vol. 346, no. 1, pp. 12–16, 2010.
- [19] M. Vasilopoulou, A. M. Douvas, D. G. Georgiadou et al., "The influence of hydrogenation and oxygen vacancies on molybdenum oxides work function and gap states for application in organic optoelectronics," *Journal of the American Chemical Society*, vol. 134, no. 39, pp. 16178–16187, 2012.

## Review Article

# Synthesis and Application of One-Dimensional $\text{La}(\text{OH})_3$ Nanostructures: An Overview

Xiang Xiao,<sup>1</sup> Yu Huang,<sup>2</sup> and Fan Dong<sup>1</sup>

<sup>1</sup> Chongqing Key Laboratory of Catalysis and Functional Organic Molecules, College of Environmental and Biological Engineering, Chongqing Technology and Business University, Chongqing 400067, China

<sup>2</sup> Key Laboratory of Aerosol Science & Technology, SKLLQG, Institute of Earth Environment, Chinese Academy of Sciences, Xi'an 710075, China

Correspondence should be addressed to Fan Dong; [dfctbu@126.com](mailto:dfctbu@126.com)

Received 19 June 2014; Accepted 1 August 2014; Published 21 August 2014

Academic Editor: Yu Xin Zhang

Copyright © 2014 Xiang Xiao et al. This is an open access article distributed under the Creative Commons Attribution License, which permits unrestricted use, distribution, and reproduction in any medium, provided the original work is properly cited.

One-dimensional (1D) semiconductor nanomaterials are of particular importance owing to their unique properties and potential applications. This review attempts to provide a comprehensive introduction of 1D  $\text{La}(\text{OH})_3$  nanostructures including nanowires, nanoneedles, nanobelts, and nanorods. Firstly, various strategies developed to fabricate the 1D  $\text{La}(\text{OH})_3$  nanostructures are discussed, such as precipitation and composite-hydroxide-mediated, hydrothermal, and solvothermal methods, accompanying the description of the corresponding growth mechanisms. Then, the unique properties such as novel physical properties of 1D  $\text{La}(\text{OH})_3$  nanostructures resulting from their unique electronic structures and numerous transition modes involving the 4f shells of these ions are represented in detail. Also, the wide applications in photocatalyst, capacitors, and photoluminescence based on the unique properties are discussed. Finally, the paper ends with a summary and some perspectives on the challenges and new directions in this emerging area.

## 1. Introduction

The properties of nanosized materials strongly depend on their size, shape, and morphology [1, 2]. Recently, one-dimensional (1D) nanostructures have attracted great attention due to their unique physical, chemical, and mechanical properties. Moreover, their particular optical, electrical, and thermal properties result in the wide applications, while solution phase synthesis of controlled one-dimensional (1D) nanostructures such as nanowires, nanobelts, nanorods, and nanotubes is still a challenging task as surface energy favours the spherical particle formation [3]. Thus, much effort has been devoted to fabricate 1D nanostructures by either deploying surfactants/polymer as capping agent or using templates. Up till now, several strategies have been developed to prepare 1D nanostructure materials, such as electrochemical methods, precipitation method, template directed growth technique, vapor-liquid-solid (VLS) synthesis, composite-hydroxide-mediated (CHM) method, and hydrothermal process.

Generally speaking, lanthanide compounds with 1D nanostructure promise as highly functionalized materials as a result of their specific shapes and quantum size effects. Also, as a consequence of their unique electronic structures and exhibiting numerous transition modes involving the 4f shells of their ions, lanthanum and its compounds have the outstanding optical, electrical, and magnetic properties [4–7]. Lanthanum, the lightest element in the lanthanide series, has been widely studied in its oxide, hydroxide, and phosphate forms and has been extensively applied in optoelectronic devices, catalysis, sensors, sorbent, solid electrolyte, and so forth. Particularly, the study of one-dimensional  $\text{La}(\text{OH})_3$  has attracted growing interest because of the promising applications in lanthanum hydroxide nanowires modified carbon paste electrode (LNW/CPE), catalyst, sorbent materials, sensors, and the process for the collection of As(III).

Various chemical methods are adopted for the preparation of lanthanum hydroxide nanostructures, including solvothermal, hydrothermal, and CHM methods. For example, Wang et al. [8, 9] reported the synthesis of  $\text{La}(\text{OH})_3$

nanorods and nanotubes through a hydrothermal method. Hu et al. [10] synthesized  $\text{La}(\text{OH})_3$  nanobelts through a CHM method and then transformed to  $\text{La}_2\text{O}_3$  nanobelts via further calcinations.  $\text{La}(\text{OH})_3$  nanorods with controlled morphology were also prepared by a nonaqueous method [11]. In addition, Wang and Li [12] reported a simple method for large-scale synthesis of  $\text{La}(\text{OH})_3$  nanowires.

Herein, this paper will provide a comprehensive review of the state-of-the-art research activities that focus on the synthetic strategies and applications of one-dimensional  $\text{La}(\text{OH})_3$ . This review is divided into two main sections. The first section introduces the synthetic methods of  $\text{La}(\text{OH})_3$ . These approaches are classified into precipitation, CHM, and solvothermal and hydrothermal methods. Besides, this section also discusses influence factors during the preparation process: the pH value, temperature, alkaline sources, and surfactant, and the use of microwaves assisted in the hydrothermal treatment. It can be found that these factors play a crucial role in controlling the morphologies of the products. Based on these fundamental physical properties of  $\text{La}(\text{OH})_3$ , the recent progress of their application will be highlighted in the next section, which includes photocatalyst, photoluminescence, and fabrication of capacitors. This paper will conclude with a prospective outlook of some scientific and technological challenges with respect to further investigation in this field.

## 2. Synthesis of One-Dimensional $\text{La}(\text{OH})_3$ Nanostructures

A variety of methods have been utilized to synthesize 1D  $\text{La}(\text{OH})_3$  nanostructures. According to the synthesis environment, they can be mainly divided into four categories: precipitation, CHM, hydrothermal, and solvothermal methods. This section will present a survey of various reports on the synthesis of 1D  $\text{La}(\text{OH})_3$  nanostructures using these methods.

**2.1. Precipitation Method.** The precipitation method is widely adopted because of its simplicity, high efficiency, and low cost. According to the precipitation method, a base ( $\text{NH}_3\cdot\text{H}_2\text{O}$ ,  $\text{NaOH}$ ,  $\text{KOH}$ ) was added into a  $\text{La}^{3+}$ -contained solution under magnetic stirring and reacted sufficiently for certain time. Several precipitation approaches have been developed to synthesize one-dimensional  $\text{La}(\text{OH})_3$  nanostructure.

Mu et al. [13] have obtained  $\text{La}(\text{OH})_3$  nanorods with uniform morphology with aspect ratio of about 10–15. The TEM images of Figure 1 illustrate the obtained samples exhibited one-dimensional rod-like nanostructures. With the concentration of CTAB increasing from 0.002 to 0.006 M, the length and radius of the  $\text{La}(\text{OH})_3$  nanorods also increased. The cationic surfactant CTAB not only provides a favorable site for the growth of the particulate assemblies, but also influences the formation process, including nucleation, growth, coagulation, and flocculation [14]. While Li et al. [15] added diethylenetriamine to induce the centripetal growth of  $\text{La}(\text{OH})_3$  nanostructures, which acts not only as an alkaline source, but also as a surfactant. A possible growth process of dendrite-like  $\text{La}(\text{OH})_3$  nanostructures can be described

as follows. The  $\text{OH}^-$  is slowly released and reacts with  $\text{La}^{3+}$ , and the resulting  $\text{La}(\text{OH})_3$  nucleates and aggregates in the presence of diethylenetriamine. The anisotropic growth and Ostwald aging lead to the dendrite-like nanostructures, while only nanorods can be achieved using sodium hydroxide and ammonia as mineralizer instead of diethylenetriamine, which confirmed the importance of diethylenetriamine as a surfactant.

Kohli et al. [16] synthesized  $\text{La}(\text{OH})_3$  nanorods with length varying from 30 to 50 nm with aspect ratio of 2–5 in aqueous solution using hydrazine hydrate as alkaline sources and using cationic CTAB and TBAB as surfactants. Lanthanum ions quickly react with hydroxyl ions to form lanthanum hydroxide because of electrostatic interactions. Due to the cationic group of surfactants molecules present in the reaction mixture, the coordinate complex  $\text{La}(\text{OH})_4^{-1}$  occurs. Thus cation  $\text{CTA}^+$  got adsorbed on the surface of  $\text{La}(\text{OH})_4^{-1}$  to form a film. The film acts as seeding source for the assembly and growth of nanocrystal in the form of rods. The surfactant serves as a growth controller as well as agglomeration inhibitor by forming a covering film on the  $\text{La}(\text{OH})_3$  rods. Adding CTAB alone in the reaction mixture resulted in formation of long fibres, while short size anisotropic rods were obtained in the presence of both CTAB and TBAB mixture due to the fact that TBAB can restrict the faster longitudinal growth to some extent.

Figure 1 is reproduced from the report of Mu et al. [13]. From Figure 1, we can find that the as-prepared  $\text{La}(\text{OH})_3$  samples exhibited one-dimensional rod-like nanostructures with hexagonal phase. Moreover, the  $\text{La}(\text{OH})_3$  nanostructures are monodisperse and display uniform size and shape with 13–15 nm in width and 150–200 nm in length (CTAB concentration is 0.004 M).

**2.2. Composite-Hydroxide-Mediated Method.** Composite-hydroxide-mediated (CHM) synthesis method [21, 22] can not only synthesize complex oxide nanostructures, but also produce hydroxide nanostructures under normal atmospheric pressure. Hu et al. [10] have developed a facile CHM synthesis method to prepare ultralong  $\text{La}(\text{OH})_3$  nanobelts. The associated SEM images were shown in Figure 2. Lanthanum hydroxide nanobelts were prepared by adding 0.1 g  $\text{La}(\text{CH}_3\text{COO})_3$  to a mixture of hydroxides ( $\text{NaOH}/\text{KOH} = 51.5 : 48.5$ ) in a Teflon vessel and treated at 200°C for 48 h in a furnace. The  $\text{La}(\text{OH})_3$  nanobelts are single-crystalline with a [110] growth direction. The possible growth mechanism for the  $\text{La}(\text{OH})_3$  nanobelts is as follows. In the molten hydroxide,  $\text{La}(\text{CH}_3\text{COO})_3$  reacts with  $\text{NaOH}/\text{KOH}$  to produce crystalline  $\text{La}(\text{OH})_3$  nuclei, which then grow along the [110] direction to form nanobelts. In this growth mechanism, disperse single-crystalline nanostructures can also be obtained in the absence of any surface-capping materials. The large viscosity of the hydroxide led to low growth rates, resulting in slow formation of  $\text{La}(\text{OH})_3$  nano-structures. Moreover, the melting points ( $T_m$ ) of both pure sodium hydroxide and potassium hydroxide are over 300°C, and the eutectic point for the composition  $\text{NaOH}/\text{KOH} = 51.5 : 48.5$  is only about 165°C. Therefore, during the reaction process,

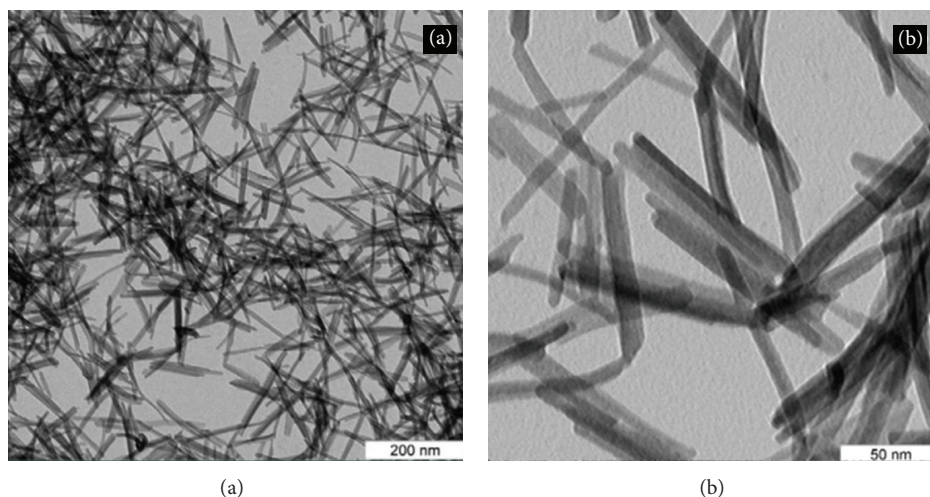


FIGURE 1: The typical TEM images of the  $\text{La}(\text{OH})_3$  nanorods [13].

TABLE 1: Summary of preparation process of  $\text{La}(\text{OH})_3$  nanostructure by precipitation.

Reference	Preparation method	Morphology	Mechanism of formation
[13]	<ol style="list-style-type: none"> <li>① 0.004 M CTAB was mixed with distilled deionized water.</li> <li>② Then 10 mL <math>\text{NH}_3 \cdot \text{H}_2\text{O}</math> was added into the CTAB solution.</li> <li>③ 0.04 M <math>\text{LaCl}_3 \cdot 7\text{H}_2\text{O}</math> was added into it and stirred for 2 h.</li> </ol>	Nanorods	$\text{La}^{3+} + 3\text{OH}^- \rightarrow \text{La}(\text{OH})_3$ .
[15]	<ol style="list-style-type: none"> <li>① <math>\text{La}(\text{NO}_3)_3</math> was dissolved (solution A).</li> <li>② Diethylenetriamine was dissolved (solution B).</li> <li>③ The solution A was heated at <math>90^\circ\text{C}</math> and solution B was dropped into solution A and then kept for 3 h.</li> </ol>	Dendrite-like $\text{La}(\text{OH})_3$ nanostructures	$\text{La}^{3+} + 3\text{OH}^- \rightarrow \text{La}(\text{OH})_3$ .
[16]	<ol style="list-style-type: none"> <li>① 5 mM of each CTAB, TBAB, and <math>\text{La}(\text{NO}_3)_3 \cdot 6\text{H}_2\text{O}</math> was dissolved.</li> <li>② 1.215 mL of hydrazine hydrate was added rapidly to this reaction mixture.</li> </ol>	Nanorods	$\text{N}_2\text{H}_4 + \text{H}_2\text{O} \leftrightarrow \text{N}_2\text{H}_5^+ + \text{OH}^-$ $\text{La}^{3+} + \text{OH}^- \rightarrow \text{La}(\text{OH})_3$

the hydroxides not only act as reactants, but also play a role as solvents for lowering the reaction temperature. The summary of preparation process for  $\text{La}(\text{OH})_3$  nanostructures by precipitation is shown in Table 1.

**2.3. Hydrothermal Method.** Hydrothermal process began with aqueous mixture of soluble metal salt of the precursor materials. Usually the mixed solution is placed in an autoclave under elevated temperature and relatively high pressure conditions. Many works have been reported to systematically manipulate uniform morphologies and well-dispersed 1D  $\text{La}(\text{OH})_3$  materials using hydrothermal approaches. In addition, according to the different heating methods, the hydrothermal method is divided into two categories: conventional hydrothermal and microwave-assisted hydrothermal methods.

**2.3.1. Conventional Hydrothermal Method.** In the traditional hydrothermal method, lanthanum hydroxide gel was firstly synthesized by precipitation or by the direct mixture of a lanthanum salt with a base solution and then transferred to Teflon autoclave and heated at an oven. Jia et al. [17] have reported that the morphologies of  $\text{La}(\text{OH})_3$  can be modulated by adjusting the pH values of the initial solution. A higher pH value implies a higher  $\text{OH}^-$  concentration and a higher

chemical potential in solution. Therefore, the nucleating process occurs faster and more nuclei of crystals are formed, resulting in the high aspect ratio of the samples. In addition, the field SEM images of Figure 3 illustrated that alkaline sources exerted significant effect on the preferential growth orientations. While using hydrazine hydrate ( $\text{N}_2\text{H}_4 \cdot \text{H}_2\text{O}$ ) as alkaline source,  $\text{La}(\text{OH})_3$  nanoprisms will be obtained. The aspect ratio of the  $\text{La}(\text{OH})_3$  nanoprisms reduces with an increase in the concentration of  $\text{N}_2\text{H}_4 \cdot \text{H}_2\text{O}$ . The hydrazine hydrate may have dual functions in the formation process of  $\text{La}(\text{OH})_3$ , acting as alkaline sources in the solution and behaving as crystal facet inhibitors in the system.

Wang et al. [18] have synthesized stable and crystalline phase Ln (Ln = Sm, Er, Gd, Dy, and Eu) doped  $\text{La}(\text{OH})_3$  ( $\text{La}(\text{OH})_3 : \text{Ln}^{3+}$ ) nanorods. The as-prepared  $\text{La}(\text{OH})_3 : \text{Ln}^{3+}$  samples are one-dimensional rod-like nanostructures, and the  $\text{La}(\text{OH})_3 : \text{Ln}^{3+}$  products with 20%  $\text{Ln}^{3+}$  doped are mainly composed of uniform short nanorods with diameters of about 10 nm and lengths of 100–150 nm. The Ln doping does not change the hexagonal structure of  $\text{La}(\text{OH})_3$ , which implies that the  $\text{Ln}^{3+}$  doping most probably occurs by substituting lanthanum atom in the crystal structure. Similarly, Zhang et al. [20] have prepared uniform  $\text{Yb}^{3+}/\text{Er}^{3+}$ ,  $\text{Yb}^{3+}/\text{Ho}^{3+}$ , and  $\text{Yb}^{3+}/\text{Tm}^{3+}$  codoped  $\text{La}(\text{OH})_3$  microrods in molten composite-hydroxide ( $\text{NaOH}/\text{KOH}$ ) medium, while

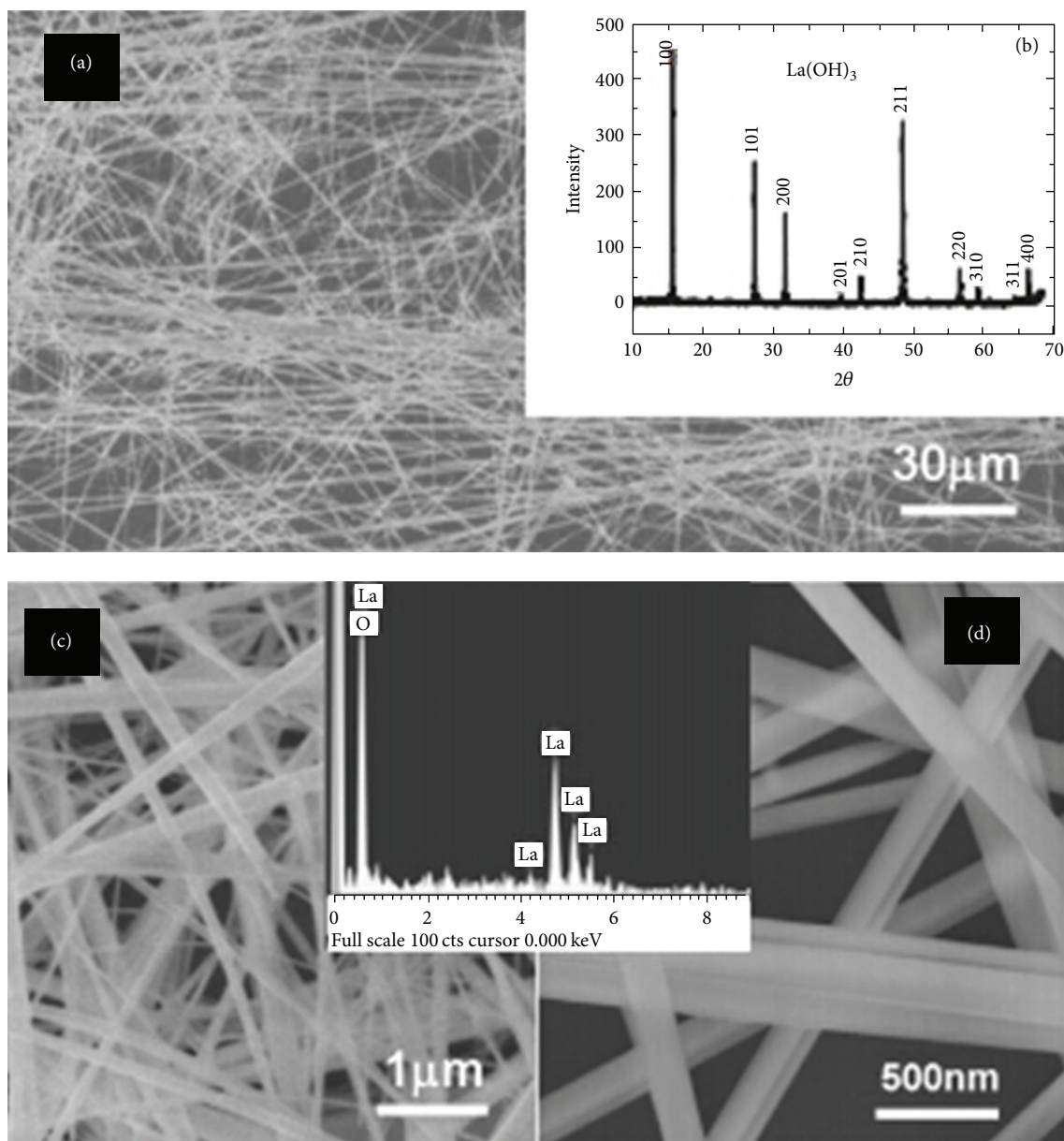


FIGURE 2: (a) Low-magnification SEM image of the  $\text{La}(\text{OH})_3$  products. (b) A typical XRD pattern of the as-synthesized  $\text{La}(\text{OH})_3$  product. (c) and (d) are the high-magnification SEM images of the  $\text{La}(\text{OH})_3$  product [10].

the  $\text{La}_2\text{O}_3 : \text{Ln}^{3+}$  ( $\text{Ln} = \text{Yb}/\text{Er}, \text{Yb}/\text{Tm}, \text{Yb}/\text{Ho}$ ) microrods were obtained by solid state reaction at  $700^\circ\text{C}$  for 6 h. In the synthesis, no catalyst, template, or surfactant were used in the reaction system to reduce the surface energy, so the growth of  $\text{La}(\text{OH})_3 : \text{Ln}^{3+}$  is governed by the inherent crystal structure and the chemical activity. The growth mechanism of microrods formation is proposed as follows. After the hydroxides are molten,  $\text{La}^{3+}$  cations can easily react with hydroxyl groups to form  $\text{La}(\text{OH})_3$  nuclear due to the opposite electric charge, whereas a large number of  $\text{Ln}^{3+}$  and  $\text{OH}^-$  ions still exist in the solution, which will be adsorbed on the preferred surfaces of  $\text{La}(\text{OH})_3$  nuclear. Therefore, long  $\text{La}(\text{OH})_3 : \text{Ln}^{3+}$  microrods will form with the increasing

reaction time.  $\text{La}_2\text{O}_3 : \text{Ln}^{3+}$  microrods can be topochemically prepared from  $\text{La}(\text{OH})_3 : \text{Ln}^{3+}$  after the thermal decomposition process [23].

**2.3.2. Microwave-Assisted Hydrothermal Method.** In the micro-wave process, heat is internally generated within the material, instead of originating from external heating sources [24]. Microwave radiation as a heating source is applied for the hydrothermal method, which is beneficial to improve the reaction kinetic constants [25]. Additionally, microwave-assisted hydrothermal method has several advantages compared to the conventional hydrothermal: less energy

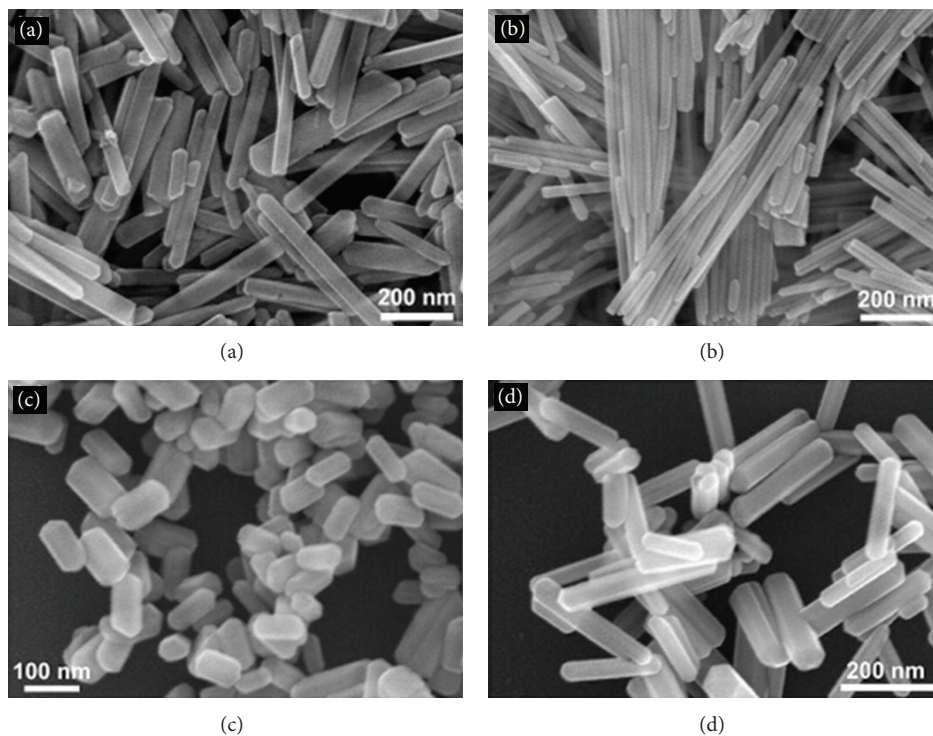


FIGURE 3: The SEM images of the  $\text{La}(\text{OH})_3$  samples prepared at (a) pH = 7 and (b) pH = 10 with ammonia as alkaline source and (c) at pH = 9 with pure hydrazine hydrate and (d) a mixture of ammonia and hydrazine hydrate as alkaline sources [17].

consumption, shorter reaction time, lower synthetic temperature, higher purity, and smaller particle size [26, 27]. Pao et al. [19] have reported that uniform  $\text{La}(\text{OH})_3$  nanowires (NWs) with a high aspect ratio of more than 200 have been successfully synthesized by a simple microwave-assisted hydrothermal (MH) process. Compared to a conventional hydrothermal (CH) one, the  $\text{La}(\text{OH})_3$  nanorods are obtained in a lower aspect ratio, higher temperature, and longer time. The formation mechanism of 1D  $\text{La}(\text{OH})_3$  NWs synthesized by the MH method was explained by an ionic solvent effect [28]. Concentrated  $\text{NH}_4\text{OH}$  was added into a solution containing  $\text{La}^{3+}$  cations and the  $\text{La}^{3+}$  cations can react with  $\text{OH}^-$  anions to form  $(\text{La}(\text{OH})_4)^-$ . Then the positive  $\text{NH}_4^+$  ions interact with  $(\text{La}(\text{OH})_4)^-$  to form  $\text{NH}_4\text{La}(\text{OH})_4$  gel complexes by the electrostatic interaction. On the optimal conditions,  $\text{NH}_4^+$  and  $\text{OH}^-$  ions were released from  $\text{NH}_4\text{La}(\text{OH})_4$ , and  $\text{La}(\text{OH})_3$  molecules nucleated and grew in the lowest energy plane at the highest growth rate as  $\text{La}(\text{OH})_3$  NWs were produced.

Figure 3 is achieved from the report of Jia et al. [17]. The report indicated that the pH value of  $\text{NH}_3\cdot\text{H}_2\text{O}$  as alkaline sources increased from 7 to 9, and the aspect ratio of the  $\text{La}(\text{OH})_3$  nanowires increased dramatically [17]. By increasing the pH value to 10, the nanowires self-assembled into bundles along their cross-sectional diameter through a direct aggregation growth process. When hydrazine hydrate ( $\text{N}_2\text{H}_4\cdot\text{H}_2\text{O}$ ) is applied as alkaline source, the as-prepared sample is almost entirely composed of short hexagonal nanoprisms. However, when the mixtures of ammonia and hydrazine hydrate are used as alkaline sources (pH 9), the

sample consisting of uniform hexagonal nanoprisms with higher aspect ratios was produced. The aspect ratios of the samples reduce with an increase in the concentration of  $\text{N}_2\text{H}_4\cdot\text{H}_2\text{O}$ .

**2.4. Solvothermal Method.** With the advantages of high purity and good homogeneity, the solvothermal synthesis method is one of the most significant technologies for the preparation of nanorods or nanowires [29]. The solvothermal process with low boiling point not only shortens reactant times, but also benefits the crystallinity of products [30]. Tang et al. [31] applied a sol-solvothermal method to synthesize  $\text{La}(\text{OH})_3$  and used microwave radiation to dry the  $\text{La}(\text{OH})_3$  nanorods. In this experiment, 60 mL 0.3 M  $\text{NH}_3\cdot\text{H}_2\text{O}$  was added to 20 mL 0.1 M aqueous  $\text{La}(\text{NO}_3)_3$  to get a light blue transparent sol. After the sol was washed with ethanol and dispersed into 16 mL benzene, the pH value was adjusted to 12 by adding n-butylamine. The products were dried for 4 min using a microwave oven. The obtained  $\text{La}(\text{OH})_3$  nanorods are single crystals and uniform with diameters ranging from 8 to 15 nm and lengths of up to 200 nm. If conventional heating is applied, the morphology of  $\text{La}(\text{OH})_3$  is irregular due to the aggregation of the nanostructures. Therefore, microwave radiation drying can keep their morphologies better than conventional drying. In contrast to conventional drying, microwave drying evaporation takes place on the surface of the sample at lower temperature because of evaporative cooling, which further ensures a more stable temperature-increasing process, effectively preventing the agglomeration

TABLE 2: Summary of preparation process of La(OH)<sub>3</sub> nanostructure by hydrothermal method.

Reference	Preparation method	Morphology	Mechanism of formation
[17]	① Ammonia solution was added to La(NO <sub>3</sub> ) <sub>3</sub> (1 M, 2 mL) aqueous solution. ② After additional agitation for 1 h, the as-obtained colloidal suspension was transferred to a 50 mL autoclave and heated at 200 °C for 24 h.	PH 7 to 9: nanowire. PH 10: nanobundles	$\text{La}^{3+} + \text{OH}^- \rightarrow \text{La(OH)}_3$
[18]	① 0.003 M CTAB was mixed with deionized water and then 40 mL of NH <sub>3</sub> ·H <sub>2</sub> O was added. ② 0.004 M LaCl <sub>3</sub> ·6H <sub>2</sub> O and LnCl <sub>3</sub> ·6H <sub>2</sub> O with the different Ln compositions were added into the mixture and then heated at 200 °C for 4 h.	Nanorods	$\text{La}^{3+} + \text{OH}^- \rightarrow \text{La(OH)}_3$
[19]	① La(NO <sub>3</sub> ) <sub>3</sub> , Yb(NO <sub>3</sub> ) <sub>3</sub> , and Er(NO <sub>3</sub> ) <sub>3</sub> and deionized water were added into a 30 mL Teflon-lined autoclave, followed by adding mixed hydroxides. ② The autoclave was preheated to 200 °C for 30 min and then the reaction progressed for 24 h.	Microrods	$\text{La}^{3+} + \text{Ln}^{3+} + \text{OH}^- \rightarrow \text{La(OH)}_3 : \text{Ln}^{3+}$
[20]	① Concentrated NH <sub>4</sub> OH was dropped to La(NO <sub>3</sub> ) <sub>3</sub> ·6H <sub>2</sub> O solution until pH at 10. ② Transfer into a Teflon-lined autoclave and heat by a 300 W microwave digestion at 150 °C for 1 h.	Nanowires	$\text{La}^{3+} + \text{OH}^- \rightarrow (\text{La(OH)}_4)^-$ $(\text{La(OH)}_4)^- + \text{NH}_4^+ \rightarrow \text{NH}_4\text{La(OH)}_4$ $\text{NH}_4\text{La(OH)}_4 \rightarrow \text{La(OH)}_3 + \text{NH}_4^+ + \text{OH}^-$

of the sample occurring in the conventional drying process [32]. The summary of preparation process of La(OH)<sub>3</sub> nanostructures by hydrothermal/solvothermal method is shown in Table 2.

### 3. Application of One-Dimensional La(OH)<sub>3</sub> Nanostructures

As the potential building blocks for future materials, 1D La(OH)<sub>3</sub> nanosystems exhibit unique physical properties due to their size and structure anisotropy. These properties have been exploited to the design and development of various electronic, fluorescent, and photocatalytic devices. In this context, 1D La(OH)<sub>3</sub> nanostructures represent an ideal channel for devices acting as capacitor and are suitable for biological labeling. In this section, applications based on photoluminescence, photocatalyst, and super capacitor will be presented.

**3.1. Photoluminescence.** To the best of our knowledge, La(OH)<sub>3</sub> nanostructures with higher crystallinity are important for phosphors. High crystallinity generally means less traps and stronger luminescence. In Jia's [17] experimental results, the luminescence properties of the as-obtained phosphors are dependent on their morphologies and sizes. The morphology and size of the lanthanide-base luminescent materials may affect the emission intensity as a result of the change in their specific surface area [33–35]. If the surface area is greatly reduced, which results in increased crystallite size, the phosphor with fewer defects would show great improvement in PL intensity [33–35]. Therefore, the nanowire phosphor has a higher PL intensity than nanoprism phosphor. As we know, the PL intensity of the phosphor is strongly influenced by the dopant concentration [36–38]. It has been proved that the Tb<sup>3+</sup>-doped La(OH)<sub>3</sub> samples

have the luminescence properties and exhibit strong green emission.

As known to all, lanthanum oxide is a promising host matrix for its good chemical durability, thermal stability, and low phonon energy, which result in high upconversion (UC) photoluminescence (PL) properties [39], while La<sub>2</sub>O<sub>3</sub> doped by rare earth ions (RE) exhibits brighter luminescence than the purity of La<sub>2</sub>O<sub>3</sub>. The emission from the RE<sup>3+</sup> dopants is mainly due to the electric and magnetic dipole optical transitions based on their unique intra-4f transitions, which are shielded by the outer 5s and 5p orbitals, consequently, leading to sharp emissions and narrow bands. Zhang et al. reported [20] that La<sub>2</sub>O<sub>3</sub>:Ln<sup>3+</sup> microrods exhibit the characteristic emissions of Er<sup>3+</sup>, Tm<sup>3+</sup>, and Ho<sup>3+</sup> and give rise to green, blue, and blackish green emission colors, respectively. In the codoped process, the emission intensities are governed by the concentration of Yb<sup>3+</sup> ions. Of course, the unique fluorescent properties facilitate a promising candidate of this La<sub>2</sub>O<sub>3</sub> based material in various color display fields on the basis of the high upconverting efficiency and high resistance against laser radiation damage.

**3.2. Photocatalysis.** Congo red (CR) is a well-known class of azo dyes that are of high toxicity and even carcinogenic to the animals and human. They are not readily degradable due to their complex aromatic structures [40]. However, photodegradation has been proved to be effective for this kind of pollution because of its strong destructive power to mineralize the pollutants into CO<sub>2</sub> and H<sub>2</sub>O. The photocatalytic activity of La(OH)<sub>3</sub>:Ln<sup>3+</sup> nanorods used as the potential photocatalytic materials for photodegradation of Congo red in the aqueous solution has been reported [18]. The photocatalytic activity of semiconductor is based on the generation of electron (e<sup>-</sup>)-hole (h<sup>+</sup>) pair. The impurity level and the lattice defects are generated in the presence

of the singly ionized oxygen vacancy ( $V_0^+$ ) defects in the as-synthesized  $\text{La}(\text{OH})_3$ ;  $V_0^+$  defect can work as electron donors to form charged oxygen vacancy ( $V_0^{++}$ ) [41] and trap the photogenerated holes to reduce the surface recombination of electrons and holes [42]. Therefore, the more the singly ionized oxygen vacancy ( $V_0^+$ ) defects, the higher the photocatalytic activity, while Ln doping is proposed to be located at substitutional positions instead of lanthanum site, so with increase in doping concentrations of Ln, the singly ionized oxygen vacancy ( $V_0^+$ ) defect concentration increases; thus the corresponding photodegradation activity of  $\text{La}(\text{OH})_3 : \text{Ln}^{3+}$  increases. Therefore, the enhanced photocatalytic activity may be ascribed to the lattice defects resulting from doping, which will accelerate the photogenerated electron-hole separation.

**3.3. Super Capacitor.** The material of  $\text{La}(\text{OH})_3$  being dielectric may be used for fabrication of super capacitors. Generally speaking, conductivity maybe depends on three factors; the first term is dependent on frequency; the second term may be a result of autoionisation or polarization; the third which may be possible is that some of free  $\text{La}^{3+}$  ions were left entrapped inside the crystal structure which may generate defects in the  $\text{La}(\text{OH})_3$  crystal. Kohli [16] has reported that capacitance values at lower frequency first decrease sharply and then slowly and become nearly constant. The capacitive behavior may be due to the space charge polarisation from inhomogeneous dielectric structure. Thus this type of electrical behavior may be useful for designing low loss super capacitors and sensors. Hu et al. [10] fabricated a pair of electrodes for connecting a single  $\text{La}(\text{OH})_3$  nanobelt to characterize its electrical transport properties. The detectable conductive behavior of a single nanobelt promises the potential application of  $\text{La}(\text{OH})_3$  nanobelts in capacitors and sensors.

## 4. Summary and Outlook

This paper provides an up-to-date review of the current achievements on 1D  $\text{La}(\text{OH})_3$  nanomaterials, ranging from synthesis to applications. Synthesis of 1D structures has been well developed and an assortment of nanowires, nanobundles, nanobelts, and nanorods is successfully obtained. Such 1D  $\text{La}(\text{OH})_3$  materials have provided a ground for fundamental studies as well as technological developments. The synthesis of 1D  $\text{La}(\text{OH})_3$  nanostructure was influenced by many parameters such as temperature, time, PH value, alkaline source, surface energy, and surfactant. The length and diameter of the as-synthesized  $\text{La}(\text{OH})_3$  nanowires were increased with the increasing reaction temperature and reaction time by hydrothermal method. The pH values of the initial solutions and the alkaline sources will influence the preferential growth orientations of nanocrystals, thus playing a crucial role in controlling the morphologies of the products. In general, the growth of nanostructure is closely related to two factors: the surface energy and growth kinetics, which determine the growth preferential and final structure, respectively. Surfactant can reduce the surface tension of the solution, which lower the energy needed to form a new

phase in reaction mixture. So surfactant-assisted synthesis is considered to be an effective methodology for shape-controlled synthesis in nanomaterials. The specific effects of different surfactants are different. Diethylenetriamine, acting not only as an alkaline source but also as a surfactant, induces the centripetal growth of  $\text{La}(\text{OH})_3$  nanostructures. The cationic CTAB surfactant serves as a growth controller as well as agglomeration inhibitor by forming a covering film on the  $\text{La}(\text{OH})_3$  rods.  $\text{N}_2\text{H}_4 \cdot \text{H}_2\text{O}$  serving as crystal facet inhibitors lead to the formation of nanoprisms. The existing methods for fabricating  $\text{La}(\text{OH})_3$  nanostructure usually need the assistance of surfactant; thus hunting for other methods to obtain the different morphology of  $\text{La}(\text{OH})_3$  is necessary.

Furthermore, these fascinating researches mainly focus on the photoluminescence and photocatalyst area. The unique fluorescent properties of  $\text{La}(\text{OH})_3$  make it a promising candidate in various color display fields on the basis of the high upconverting efficiency and high resistance against laser radiation damage. Moreover,  $\text{La}(\text{OH})_3$  may find potential applications in many fields such as optoelectronic and nanoscale devices due to the unique luminescence properties and controllable morphology and size. The photocatalytic activity of semiconductor is based on the generation of electron-hole pairs, and  $\text{La}(\text{OH})_3$  semiconductor can separate the electron-hole pairs. Therefore,  $\text{La}(\text{OH})_3$  is a promising material for potential application in photodegradation pollutants. Besides, the as-synthesized  $\text{La}(\text{OH})_3 : \text{Ln}^{3+}$  exhibit higher photodegradation activity compared with pure  $\text{La}(\text{OH})_3$  due to the fact that doping can result in lattice defects. Nevertheless, there is much new science awaiting to elucidate, especially the mechanism of photocatalysis by  $\text{La}(\text{OH})_3$  nanomaterials. In addition, except tuning the morphology of  $\text{La}(\text{OH})_3$  nanostructure, technologies such as doping of nonmetal elements, surface modification, and formation of heterostructure can also be applied to improve the photocatalytic activity.

## Conflict of Interests

The authors declare that there is no conflict of interests regarding the publication of this paper.

## References

- [1] L.-X. Yang, Y. Liang, H. Chen, Y.-F. Meng, and W. Jiang, "Controlled synthesis of  $\text{Mn}_3\text{O}_4$  and  $\text{MnCO}_3$  in a solvothermal system," *Materials Research Bulletin*, vol. 44, no. 8, pp. 1753–1759, 2009.
- [2] Q. T. Li, J. S. Ni, Y. Q. Wu, Y. N. Du, W. Z. Ding, and S. Geng, "Synthesis and characterization of  $\text{La}(\text{OH})_3$  nanopowders from hydrolysis of lanthanum carbide," *Journal of Rare Earths*, vol. 29, no. 5, pp. 416–419, 2011.
- [3] C. J. Murphy, T. K. Sau, A. M. Gole et al., "Anisotropic metal nanoparticles: synthesis, assembly, and optical applications," *The Journal of Physical Chemistry B*, vol. 109, no. 29, pp. 13857–13870, 2005.
- [4] J. W. Stouwdam, G. A. Hebbink, J. Huskens, and F. C. J. M. van Veggel, "Lanthanide-doped nanoparticles with excellent luminescent properties in organic media," *Chemistry of Materials*, vol. 15, no. 24, pp. 4604–4616, 2003.

- [5] L. F. Liang, H. F. Xu, Q. Su et al., "Hydrothermal synthesis of prismatic  $\text{NaHoF}_4$  microtubes and  $\text{NaSmF}_4$  nanotubes," *Inorganic Chemistry*, vol. 43, no. 5, pp. 1594–1596, 2004.
- [6] M. S. Palmer, M. Neurock, and M. M. Olken, "Periodic density functional theory study of methane activation over  $\text{La}_2\text{O}_3$ : activity of  $\text{O}^{2-}$ ,  $\text{O}^-$ ,  $\text{O}_2^{2-}$ , oxygen point defect, and  $\text{Sr}^{2+}$ -doped surface sites," *Journal of the American Chemical Society*, vol. 124, no. 28, pp. 8452–8461, 2002.
- [7] J. L. Zhuang, L. F. Liang, H. H. Y. Sung et al., "Controlled hydrothermal growth and up-conversion emission of  $\text{NaNbF}_4$  ( $\text{Ln} = \text{Y}, \text{Dy-Yb}$ )," *Inorganic Chemistry*, vol. 46, no. 13, pp. 5404–5410, 2007.
- [8] X. Wang and Y. Li, "Synthesis and characterization of lanthanide hydroxide single-crystal nanowires," *Angewandte Chemie International Edition*, vol. 41, no. 24, pp. 4790–4793, 2002.
- [9] X. Wang, X. Sun, D. Yu, B. Zou, and Y. Li, "Rare earth compound nanotubes," *Advanced Materials*, vol. 15, no. 17, pp. 1442–1445, 2003.
- [10] C. G. Hu, H. Liu, W. T. Dong et al., " $\text{La}(\text{OH})_3$  and  $\text{La}_2\text{O}_3$  nanobelts—synthesis and physical properties," *Advanced Materials*, vol. 19, no. 3, pp. 470–474, 2007.
- [11] I. Djerdj, G. Garnweitner, D. Sheng Su, and M. Niederberger, "Morphology-controlled nonaqueous synthesis of anisotropic lanthanum hydroxide nanoparticles," *Journal of Solid State Chemistry*, vol. 180, no. 7, pp. 2154–2165, 2007.
- [12] X. Wang and Y. D. Li, "Synthesis and characterization of lanthanide hydroxide single-crystal nanowires," *Angewandte Chemie*, vol. 41, no. 24, pp. 4790–4793, 2002.
- [13] Q. Mu, T. Chen, and Y. Wang, "Synthesis, characterization and photoluminescence of lanthanum hydroxide nanorods by a simple route at room temperature," *Nanotechnology*, vol. 20, no. 34, Article ID 345602, 2009.
- [14] S. G. Dixit, A. K. Vanjara, J. Nagarkar, M. Nikoorazm, and T. Desai, "Co-adsorption of quaternary ammonium compounds—nonionic surfactants on solid-liquid interface," *Colloids and Surfaces A*, vol. 205, no. 1-2, pp. 39–46, 2002.
- [15] S. C. Li, S. J. Hu, N. Du, J. N. Fan, L. J. Xu, and J. Xu, "Low-temperature chemical solution synthesis of dendrite-like  $\text{La}(\text{OH})_3$  nanostructures and their thermal conversion to  $\text{La}_2\text{O}_3$  nanostructures," *Rare Metals*, 2014.
- [16] P. S. Kohli, M. Kumar, K. K. Raina, and M. L. Singla, "Mechanism for the formation of low aspect ratio of  $\text{La}(\text{OH})_3$  nanorods in aqueous solution: thermal and frequency dependent behaviour," *Journal of Materials Science: Materials in Electronics*, vol. 23, no. 12, pp. 2257–2263, 2012.
- [17] G. Jia, Y. Huang, Y. Song, M. Yang, L. Zhang, and H. You, "Controllable synthesis and luminescence properties of  $\text{La}(\text{OH})_3$  and  $\text{La}(\text{OH})_3:\text{ITb}^{3+}$  nanocrystals with multiform morphologies," *European Journal of Inorganic Chemistry*, no. 25, pp. 3721–3726, 2009.
- [18] Y. Wang, S. Liu, Y. Cai et al., " $\text{La}(\text{OH})_3:\text{Ln}^{3+}$  ( $\text{Ln} = \text{Sm}, \text{Er}, \text{Gd}, \text{Dy}$ , and  $\text{Eu}$ ) nanorods synthesized by a facile hydrothermal method and their enhanced photocatalytic degradation of Congo red in the aqueous solution," *Ceramics International*, vol. 40, no. 3, pp. 5091–5095, 2014.
- [19] O. Yayapao, S. Thongtem, A. Phuruangrat, and T. Thongtem, "A simple microwave-assisted hydrothermal synthesis of lanthanum hydroxide nanowires with a high aspect ratio," *Journal of Ceramic Processing Research*, vol. 13, no. 4, pp. 466–469, 2012.
- [20] X. Zhang, P. Yang, D. Wang et al., " $\text{La}(\text{OH})_3:\text{Ln}^{3+}$  and  $\text{La}_2\text{O}_3:\text{Ln}^{3+}$  ( $\text{Ln} = \text{Yb/Er}, \text{Yb/Tm}, \text{Yb/Ho}$ ) microrods: synthesis and up-conversion luminescence properties," *Crystal Growth and Design*, vol. 12, no. 1, pp. 306–312, 2012.
- [21] H. Liu, C. G. Hu, and Z. L. Wang, "Composite-hydroxide-mediated approach for the synthesis of nanostructures of complex functional-oxides," *Nano Letters*, vol. 6, no. 7, pp. 1535–1540, 2006.
- [22] C. G. Hu, H. Liu, C. S. Lao, L. Y. Zhang, D. Davidovic, and Z. L. Wang, "Size-manipulable synthesis of single-crystalline  $\text{BaMnO}_3$   $\text{BaTi}_{1/2}\text{Mn}_{1/2}\text{O}_3$ ," *Journal of Physical Chemistry B*, vol. 110, no. 29, pp. 14050–14054, 2006.
- [23] J. Yang, C. K. Lin, Z. L. Wang, and J. Lin, " $\text{In}(\text{OH})_3$  and  $\text{In}_2\text{O}_3$  nanorod bundles and spheres: microemulsion-mediated hydrothermal synthesis and luminescence properties," *Inorganic Chemistry*, vol. 45, no. 22, pp. 8973–8979, 2006.
- [24] S. Möhmel, I. Kurzawski, D. Uecker, D. Müller, and W. Geßner, "The influence of a hydrothermal treatment using microwave heating on the crystallinity of layered double hydroxides," *Crystal Research and Technology*, vol. 37, no. 4, pp. 359–369, 2002.
- [25] X. Y. Ma, H. Zhang, Y. J. Ji, J. Xu, and D. Yang, "Synthesis of ultra-fine lanthanum hydroxide nanorods by a simple hydrothermal process," *Materials Letters*, vol. 58, no. 7-8, pp. 1180–1182, 2004.
- [26] F. V. Motta, R. C. Lima, A. P. A. Marques et al., "Indium hydroxide nanocubes and microcubes obtained by microwave-assisted hydrothermal method," *Journal of Alloys and Compounds*, vol. 497, no. 1-2, pp. L25–L28, 2010.
- [27] G. Gaspell, L. Fuoco, and M. S. El-Shall, "Microwave synthesis of supported Au and Pd nanoparticle catalysts for CO oxidation," *Journal of Physical Chemistry B*, vol. 109, no. 37, pp. 17350–17355, 2005.
- [28] M. Mazloumi, S. Zanganeh, A. Kajbafvala, M. R. Shayegh, and S. K. Sadrnezhad, "Formation of Lanthanum hydroxide nanostructures: effect of NaOH and KOH solvents," *International Journal of Engineering, Transactions B: Applications*, vol. 21, no. 2, pp. 169–176, 2008.
- [29] K. Tang, Y. Qian, J. Zeng, and X. Yang, "Solvothermal route to semiconductor nanowires," *Advanced Materials*, vol. 15, no. 5, pp. 448–450, 2003.
- [30] K. Byrappa and M. Yoshimura, "Hydrothermal technology for nanotechnology," in *Handbook of Hydrothermal Technology*, pp. 615–762, 2013.
- [31] B. Tang, J. C. Ge, C. J. Wu et al., "Sol-solvothermal synthesis and microwave evolution of  $\text{La}(\text{OH})_3$  nanorods to  $\text{La}_2\text{O}_3$  nanorods," *Nanotechnology*, vol. 15, no. 9, pp. 1273–1276, 2004.
- [32] K. J. Rao, B. Vaidyanathan, M. Ganguli, and P. A. Ramakrishnan, "Synthesis of inorganic solids using microwaves," *Chemistry of Materials*, vol. 11, no. 4, pp. 882–895, 1999.
- [33] J. Yang, C. Li, Z. Cheng et al., "Size-tailored synthesis and luminescent properties of one-dimensional  $\text{Gd}_2\text{O}_3:\text{Eu}^{3+}$  nanorods and microrods," *Journal of Physical Chemistry C*, vol. 111, no. 49, pp. 18148–18154, 2007.
- [34] J. Yang, X. M. Liu, C. X. Li, Z. W. Quan, D. Y. Kong, and J. Lin, "Hydrothermal synthesis of  $\text{SrCO}_3:\text{Eu}^{3+}/\text{Tb}^{3+}$  microneedles and their luminescence properties," *Journal of Crystal Growth*, vol. 303, no. 2, pp. 480–486, 2007.
- [35] J. Wan, Z. Wang, X. Chen, L. Mu, and Y. Qian, "Shape-tailored photoluminescent intensity of red phosphor  $\text{Y}_2\text{O}_3:\text{Eu}^{3+}$ ," *Journal of Crystal Growth*, vol. 284, no. 3-4, pp. 538–543, 2005.
- [36] M. Yu, J. Lin, Z. Wang et al., "Fabrication, patterning, and optical properties of nanocrystalline  $\text{YVO}_4:\text{A}$  ( $\text{A} = \text{Eu}^{3+}, \text{Dy}^{3+}, \text{Sm}^{3+}, \text{Er}^{3+}$ ) phosphor films via sol-gel soft lithography," *Chemistry of Materials*, vol. 14, no. 5, pp. 2224–2231, 2002.
- [37] K. Kim, Y. Kim, H. Chun, T. Cho, J. Jung, and J. Kang, "Structural and optical properties of  $\text{BaMgAl}_{10}\text{O}_{17}:\text{Eu}^{2+}$  phosphor," *Chemistry of Materials*, vol. 14, no. 12, pp. 5045–5052, 2002.

- [38] K. Y. Jung, H. W. Lee, and H. Jung, "Luminescent properties of (Sr, Zn)Al<sub>2</sub>O<sub>4</sub>:Eu<sup>2+</sup>, B<sup>3+</sup> particles as a potential green phosphor for UV LEDs," *Chemistry of Materials*, vol. 18, no. 9, pp. 2249–2255, 2006.
- [39] H. Q. Liu, L. L. Ying, and S. G. Chen, "Effect of Yb<sup>3+</sup> concentration on the upconversion of Er<sup>3+</sup> ion doped La<sub>2</sub>O<sub>3</sub> nanocrystals under 980 nm excitation," *Materials Letters*, vol. 61, no. 17, pp. 3629–3631, 2007.
- [40] Z. J. Yang, J. J. Wei, H. X. Yang, L. Liu, H. Liang, and Y. Z. Yang, "Mesoporous CeO<sub>2</sub> hollow spheres prepared by ostwald ripening and their environmental applications," *European Journal of Inorganic Chemistry*, no. 21, pp. 3354–3359, 2010.
- [41] S. Y. Liu, Y. Cai, X. Y. Cai et al., "Catalyzed degradation Congo red in the aqueous solution by Ln(OH)<sub>3</sub> (Ln1/4Nd, Sm, Eu, Gd, Tb, and Dy) nanorods," *Applied Catalysis A*, vol. 453, pp. 45–53, 2013.
- [42] Y. Hu and H.-J. Chen, "Origin of green luminescence of ZnO powders reacted with carbon black," *Journal of Applied Physics*, vol. 101, no. 12, pp. 124902–124905, 2007.

## Research Article

# Investigations of the Montmorillonite and Aluminium Trihydrate Addition Effects on the Ignitability and Thermal Stability of Asphalt

**Kai Zhu, Ke Wu, Bin Wu, and Zhiyi Huang**

*College of Civil and Architecture Engineering, Zhejiang University, Hangzhou 310027, China*

Correspondence should be addressed to Ke Wu; [wuke@zju.edu.cn](mailto:wuke@zju.edu.cn)

Received 4 June 2014; Accepted 14 July 2014; Published 6 August 2014

Academic Editor: Ying Zhou

Copyright © 2014 Kai Zhu et al. This is an open access article distributed under the Creative Commons Attribution License, which permits unrestricted use, distribution, and reproduction in any medium, provided the original work is properly cited.

By means of limiting oxygen index (LOI), cone calorimeter, and TG-DSC tests, this paper investigated the effect of unmodified montmorillonite (MMT), organically modified montmorillonite (OMMT), and aluminium trihydrate (ATH) additions on the flame retardancy for asphalt combustion. Experimental results showed that adding a small amount of montmorillonite did not significantly increase the oxygen index of the asphalt but reduced the heat release rate during asphalt combustion. TGA tests had indicated that the montmorillonite (MMT and OMMT) could suppress the release of flammable volatiles and form more asphaltenes, which hence postponed the burnout time of asphalt. Furthermore, the combination of montmorillonite (MMT and OMMT) and ATH had yielded a synergistic effect, which had further reduced the heat release rate and also increased the oxygen index of asphalt. In particular, after further addition of OMMT, the barrier layer showed less crack, leading to a significant decrease in the heat release rate as compared to the adding of ATH alone.

## 1. Introduction

Asphalt is a viscoelastic liquid or semisolid with remarkable rheology properties and impermeability. It has been widely used as binder and matrix precursor in road pavement, water proofing, composite synthesis, and so forth. However, the asphalt materials are generally flammable, which would be decomposed at a relatively low temperature (ca. 300°C) [1]. During asphalt combustion (especially in the case of tunnel fire) [2], the generated heat and toxic fumes [3] will promote the spread of fire and seriously endanger any personnel within the affected areas. As such, studies on the flame retardancy of asphalt materials become highly desirable.

Due to the nontoxic and smoke suppression properties, metal hydroxides, such as magnesium hydroxide (MH) [4, 5] and aluminum hydroxide (ATH) [6], have been extensively utilized as halogen-free flame retardants. However, the usage of metal hydroxides will reduce the ductility of asphalt, which leads to the requirement of excessive metal hydroxides addition (at ca. 35 to 65 wt%) in order to pass the flame

retardancy tests [7] and hence renders the asphalt fragile and brittle [8].

Synergistic combinations are well-known allowing the reductions of flame retardant loading with fewer negative effects, where nanoclays have been reported to possess positive effects on the flame retardant properties of polymers [9] and show potential synergists with metal hydroxide flame retardants [10, 11]. A small amount (1–5 wt%) of nanoclays can significantly slow down the heat release rate of polymer combustion and improve the polymer mechanical properties, for example, tension, compression, bending, and fracture [12]. And the nanomodified asphalt may improve the rutting, crack, and fatigue resistance of asphalt mixtures [13, 14]. However, the flame retardant effect of montmorillonite on asphalts still has no consensus. Bonati et al. [15] proved that when ATH was coupled with organically modified montmorillonite (OMMT), a dramatic decrease of heat and smoke releases as generated by asphalt mixture combustion could be achieved, which was proposed due to the enhanced protective char layer that acts as an insulator and mass

transport barrier. Wu et al. [16] reported that a 5 wt% OMMT could improve the LOI of asphalt from 19.8% to 23.6% and reduce the heat release rate of the asphalt combustion. However, Bourbigot et al. [17] reported an inconsistent result that a 5 wt% OMMT did not enhance the fire behavior of asphalt, but the peak heat release rate was even increased by 18%. Furthermore, it has been well reported that the flame retardancy of nanocomposites are closely related to the degree of nanoclays dispersion in the matrix, where a good dispersion would always result in remark flame retardancy [18, 19]. However, Barral et al. [20] have indicated that comparing to a mixture of ATH and modified sepiolite, the mixture of ATH and unmodified sepiolite that was with poor affinity could result in a relatively good fire performance. Accordingly, a detailed and more comprehensive study on the effects of montmorillonite and/or metal hydroxide addition on the ignitability and thermal stability of asphalt is still highly demanded with an aim to untangle the aforementioned debates.

In this paper, the limiting oxygen index (LOI), cone calorimeter, and TG-DSC test have been conducted to investigate the combustion characteristics of the asphalt with unmodified and modified montmorillonite, where the synergistic effects of montmorillonite and aluminium trihydrate were discussed. We expect that the work conducted herein could provide a scientific basis and reference for the selection of high performance and cost effective flame retardant for asphalt combustion.

## 2. Experimental

**2.1. Materials.** 70# heavy traffic asphalt was obtained from BaoLi Asphalt Co., Ltd., in Jiangsu province, China. The flash point is 340°C and the ignition point is 375°C.

Three different flame retardants were used: (1) aluminum hydroxide (ATH), analytically pure with  $d_{50}$  of 13.5  $\mu\text{m}$ ; (2) unmodified montmorillonite K-10 (MMT) with specific surface area at 240  $\text{m}^2/\text{g}$ ; (3) DK2 series organically modified montmorillonite (OMMT), industrial grade. The OMMT was purchased from Fenghong New Material Co., Ltd. (Zhejiang, China), which was modified with methyl tallow bis(2-hydroxyethyl) ammonium. The addition of ammonium can change the surface properties of montmorillonite from hydrophilic to lipophilic and improve the affinity of the montmorillonite and asphalt.

Melt blending method was used to prepare the flame retardant asphalt, where approximately 500 mL asphalt was loaded into a stainless steel can and heated up to  $170 \pm 5^\circ\text{C}$  by an electric furnace. Then, the mineral fillers (ATH, MMT, and OMMT) were added gradually, which were mixed by using a BME100LT high shear machine. The rotation speed was set as 5000 rpm for 30 min to ensure the dispersion of mineral fillers, following by a lower speed of 500 rpm for 15 min with an aim to expel the air bubbles.

**2.2. Testing Methods.** X-ray diffraction (XRD) technique was used to determine the dispersion of montmorillonite (MMT and OMMT) in modified asphalts. The XRD patterns were obtained using a Rigaku D/Max 2550 diffractometer with

Cu  $K\alpha$  radiation ( $\lambda = 0.154 \text{ nm}$ ) at 40 kV and 100 mA. The diffractograms were scanned in the  $2\theta$  range from  $1^\circ$  to  $30^\circ$ .

Limiting oxygen index (LOI) is the minimal oxygen concentration that allows the sample to burn in a stable way. Samples with high LOI will need higher oxygen concentrations to ignite them. As such, an effective flame retardant would significantly increase the LOI of the asphalt. The LOI was determined according to an ASTM D 2863, which was performed by a HC-2 limiting oxygen index analyzer. Since the asphalt is subjected to melting and dripping while burning, glass fiber mat was used to support the asphalt during the test. Samples were prepared at 20/1 asphalt/glass fiber mat ratio by weight with dimensions of 120 mm  $\times$  3 mm  $\times$  3 mm. The test procedure was described in detail by Cong et al. [21].

Cone calorimeter was used to investigate the combustion characters of asphalt with mineral fillers, which is considered as a fitting laboratory test to describe the actual fire response of road pavement with asphalt [6]. During the test, samples were poured into a round cake with 70 mm diameter and 10 mm thickness, which were then exposed to a FTT 0007 cone calorimeter (FTT Company, UK) according to ISO-5660 standard procedures under a heat flux of 50  $\text{kW}/\text{m}^2$ . Different fire properties of the asphalts were evaluated, such as time to ignition (TTI), heat release rate (HRR), effective heat combustion (EHC), CO yield (COY), total heat release (THR), and total smoke release (TSR) (see Table 4).

Thermogravimetry analysis (TGA) was conducted to study the thermal properties of asphalts. The test was performed by a thermogravimetric analyzer (STA-409PC, NET-ZSCH, 6 Germany) under an air atmosphere with the gas flux of 20 mL/min. Approximately 10 mg of the sample was placed in an aluminum oxide crucible with a cross-section area of  $4.9 \times 10^{-4} \text{ m}^2$ . Samples were heated from 30°C to 850°C at a heating rate of 10°C/min.

## 3. Results and Discussion

**3.1. Dispersion of Clay Particles in Montmorillonite Modified Asphalts.** As reported, the flame retardancy of nanocomposites is closely related to the degree of nanoclays dispersion in the matrix, where the XRD techniques can be used to determine the dispersion of the layered clays in polymers [13]. When the asphalt chains are inserted into the gallery space between the silicate layers, the interlayer spacing of the clays ( $d(001)$ ) would be widened. So according to the Bragg equation the diffraction angle ( $2\theta$ ) of the  $d(001)$  peak of XRD pattern would shift to a lower angle. When the layered clays are fully exfoliated, the individual silicate layers are no longer close enough to interact with each other and the  $d(001)$  peak would disappear. Figure 1 shows the XRD patterns of the clays (MMT and OMMT) and the modified asphalts with 3 wt% OMMT or OMMT (called 3% MMT and 3% OMMT), respectively.

It is observed that the modified asphalt with 3 wt% MMT shows a larger diffraction peak width than the original MMT, indicating that the inhomogeneity of interlayer spacing of the modified asphalt was increased and part of asphalt had entered into the clay gallery. Since the MMT losses its crystal

TABLE 1: LOI value of asphalt with montmorillonites.

Samples	Asphalt	1% MMT	3% MMT	5% MMT	1% OMMT	3% OMMT	5% OMMT
LOI/%	19.8	20.1	20.4	20.6	19.9	20.2	20.3

TABLE 2: Fire properties of asphalt with montmorillonites obtained from cone calorimeter.

Samples	TTI/s	HRR/(kW·m <sup>-2</sup> )		EHC/(MJ·kg <sup>-1</sup> )	COY/(kg·kg <sup>-1</sup> )	THR/(MJ·m <sup>-2</sup> )	TSR/(m <sup>2</sup> ·m <sup>-2</sup> )
		Average	Peak/Time				
Base asphalt	23	289.6	581.2/195	29.41	0.0729	165.1	9515
3% MMT	43	245.1	500.7/155	31.26	0.0782	185.1	10503
3% OMMT	22	259.8	498.1/130	29.81	0.0744	188.3	10692

\* TTI: time to ignition, HRR: heat release rate, EHC: effective heat combustion, COY: CO yield, THR: total heat release, and TSR: total smoke release.

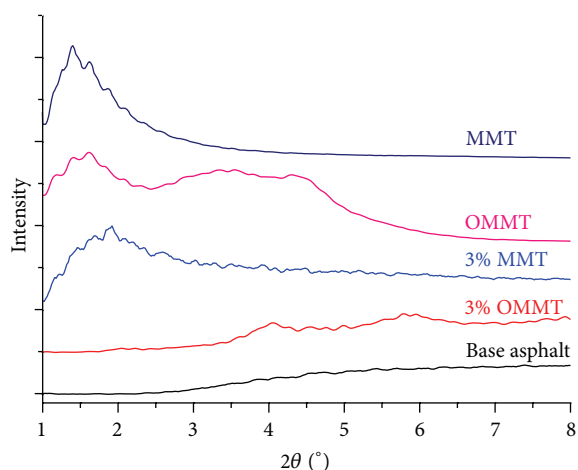


FIGURE 1: X-ray diffraction patterns of montmorillonites and asphalts.

water during the mixing process, the interlayer spacing of the MMT would be slightly reduced after mixing. Consequently, the modified asphalt with 3 wt% MMT would possess an immiscible/intercalated structure.

The OMMT powder shows a 5.45 nm *d*-spacing, while the modified asphalt with 3 wt% OMMT shows no significant diffraction peak. This indicates that the modified OMMT had resulted in an exfoliated structure in the asphalt. This structure was generally achieved due to the quaternary ammonium compound that works as an organic intermediate between the hydrophobic asphalt and hydrophilic montmorillonite. As such, most of OMMT layers would be peeled off during the mixing process, forming a more uniform dispersion structure.

### 3.2. Flame Retardancy of Montmorillonite Modified Asphalts.

The limiting oxygen index (LOI) technique can provide a quantitative measurement on the flammability of polymers. Generally, polymers with LOI < 21% belong to flammable materials, where those with 21% < LOI < 27% are conventionally classified as “slow burning” materials and LOI > 27% as “self-extinguishing” materials [22].

It can be seen that the base asphalt has the LOI to be equal to 19.8%. Since the oxygen volumetric content in atmosphere

is approximately 21%, materials characterized by LOI smaller than 21% can be ignited by an open fire and burn stably in air. From Table 1, we can observe that the limited oxygen index of asphalt was increased slightly with the contents of MMT or OMMT. The LOI of asphalts with MMT were larger than that with OMMT of the same content. However, the induced LOI rise of MMT and OMMT were not significant, leading to that the modified asphalt still belongs to the flammable materials. According to the GB/T 29051-2012, the limited oxygen index of tunnel asphalt pavement should be greater than 23%. Therefore, only adding montmorillonite cannot meet the LOI standard for the asphalt materials.

However, it should be noted that although the LOI test is effective as a screening tool for flame retardants, its test condition cannot fully represent a real fire scenario. In order to further determine the impact of montmorillonite on the combustion characteristics and fire hazard of asphalt under a high heat flux condition, cone calorimeter test was then used to analyze the combustion characteristics of the asphalt under an external thermal radiant flux of 50 kW/m<sup>2</sup>. The results are present in Table 2.

It can be seen that the time to ignition (TTI) was increased from 23 to 43 s upon the addition of a 3 wt% MMT. This is due to the fact that the dispersed clays in the asphalt can prevent the permeation of oxygen, so that the chain oxidation reaction of asphalt could be inhibited as well as the ignition could be retarded. In Barral et al.’s research [20], a significant delay of the ignition time was also observed when a 4 wt% unmodified sepiolite (another layered silicate) was added. However, after adding 3 wt% OMMT, the ignition time of asphalt was substantially constant. This is because of the fact that the organic modifier (alkyl quaternary ammonium) has a low thermal stability, which would increase the flammability of the asphalt.

Heat release rate is the critical factor in predicting the contribution of a burning material to the growth of a fire. From Figure 2, the heat release rate was increased rapidly after the base asphalt was ignited, which reached a maximum value (>500 kW·m<sup>-2</sup>) within 5 min. After adding 3 wt% MMT or OMMT, the heat release rates were decreased by 13.9% or 14.3%, respectively. The decomposition products of the montmorillonite migrate to the surface in high temperature range, leading to the reduction of small amounts of carbon

TABLE 3: LOI value of asphalt with ATH and montmorillonite.

Samples	5% ATH	10% ATH	17.5% ATH	25% ATH	3% MMT + 25% ATH	3% OMMT + 25% ATH
LOI/%	21.0	22.7	24.2	26.9	28.8	26.6

TABLE 4: Fire properties of asphalt with ATH and montmorillonite obtained from cone calorimeter.

Samples	TTI/s	HRR/(kW·m <sup>-2</sup> )		EHC/(MJ·kg <sup>-1</sup> )	COY/(kg·kg <sup>-1</sup> )	THR/(MJ·m <sup>-2</sup> )	TSR/(m <sup>2</sup> ·m <sup>-2</sup> )
		Average	Peak/Time				
25% ATH	34	180.6	450.0/135	27.05	0.0557	186.1	8984
25% ATH + 3% MMT	43	161.6	393.2/120	30.37	0.0631	207.6	9668
25% ATH + 3% OMMT	31	139.0	247.5/60	31.02	0.0647	175.2	8037

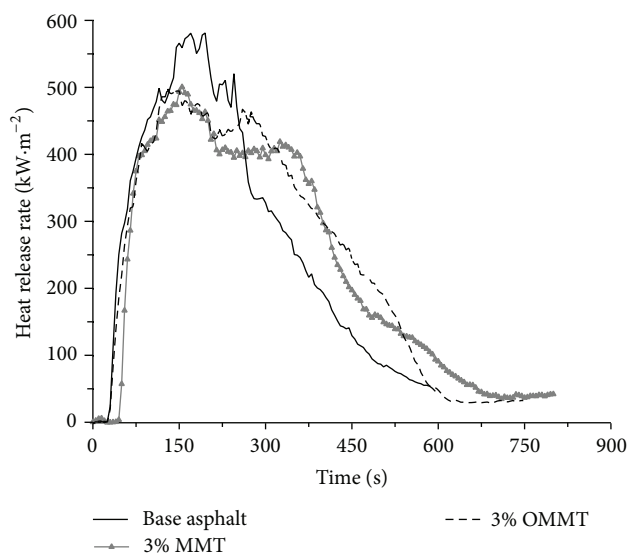


FIGURE 2: Heat release rate curves for asphalt with montmorillonites.

atoms [23], and the formation of a barrier layer is shown in Figure 3. The formed barrier layer would reduce the heat and mass transfer between the asphalt surface and external environment [7], resulting in the development of fire being limited. In addition as shown in Table 2, the addition of montmorillonite (MMT and OMMT) had no obvious effect on the effective heat combustion and CO yield for the asphalt combustion.

According to the aforementioned results, it can be concluded that addition of a small amount of montmorillonite (MMT and OMMT) cannot significantly increase the limiting oxygen index of the asphalt, but the ignition time in cone calorimeter test could be improved from 23 to 43 s after the 3 wt% MMT was added. Adding montmorillonite (MMT and OMMT) also showed a relatively obvious decline of the heat release rate. Clearly, the results of LOI test and cone calorimeter test were not well unified. The asphalt is a polymer whose melting temperature is lower than its pyrolysis temperature. At a low heat flux (e.g., LOI test), the heating rate is relatively low, which has led to the fact that the melting would precede the volatilization and ignition. Furthermore, since the asphalt can flow or drip, it would further remove the heat from the surface. However, adding

montmorillonite will increase the viscosity of the asphalt [14], thereby inhibiting the dripping of asphalt and promoting the combustion. This effect would offset the barrier effect of the montmorillonite partially, leading to the increase of LOI being limited. On the other hand, at a higher heat flux (e.g., cone calorimeter test), the temperature was increased rapidly and the ignition may occur before the surface is heated to a sufficient depth for the melted material to flow [24]. Accordingly, the montmorillonite might promote the formation of the barrier layer, so the thermal stability of the montmorillonite modified asphalt was improved.

**3.3. Flame Retardancy of Montmorillonite and Aluminium Trihydrate.** As shown in Section 2.2, the flame retardant effect of the montmorillonite (MMT and OMMT) mainly focuses on reducing the heat release rate of the asphalt combustion, where adding montmorillonite had shown no significant improvement on asphalt's flammability and CO yield. Since aluminum hydroxide had shown flame retardant and smoke suppressant properties, it was then used with montmorillonite to synergistically reduce the flammability and heat release of the asphalt.

Table 3 presents the LOI value of the asphalt with different contents of ATH and montmorillonite (MMT and OMMT). As the ATH content was increased from 0% to 25 wt%, the LOI was rapidly increased from 19.8% to 26.9%. It is noted that the change of ATH content has an obvious effect on the flammability of the asphalt. Synergistically adding 3 wt% OMMT with 25 wt% ATH, the LOI had declined to 26.6%, whilst adding 3 wt% MMT with 25 wt% ATH, the LOI had further increased to 28.8% (i.e., yielding a self-extinguishing material for asphalt). This increase was much higher than that added 3 wt% MMT in the base asphalt (from 19.8% to 20.4%).

Cone calorimeter test was used to analyze the combustion characteristics of the modified asphalt with ATH and montmorillonite under an external thermal radiant flux of 50 kW/m<sup>2</sup>. The ignition of 25% ATH occurred at 34 s, which was later than that of base asphalt (at 23 s). The ignition time was further increased to 43 s after adding 3 wt% MMT in 25% ATH but was decreased after adding 3 wt% OMMT. This was similar to that of adding montmorillonite in the base asphalt. It is well known that about 90% of fire deaths are the result of too much toxic smoke, where the carbon monoxide is always the primary one [25]. As such, the reduction of smoke and

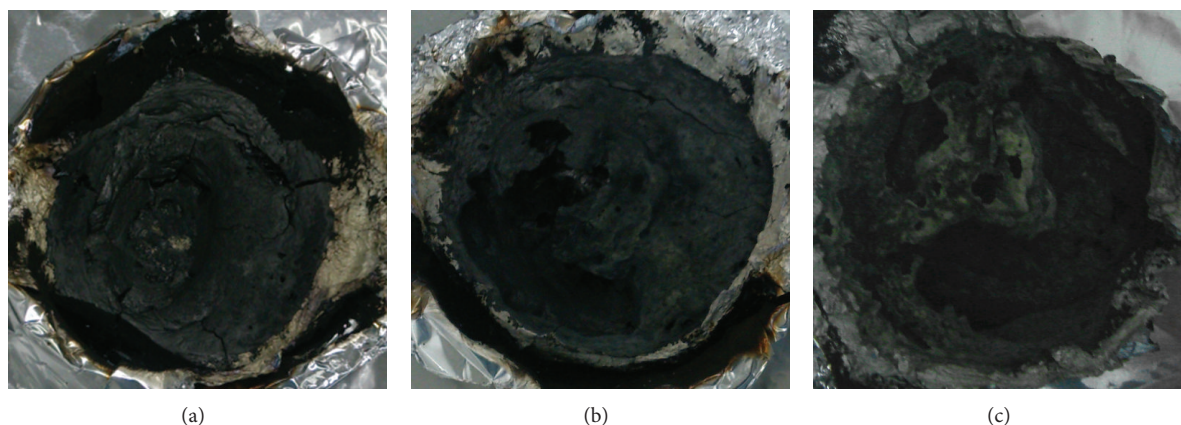


FIGURE 3: Cone residues of asphalt: (a) base asphalt; (b) 3% OMMT; (c) 3% MMT.

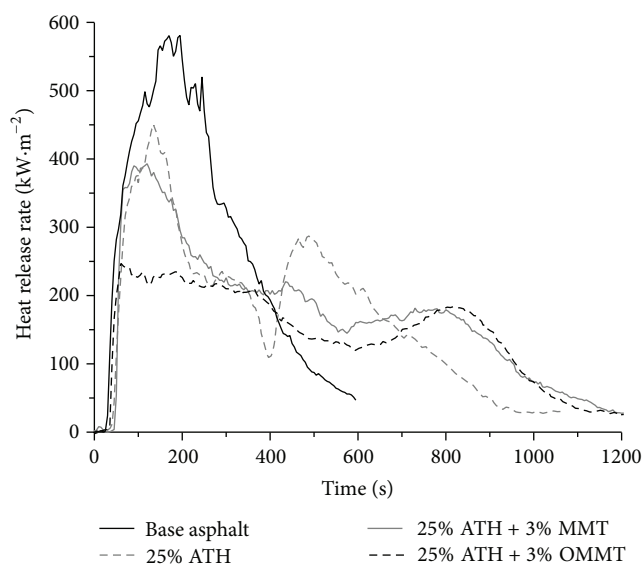


FIGURE 4: Heat release rate curves for asphalt with montmorillonite and ATH.

CO release during the asphalt combustion would be very beneficial for its practical application.

As shown in Figure 4, there were two main peaks in the heat release curve for adding 25 wt% ATH. The first peak was much lower than that of base asphalt. This was owed to the endothermic reaction of the ATH decomposition, which formed  $\text{Al}_2\text{O}_3$  barrier layer that decreased the heat and mass transfer between the flame and material. As the combustion proceeded, the barrier layer structure was destroyed, which led to an evolution of the flammable volatile and the combustion of unburned asphalt. The second heat release peak then appeared. The addition of 25 wt% ATH had yielded a 37.6% reduction of the average heat release rate compared to the base asphalt, which had significantly increased the burnout time.

The incorporation in asphalt of 25 wt% ATH + 3 wt% MMT and 25 wt% ATH + 3 wt% OMMT had decreased the

average heat release rates by 44.2% and 52.0% to base asphalt, respectively. Additional 3 wt% MMT and 3 wt% OMMT even yielded 10.5% and 26.7% reduction of average HRR compared to the 25% ATH. In particular, when the OMMT was added, the shape of the HRR curve shows a plateau-like behavior. This behavior was typical for the char- or residue-forming materials [24]. The peak heat release rate was observed to be decreased by 45.0% compared to 25% ATH. Obviously, the OMMT and ATH had both shown excellent synergistic flame retardant effect on reducing the heat release rate of the asphalt combustion. The formation of an inert barrier layer was probably the most important factor for flame retardant as it might keep the heat and oxygen out of the asphalt matrix. Furthermore, the additional incorporation of 3 wt% OMMT had resulted in the formation of a denser barrier layer with less crack (Figure 5(b)). This could be due to the good dispersion of the OMMT, which stripped to form a network structure in the asphalt matrix. Such network structure would increase the asphalt's viscosity, leading to a more "solid-like" behavior for the asphalt during the combustion, which hence resulted in the formation of barrier.

The silicate layer of the montmorillonite not only strengthens the char, making it more resistant to ablation, but also plays an active role in the formation of the char. The mass loss curves of Figure 6 show that the additions of montmorillonite (MMT and OMMT) had yielded an increase of the residue mass. The increase is about 1%-2%, which is mainly owing to the unreacted montmorillonite. When the montmorillonite was coordinated with the ATH, such increase would be more significant (8%-10%). The increase is much more than the ratio of montmorillonite (3%). This is mainly because the montmorillonite makes the barrier layer denser, part of asphalt could not burn completely, and the mass of residue increases.

In addition, it is noteworthy to mention that adding the ATH did not decrease the effective heat of the asphalt combustion, the total heat release, and the total smoke release significantly. This implied that the reaction between the ATH and asphalt was only a physical blending process, where the chemical interactions did not play a major role during the process.

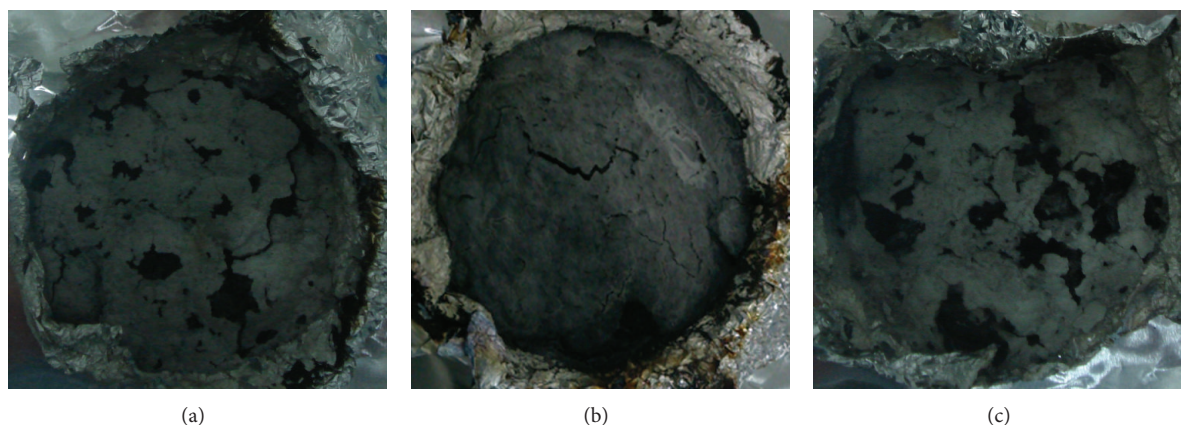


FIGURE 5: Cone residues of asphalt: (a) 25% ATH; (b) 25% ATH + 3% OMMT; (c) 25% ATH + 3% MMT.

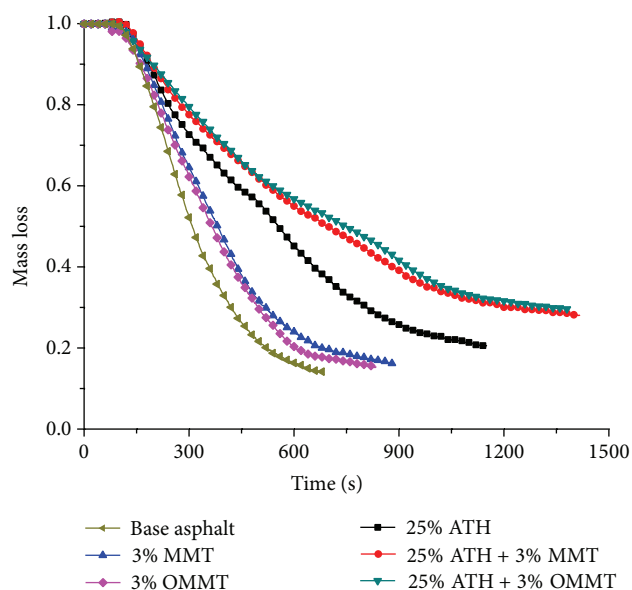


FIGURE 6: Mass loss curves for asphalt with montmorillonite and ATH.

**3.4. Thermal Analysis.** TGA experiments were performed to examine the decomposition behavior of the flame retardants. The mass loss (TG) curves are shown in Figure 7, which reflects the relationship between the mass loss and temperature. It was observed that there is an obvious mass loss rate peak in the DTG curve for both the MMT and OMMT addition at the temperature range of 70–100°C. This peak was known to correspond to the loss of crystal water. Since this temperature was much lower than the mixing temperature of the asphalt mixture, the process played no effect on the flame retardancy for the asphalt. As the temperature rose, the ATH began to decompose at about 300°C, whereas the ammonium in the OMMT was ignited. Since this temperature was lower than the ignition point of the base asphalt, the OMMT could not reduce the ignitability of the asphalt, which had led to the ignition time being shortened during the cone calorimeter tests.

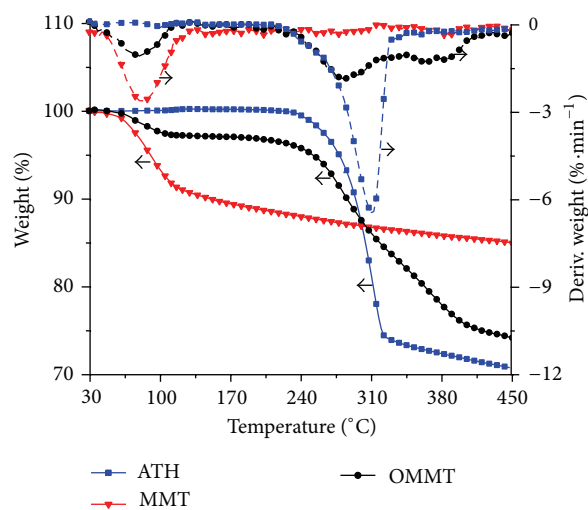


FIGURE 7: Thermal gravimetric analysis of fillers.

The TGA experiments were also performed to test the combustion behavior of the asphalts with different flame retardants (see Figure 8). DTG curves of the asphalts after or before adding montmorillonite (MMT and OMMT) both indicated that the combustion process could be mainly divided into two stages. The first peak was present in the initial combustion stage of the asphalt combustion, which was owing to the release of oil content and resin [26]. At this stage, the addition of 3 wt% MMT and 3 wt% OMMT could both result in the peak shifting to lower temperature range. This implied that the montmorillonite could not significantly reduce the ignition of asphalt. However, the mass loss at this stage was reduced from 66.5% to 61.3% or 62.4% for 3% MMT or 3% OMMT, respectively. This is because of the fact that the montmorillonite had increased the viscosity of asphalt [13] and suppresses the release of flammable volatiles. This may lead to a longer reaction time, where more active ingredients cannot diffuse out at the lower temperature but convert themselves into more stable products, for example, asphaltenes. As such, the mass loss of 3% MMT and 3%

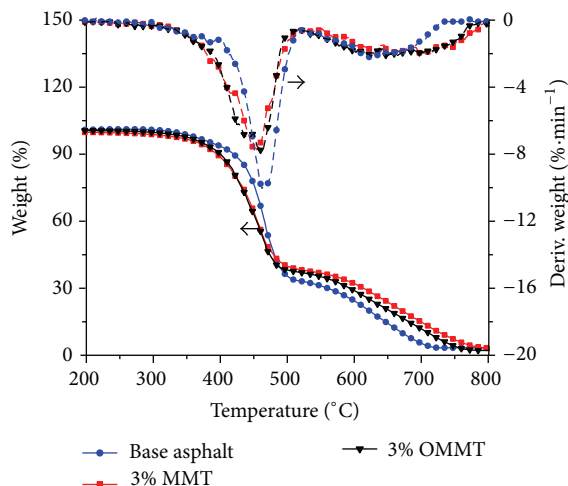


FIGURE 8: Thermal gravimetric analysis of asphalt with nanoclays.

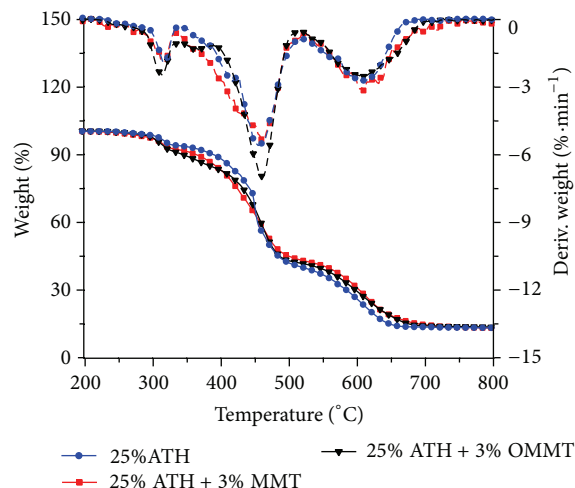


FIGURE 9: Thermal gravimetric analysis of asphalt with nanoclay and ATH.

OMMT became less than that of base asphalt at stage one. The second peak corresponded to the stage of asphaltene combustion [26]. After montmorillonite was added, the temperature range of this stage was postponed, where the burnout temperature was raised by more than 50°C, leading to the reduction on heat release and fire expansion.

Compared to montmorillonite addition alone, the DTG curve of asphalt combustion had three main peaks after adding ATH. As shown in Figure 9, the first peak occurred at about 300°C, which corresponded to the decomposition of ATH and the combustion of ammonium in OMMT. There were significant amounts of heats being absorbed from the asphalt due to the ATH decomposition, which would cause a falling of the temperature in the combustion zone, leading to the retarding on the reaction. The second peak corresponded to the first stage of asphalt combustion. The mass loss and maximum mass loss rate were reduced compared to the base asphalt, which was owing to the barrier effect of the residue of ATH decomposition. When ATH was combined with montmorillonite (MMT or OMMT), the mass loss at the stage two would be further reduced from 53.7% to 49.4% or 48.4%, respectively. This led to the increase in the formation of asphaltene and the prolongation of asphaltene combustion, which was similar to that of adding montmorillonite alone during asphalt combustion.

#### 4. Conclusions

- (1) Adding a small amount of montmorillonite (MMT and OMMT) cannot significantly increase the oxygen index of asphalt. However, it could promote the formation of barrier layer during asphalt combustion and suppress the release of flammable volatiles. Consequently, the heat release rate would be reduced and the burnout time of asphalt would be postponed.
- (2) The addition of montmorillonite (MMT and OMMT) and aluminum hydroxide had shown a synergistic

effect on flame retardancy. The addition of montmorillonite and aluminum hydroxide further reduced the heat release rate. After further addition of OMMT, the heat release rate was significantly decreased. This could be attributed to the formation of barrier layer, which acted as a mass and heat barrier to protect the underlying material from further burning.

- (3) Adding a small amount of unmodified montmorillonite could increase the ignition time of asphalt, while adding OMMT asphalt cannot. This was owing to the flammability of the ammonium in the modified montmorillonite.

To sum, it can be concluded that the OMMT can reduce the heat release rate of the asphalt and has a remark synergistic effect on the flame retardancy when it is used together with aluminum hydroxide, showing a promising flame retardant for asphalt combustion. However, since the traditional alkyl ammonium modifier is generally flammable, it is necessary to synthesis an organic modifier with fire-retardant properties in the future.

#### Conflict of Interests

The authors declare that there is no conflict of interests regarding the publication of this paper.

#### Acknowledgments

This work is supported by the Zhejiang Provincial Natural Science Foundation of China (no. LY14E080014) and the National Natural Science Foundation of China (no. 5140080784). The authors would like to thank Dr. Xiaole Weng at College of Environmental & Resource Sciences of Zhejiang University for his help in this paper.

## References

- [1] T. Xu, X. Huang, and Y. Zhao, "Investigation into the properties of asphalt mixtures containing magnesium hydroxide flame retardant," *Fire Safety Journal*, vol. 46, no. 6, pp. 330–334, 2011.
- [2] R. Carvel and J. Torero, "The contribution of asphalt road surfaces to fire risk in tunnel fire, in the contribution of asphalt road surfaces to fire risk in tunnel fires: preliminary findings," in *Proceedings of the International Conference on Risk and Fire Engineering for Tunnels, Stations and Linked Underground Spaces*, pp. 19–20, Hong Kong, 2006.
- [3] K. Wu, K. Zhu, Z. Huang, J. Wang, Q. Yang, and P. Liang, "Research on the combustion mechanism of asphalt and the composition of harmful gas based on infrared spectral analysis," *Spectroscopy and Spectral Analysis*, vol. 32, no. 8, pp. 2089–2094, 2012.
- [4] T. Xu and X. Huang, "A TG-FTIR investigation into smoke suppression mechanism of magnesium hydroxide in asphalt combustion process," *Journal of Analytical and Applied Pyrolysis*, vol. 87, no. 2, pp. 217–223, 2010.
- [5] T. Xu and X. Huang, "Combustion properties and multistage kinetics models of asphalt binder filled with flame retardant," *Combustion Science and Technology*, vol. 183, no. 10, pp. 1027–1038, 2011.
- [6] A. Bonati, F. Merusi, G. Polacco, S. Filippi, and F. Giuliani, "Ignitability and thermal stability of asphalt binders and mastics for flexible pavements in highway tunnels," *Construction and Building Materials*, vol. 37, pp. 660–668, 2012.
- [7] A. B. Morgan, "Flame retarded polymer layered silicate nanocomposites: a review of commercial and open literature systems," *Polymers for Advanced Technologies*, vol. 17, no. 4, pp. 206–217, 2006.
- [8] R. M. Recasens, A. Martínez, F. P. Jiménez, and H. Bianchetto, "Effect of filler on the aging potential of asphalt mixtures," *Transportation Research Record*, vol. 1901, no. 1, pp. 10–17, 2005.
- [9] T. Kashiwagi, F. Du, J. F. Douglas, K. I. Winey, R. H. Harris Jr., and J. R. Shields, "Nanoparticle networks reduce the flammability of polymer nanocomposites," *Nature Materials*, vol. 4, no. 12, pp. 928–933, 2005.
- [10] S. Bourbigot and S. Duquesne, "Fire retardant polymers: recent developments and opportunities," *Journal of Materials Chemistry*, vol. 17, no. 22, pp. 2283–2300, 2007.
- [11] G. Beyer, "Flame retardancy of nanocomposites based on organoclays and carbon nanotubes with aluminum trihydrate," *Polymers for Advanced Technologies*, vol. 17, no. 4, pp. 218–225, 2006.
- [12] M. Alexandre and P. Dubois, "Polymer-layered silicate nanocomposites: preparation, properties and uses of a new class of materials," *Materials Science and Engineering R: Reports*, vol. 28, no. 1, pp. 1–63, 2000.
- [13] Z. You, J. Mills-Beale, J. M. Foley et al., "Nanoclay-modified asphalt materials: preparation and characterization," *Construction and Building Materials*, vol. 25, no. 2, pp. 1072–1078, 2011.
- [14] J. Yu, X. Zeng, S. Wu, L. Wang, and G. Liu, "Preparation and properties of montmorillonite modified asphalts," *Materials Science and Engineering A*, vol. 447, no. 1-2, pp. 233–238, 2007.
- [15] A. Bonati, F. Merusi, G. Bochicchio et al., "Effect of nanoclay and conventional flame retardants on asphalt mixtures fire reaction," *Construction and Building Materials*, vol. 47, pp. 990–1000, 2013.
- [16] S. Wu, Y. Zhang, and J. Wang, "A novel potential flame-retarded bitumen nanoclay modified bitumen," *Road Materials and Pavement Design*, vol. 10, supplement 1, pp. 115–128, 2009.
- [17] S. Bourbigot, O. Cerin, S. Duquesne, and N. Clavel, "Flame retardancy of bitumen: a calorimetry study," *Journal of Fire Sciences*, vol. 31, no. 2, pp. 112–130, 2013.
- [18] J. W. Gilman, T. Kashiwagi, A. B. Morgan et al., *Flammability of Polymer Clay Nanocomposites Consortium: Year One Annual Report*, US Department of Commerce, Technology Administration, National Institute of Standards and Technology, 2000.
- [19] M.-A. Paul, M. Alexandre, P. Degée, C. Henrist, A. Rulmont, and P. Dubois, "New nanocomposite materials based on plasticized poly (L-lactide) and organo-modified montmorillonites: thermal and morphological study," *Polymer*, vol. 44, no. 2, pp. 443–450, 2003.
- [20] M. Barral, P. Garmendia, M. E. Muñoz et al., "Novel bituminous mastics for pavements with improved fire performance," *Construction and Building Materials*, vol. 30, pp. 650–656, 2012.
- [21] P. Cong, S. Chen, J. Yu, and S. Wu, "Effects of aging on the properties of modified asphalt binder with flame retardants," *Construction and Building Materials*, vol. 24, no. 12, pp. 2554–2558, 2010.
- [22] M. Burns, U. Wagenknecht, B. Kretzschmar, and W. W. Focke, "Effect of hydrated fillers and red phosphorus on the limiting oxygen index of poly(ethylene-co-vinyl acetate)-poly(vinyl butyral) and low density polyethylene-poly(ethylene-co-vinyl alcohol) blends," *Journal of Vinyl and Additive Technology*, vol. 14, no. 3, pp. 113–119, 2008.
- [23] H. Ma, P. Song, and Z. Fang, "Flame retarded polymer nanocomposites: development, trend and future perspective," *Science China Chemistry*, vol. 54, no. 2, pp. 302–313, 2011.
- [24] A. B. Morgan and C. A. Wilkie, *Flame Retardant Polymer Nanocomposites*, Wiley-Interscience, 2007.
- [25] K. M. Butler and G. W. Mulholland, "Generation and transport of smoke components," *Fire Technology*, vol. 40, no. 2, pp. 149–176, 2004.
- [26] W. Ke, K. Zhu, J. Han, J. Wang, Z. Huang, and P. Liang, "Non-isothermal kinetics of styrene—butadiene—styrene asphalt combustion," *Chinese Physics B*, vol. 22, no. 6, Article ID 068801, 2013.

## Research Article

# A Study on the Morphology of a Dispersed Particle Gel Used as a Profile Control Agent for Improved Oil Recovery

Qing You,<sup>1,2,3</sup> Yongchun Tang,<sup>4</sup> Caili Dai,<sup>5</sup> Mingwei Zhao,<sup>5</sup> and Fulin Zhao<sup>5</sup>

<sup>1</sup> School of Energy Resources, China University of Geosciences, Beijing 100083, China

<sup>2</sup> Key Laboratory of Marine Reservoir Evolution and Hydrocarbon Accumulation Mechanism, Ministry of Education, China University of Geosciences, Beijing 100083, China

<sup>3</sup> Key Laboratory of Shale Gas Exploration and Evaluation, Ministry of Land and Resources, China University of Geosciences, Beijing 100083, China

<sup>4</sup> Power, Environmental and Energy Research Institute, Los Angeles, CA 91722, USA

<sup>5</sup> School of Petroleum Engineering, China University of Petroleum, Qingdao, Shandong 266580, China

Correspondence should be addressed to Qing You; [youqing@cugb.edu.cn](mailto:youqing@cugb.edu.cn)

Received 15 April 2014; Accepted 27 June 2014; Published 20 July 2014

Academic Editor: Yu Xin Zhang

Copyright © 2014 Qing You et al. This is an open access article distributed under the Creative Commons Attribution License, which permits unrestricted use, distribution, and reproduction in any medium, provided the original work is properly cited.

To achieve in-depth profile control of injection water and improve oil recovery, a new profile control agent, termed as dispersed particle gel (DPG), has been developed and reported. In this paper, the morphology of DPG and the factors that influence its morphology are systematically investigated using atomic force microscopy (AFM). The AFM studies show that DPG is composed of small pseudospherical particles and that their sizes can be controlled by adjusting the shearing rate, the initial polymer mass concentration, and the salinity. Dynamic light scattering (DLS) is used to study the effects of the initial polymer mass concentration, the shearing rate, the salinity, and the high-temperature aging on the particle size of DPG. The aggregation ability of DPG is explained using the DLVO theory and space stability theory. This work provides a scientific basis and technical support for the formula design of DPG and its application in the oil and gas field.

## 1. Introduction

Oil and gas, as efficient sources of energy, play an important role in the world's economy. With the rapid growth of the world economy, the demand for oil and gas is on the rise. Exploration has become more difficult in recent years, which makes it necessary to improve oil and gas recovery. Moreover, the long-term flooding of oilfields has resulted in the fast injection of water into the oil wells along the high-permeability zones and a dramatic reduction in oil production. Reducing the water production rate is a key to stabilizing and increasing oil production.

Until now, the most effective method of reducing the water production rate is to use profile control agents to block high-permeability zones. The widely adopted profile control agents include bulk gels, colloidal dispersion gels, and polymer gel microspheres, such as bright water, microgels, preformed particle gels, and soft gels. However, these different

gels all have limited application in practice. The bulk gel is easily affected by shearing from ground equipment and porous media, by chromatographic separation effect, by dilution from the formation water, and by touch physical and chemical conditions (temperature, pressure, and salinity) in formation; thus, it is hard to control the gelation time, gel strength, and the entering-formation depth of the gel when using bulk gel in a field test [1]. The colloidal dispersion gel [2], polymer gel microsphere [3, 4], microgel [5–7], preformed particle gel, and soft gel [8–10] are all expensive, which inhibits the large-scale application. Therefore, a new in-depth profile control agent that can achieve deep plugging with good stability, control the injection of water, and improve oil recovery needs to be developed.

Because of the problems with the existing profile control agents, it is necessary to develop a new profile control agent. A dispersed particle gel (DPG) that was prepared using the shearing cross-linking method in pipe flow with a polymer

and a cross-linker was designed as a new in-depth profile control agent and has been previously reported [11]. The strength and particle size of DPG are controllable with a particle size distribution from nanometers to millimeters. DPG is not sensitive to reservoir conditions, is environmentally friendly, and is low cost. According to the lab core test results, DPG can block large formation channels and modify the flow profile to achieve a deep profile control effect that diverts water to middle-to-low permeability zones, thus improving the sweep efficiency as well as the oil recovery ratio [12].

DPG is an excellent profile control agent with much potential to solve the problem of a high water cut; therefore, the systematic study of its characteristics has significant practical value. The morphology of DPG, including the shape and particle size, should be studied first because it is the fundamental property of the material. The morphology of DPG and the factors that influence the morphology are studied in this paper to provide a scientific basis and technical support for its IOR mechanism and its application in the field.

## 2. Materials and Methods

### 2.1. Materials

**Polymer.** The hydrophobically associating polymer is from ChemEOR Inc. Its relative molecular weight is  $8.0 \times 10^6$ , its degree of hydrolysis is 26.65%, its solid content is 94%, and its water-insoluble material is 0.24%.

**Cross-Linker.** Chromium acetate is also from ChemEOR Inc.

**DPG Samples.** The DPG samples are prepared as previously described [11]. Briefly, first prepare the gels that are composed of polymer and cross-linker. Then, use a peristaltic pump as the shearing cross-linking equipment to prepare DPG using a certain shearing rate for 2 to 3 hours at room temperature. Adjust the shearing parameters (shearing rate and tube diameter size) and the polymer concentration to obtain a series of DPG products of various sizes. The formation process and formation mechanism in peristaltic pump are shown in Figures 1 and 2.

### 2.2. Methods

**2.2.1. Morphology of DPG.** First, dilute the DPG sample to  $1000 \text{ mg}\cdot\text{L}^{-1}$  and pipette 2.0 mL of the DPG sample onto a freshly stripped mica chip ( $2 \text{ cm} \times 2 \text{ cm}$ ). Wait for 2 minutes to allow DPG to adhere to the mica chip; then flush the DPG sample one or two times with ultrapure water and dry it immediately with nitrogen. Observe the morphology of the DPG sample at room temperature ( $25.0 \pm 0.1^\circ\text{C}$ ) using a Veeco Nanoscope IIIa multifunctional atomic force microscopy (AFM) instrument in tapping mode.

**2.2.2. Particle Size of DPG.** First, place the sample needle at the bottom of the sample pool. Then, place 1.0 mL of the DPG sample into the sample pool while slowly lifting the sample needle to avoid the formation of bubbles. Next, use a dynamic

light scattering (DLS) device (Malvern Zetasizer Nano S) to determine the particle size of DPG. Test temperature is  $25^\circ\text{C}$ , scattering angle is  $173^\circ$ , and incident light wave length is 633 nm.

## 3. Experimental Results

### 3.1. Morphology of DPG and the Influencing Factors

**3.1.1. The Effect of the Polymer Mass Concentration on the Morphology of DPG.** Because the DPG solution is a homogeneous phase and is transparent, it is difficult to observe its morphology using an optical microscope. In this work, AFM is used to observe the morphology of DPG.

Figure 4 shows the morphologies of the DPG samples that were formed using polymer and cross-linking agent. As observed in Figure 3, the shape of DPG in aqueous solution is spherical, and the particles are small; the average particle size of DPG increases slightly with the initial polymer mass concentration [13].

Figure 3(a) shows that the long axis of the DPG sample is approximately  $0.5 \mu\text{m}$  and the short axis of the DPG sample is approximately  $0.4 \mu\text{m}$ , with the axial ratio close to 1. During the process of shearing and cross-linking in pipe flow, the gelation system flows in a certain direction, and there is shear action perpendicular to the direction of flow. If the gel deformation cannot withstand the shearing action during the process, the gel will be broken into small pieces. The cross-linking ability in the direction of flow is greater than that in the vertical direction. As the shearing rate increases, the cross-linking ability in the direction of flow becomes weak, which makes the cross-linking abilities in the two directions (parallel to the flow and vertical to the flow) becoming more balanced; thus, the DPG particles obtain a globular shape. Figure 3(b) shows that the long axis of the DPG sample is approximately  $0.9 \mu\text{m}$  and the short axis is approximately  $0.7 \mu\text{m}$ , with the axial ratio close to 1. The particle size has increased compared to Figure 3(a). The size of the polymer molecules and their cross-linking ability increase with the polymer concentration. Therefore, given the same shear force conditions, the particle size of DPG is larger at higher polymer concentration.

To verify the AFM results, the particle size of DPG is also measured. The sedimentation method, static light scattering method, screening method, image method, resistance method, scraper method, settlement bottles method, ventilation method, ultrasonic method, and DLS method are all widely used to determine particle size. Because the DPG solution is an isotropic aqueous solution, its scattered light signal, when determined using a laser particle size analyzer, is too weak to generate an accurate measurement of the particle size. The DLS method has the advantages of rapid measurement process, high detection sensitivity, real-time monitoring of samples, easy sample preparation with no special treatment, and the absence of interference with the nature of the sample during the measurement process. Therefore, the DLS method is preferred in determining the hydrodynamic diameter of DPG and its distribution.



FIGURE 1: The formation process of DPG in peristaltic pump.

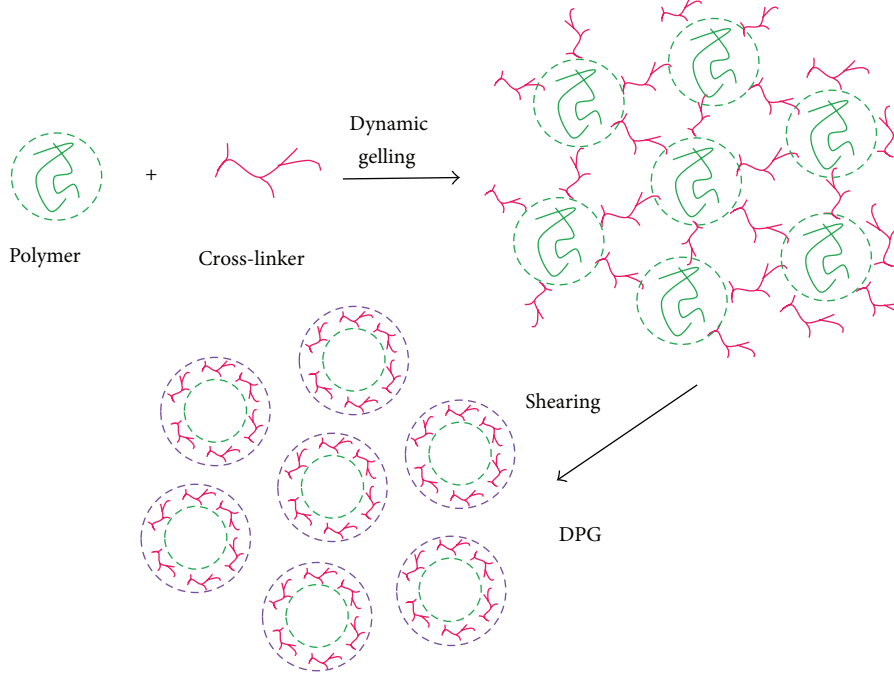


FIGURE 2: The proposed formation mechanism of DPG.

The particle size distribution curves of the two DPG samples with different initial polymer mass concentrations (shown in Figure 3) are determined using DLS and shown in Figure 4.

There are still two peaks in the particle size distribution curves. Weighted average particle sizes of over 200 nm are obtained using the volume percentages and formula (1), which describes the relationship between the hydrodynamic diameter of a DPG sample and the initial polymer mass concentration, the values of which are given in Table 1. Consider

$$d = \frac{\sum (d_i \cdot i)}{\sum i}, \quad (1)$$

where  $d$  is the weighted average particle size in nm,  $i$  is the distribution intensity with the  $d_i$  particle size as the upper limit, and  $d_i$  is the particle size in nm.

As observed in Table 1, the average particle size of DPG increases with the initial polymer mass concentration. A high polymer mass concentration results in a faster rate of cross-linking during the shearing and cross-linking reactions. The amount of cross-linking increases and makes the particle more difficult to cut into pieces and therefore larger.

According to the rupture criteria of DPG [14], under the same shearing rate conditions, the torque generated by the gyration radius  $R_a$  of DPG in a polymer solution with

TABLE 1: Relationship between the particle size of DPG and the initial polymer mass concentration.

Items	Sample	
	1	2
Initial polymer mass concentration/(mg·L <sup>-1</sup> )	3000	4000
Particle size of DPG/nm	1100	1850

a viscosity of  $\eta_p$  is equal to the torque generated by the gyration radius  $R_p$  of DPG in a polymer solution with a viscosity of  $\eta_a$ , as described in (2) and (3). Consider

$$\eta_p \gamma R_a^3 = \eta_a \gamma R_p^3, \quad (2)$$

$$\frac{\eta_a}{\eta_p} = \left( \frac{R_a}{R_p} \right)^3. \quad (3)$$

According to (2) and (3), a higher initial viscosity results in a larger particle size of DPG. There is a certain ratio between the initial viscosity and the initial polymer mass concentration, and the experimental results are consistent with the theoretical analysis.

**3.1.2. Effect of Shearing Rate on the Morphology of DPG.** The morphology of DPG formed from 3000 mg·L<sup>-1</sup> polymer and

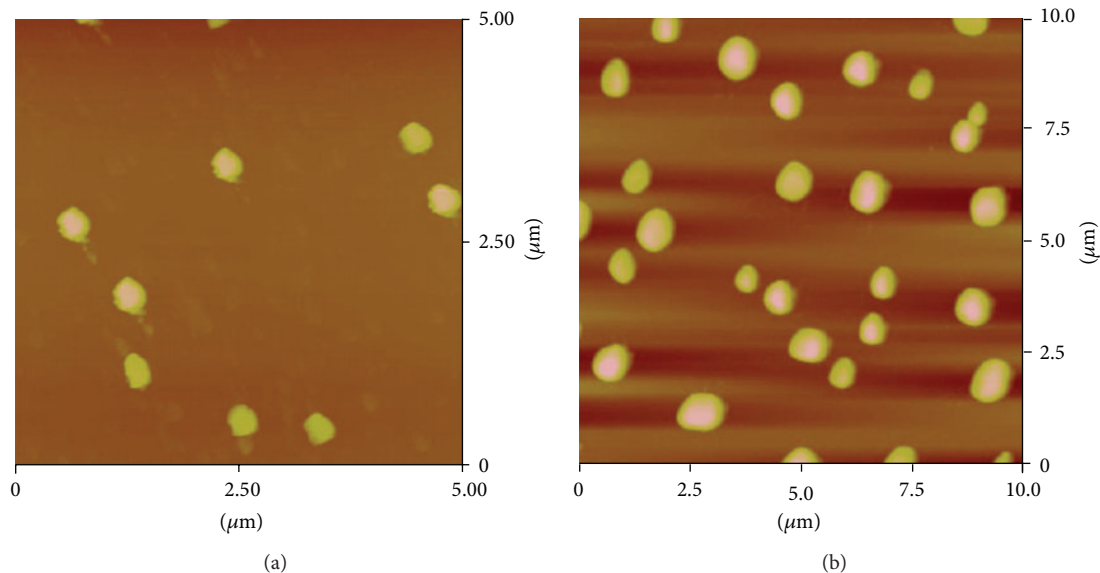


FIGURE 3: AFM image of DPG prepared using different initial polymer mass concentrations. (The scanned area in Figures 3(a) or 3(b) is  $5 \times 5 \mu\text{m}$ .) (a)  $3000 \text{ mg-L}^{-1}$  polymer +  $500 \text{ mg-L}^{-1}$   $\text{Cr}(\text{Ac})_3$ ; (b)  $4000 \text{ mg-L}^{-1}$  polymer +  $500 \text{ mg-L}^{-1}$   $\text{Cr}(\text{Ac})_3$ .

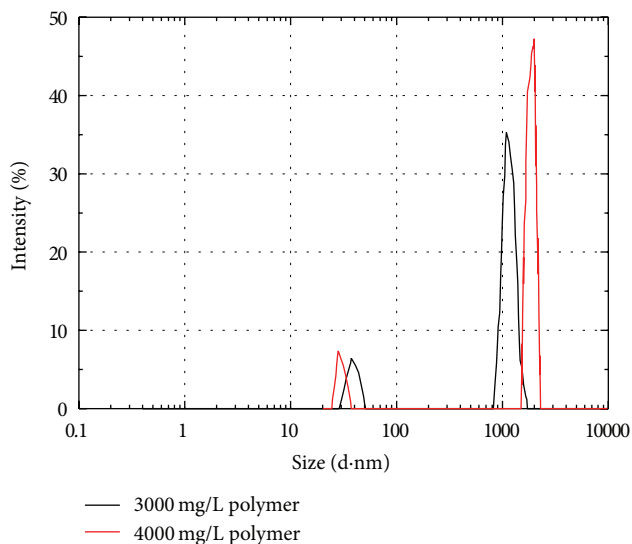


FIGURE 4: Particle size distribution curves of DPG with two different initial polymer mass concentrations.

$500 \text{ mg-L}^{-1}$   $\text{Cr}(\text{Ac})_3$  was studied at average shearing rates of  $194 \text{ s}^{-1}$  and  $168 \text{ s}^{-1}$  at  $30^\circ\text{C}$ . The results are shown in Figure 5.

As observed in Figure 5, the size of DPG increases when the shearing rate decreases from  $194 \text{ s}^{-1}$  to  $168 \text{ s}^{-1}$ , and the morphology becomes less spherical. As the shearing rate increases, the cross-linking ability in the flow direction decreases, which results in a reduction difference of cross-linking ability between the direction of flow and the vertical direction. The cross-linking abilities tend toward balance, which makes the shape of the DPG particles closer to spherical.

Figure 5(b) shows that the distribution of the particle sizes is heterogeneous. Compared with Figure 5(a), the shearing

rate in Figure 5(b) is smaller, and the cross-linking ability in the direction of flow is greater than that in the vertical direction. Thus, the particle size of the prepared DPG particles is heterogeneous. A trend towards aggregation in the DPG system also emerges, which is mainly caused by a mutual effect among the DPG particles.

The aggregation phenomenon indicates that the stability of DPG is poor and that DPG is generally characterized by its aggregation stability. According to the DLVO theory, the aggregation stability of DPG in certain conditions is determined by its gravitation and repulsion. When the repulsion surpasses the gravitation, the system is stable and vice versa. The gravitation between particles is essentially the van der Waals force. With two spherical particles of the same size, the gravitational potential energy is given by

$$E_A = -\frac{Aa}{12H}, \quad (4)$$

where  $E_A$  is the gravitational potential energy,  $A$  is the Hamaker constant,  $a$  is the radius of each particle, and  $H$  is the shortest distance between the two particles.

In (4), the minus sign means that gravitational potential energy has a positive correlation with the particle size.

The repulsion between the colloidal particles is an electrostatic repulsion generated by the diffuse electric double layers around the particles. With two spherical particles of the same size, the repulsive potential energy  $E_R$  is generally given by

$$E_R = \frac{64\pi a n_0 k T \gamma_0^2}{K^2} \exp(-KH), \quad (5)$$

where  $E_R$  is the repulsive potential energy,  $a$  is the radius of each particle,  $H$  is the shortest distance between the two particles,  $K$  is the reciprocal of the thickness of the diffuse electric double layers,  $n_0$  is the total ion concentration of the system,  $k$  is the Boltzmann constant,  $T$  is the absolute

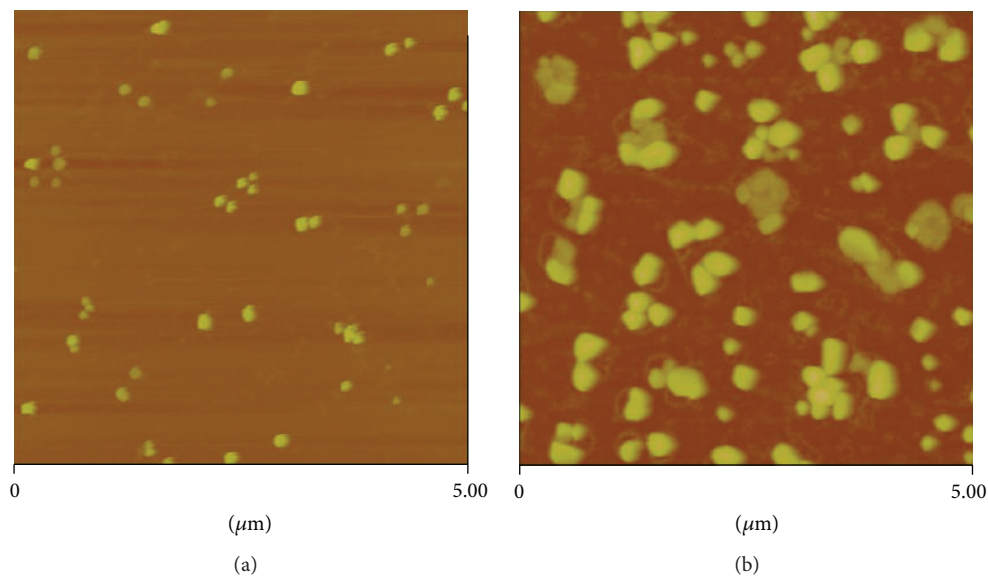


FIGURE 5: AFM images of DPG at different shearing rates. (The scanned area in Figure 6 is  $5 \times 5 \mu\text{m}$ ).

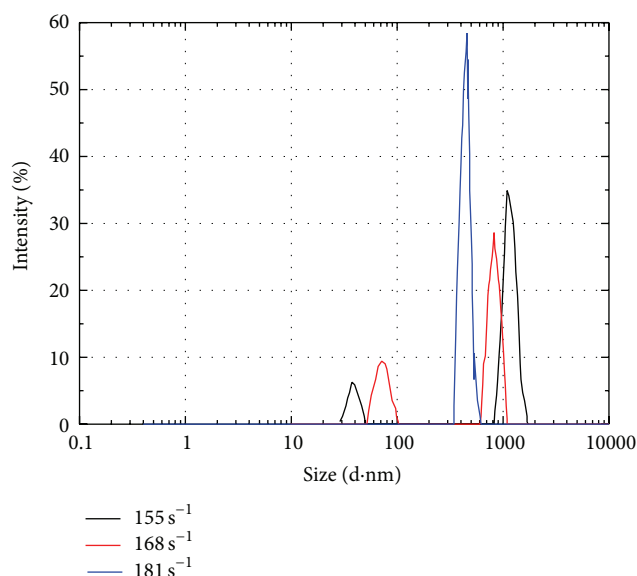


FIGURE 6: Particle size distribution curve of DPG at different shearing rates.

temperature, and  $\gamma_0$  is a complicated function of surface potential given by

$$\gamma_0 = \frac{\exp(Ze\psi_0/2kT) - 1}{\exp(Ze\psi_0/2kT) + 1}, \quad (6)$$

where  $Z$  is the valence number of the particles in the diffuse layers,  $e$  is the charge number of the particles in the diffuse layers, and  $\psi_0$  is the surface potential of the particles.

Formula (5) shows that the repulsion has a positive correlation with the particle size, the thickness of the diffuse electric double layers, and the surface potential. As the shearing rate decreases, the particle size of DPG increases.

Cross-linking density is defined as the ratio of the number of cross-linked construction units to all of the construction units. If the particle size of DPG increases and the cross-linking density stays constant, then the repulsive and gravitational potential energies increase simultaneously, and the surface potential of the particles also increases. Formula (6) shows that the complicated function  $\gamma^0$  of the surface potential changes within a small range; thus, the increase in the rate of the repulsive potential is smaller than that of the gravitational potential, which results in an enhanced attraction between the particles in the DPG system. As the shearing rate decreases, the gelation system is rarely influenced by the shearing action; thus, cross-linking opportunities and the cross-linking density increase; both the charge density of the DPG particles (the system has a negative charge) and surface potential decrease. All of the above factors lead to the decrease in the repulsive potential and the increase in attraction among the particles [15]. Thus, there is a trend toward aggregation among the DPG particles.

The particle size distribution curve of the DPG samples prepared at different shearing rates was obtained using DLS and is shown in Figure 6. The relationship between the hydrodynamic diameter of each DPG sample and its shearing rate is shown in Table 2. The average particle size of DPG decreases with an increase in shearing rate. At a greater shearing rate, the gelation system suffers more axial shearing stress, making the gelation system more easily broken, which leads to the decrease in the particle size of DPG.

The relationship between the hydrodynamic diameter of each DPG sample and its initial shearing rate is shown in Table 2.

### 3.1.3. The Effect of Salinity on the Morphology of DPG.

The morphology of DPG was studied at various NaCl and  $\text{CaCl}_2$  concentrations in the same gelation system ( $3000 \text{ mg}\cdot\text{L}^{-1}$  polymer and  $500 \text{ mg}\cdot\text{L}^{-1}$   $\text{Cr}(\text{Ac})_3$ ) at  $30^\circ\text{C}$

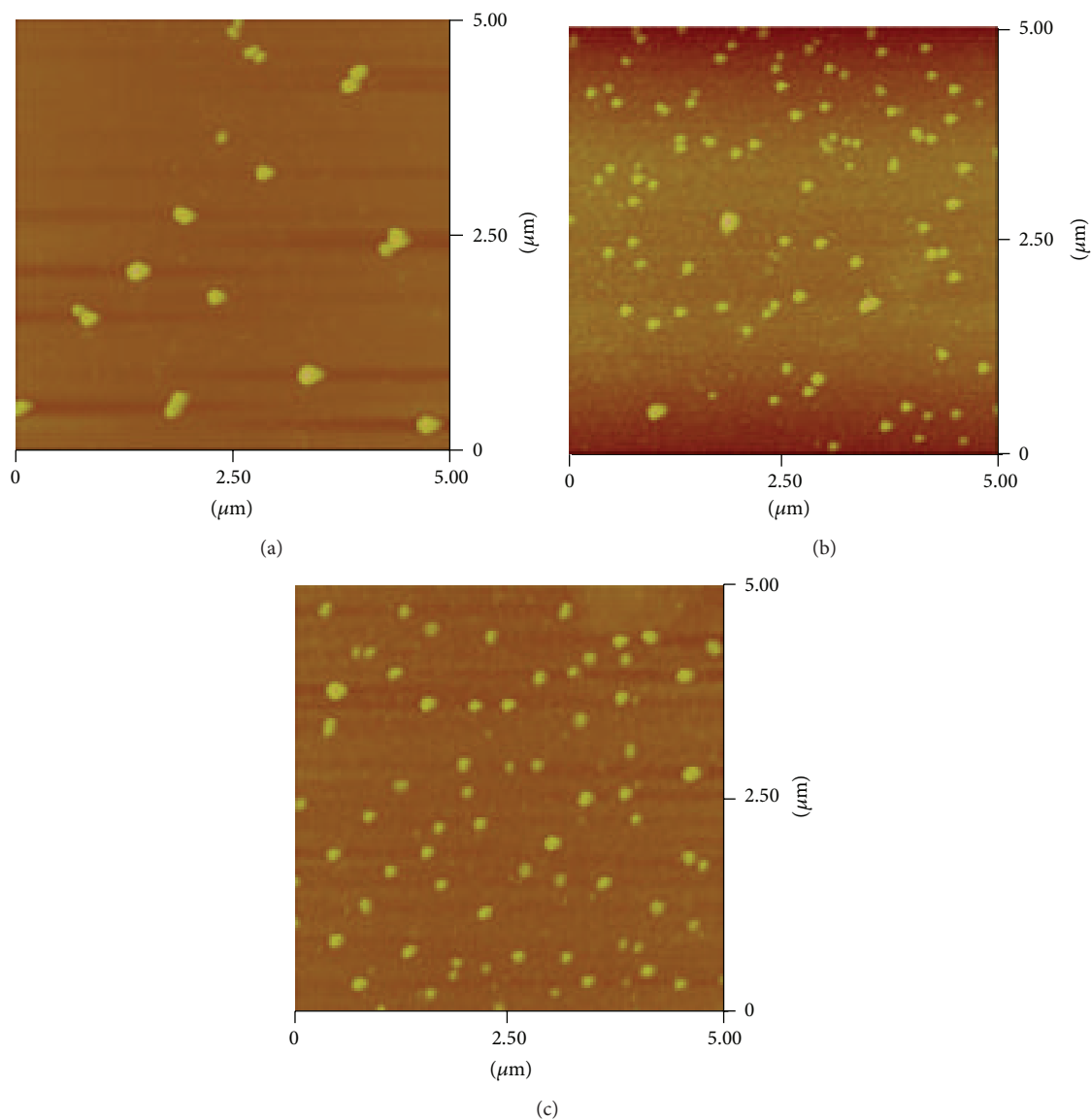


FIGURE 7: AFM images of DPG at various salinities.

TABLE 2: Relationship between the particle size of the gel dispersion and the average shear rate.

Items	Sample		
	1	2	3
Average shearing rate/ $s^{-1}$	155	168	181
Particle size of DPG/nm	1100	750	410

and with a shearing rate of  $181 s^{-1}$ . The DPG system was aged for 10 days before the variations in the morphology were studied. The results are shown in Figure 7.

As shown in Figure 7, the different concentrations and ion types have little influence on the morphology of DPG, which indicates that the system has an excellent resistance to salinity.

The DPG system generally has negative charges due to the adsorption by the polymer molecules at its surface. The ions

and counter ions are both solvated; thus, there is a hydration film on the surface of DPG. The water molecules in the hydration film usually have an exact arrangement. When the gel particles approach each other, the hydration film is squeezed and deformed. The gravitational force that causes the exact arrangement tries to recover the original arrangement of the water molecules, which results in elasticity in the system [16]. Simultaneously, the viscosity of the water in the hydration film is larger than the viscosity of the free water in the system, which hinders the aggregation of DPG and stabilizes the system. When an electrolyte is added to the DPG system, it can cause coagulation of DPG. If the amount of the electrolyte is limited, it only compresses the diffuse electric double layer. Due to the existence of the hydration film, which acts as a buffer, the electrolyte only compresses the hydration film to a small extent without influencing the morphology of DPG.

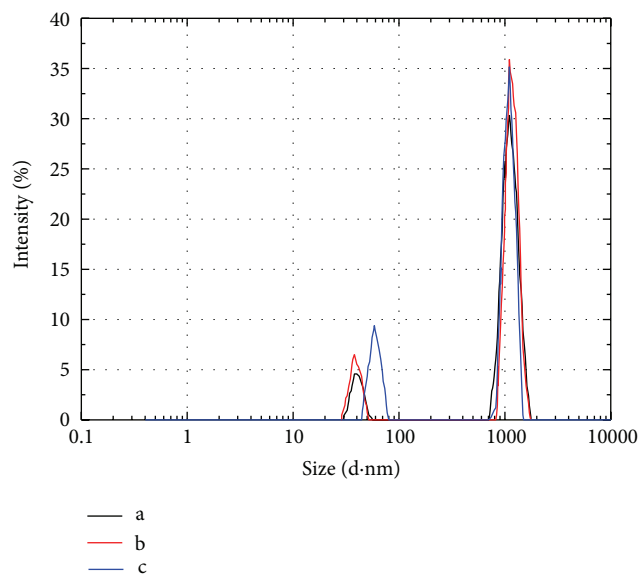


FIGURE 8: The effect of the salinity on the particle size of DPG. (a) In distilled water, (b) with 10,000 mg/L NaCl added, and (c) with 10,000 mg/L NaCl and 2000 mg/L CaCl<sub>2</sub> added.

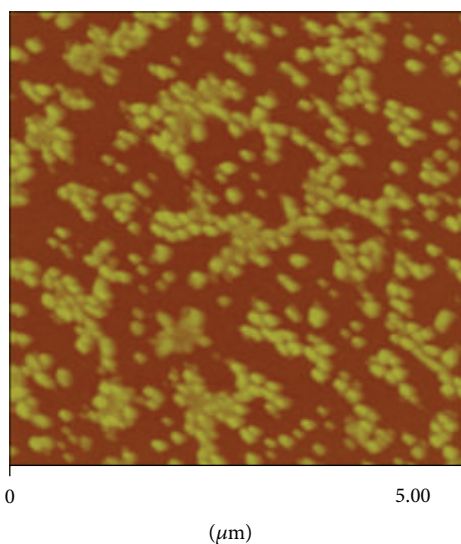


FIGURE 9: AFM photo of DPG after high-temperature aging. The scanned area is  $5 \times 5 \mu\text{m}$ .

The particle size distribution curves of the DPG samples that were prepared at the different salinities at 30°C and aged for ten days (shown in Figure 7) were measured using DLS and are shown in Figure 8.

In Figure 8, there are two peaks in each of the particle size distribution curves of the three DPG samples. There is little variation among the second peaks, which are located at 1166 nm, 1132 nm, and 1100 nm. This suggests that an appropriate salinity has no effect on the particle size of DPG, which shows that DPG has a good tolerance to salinity. The DLS results are consistent with the AFM images of DPG.

**3.1.4. The Effect of High Temperature on the Morphology of DPG.** To study the influence of temperature, the DPG sample that was formed from 3000 mg·L<sup>-1</sup> polymer and the 500 mg·L<sup>-1</sup> Cr(Ac)<sub>3</sub> at 30°C and with a shearing rate of 181 s<sup>-1</sup> was placed in an incubation chamber at 90°C for 15 days. The variations in this DPG system were studied, and the AFM images are shown in Figures 9 and 10 [13].

Figures 9 and 10 show that the DPG particles aggregate in large numbers at high temperatures. The particle size of DPG is small and the surface energy is high; thus, the DPG system tends to aggregate. Smaller particle sizes produce a greater effect. In a macroscopic view, the aggregation leads to some white insoluble floccus in the system.

According to the space stability theory, DPG can be regarded as gel particles that adsorb some polymer molecules on their surfaces; thus, there is a space repulsion potential energy in addition to the repulsive and gravitational potential energies between the particles. When DPG undergoes high-temperature aging, the Brownian movement of the particles increases and the chances of contact also increase such that the two cases shown in Figure 11 may occur.

When the DPG particles with adsorbed polymer layers touch each other, the high temperature leads to an increase in the thermal motion of the polymer molecules in the adsorbed layer, and the contact rate of polymer molecule chains increases, both of which lead to twining between the molecule chains and associations between the hydrophobic groups. Thus, overlap and penetration occur between the adsorbed layers. Moreover, as the particles become larger, their attraction to other particles increases, which accelerates the aggregation of DPG.

Figure 9 shows that DPG has a good temperature resistance and does not degrade or dehydrate during a high-temperature aging process at 90°C. Thus, we can take advantage of the adhesion and aggregation properties of DPG at high temperatures and use it to plug deep reservoirs in practical applications.

The particle size distribution curves were measured using DLS before and after aging at 90°C for 15 days and are shown in Figures 12 and 13. After aging at high temperatures, the value of the characteristic peak changes from 400 nm to three different characteristic peaks at 186.6, 796.2, and 4450 nm. DPG tends to aggregate at high temperatures, which makes the particle size larger and is consistent with previous results on the morphology of DPG. The flocculation is the DPG aggregates of largest particle sizes (over 5 μm).

## 4. Conclusions

- (1) AFM studies show that DPG is made of small pseudospherical particles and that the particle size can be controlled by adjusting the shearing rate. The particles of DPG have a ratio between their major and minor axis lengths close to 1. As the shearing rate increases, the ratio approaches 1. Higher initial polymer mass concentrations result in larger DPG particle sizes. Salinity has a minor effect on the micromorphology, and an aggregation phenomenon occurs with aging.

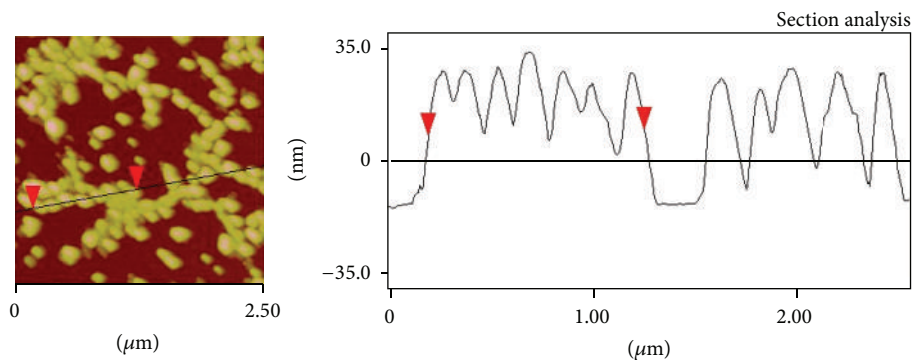


FIGURE 10: Section analysis of DPG after high-temperature aging.

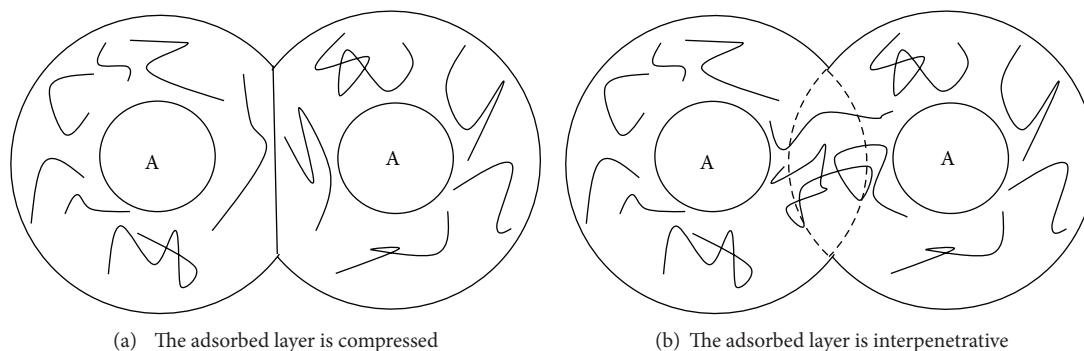


FIGURE 11: The interaction between two DPG particles with adsorbed polymer layers.

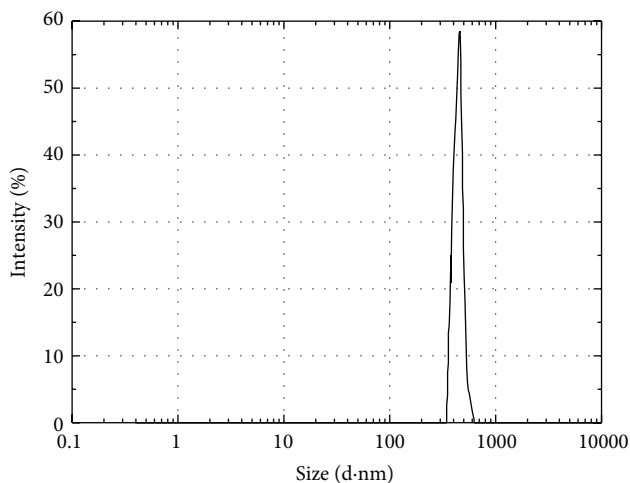


FIGURE 12: The particle size distribution curve of DPG before high-temperature aging.

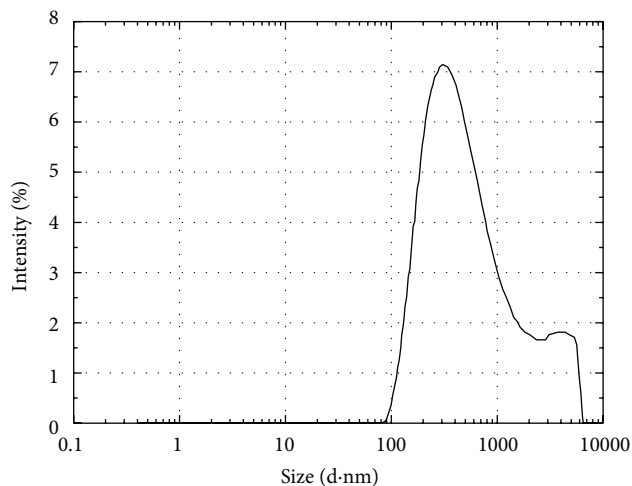


FIGURE 13: The particle size distribution curve of DPG after high-temperature aging.

- (2) DLS studies of the effects of the initial polymer mass concentration, the shearing rate, the salinity, and the high-temperature aging on the particle size of DPG are consistent with the AFM results.
- (3) Using the DLVO theory and the space stability theory, this paper clarifies the factors that make DPG aggregate easily. The easy aggregation is the result of a synergistic effect that includes the gravitational

potential energy  $E_A$ , the repulsive potential energy  $E_R$ , and the space repulsive potential  $E_R^s$ .

- (4) The morphology of DPG and the factors that influence the morphology are studied in this paper to provide a scientific basis and technical support for the IOR mechanism of DPG and its application in the field.

## Conflict of Interests

The authors declare that they have no conflict of interests regarding the publication of this paper.

## Acknowledgments

This paper was supported by the Fundamental Research Funds for the Central Universities (no. 2-9-2014-007), the National Natural Science Foundation of China (no. 51174221), and the Program for New Century Excellent Talents in University (no. 20110226).

## References

- [1] X. F. Tang, Q. Wu, G. H. Liu, S. R. Gu, and H. Y. Li, "Field test on integral modifying and flooding project in regional reservoir with weak gel," *Acta Petrolei Sinica*, vol. 24, no. 4, pp. 58–61, 2003.
- [2] J. H. Liu and T. X. Ye, "Study on the valuation of low concentration HPAM/AlCl<sub>3</sub> system and its gelation influencing factors," *Chemical Engineering of Oil and Gas*, vol. 3, pp. 375–378, 2003.
- [3] H. Frampton, J. C. Morgan, S. K. Cheung, L. Munson, and K. T. Chang, "Development of a novel waterflood conformance control system," in *Proceedings of the SPE/DOE 14th Symposium on Improved Oil Recovery (IOR '04)*, Tulsa, Ok, USA, 2004.
- [4] J. Pritchett, H. Frampton, J. Brinkman et al., "Field application of a new in-depth waterflood conformance improvement tool," in *Proceedings of the SPE International Improved Oil Recovery Conference in Asia Pacific (IIORC '03)*, pp. 365–372, Kuala Lumpur, Malaysia, October 2003, SPE 84897.
- [5] A. Omari, G. Chauveteau, and J. Rose, "New size-controlled microgels for oil production," in *Proceedings of the SPE International Symposium on Oilfield Chemistry*, pp. 1–8, Houston, Tex, USA, February 2001.
- [6] D. Rousseau, G. Chauveteau, M. Renard et al., "Rheology and transport in porous media of new water shutoff/conformance control microgels," in *Proceeding of the SPE International Symposium on oilfield Chemistry*, The Woodlands, Tex, USA, February 2005.
- [7] A. Zaitoun, R. Tabary, D. Rousseau et al., "Using microgels to shut off water in a gas storage well," in *Proceedings of the SPE International Symposium on Oilfield Chemistry*, vol. 106042, pp. 221–228, Houston, Tex, USA, March 2007.
- [8] J. P. Coste, "In-depth fluid diversion by pre-gelled particles," in *Proceedings of the SPE/DOE Improved Oil Recovery Symposium*, SPE 59362, Laboratory Study and Pilot Testing, Tulsa, Okla, USA, April 2000.
- [9] B. J. Bai, "Case study on preformed particle gel for in-depth fluid diversion," in *Proceedings of the SPE Symposium on Improved Oil Recovery*, SPE-113997-MS, Tulsa, Okla, USA, April 2008.
- [10] H. W. Ma, Y. Z. Liu, and Y. K. Li, "Research on flexible particle migration in porous media," *Oil Drilling & Production Technology*, vol. 4, pp. 80–82, 2007.
- [11] Q. You, Y. C. Tang, and C. L. Dai, "Research on a new profile control agent: dispersed particle gel," in *Proceedings of the SPE Enhanced Oil Recovery Conference*, SPE 143514, Kuala Lumpur, Malaysia, July 2011.
- [12] F. L. Zhao, *Principle of Enhanced Oil Recovery*, China University of Petroleum Press, Dongying, China, 2006.
- [13] Q. You, C. L. Dai, and Y. C. Tang, "Study on performance evaluation of dispersed particle gel for improved oil recovery," *Journal of Energy Resources Technology*, vol. 135, no. 4, Article ID 042903, 7 pages, 2013.
- [14] J. S. Qin and A. F. Li, *Reservoir Physics*, China University of Petroleum Press, Dongying, China, 2nd edition, 2006.
- [15] K. Chen, *Study on Preparation, Performance Evaluation and Application of Microgel*, China University of Petroleum Press, Dongying, China, 2007.
- [16] Z. Sheng, Z. G. Zhao, and G. T. Wang, *Colloid and Surface Chemistry*, Chemical Industry Press, Beijing, China, 2012.

## Research Article

# Catalytic Combustion of Low Concentration Methane over Catalysts Prepared from Co/Mg-Mn Layered Double Hydroxides

Hongfeng Liu,<sup>1,2</sup> Xingrui Fu,<sup>1,2</sup> Xiaole Weng,<sup>1,2</sup> Yue Liu,<sup>1,2</sup>  
Haiqiang Wang,<sup>1,2</sup> and Zhongbiao Wu<sup>1,2</sup>

<sup>1</sup> Department of Environmental Engineering, Zhejiang University, Zijingang Campus, Yuhangtang Road 388, Hangzhou 310058, China

<sup>2</sup> Zhejiang Provincial Engineering Research Center of Industrial Boiler & Furnace Flue-Gas Pollution Control, Hangzhou 310058, China

Correspondence should be addressed to Xiaole Weng; [xlweng@zju.edu.cn](mailto:xlweng@zju.edu.cn) and Yue Liu; [yueliu@zju.edu.cn](mailto:yueliu@zju.edu.cn)

Received 22 May 2014; Accepted 4 June 2014; Published 1 July 2014

Academic Editor: Fan Dong

Copyright © 2014 Hongfeng Liu et al. This is an open access article distributed under the Creative Commons Attribution License, which permits unrestricted use, distribution, and reproduction in any medium, provided the original work is properly cited.

A series of Co/Mg-Mn mixed oxides were synthesized through thermal decomposition of layered double hydroxides (LDHs) precursors. The resulted catalysts were then subjected for catalytic combustion of methane. Experimental results revealed that the Co<sub>4.5</sub>Mg<sub>1.5</sub>Mn<sub>2</sub>LDO catalyst possessed the best performance with the  $T_{90} = 485^\circ\text{C}$ . After being analyzed via XRD, BET-BJH, SEM, H<sub>2</sub>-TPR, and XPS techniques, it was observed that the addition of cobalt had significantly improved the redox ability of the catalysts whilst certain amount of magnesium was essential to guarantee the catalytic activity. The presence of Mg was helpful to enhance the oxygen mobility and, meanwhile, improved the dispersion of Co and Mn oxides, preventing the surface area loss after calcination.

## 1. Introduction

Low concentration methane such as coal mine methane is usually emitted directly into the atmosphere or burned immediately due to its low calorific value, resulting in either greenhouse effect or a huge waste of resource. Moreover, NO<sub>x</sub> can be also produced during thermal combustion. Therefore, it is necessary to develop a cost-effective technology for capturing and utilizing the low concentration methane.

So far, a number of studies have focused on the catalytic oxidation of methane, especially on the noble metal catalysts [1–4]. Nevertheless, noble metal catalysts normally show some shortcomings for real application like volatility, high sintering rates, poisoning in the presence of disturbing compounds, and high price [5]. As such, the mixed metal oxide catalysts have been attracting rising concern recently for methane catalytic combustion [6, 7]. And some reporter showed that the activity of mixed metal oxide catalysts was not necessarily worse than noble metal catalysts for VOCs catalytic oxidation [8–10].

Layered double hydroxides (LDHs) are known as a series of anion layered compounds whose chemical composition can be represented as  $[\text{M}_{1-x}^{\text{II}}\text{M}_x^{\text{III}}(\text{OH})_2]^{x+} [\text{A}_{x/n}^{n-} \cdot y\text{H}_2\text{O}]^{x-}$ . M<sup>II</sup> and M<sup>III</sup> are bivalent and trivalent metal cations, A<sup>n-</sup> is an *n*-valent anion, and the values of *x* usually range from 0.20 to 0.33. After thermal decomposition, LDHs could be potential materials for total oxidation catalysts due to their large surface area, high metal dispersion, small crystallite size, and stability against sintering [11]. Up to now, a lot of efforts have been dedicated to developing the LDHs catalysts for volatile organic compounds (VOCs) degradation and the methane catalytic combustion [5, 12].

In light of the above points, we synthesized a series of LDHs related catalysts, in which the transition metals Co and Mn were induced as bivalent and trivalent metal cations, respectively, for the methane catalytic combustion. Then, the catalysts were characterized by various methods to show the relationships between the chemophysical properties of the catalysts and their performances.

## 2. Experimental Section

**2.1. Catalyst Preparation.** The LDHs precursors Co/Mg-Mn were prepared by coprecipitation method at a constant pH value ( $10 \pm 0.5$ ). Mixed salt solution (100 mL) and 2 M NaOH (100 mL) solution were added dropwise into 100 mL 0.45 M  $\text{Na}_2\text{CO}_3$  solution simultaneously under vigorous mechanical stirring at  $60^\circ\text{C}$  in water bath for 1 h. The mixed salt solution consists of a total cation concentration of 2 M from  $\text{Mg}(\text{NO}_3)_2 \cdot 6\text{H}_2\text{O}$ ,  $\text{Co}(\text{NO}_3)_2 \cdot 6\text{H}_2\text{O}$ , and  $\text{Mn}(\text{NO}_3)_2$  with  $(\text{Mg} + \text{Co})/\text{Mn} = 3.0$ . The addition of the alkaline solution and the pH value were controlled by a pH meter. Precipitates formed were aged with the mother liquid overnight at  $60^\circ\text{C}$  under vigorous stirring and then filtered and thoroughly washed with distilled water to  $\text{pH} = 7.0$ . After that, the resulting solid (LDHs precursors) was dried at  $100^\circ\text{C}$  for 12 h. Then, these LDHs precursors (denoted as  $\text{Co}_x\text{Mg}_{6-x}\text{Mn}_2\text{LDH}$ ) were calcined at  $600^\circ\text{C}$  for 4 h to derive Co/Mg-Mn mixed oxide catalysts (denoted as  $\text{Co}_x\text{Mg}_{6-x}\text{Mn}_2\text{LDO}$ ). Finally, the oxide catalysts were crushed and sized in 40–60 mesh for activity test and characterizations.

**2.2. Catalytic Activity Testing.** The catalytic activity tests of methane were performed in a fixed bed with an inside steel tube reactor operated at atmospheric pressure. 0.5 g catalyst diluted with equal volume silica sand was used during the test with a gas mixture of  $\text{CH}_4 : \text{O}_2 : \text{N}_2 = 1.6 : 16 : 144$  at a total flow rate of around 160 mL/min passing through the reactor. The gas flow rate was controlled by mass flow meter. The internal diameter of the reactor is 8.20 mm and the length is 450 mm. Catalytic activity tests were carried out with a gas hourly space velocity (GHSV) of  $25,000 \text{ h}^{-1}$ , at the temperature ranging from  $350$  to  $600^\circ\text{C}$ . The reactants and products were online analyzed by Agilent GC and equipped with flame ionization detection (FID). Before each test, the catalysts were preheated at  $500^\circ\text{C}$  for 30 min and then cooled to  $350^\circ\text{C}$  to start the test. The methane conversion rate was calculated based on the integrated GC peak areas.

**2.3. Catalytic Characterization.** X-ray diffraction patterns (XRD) were recorded using a Rigaku D/Max RA diffractometer to identify the crystal structure of the samples with the monochromatic  $\text{Cu K}\alpha$  radiation at  $2\theta$  ranging from  $5$  to  $80^\circ$  with a scanning rate of  $4^\circ/\text{min}$ . The textural properties of the derived oxides were analyzed by  $\text{N}_2$  adsorption/desorption at  $77 \text{ K}$  in a JW-BK132F static adsorption analyzer. Before each test, the catalyst was pretreated at  $100^\circ\text{C}$  for 3 h in vacuum. The specific surface area was calculated with the BET equation, and the pore volume and pore size distribution were obtained by the BJH method. The micromorphology characteristics were examined by scanning electron microscope (SEM: Ultra 55, Carl Zeiss AG, USA). A custom-made TCD setup was employed to run the temperature programmed reduction (TPR) test by using 50 mg catalysts. Prior to the test, a preheat treatment was performed in  $5\% \text{ O}_2/\text{He}$  at  $500^\circ\text{C}$  for 2 h. Then, the sample was cooled down to  $100^\circ\text{C}$  and kept at this temperature for 30 min. After that, TPR tests were carried out at a heating rate of  $10^\circ\text{C}/\text{min}$  with 30 mL/min

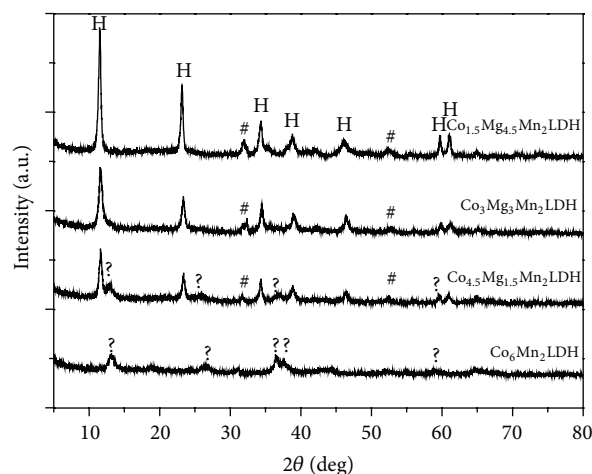


FIGURE 1: XRD patterns of the  $\text{Co}_x\text{Mg}_{6-x}\text{Mn}_2\text{LDH}$  precursors (H: hydrotalcite-like compounds; #:  $\text{MnCO}_3$ ; ?: unidentified phases).

$6\% \text{ H}_2$  balanced with He going through. X-ray photoelectron spectroscopy with Al  $\text{K}\alpha$  X-ray ( $h\nu = 1486.6 \text{ eV}$ ) radiation operated at 150 W (Thermo ESCALAB 250Xi, USA) was used to investigate the surface atomic state of the sample. All the binding energies obtained were corrected using the C 1s level at  $284.8 \text{ eV}$  as an internal standard.

## 3. Results and Discussions

XRD patterns of all the  $\text{Co}_x\text{Mg}_{6-x}\text{Mn}_2\text{LDH}$  precursors and calcined mixed oxides are exhibited in Figures 1 and 2, respectively. From Figure 1, a well-crystallized LDHs phase ( $2\theta = 11.5^\circ, 23^\circ, 34^\circ$ ) could be detected in all the samples except the  $\text{Co}_6\text{Mn}_2\text{LDH}$ . Meanwhile, the reflections corresponding to  $\text{MnCO}_3$  (PDF-No. 44-1472) also appeared in the former three samples [13]. However, the intensity referred to  $\text{Co}_6\text{Mn}_2\text{LDH}$  sample was particularly low. And its crystallized phases could not be identified based on the phase analysis software, Jade5. The similar finding had been also reported by Kovanda et al. [14] in their study regarding Co and Mn containing layered double hydroxides. After calcination at  $600^\circ\text{C}$  for 4 h, spinel-type mixed oxides were formed in all the samples including  $\text{Co}_6\text{Mn}_2\text{LDO}$ . Such samples probably consist of one or mixture of  $\text{MnCo}_2\text{O}_4$  (PDF number: 23-1237),  $\text{CoMn}_2\text{O}_4$  (PDF number: 01-1126),  $\text{Mg}_6\text{MnO}_8$  (PDF number: 19-0766),  $\text{Co}_3\text{O}_4$  (PDF number: 43-1003), and  $\text{MgCoMnO}_4$  (PDF number: 39-1157), considering that their peaks were almost superimposed. At low Co loading content ( $\text{Co}_{1.5}\text{Mg}_{4.5}\text{Mn}_2\text{LDO}$ ),  $\text{MnCo}_2\text{O}_4$  could be the main phase. And, with the increase of Co content, the peaks would gradually shift to higher angle range. For the sample  $\text{Co}_6\text{Mn}_2\text{LDO}$ , the obtained phases were mainly  $\text{Co}_3\text{O}_4$  phase. Compared with the other three samples, it could be also found that the signal of Mg-free sample ( $\text{Co}_6\text{Mn}_2\text{LDO}$ ) became sharper and higher, indicating that the primary particle size was probably larger than the others. For instance, the primary particle size calculated by Scherrer

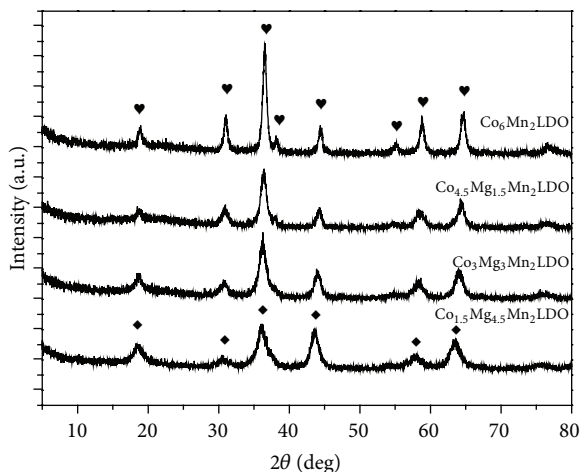


FIGURE 2: XRD patterns of the  $\text{Co}_x\text{Mg}_{6-x}\text{Mn}_2\text{LDO}$  samples (◆:  $\text{MnCo}_2\text{O}_4$  phases; ♥:  $\text{Co}_3\text{O}_4$ ).

equation increased from 8.1 nm for  $\text{Co}_{4.5}\text{Mg}_{1.5}\text{Mn}_2\text{LDO}$  to 12.9 nm for  $\text{Co}_6\text{Mn}_2\text{LDO}$ .

From the activity tests (which will be discussed in Figure 6), we found that the activity of  $\text{Co}_6\text{Mn}_2\text{LDO}$  sample was lower than the Mg-containing sample  $\text{Co}_{4.5}\text{Mg}_{1.5}\text{Mn}_2\text{LDO}$ . To further investigate the reason, we tried to get a clue from the SEM images of their  $\text{Co}_x\text{Mg}_{6-x}\text{Mn}_2\text{LDH}$  precursors. The results are shown in Figure 3. From Figures 3(a) and 3(c), the  $\text{Co}_{4.5}\text{Mg}_{1.5}\text{Mn}_2\text{LDH}$  samples showed a flake-like morphology and the size of flakes was approximately 400–450 nm. Without addition of magnesium, the sheet structure also appeared in the precursors, but the size and thickness grew larger. At the same time, we could also observe a lot of sintered particles from the image. This was probably attributed to the aggregation of the primary particles, since Mg-free sample should be of smaller primary particle size according to the XRD results in Figure 1. And the aggregation of the particles would lead to the easy sintering of the calcined oxides. This was consistent with the results of the LDO-XRD (Figure 2).

The specific areas of the  $\text{Co}_x\text{Mg}_{6-x}\text{Mn}_2\text{LDH}$  precursors and the derived LDO samples are presented in Table 1. It could be observed that the surface area of LDH increased from 49.09  $\text{m}^2/\text{g}$  to 130.88  $\text{m}^2/\text{g}$ , which was in accordance with the result of LDH-XRD (Figure 1) that the peaks of the samples were getting broader with the addition of Co, indicating the decreasing of the grain size. However, the Mg-free LDO sample got the greatest loss in surface area (from 130.88 to about 45  $\text{m}^2/\text{g}$ ), together with the decreases of the pore diameter and volume. This fitted well with the result of LDO-XRD (see Figure 2) that the grain size would grow bigger without Mg being involved. According to the literatures [15–17], the alkaline earth could isolate transition metals effectively by strong interaction to reduce the agglomeration of the particles, thus reducing the loss of the specific area after calcination.

$\text{H}_2$ -TPR (see Figure 4) showed the differences in reducibility of the prepared LDO samples caused by the

TABLE 1: Porous properties of the  $\text{Co}_x\text{Mg}_{6-x}\text{Mn}_2\text{LDH}$  (a) and LDO (b).

Sample	$S_{\text{BET}}^{\text{a}}$ ( $\text{m}^2/\text{g}$ )	$S_{\text{BET}}^{\text{b}}$ ( $\text{m}^2/\text{g}$ )	$D_p^{\text{b}}$ (nm)	$V_p^{\text{b}}$ ( $\text{cm}^3/\text{g}$ )
$x = 1.5$	49.09	43.88	28.66	0.31
$x = 3$	58.07	44.1	26.37	0.29
$x = 4.5$	85.15	50.87	24.36	0.28
$x = 6$	130.89	45.23	20.11	0.23

increasing content of Co. Based on the literatures [18, 19], the broad reduction peaks from 250 to 500°C were the results of overlapping peaks related to the reductions of Co/Mn oxides, which consists of the reduction process of  $\text{Co}^{\text{III}} \rightarrow \text{Co}^{\text{II}} \rightarrow \text{Co}^0$  in  $\text{Co}_3\text{O}_4$  phase and  $\text{Mn}^{\text{IV}}$  species reduction. With the increase of Co content, the peaks first shifted to higher temperature and then the peaks shifted obviously to the lower temperature and a shoulder peak appeared at 284°C, which could be assigned to the reduction of  $\text{Co}^{\text{III}} \rightarrow \text{Co}^{\text{II}}$  [18], while, for the catalyst  $\text{Co}_6\text{Mn}_2\text{LDO}$ , the peaks shifted to higher temperature again and an additional peak at about 680°C became more evident. This high temperature peak might be attributed to the reduction of Co-Mn mixed oxide due to the sintering of catalyst in absence of Mg. The possible reason is that the existence of Mg could suppress the sintering and improve the dispersion of the active substance.

Oxygen normally played a very important role in the decomposition of methane according to the catalytic mechanism [20]. As such, the oxygen states on the catalysts herein were investigated by XPS characterization and the binding energies of O1s were given in Figure 5. Generally, there are three different types of oxygen in the catalysts with binding energy of O1s electrons, 529.0–530.0 eV, 531.3–531.9 eV, and 532.7–533.5 eV, which could be ascribed to lattice oxygen ( $\text{O}_a$ ), surface adsorbed oxygen ( $\text{O}_b$ ), and oxygen bonded in OH group ( $\text{O}_c$ ), respectively [21–23]. In case of our catalysts (see Figure 5), oxygen with binding energy of 529.5–530.3 eV was the most intensive form and could be assigned to the lattice oxygen [22]. And oxygen species with binding energy of 531.0–531.5 eV can be attributed to the surface adsorbed oxygen ( $\text{O}_b$ ) which could be considered the most active oxygen [24]. The percentage of  $\text{O}_b$  in total surface oxygen is listed in Table 2, from which we could clearly notice the tendency that  $\text{O}_b$  decreased with the introduction of Co, especially for the Mg-free one. In other words, the magnesium was necessary for keeping a certain amount of surface active oxygen possibly due to its well electronic donation property as a typical alkali earth metal. At last, oxygen with binding energy of 532.1–532.9 eV was originated from carbonated species or molecular adsorbed water [25].

The catalytic activities of the  $\text{Co}_x\text{Mg}_{6-x}\text{Mn}_2\text{LDO}$  samples derived from LDH precursors in methane total oxidation tested within the temperature range of 330–600°C are shown in Figure 6, where the methane conversion is plotted as a function of the reaction temperature. As shown in Figure 6, it could be clearly observed that the  $T_{90}$  (defined as 90% methane conversion) went down with the increase of Co content at first and then increased for

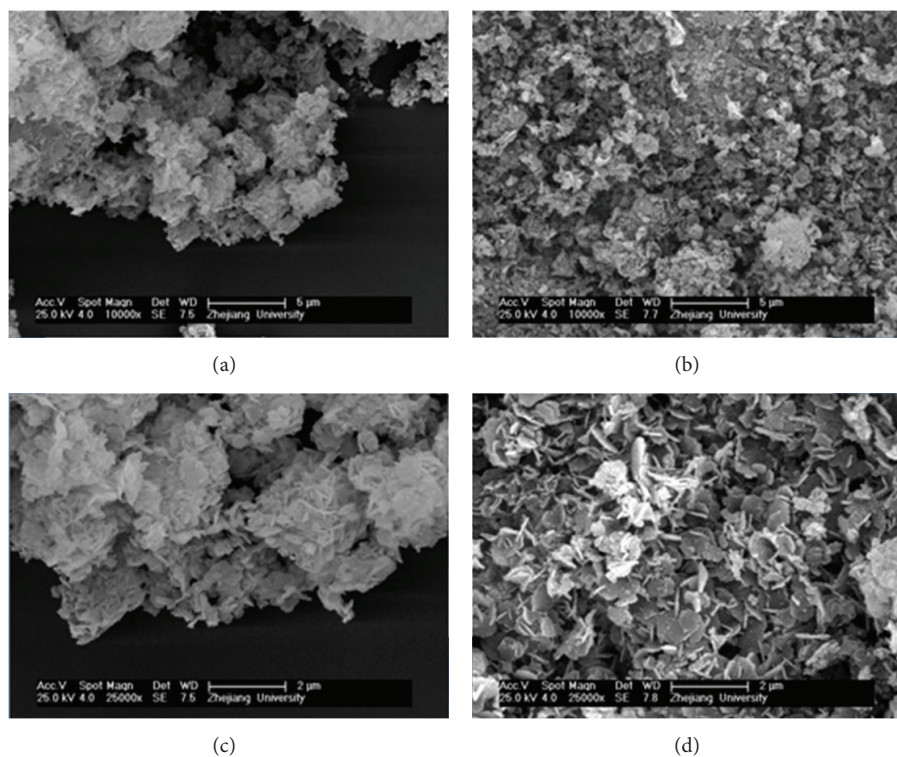


FIGURE 3: SEM images of  $\text{Co}_x\text{Mg}_{6-x}\text{Mn}_2\text{LDH}$  precursors (a) and (c),  $x = 4.5$ , and (b) and (d),  $x = 6$ .

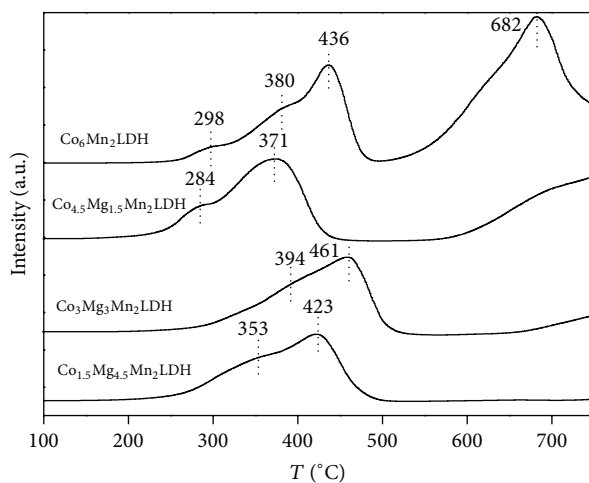


FIGURE 4:  $\text{H}_2$ -TPR patterns of  $\text{Co}_x\text{Mg}_{6-x}\text{Mn}_2\text{LDO}$  samples.

the  $\text{Co}_6\text{Mn}_2\text{LDO}$  sample. The  $\text{Co}_{4.5}\text{Mg}_{1.5}\text{Mn}_2\text{LDO}$  catalyst showed the best performance with the  $T_{90} = 485^\circ\text{C}$ . This result was in agreement with our previous  $\text{H}_2$ -TPR characterization where  $\text{Co}_{4.5}\text{Mg}_{1.5}\text{Mn}_2\text{LDO}$  exhibits the best low-temperature reducibility. As we know, active oxygen was a critical factor for the catalytic oxidation reaction. The various valences of transition metal Co could supply abundant active oxygen in the catalysts, so the activity improved with the increase of Co at first, but when Mg is totally substituted by Co, the activity decreases because Mg could act as an electronic promoter in the catalysts to guarantee the oxygen mobility which was of

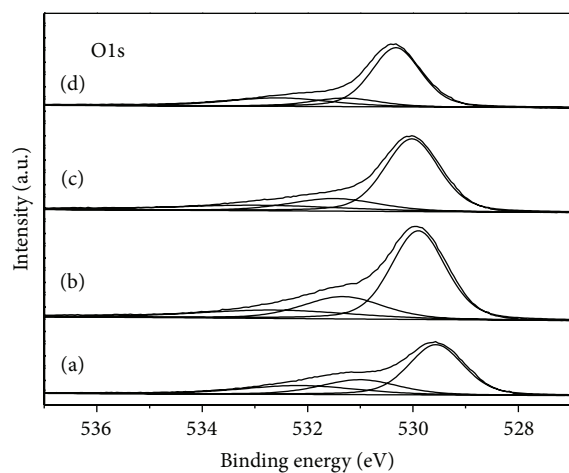
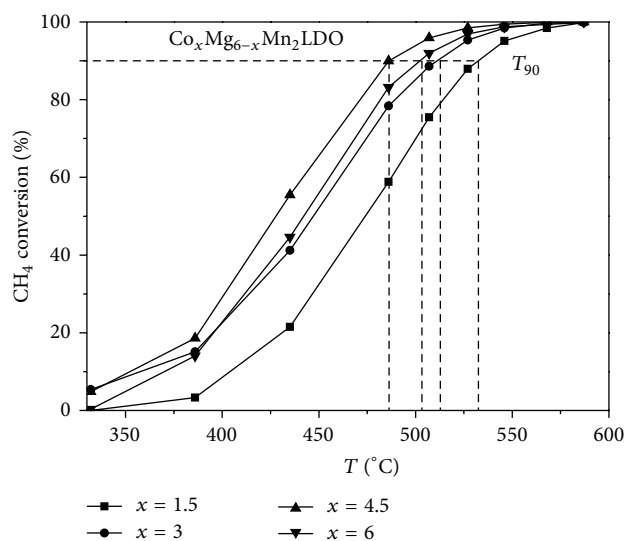
great importance for the catalytic oxidation reactions. The enhanced oxygen mobility after Ca-doping was reported in the literatures, which might indirectly support our assumption [24, 26].

#### 4. Conclusions

A series of Co/Mg-Mn mixed oxide based catalysts were prepared via the calcination of layered double hydroxides with (Co+Mg)/Mn ratio at 3 and Co/Mg ratio from 1.5/4.5

TABLE 2: The amount of the surface elements of  $\text{Co}_x\text{Mg}_{6-x}\text{Mn}_2\text{LDO}$ .

Sample	Co (%)	Mg (%)	Mn (%)	O (%)	$\text{O}_b/\text{O}_{\text{total}}$
$\text{Co}_x\text{Mg}_{6-x}\text{Mn}_2\text{LDO } x = 1.5$	5.3	27.8	7.4	59.5	23.45
$\text{Co}_x\text{Mg}_{6-x}\text{Mn}_2\text{LDO } x = 3$	11.3	19.6	8.5	60.6	22.59
$\text{Co}_x\text{Mg}_{6-x}\text{Mn}_2\text{LDO } x = 4.5$	16.4	12.6	9.6	61.4	18.70
$\text{Co}_x\text{Mg}_{6-x}\text{Mn}_2\text{LDO } x = 6$	21.3	0	12.5	66.2	13.12

FIGURE 5: O1s XPS patterns of  $\text{Co}_x\text{Mg}_{6-x}\text{Mn}_2\text{LDO}$  samples: (a)  $x = 1.5$ , (b)  $x = 3$ , (c)  $x = 4.5$ , and (d)  $x = 6$ .FIGURE 6: Catalytic activity of  $\text{Co}_x\text{Mg}_{6-x}\text{Mn}_2\text{LDO}$  samples (1% vol.  $\text{CH}_4$ , 10% vol.  $\text{O}_2$ , GHSV =  $25000 \text{ h}^{-1}$ ).

to 6/0, respectively. And then these catalysts were characterized by various methods and tested for their activities for methane catalytic combustion. The typical LDH lamellar structures were identified by X-ray diffraction except for the last  $\text{Co}_6\text{Mn}_2\text{LDH}$  sample. But spinel structures were formed in all samples after calcination. The catalytic activities of the prepared catalysts expressed as the methane conversion decreased in the following sequence:  $\text{Co}_{4.5}\text{Mg}_{1.5}\text{Mn}_2\text{LDO}$

$> \text{Co}_6\text{Mn}_2\text{LDO} > \text{Co}_3\text{Mg}_3\text{Mn}_2\text{LDO} > \text{Co}_{1.5}\text{Mg}_{4.5}\text{Mn}_2\text{LDO}$ . Though the addition of Co would increase the redox ability of the catalyst, a certain amount of magnesium was necessary for high activity. Magnesium oxide would be beneficial to the dispersion of the cobalt and manganese mixed oxides. Furthermore, the existence of Mg could reduce the surface area loss after calcination and increase the surface active oxygen content.

### Conflict of Interests

The authors declare that there is no conflict of interests regarding the publication of this paper.

### Acknowledgment

This work is financially supported by Zhejiang Provincial "151" Talents Program.

### References

- [1] J. Yin, S. Su, X. X. Yu, and Y. Weng, "Thermodynamic characteristics of a low concentration methane catalytic combustion gas turbine," *Applied Energy*, vol. 87, no. 6, pp. 2102–2108, 2010.
- [2] H. Arai, T. Yamada, K. Eguchi, and T. Seiyama, "Catalytic combustion of methane over various perovskite-type oxides," *Applied Catalysis*, vol. 26, pp. 265–276, 1986.
- [3] P. Gélin and M. Primet, "Complete oxidation of methane at low temperature over noble metal based catalysts: a review," *Applied Catalysis B: Environmental*, vol. 39, no. 1, pp. 1–37, 2002.
- [4] D. Ciuparu, M. R. Lyubovsky, E. Altman, L. D. Pfeifferle, and A. Datye, "Catalytic combustion of methane over palladium-based catalysts," *Catalysis Reviews: Science and Engineering*, vol. 44, no. 4, pp. 593–649, 2002.
- [5] S. Tanasoi, N. Tanchoux, A. Urdă et al., "New Cu-based mixed oxides obtained from LDH precursors, catalysts for methane total oxidation," *Applied Catalysis A: General*, vol. 363, no. 1–2, pp. 135–142, 2009.
- [6] L. Hu, Q. Peng, and Y. Li, "Selective synthesis of  $\text{Co}_3\text{O}_4$  nanocrystal with different shape and crystal plane effect on catalytic property for methane combustion," *Journal of the American Chemical Society*, vol. 130, no. 48, pp. 16136–16137, 2008.
- [7] J. Kirchnerova, M. Alifanti, and B. Delmon, "Evidence of phase cooperation in the  $\text{LaCoO}_3\text{-CeO}_2\text{-Co}_3\text{O}_4$  catalytic system in relation to activity in methane combustion," *Applied Catalysis A: General*, vol. 231, no. 1–2, pp. 65–80, 2002.
- [8] W. B. Li, W. B. Chu, M. Zhuang, and J. Hua, "Catalytic oxidation of toluene on Mn-containing mixed oxides prepared in reverse microemulsions," *Catalysis Today*, vol. 93–95, pp. 205–209, 2004.

- [9] W. B. Li, J. X. Wang, and H. Gong, "Catalytic combustion of VOCs on non-noble metal catalysts," *Catalysis Today*, vol. 148, no. 1-2, pp. 81–87, 2009.
- [10] M. R. Morales, B. P. Barbero, and L. E. Cadús, "Total oxidation of ethanol and propane over Mn-Cu mixed oxide catalysts," *Applied Catalysis B: Environmental*, vol. 67, no. 3-4, pp. 229–236, 2006.
- [11] F. Zhang, X. Xiang, F. Li, and X. Duan, "Layered double hydroxides as catalytic materials: recent development," *Catalysis Surveys from Asia*, vol. 12, no. 4, pp. 253–265, 2008.
- [12] K. Bahranowski, E. Bielańska, R. Janik, T. Machej, and E. M. Serwicka, "LDH-derived catalysts for complete oxidation of volatile organic compounds," *Clay Minerals*, vol. 34, no. 1, pp. 67–77, 1999.
- [13] Q. Li, M. Meng, H. Xian et al., "Hydrotalcite-derived  $Mn_xMg_{3-x}AlO$  catalysts used for soot combustion,  $NO_x$  storage and simultaneous soot- $NO_x$  removal," *Environmental Science & Technology*, vol. 44, no. 12, pp. 4747–4752, 2010.
- [14] F. Kovanda, T. Rojka, J. Dobešová et al., "Mixed oxides obtained from Co and Mn containing layered double hydroxides: preparation, characterization, and catalytic properties," *Journal of Solid State Chemistry*, vol. 179, no. 3, pp. 812–823, 2006.
- [15] P. Peshev, A. Toshev, and G. Gyurov, "Preparation of high-dispersity  $MCo_2O_4$  ( $M = Mg, Ni, Zn$ ) spinels by thermal dissociation of coprecipitated oxalates," *Materials Research Bulletin*, vol. 24, no. 1, pp. 33–40, 1989.
- [16] X. Yang, X. Xia, and N. Wu, "Molybdate anion pillared Mg-Al hydrotalcite as precursors for HDS catalysts I. Chemical state and dispersity of  $MoO_3$  in  $MoO_3/Mg(Al)O$ ," *Chinese Journal of Catalysis*, vol. 22, no. 4, pp. 358–360, 2001.
- [17] Q. Miao, G. Xiong, S. Sheng, W. Cui, and X. Guo, "The oxidative transformation of methane over the nickel-based catalysts modified by alkali metal oxide and rare earth metal oxide," *Studies in Surface Science and Catalysis*, vol. 101, pp. 453–462, 1996.
- [18] L. Obalová, K. Pacultová, J. Balabánová et al., "Effect of Mn/Al ratio in CoMnAl mixed oxide catalysts prepared from hydrotalcite-like precursors on catalytic decomposition of  $N_2O$ ," *Catalysis Today*, vol. 119, no. 1–4, pp. 233–238, 2007.
- [19] L. Obalová, K. Karásková, K. Jiráková, and F. Kovanda, "Effect of potassium in calcined Co-Mn-Al layered double hydroxide on the catalytic decomposition of  $N_2O$ ," *Applied Catalysis B: Environmental*, vol. 90, no. 1-2, pp. 132–140, 2009.
- [20] T. Ito, T. Watanabe, T. Tashiro, and K. Toi, "Reaction of preadsorbed methane with oxygen over magnesium oxide at low temperatures," *Journal of the Chemical Society*, vol. 85, no. 8, pp. 2381–2395, 1989.
- [21] M. Kang, E. D. Park, J. M. Kim, and J. E. Yie, "Manganese oxide catalysts for  $NO_x$  reduction with  $NH_3$  at low temperatures," *Applied Catalysis A: General*, vol. 327, no. 2, pp. 261–269, 2007.
- [22] A. Machocki, T. Ioannides, B. Stasinska et al., "Manganese-lanthanum oxides modified with silver for the catalytic combustion of methane," *Journal of Catalysis*, vol. 227, no. 2, pp. 282–296, 2004.
- [23] E. Ksepko, E. Talik, A. Ratuszna, A. Molak, Z. Ujma, and I. Gruszka, "XPS examination of newly obtained  $(Na_{0.5}Pb_{0.5})(Mn_{0.5}Nb_{0.5})O_3$  ceramics," *Journal of Alloys and Compounds*, vol. 386, no. 1-2, pp. 35–42, 2005.
- [24] T. Gu, R. Jin, Y. Liu, H. Liu, X. Weng, and Z. Wu, "Promoting effect of calcium doping on the performances of  $MnO_x/TiO_2$  catalysts for  $NO$  reduction with  $NH_3$  at low temperature," *Applied Catalysis B: Environmental*, vol. 129, pp. 30–38, 2013.
- [25] K. Jiráková, J. Mikulová, J. Klempa, T. Grygar, Z. Bastl, and F. Kovanda, "Modification of Co-Mn-Al mixed oxide with potassium and its effect on deep oxidation of VOC," *Applied Catalysis A: General*, vol. 361, no. 1-2, pp. 106–116, 2009.
- [26] H. Song and U. S. Ozkan, "Changing the oxygen mobility in Co/Ceria catalysts by Ca incorporation: implications for ethanol steam reforming," *The Journal of Physical Chemistry A*, vol. 114, no. 11, pp. 3796–3801, 2010.

## Research Article

# Inhibition Effect of Glycerol on the Corrosion of Copper in NaCl Solutions at Different pH Values

Santos Lorenzo Chi-Ucán,<sup>1</sup> Andrea Castillo-Atoche,<sup>1</sup>  
Pedro Castro Borges,<sup>1</sup> José Antonio Manzanilla-Cano,<sup>2</sup> Gerardo González-García,<sup>1</sup>  
Rodrigo Patiño,<sup>1</sup> and Luis Díaz-Ballote<sup>1</sup>

<sup>1</sup>Departamento de Física Aplicada, Centro de Investigación y de Estudios Avanzados, Unidad Mérida, Antigua Carretera a Progreso Km. 6, 97310 Mérida, YUC, Mexico

<sup>2</sup>Laboratorio de Electroquímica Analítica, Facultad de Química, Universidad Autónoma de Yucatán, Calle 41 No. 421 entre 26 y 28, Colonia Industrial, 97150 Mérida, YUC, Mexico

Correspondence should be addressed to Luis Díaz-Ballote; [luisdiaz@mda.cinvestav.mx](mailto:luisdiaz@mda.cinvestav.mx)

Received 11 April 2014; Revised 29 May 2014; Accepted 3 June 2014; Published 30 June 2014

Academic Editor: Ying Zhou

Copyright © 2014 Santos Lorenzo Chi-Ucán et al. This is an open access article distributed under the Creative Commons Attribution License, which permits unrestricted use, distribution, and reproduction in any medium, provided the original work is properly cited.

The inhibitory effect of glycerol on copper corrosion in aerated NaCl (0.5 M) solutions at three pH values (4, 7, and 10) was evaluated. Inhibition efficiency was assessed with conventional electrochemical techniques: open circuit potential, potentiodynamic polarization, and electrochemical impedance analysis. Glycerol reduced the corrosion rate of copper in NaCl solutions. The best inhibition effect ( $\eta \approx 83\%$ ) was produced in alkaline (pH 10) chloride media. This effect can be ascribed to increased viscosity and the presence of copper-glycerol complexes.

## 1. Introduction

As worldwide biodiesel production increases so does production of the byproduct glycerol [1, 2]. For every gallon (3.78 L) of biodiesel produced approximately 0.3 Kg glycerol results. By 2016, the global biodiesel market is expected to be 37 billion gallons [3], consequently resulting in production of 11.1 billion kilograms of glycerol. This looming glycerol glut means that new uses for glycerol need to be found or conversion processes developed to convert it into more valuable chemicals [4]. Finding new uses for glycerol would also help to lower the cost of biodiesel, the main factor behind decreasing production rates. Electrochemical studies have shown glycerol to be useful as an additive in electrochemical baths for coating formation [5–7]. It has also been used in combination with traditional corrosion inhibitors to improve efficiency, but very few studies have focused on glycerol alone as a corrosion inhibitor. Shaker and Abdel-Rahman [8] reported that the corrosion rate of copper decreases at higher glycerol proportions in water-glycerol solutions. The authors

show that the reactions were controlled by diffusion. A key aspect of glycerol is its viscosity and its potential to form a metal-glycerol complex. Viscosity in water-glycerol solutions increases as glycerol concentration increases [9]; therefore, an increase in viscosity can also be expected to decrease mass transfer of ions. A decrease in oxygen concentration can affect the cathodic reaction. In alkaline solutions, glycerol is known to form a Me-glycerol complex (Me = Zn, Fe, and Cu) [10, 11] which may act as a barrier to inhibit corrosion of metals. The present study aim was to evaluate the inhibitory effect of glycerol (Figure 1) alone on corrosion of copper exposed to NaCl solutions at three pH values.

## 2. Experimental Procedure

Deionized water and reagent grade NaCl, HCl, and NaOH were used to prepare NaCl solutions with three different pH values. Glycerol (99.5%) was purchased from Sigma-Aldrich (CAS 56-81-5). Samples were cut from a pure (99.999%)

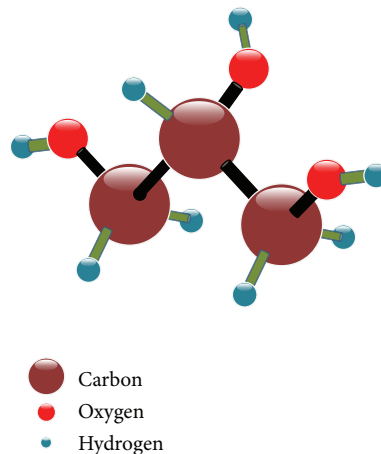


FIGURE 1: Chemical structure of glycerol.

copper rod (Goodfellow, 5.0 mm diameter) and embedded in epoxy resin. A bar cross section was exposed to the NaCl solution. Before each exposure, the sample was abraded with a series of different grade emery papers (up to 1200), rinsed with water and ethanol, and dried with hot air.

All electrochemical measurements were done using a standard three-electrode cell configuration. Electrochemical experiments were run in the following order: open corrosion potential (OCP), electrochemical impedance spectroscopy (EIS), and potentiodynamic scan. All experiments were carried out using a Gamry PCI4 Potentiostat/Galvanostat/ZRA instrument with CMS 100 and 300 software. OCP was measured for 15 min prior to each impedance experiment, which was done at 10 kHz to 20 mHz with a 10 mV peak-to-peak amplitude using ac signals at OCP. The potentiodynamic scan was begun immediately after EIS by scanning from  $-0.25$  to  $0.25$  V versus OCP at a  $1 \text{ mVs}^{-1}$  sweep rate. A standard calomel electrode (SCE) was used as a reference in all electrochemical experiments. Impedance data were examined for causality, stability, and linearity with the Kramer-Kronig relationship using the method described by Boukamp [12] and adapted in the Gamry Echem analyst software.

A scanning electron microscope (SEM, Philips XL30 ESEM) was used to examine any inhibitory effect of glycerol on copper corrosion. Samples examined with SEM were abraded with emery paper (up to 2000), polished with a  $0.25 \mu\text{m}$  diamond solution, rinsed with water and acetone, and dried with hot air. Copper samples were immersed for 120 hours in 0.5 M NaCl (pH 7) solution with and without 2 M glycerol.

### 3. Results and Discussion

The OCP ( $E_{oc}$ ) recorded as a function of time for copper in NaCl (0.5 M) with and without different glycerol concentrations at three pH values shows that overall the presence of glycerol at pH 4 shifted the OCP towards negative potentials (Figures 2(a)–2(c)). The drop in OCP during the first 200 seconds is frequently ascribed to dissolution of a native oxide

previously formed on the copper surface as a result of contact with the atmosphere. A shift to the negative region is also an indication of an active surface. The general behavior of  $E_{oc}$  at pH 7 consisted of a shift to noble potentials and was similar with or without glycerol (Figure 2(b)). At pH 7, increasing glycerol concentration had no effect on OCP. At pH 10, glycerol concentration had a clear effect on  $E_{oc}$ , causing it to move gradually toward the positive potential region and indicating formation of corrosion products or adsorption of species onto the copper surface.

The polarization curves for copper in NaCl (0.5 M) solutions with and without glycerol in different concentrations at three pH values showed how the Cu corrosion potential ( $E_{corr}$ ) changed slightly from negative to positive as a function of pH (Figures 3(a)–3(c)). This trend coincided with the shift observed for OCP at all pH values. The cathodic branch of the polarization curves exhibited behavior typical of a reduction reaction with mass transfer limitations. Reduction of dissolved oxygen with formation of hydroxide [13], or reduction of water molecules, is commonly responsible for the cathodic reaction [14]. Another cathodic reaction in acid is the reduction of oxygen to form water molecules. Reduction of hydrogen is an unlikely cathodic reaction because hydrogen is more active than copper in the electromotive series. In the present results, neither pH nor glycerol concentration affected the shape of the cathodic branch (Figures 3(a)–3(c)), indicating that pH and glycerol did not influence cathodic reaction type. Glycerol concentration did reduce cathodic current very slightly, a reaction more noticeable at pH 10. This reduction may be explained by reduction of mass transfer due to increased viscosity as glycerol concentration increased.

No significant change was observed in the polarization curve anodic current at pH 4, indicating that the anodic reaction was unaffected by addition of glycerol. Glycerol's effect became apparent at pH 7 and even more obvious at pH 10. In all cases, a linear portion of the polarization curve was not easily determined. Extrapolation of both sides of the polarization curves to calculate corrosion parameters is preferable, although occasionally just one side is used, mainly when a Tafel linear region is too small or is difficult to observe

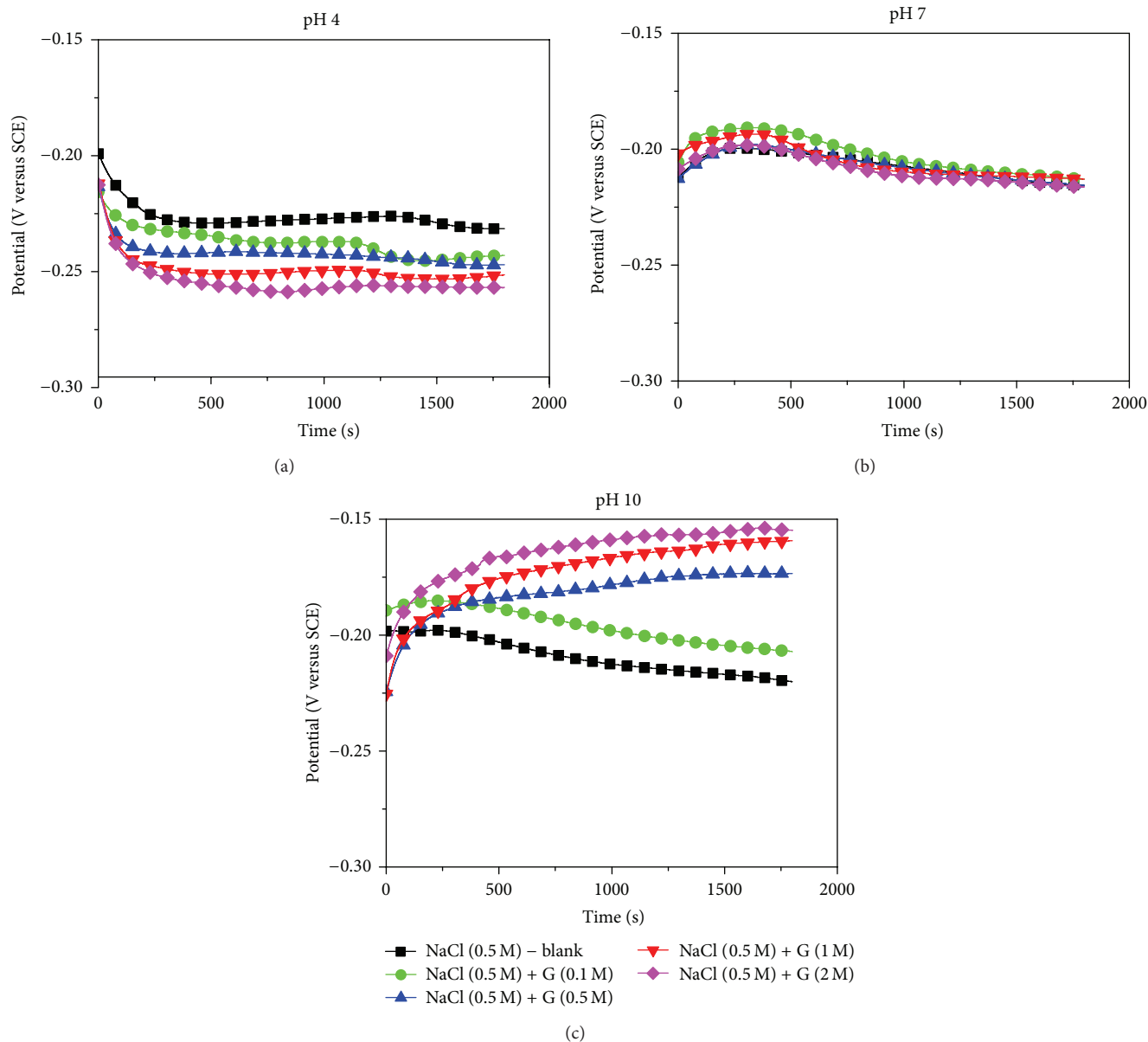


FIGURE 2: Open circuit potential (OCP) for Cu in NaCl (0.5 M) solutions with and without glycerol at three pH values: (a) pH 4, (b) pH 7, and (c) pH 10.

[15]. Therefore, in the present study the cathodic branch was chosen to calculate corrosion parameters using the Tafel extrapolation method [16, 17]. Of note is that at pH 10 the anodic branch exhibited a major reduction in anodic current as glycerol concentration increased. The corrosion parameters calculated from extrapolation of the cathodic branch showed that, at all pH values, corrosion current decreased as glycerol concentration increased (Table 1). The percentage inhibition efficiency was calculated using corrosion current and the following equation [18, 19]:

$$\eta_T (\%) = \frac{i_{\text{corr}}^0 - i_{\text{corr}}}{i_{\text{corr}}} \times 100, \quad (1)$$

where  $i_{\text{corr}}^0$  is the corrosion current measured in a NaCl solution in absence of glycerol and  $i_{\text{corr}}$  is the corrosion current measured in a NaCl solution containing glycerol as inhibitor.

The best inhibition efficiency was attained at pH 10, possibly due to formation of a layer of copper-glycerol complexes near the copper surface, effectively reducing the reaction area and producing an inhibitory effect [11]. The two main copper-glycerol complexes are  $\text{CuGl}(\text{OH})_3^{-2}$  and  $\text{CuGl}_2(\text{OH})_2^{-2}$ , where  $\text{Gl}^-$  is a glycerol anion [20].

In the example shown in Figures 4(a)–4(c), the calculated Kramer-Kronig data fit well in both the Bode and Nyquist diagrams. Residual error was within 0.5%, and goodness-of-fit was  $24.86 \times 10^{-6}$ . However, residual error was generally

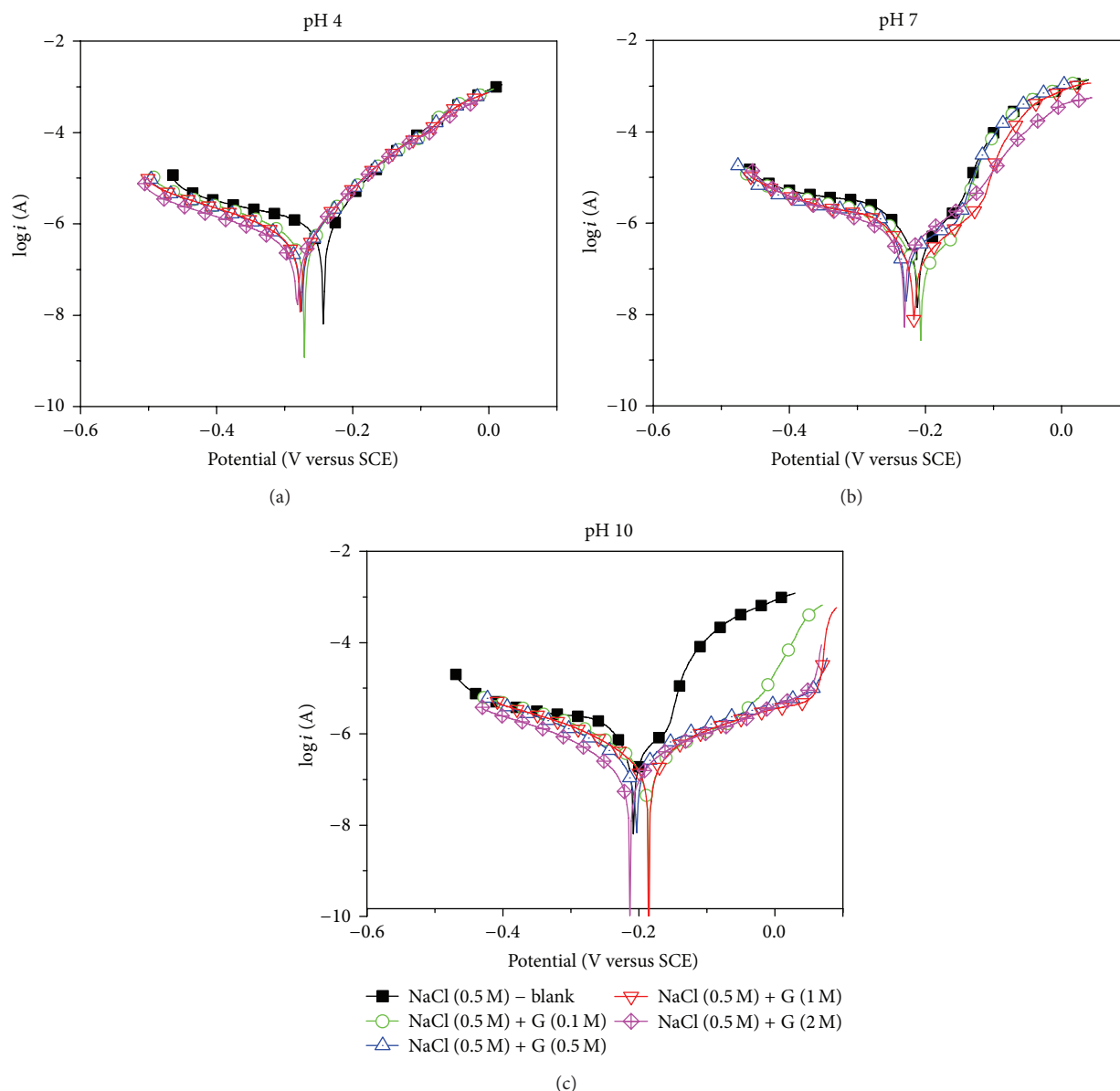


FIGURE 3: Polarization curves for Cu in NaCl (0.5 M) solutions with and without glycerol at three pH values: (a) pH 4, (b) pH 7, and (c) pH 10.

<0.5% for both acid and neutral NaCl solutions. Residual error in alkaline (pH 10) solutions (with and without glycerol) was <1.5%. This increase in residual error was probably caused by formation of copper-glycerol complexes on the copper surface. An increase in error reported in the literature was ascribed to passive film formation [21]; in this study, goodness-of-fit in all solutions was on the order of  $10^{-6}$ .

The Nyquist impedance plots for copper in NaCl (0.5 M) solutions with and without glycerol at three pH values show a depressed semicircle the diameter of which can be obtained by extrapolating toward the low frequency value limit ( $\omega \rightarrow 0$ ), which increases with addition of glycerol (Figures 5(a)–5(c)). Semicircle diameter is correlated to the polarization resistance ( $R_p$ ) value, which is

considered inversely proportional to corrosion rate. Then, independent of the equivalent circuit used to model the EIS data, the glycerol's inhibitory performance can be observed by comparing  $R_p$  from the diameter of the impedance spectra. Various equivalent circuits have been reported for modeling impedance data of copper in NaCl solutions [20–22]. The equivalent circuit shown in Figure 6 was used in analysis of the Nyquist plots because it has been used to study coating for corrosion protection, pitting corrosion [22], or copper corrosion in the presence of inhibitors [23–26]. Fitting the equivalent circuit model produced estimated parameters (Table 2).  $R_s$  represents the solution resistance, while  $CPE_1$  and  $CPE_2$  are constant phase elements that absorb inhomogeneities of the double layer capacitance and

TABLE 1: Electrochemical parameters determined by Tafel extrapolation of the cathodic branch of the potentiodynamic polarization curves for copper in aerated NaCl (0.5 M) with and without glycerol at three pH values.

pH	Glycerol (M)	$E_{\text{corr}}$ (mV versus SCE)	$I_{\text{corr}}$ ( $\mu\text{A}\cdot\text{cm}^{-2}$ )	$b_c$ ( $\text{mV}\cdot\text{d}^{-1}$ )	$b_a$ ( $\text{mV}\cdot\text{d}^{-1}$ )	$\eta_T$ (%)
pH 4	0.0	-243	5.27	-335	61.9	Blank
	0.1	-270	2.97	-201	66.7	43.6
	0.5	-275	2.69	-207	65.1	48.9
	1	-277	2.89	-208	65.9	45.1
	2	-281	1.98	-209	62.6	62.4
pH 7	0.0	-212	11.2	-575	64.1	Blank
	0.1	-206	6.57	-442	72.8	41.3
	0.5	-228	5.88	-313	103.0	47.5
	1	-217	5.19	-384	82.7	53.6
	2	-215	3.03	-215	93.2	72.9
pH 10	0.0	-208	9.7	-750	81.3	Blank
	0.1	-186	3.9	-261	161.3	60
	0.5	-203	2.3	-203	206.4	76.2
	1	-185	2.1	-208	205.0	78.1
	2	-213	1.6	-209	200.0	83.2

TABLE 2: Electrochemical impedance parameters obtained by fitting the Nyquist plots for Cu in aerated NaCl (0.5 M) with and without glycerol at three pH values.

0.5 M NaCl (pH)	GC (M)	$R_s$ ( $\Omega\text{ cm}^2$ )	$R_{p_1}$ ( $\Omega\text{ cm}^2$ )	$CPE_1$ ( $Y_0$ ( $\Omega^{-1}\text{ cm}^{-2}\text{ S}^{n_1}$ ))	$n_1$	$R_{p_2}$ ( $\Omega\cdot\text{cm}^2$ )	$CPE_2$ ( $Y_0$ ( $\Omega^{-1}\text{ cm}^{-2}\text{ S}^{n_2}$ ))	$n_2$	$W$ ( $Y_0$ ( $\Omega^{-1}\text{ cm}^{-2}\text{ S}^{0.5}$ ))	$\eta_z$ (%)
4	0	15.0	106	$3.9 \times 10^{-5}$	0.88	60.6	$8.9 \times 10^{-4}$	0.45	$6.0 \times 10^{-5}$	bk
	0.1	17.7	105	$6.9 \times 10^{-5}$	0.82	81.9	$8.4 \times 10^{-4}$	0.46	$5.3 \times 10^{-5}$	10
	0.5	17.4	175	$7.1 \times 10^{-5}$	0.83	56.1	$7.2 \times 10^{-4}$	0.46	$3.4 \times 10^{-5}$	28
	1	23.2	200	$2.6 \times 10^{-5}$	0.93	15.7	$4.6 \times 10^{-4}$	0.48	$2.8 \times 10^{-4}$	28
	2	16.6	247	$4.2 \times 10^{-5}$	0.88	62.9	$5.6 \times 10^{-4}$	0.48	$1.4 \times 10^{-4}$	46
7	0	16.7	5002	$6.6 \times 10^{-6}$	0.989	$3.27 \times 10^{-3}$	$1.2 \times 10^{-4}$	0.49	$5.1 \times 10^{-2}$	bk
	0.1	15.2	6569	$8.2 \times 10^{-6}$	0.980	$2.0 \times 10^{-3}$	$7.9 \times 10^{-5}$	0.51	$3.1 \times 10^{-2}$	23
	0.5	16.1	7871	$7.4 \times 10^{-6}$	0.980	$4.9 \times 10^{-3}$	$3.9 \times 10^{-5}$	0.55	$5.4 \times 10^{-2}$	36
	1	16.0	13590	$1.0 \times 10^{-5}$	0.934	$2.4 \times 10^{-3}$	$3.3 \times 10^{-5}$	0.47	$1.1 \times 10^{-1}$	63
	2	16.6	14660	$6.2 \times 10^{-6}$	0.980	$3.0 \times 10^{-3}$	$2.5 \times 10^{-5}$	0.20	$1.2 \times 10^{-1}$	65
10	0	15.8	6190	$47.9 \times 10^{-6}$	0.60	$835.5 \times 10^{-3}$	$5.9 \times 10^{-6}$	0.92	$123.9 \times 10^{-3}$	bk
	0.1	15.0	13560	$37.3 \times 10^{-6}$	0.38	$292.5 \times 10^{-3}$	$13.9 \times 10^{-6}$	0.82	$12.8 \times 10^{-3}$	54
	0.5	15.4	22540	$35.8 \times 10^{-6}$	0.32	$15.6 \times 10^{-3}$	$13.6 \times 10^{-6}$	0.91	$1.3 \times 10^{-3}$	72
	1	19.6	27530	$30.6 \times 10^{-6}$	0.30	$2.65 \times 10^{-3}$	$12.96 \times 10^{-6}$	0.90	$0.1 \times 10^{-3}$	77
	2	19.7	36750	$29.0 \times 10^{-6}$	0.32	$2.2 \times 10^{-3}$	$11.6 \times 10^{-6}$	0.90	$0.2 \times 10^{-3}$	83

GC = glycerol concentration.

improve model fit. The characteristic parameters of the constant phase elements are  $Y$  and  $n$ . Estimated  $R_p$  from the semicircle diameter corresponded to the impedance of an anodic reaction occurring in two stages with magnitudes represented as  $R_{p_1} + R_{p_2}$  [27]. Although an exact difference between both resistances has been neither fully understood nor fully described [28], a number of studies use these parameters for modeling corrosion behavior of copper in the presence of an inhibitor. Inhibition efficiency was calculated

using polarization resistance ( $R_{p_1} + R_{p_2}$ ) and the following equation [19, 29]:

$$\eta_z (\%) = \frac{R_p - R_p^0}{R_p} \times 100, \quad (2)$$

where  $R_p^0$  is the polarization resistance measured in a NaCl solution in the absence of glycerol and  $R_p$  is the polarization

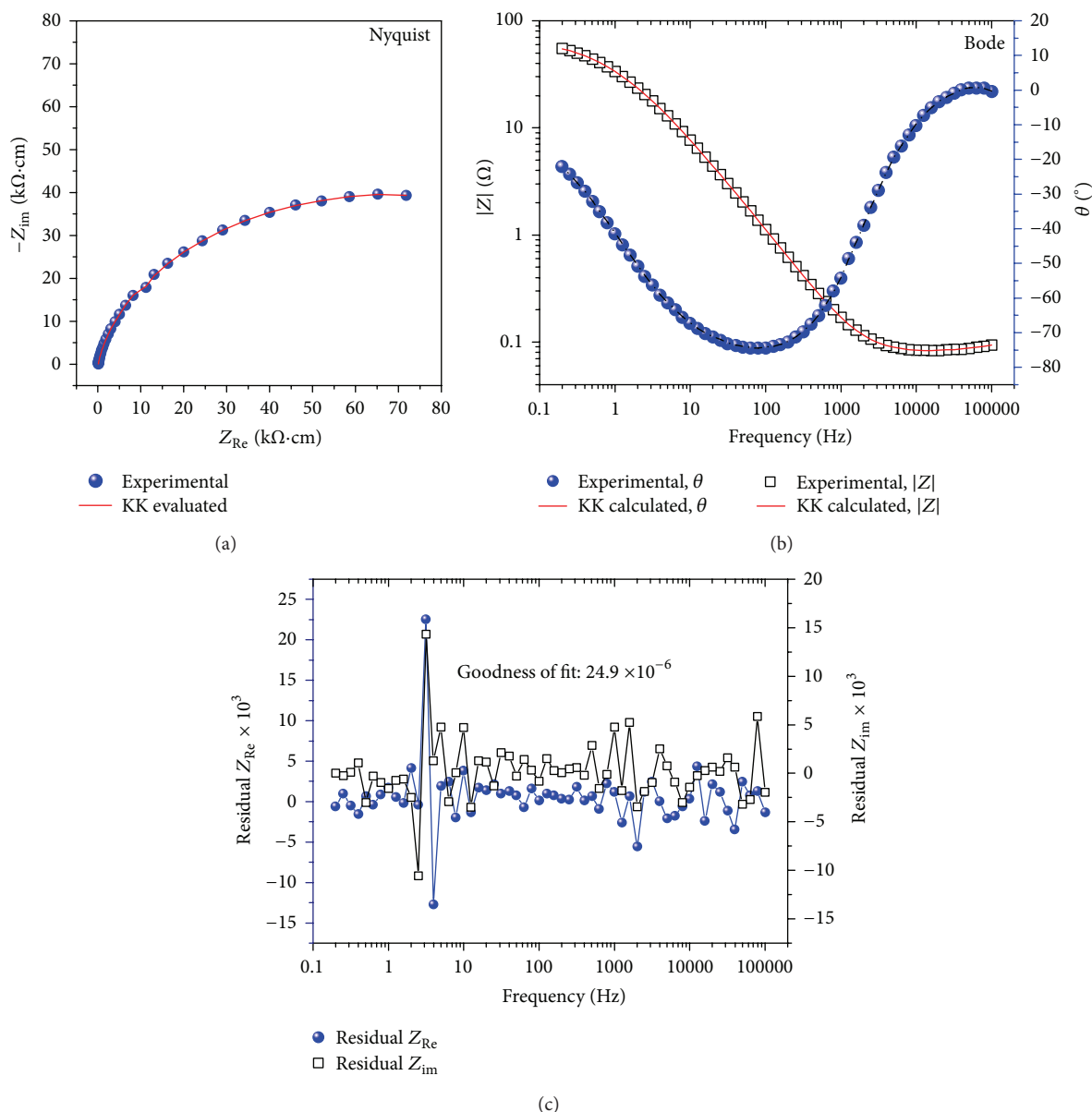


FIGURE 4: Typical Kramer-Kronig analysis results for Cu in NaCl (0.5 M, pH 10) solution containing glycerol (2 M). (a) Nyquist diagram, (b) Bode diagram, and (c) residual error ( $\Delta Z/Z$ ) for the real and imaginary components of the impedance data.

resistance measured in a NaCl solution containing glycerol as inhibitor.

The fit was generated using the equivalent circuit in Figure 6. Typical results of fitting analysis are shown in Bode (Figure 7(a)) and Nyquist (Figures 7(b)-7(c)) plots (symbols represent measured data and solid lines represent fitted curves). In general, there was a good fit between the calculated and experimental impedance data.

The most significant parameters are total polarization resistance ( $R_p = R_{p1} + R_{p2}$ ), the constant phase element, which represents the double layer capacitance ( $CPE_1$ ), and inhibition efficiency. Other parameters also exhibit glycerol's inhibitory effect but are less notable. Polarization resistance increased and  $CPE_{1,2}$  values decreased in response to pH

levels and glycerol concentration (Table 2). The  $R_p$  and CPE behaviors agree with the potentiodynamic polarization measurement results, and the values of both parameters suggest the presence of a film thickening process that could act as a barrier to corrosion and thus be responsible for the inhibitory effect. Presence of a film was more evident at pH 10; indeed, the best agreement between the inhibition efficiency values determined by the Tafel extrapolation of the cathodic current and the impedance data was observed at pH 10. These findings support the assumption of formation of a copper-glycerol complex on the copper surface.

Comparison of the inhibition efficiency obtained by potentiodynamic polarization and the impedance data shows that both results follow the same trend. The very slight

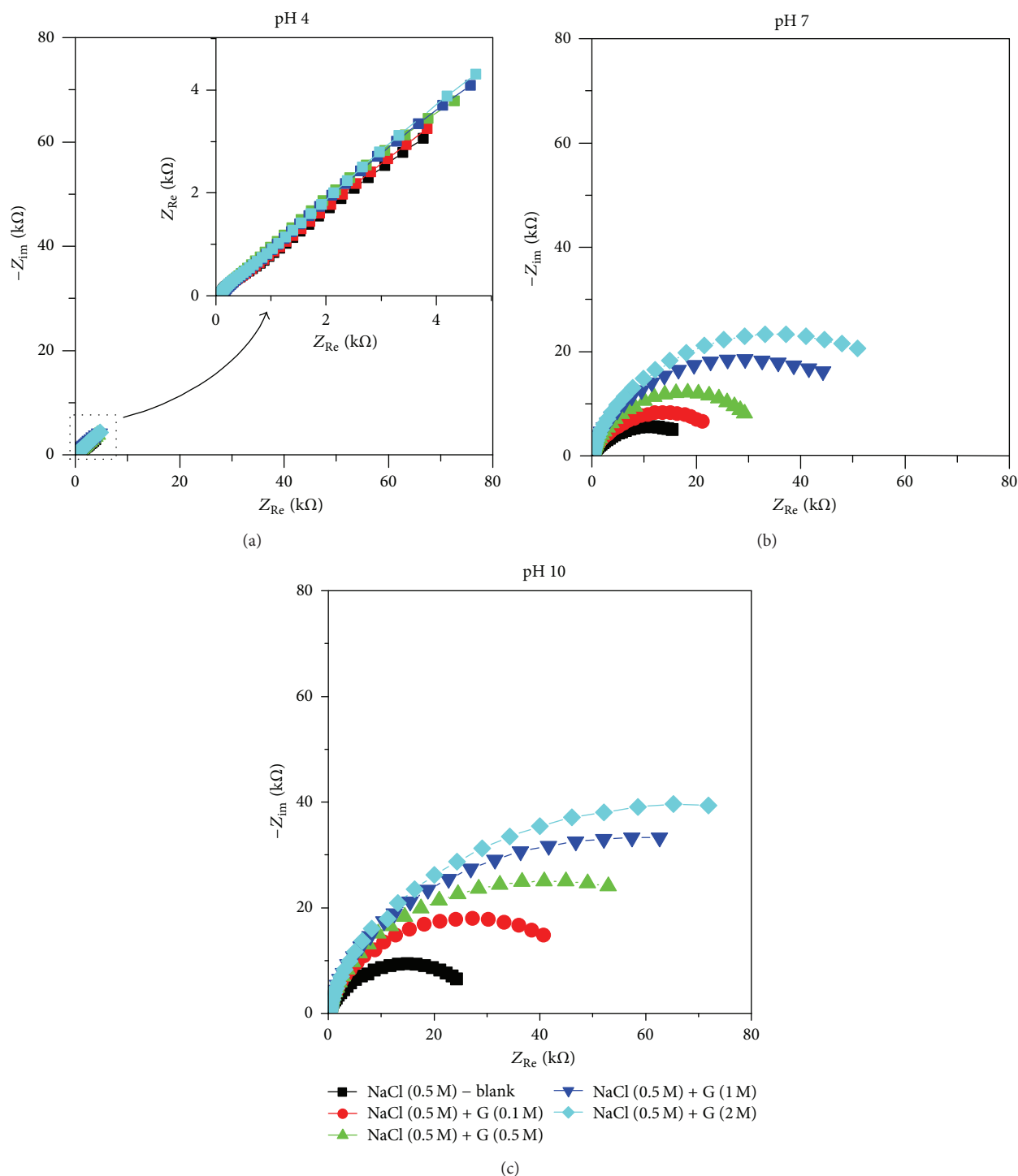


FIGURE 5: Nyquist plot for Cu in NaCl (0.5 M) at four glycerol concentrations as a function of three pH levels: (a) pH 4, (b) pH 7, and (c) pH 10.

difference in values was probably caused by differences in measurement time [30]. The order of the electrochemical measurements was open circuit potential, impedance, potentiodynamic polarization, meaning the layer of adsorbed molecules during each measurement would be slightly different. However, impedance was most effective at demonstrating glycerol's inhibitory effect on copper corrosion.

Micrographs (SEM) of copper samples exposed to 0.5 M NaCl at pH 7 with and without added glycerol showed no visible indications of ion chloride attack on the copper surface in the presence of glycerol (Figure 8(a)). In contrast, the copper exposed to NaCl in the absence of glycerol exhibited evidence of localized corrosion, such as micro- and macropitting across the entire copper surface (Figure 8(b)).

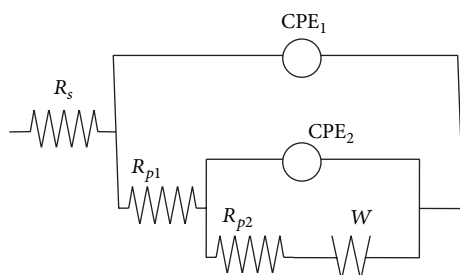


FIGURE 6: Equivalent circuit model used to fit the impedance data from the copper/NaCl (0.5M) interface with and without glycerol.

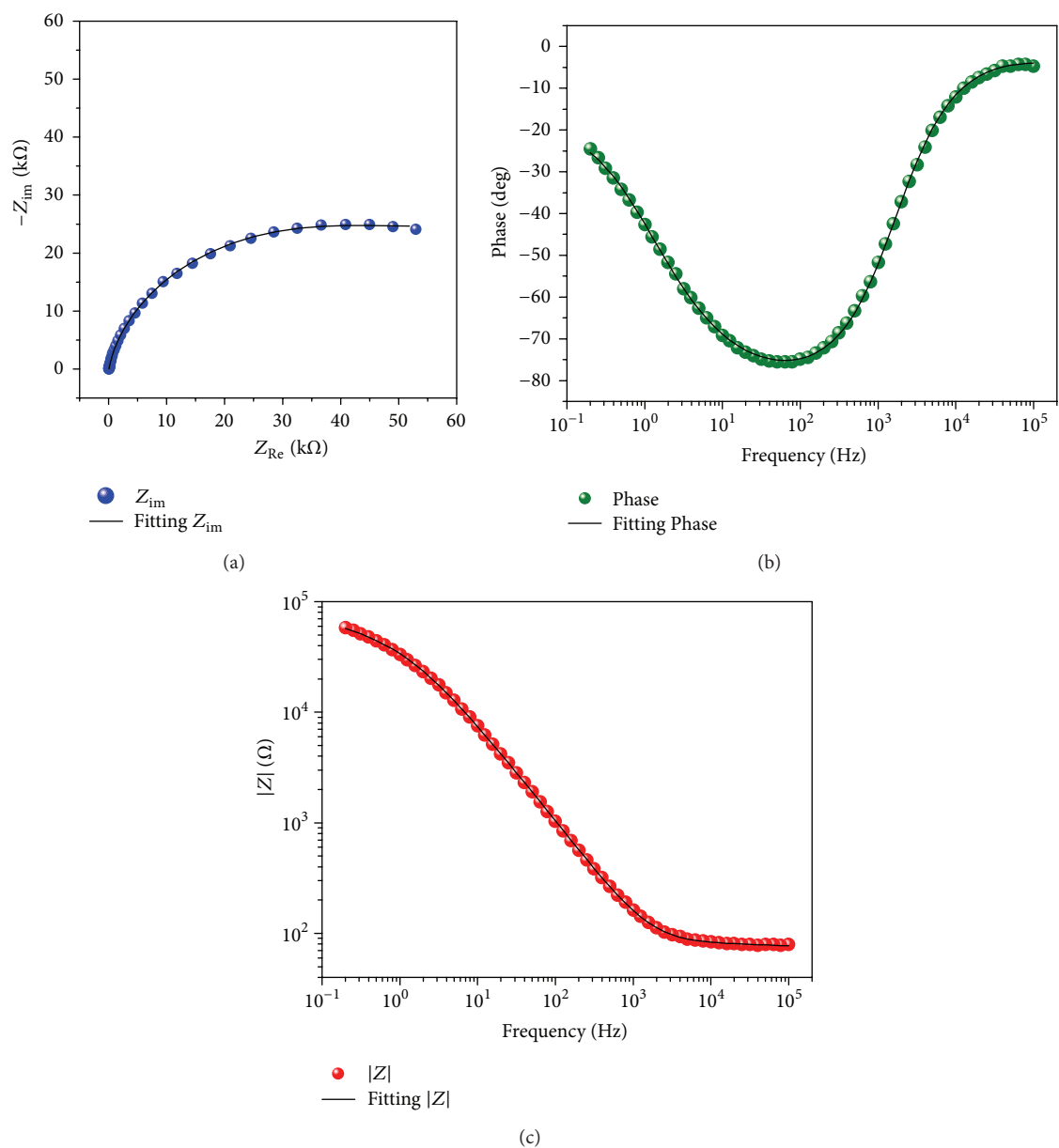


FIGURE 7: Equivalent circuit fit for Cu in 0.5 M NaCl (pH 10) + 0.5 M glycerol; (a) Nyquist, (b) phase, and (c) modulus.

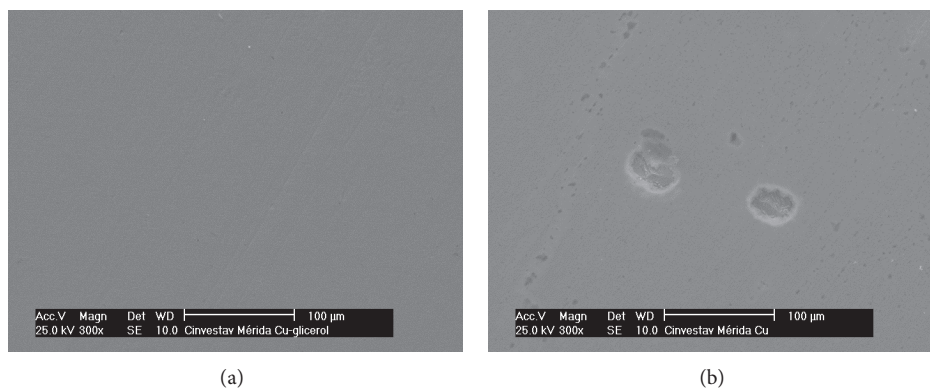


FIGURE 8: SEM micrographs of copper surface after 120 hours of immersion at room temperature (a) in aerated 0.5 M NaCl (pH 10) + 2 M glycerol and (b) in aerated 0.5 M NaCl (pH 10).

These observations agree with the electrochemical results and confirm that glycerol effectively inhibits copper corrosion.

#### 4. Conclusions

Glycerol inhibits corrosion of copper in aerated NaCl (0.5 M) solutions. Inhibition efficiency increases with increasing glycerol concentration and is especially notable at high pH values. Glycerol does not affect the anodic or cathodic reactions, suggesting that increased viscosity reducing mass transport apparently explains the reduction in corrosion rate from acid to neutral solutions. The reduced anodic corrosion rate at pH 10 is probably due to two causes: an increase in solution viscosity and presence of a film on the copper surface, most likely composed of copper-glycerol complexes. SEM images confirm the effectiveness of glycerol as an inhibitor of copper corrosion in NaCl solutions.

#### Conflict of Interests

The authors declare that there is no conflict of interests regarding the publication of this paper.

#### Acknowledgments

The authors thank the Consejo Nacional de Ciencia y Tecnología for financial support via Grants no. 205050, FOMIX-Yucatán 2008-108160, and CONACYT LAB-2009-01 no. 123913. The authors also thank Biol. Ana Ruth Cristobal Ramos for her technical assistance.

#### References

- [1] J. C. Thompson and B. B. He, "Characterization of crude glycerol from biodiesel production from multiple feedstocks," *Applied Engineering in Agriculture*, vol. 22, no. 2, pp. 261–265, 2006.
- [2] M.-Y. Seo, J.-W. Seo, S.-Y. Heo et al., "Elimination of by-product formation during production of 1,3-propanediol in *Klebsiella pneumoniae* by inactivation of glycerol oxidative pathway," *Applied Microbiology and Biotechnology*, vol. 84, no. 3, pp. 527–534, 2009.
- [3] X. Fan, R. Burton, and Y. Zhou, "Glycerol (byproduct of biodiesel production) as a source for fuels and chemicals—mini review," *Open Fuels and Energy Science Journal*, vol. 3, pp. 17–22, 2010.
- [4] F. Yang, M. Hanna, and R. Sun, "Value-added uses for crude glycerol—a byproduct of biodiesel production," *Biotechnology for Biofuels*, vol. 5, p. 13, 2012.
- [5] B. Y. Johnson, J. Edington, and M. J. O'Keefe, "Effect of coating parameters on the microstructure of cerium oxide conversion coatings," *Materials Science and Engineering A*, vol. 361, no. 1-2, pp. 225–231, 2003.
- [6] I. A. Carlos, M. A. Malaquias, M. M. Oizumi, and T. T. Matsuo, "Study of the influence of glycerol on the cathodic process of lead electrodeposition and on its morphology," *Journal of Power Sources*, vol. 92, no. 1-2, pp. 56–64, 2001.
- [7] C. Siva Kumar, V. S. Rao, V. S. Raja, A. K. Sharma, and S. M. Mayanna, "Corrosion behaviour of solar reflector coatings on AA 2024T3—an electrochemical impedance spectroscopy study," *Corrosion Science*, vol. 44, no. 3, pp. 387–393, 2002.
- [8] M. A. Shaker and H. H. Abdel-Rahman, "Corrosion of copper metal in presence of binary mixtures," *The American Journal of Applied Sciences*, vol. 4, no. 8, pp. 554–564, 2007.
- [9] J. B. Segur and H. E. Oberstar, "Viscosity of glycerol and its aqueous solutions," *Industrial & Engineering Chemistry*, vol. 43, no. 9, pp. 2117–2120, 1951.
- [10] E. Radoslovich, M. R. Raupach, P. G. Slade, and R. M. Taylor, "Crystalline cobalt, zinc, manganese, and iron alkoxides of glycerol," *Australian Journal of Chemistry*, vol. 23, no. 10, pp. 1963–1971, 1970.
- [11] H. Koyano, M. Kato, and H. Takenouchi, "Electroless copper plating from copper-glycerin complex solution," *Journal of the Electrochemical Society*, vol. 139, no. 11, pp. 3112–3116, 1992.
- [12] B. A. Boukamp, "Linear Kronig-Kramers transform test for immittance data validation," *Journal of the Electrochemical Society*, vol. 142, no. 6, pp. 1885–1894, 1995.
- [13] K. F. Khaled, "Studies of the corrosion inhibition of copper in sodium chloride solutions using chemical and electrochemical measurements," *Materials Chemistry and Physics*, vol. 125, no. 3, pp. 427–433, 2011.
- [14] E.-S. M. Sherif, "Inhibition of copper corrosion reactions in neutral and acidic chloride solutions by 5-ethyl-1,3,4-thiadiazol-2-amine as a corrosion inhibitor," *International Journal of Electrochemical Science*, vol. 7, no. 4, pp. 2832–2845, 2012.

- [15] E. McCafferty, "Validation of corrosion rates measured by the Tafel extrapolation method," *Corrosion Science*, vol. 47, no. 12, pp. 3202–3215, 2005.
- [16] M. A. Amin and M. M. Ibrahim, "Corrosion and corrosion control of mild steel in concentrated  $H_2SO_4$  solutions by a newly synthesized glycine derivative," *Corrosion Science*, vol. 53, no. 3, pp. 873–885, 2011.
- [17] F. Zucchi and I. H. Omar, "Plant extracts as corrosion inhibitors of mild steel in HCl solutions," *Surface Technology*, vol. 24, no. 4, pp. 391–399, 1985.
- [18] H. Amar, A. Tounsi, A. Makayssi, A. Derja, J. Benzakour, and A. Outzourhit, "Corrosion inhibition of Armco iron by 2-mercaptobenzimidazole in sodium chloride 3% media," *Corrosion Science*, vol. 49, no. 7, pp. 2936–2945, 2007.
- [19] S. Hong, W. Chen, H. Q. Luo, and N. B. Li, "Inhibition effect of 4-amino-antipyrine on the corrosion of copper in 3wt.% NaCl solution," *Corrosion Science*, vol. 57, pp. 270–278, 2012.
- [20] E. Norkus, "Diffusion coefficients of Cu(II) complexes with ligands used in alkaline electroless copper plating solutions," *Journal of Applied Electrochemistry*, vol. 30, no. 10, pp. 1163–1168, 2000.
- [21] A. K. Iversen, "Stainless steels in bipolar plates—surface resistive properties of corrosion resistant steel grades during current loads," *Corrosion Science*, vol. 48, no. 5, pp. 1036–1058, 2006.
- [22] A. Królikowski and J. Kuziak, "Impedance study on calcium nitrite as a penetrating corrosion inhibitor for steel in concrete," *Electrochimica Acta*, vol. 56, no. 23, pp. 7845–7853, 2011.
- [23] E. M. Sherif and S. Park, "Inhibition of copper corrosion in 3.0% NaCl solution by N-phenyl-1,4-phenylenediamine," *Journal of the Electrochemical Society*, vol. 152, no. 10, pp. B428–B433, 2005.
- [24] E. M. Sherif and S. Park, "2-Amino-5-ethyl-1,3,4-thiadiazole as a corrosion inhibitor for copper in 3.0% NaCl solutions," *Corrosion Science*, vol. 48, no. 12, pp. 4065–4079, 2006.
- [25] E.-S. M. Sherif, "Effects of 2-amino-5-(ethylthio)-1,3,4-thiadiazole on copper corrosion as a corrosion inhibitor in 3% NaCl solutions," *Applied Surface Science*, vol. 252, no. 24, pp. 8615–8623, 2006.
- [26] K. F. Khaled, "Guanidine derivative as a new corrosion inhibitor for copper in 3% NaCl solution," *Materials Chemistry and Physics*, vol. 112, no. 1, pp. 104–111, 2008.
- [27] P. R. Seré, J. D. Culcasi, C. I. Elsner, and A. R. Di Sarli, "Relationship between texture and corrosion resistance in hot-dip galvanized steel sheets," *Surface and Coatings Technology*, vol. 122, no. 2-3, pp. 143–149, 1999.
- [28] E. M. Sherif, R. M. Erasmus, and J. D. Comins, "Inhibition of copper corrosion in acidic chloride pickling solutions by 5-(3-aminophenyl)-tetrazole as a corrosion inhibitor," *Corrosion Science*, vol. 50, no. 12, pp. 3439–3445, 2008.
- [29] V. V. Torres, R. S. Amado, C. F. de Sá et al., "Inhibitory action of aqueous coffee ground extracts on the corrosion of carbon steel in HCl solution," *Corrosion Science*, vol. 53, no. 7, pp. 2385–2392, 2011.
- [30] B. El Mehdi, B. Mernari, M. Traisnel, F. Bentiss, and M. Lagrenée, "Synthesis and comparative study of the inhibitive effect of some new triazole derivatives towards corrosion of mild steel in hydrochloric acid solution," *Materials Chemistry and Physics*, vol. 77, no. 2, pp. 489–496, 2003.

## Research Article

# Phthaloylchitosan-Based Gel Polymer Electrolytes for Efficient Dye-Sensitized Solar Cells

S. N. F. Yusuf,<sup>1</sup> M. F. Aziz,<sup>1</sup> H. C. Hassan,<sup>1</sup> T. M. W. J. Bandara,<sup>2,3</sup>  
B.-E. Mellander,<sup>2</sup> M. A. Careem,<sup>1</sup> and A. K. Arof<sup>1</sup>

<sup>1</sup> Department of Physics, Centre for Ionics University of Malaya, Faculty of Science, University of Malaya, 50603 Kuala Lumpur, Malaysia

<sup>2</sup> Department of Applied Physics, Chalmers University of Technology, 412 96 Gothenburg, Sweden

<sup>3</sup> Department of Physical Sciences, Rajarata University of Sri Lanka, 50300 Mihintale, Sri Lanka

Correspondence should be addressed to S. N. F. Yusuf; farhanayusuf@gmail.com

Received 24 April 2014; Accepted 6 June 2014; Published 23 June 2014

Academic Editor: Yu Xin Zhang

Copyright © 2014 S. N. F. Yusuf et al. This is an open access article distributed under the Creative Commons Attribution License, which permits unrestricted use, distribution, and reproduction in any medium, provided the original work is properly cited.

Phthaloylchitosan-based gel polymer electrolytes were prepared with tetrapropylammonium iodide, Pr<sub>4</sub>NI, as the salt and optimized for conductivity. The electrolyte with the composition of 15.7 wt.% phthaloylchitosan, 31.7 wt.% ethylene carbonate (EC), 3.17 wt.% propylene carbonate (PC), 19.0 wt.% of Pr<sub>4</sub>NI, and 1.9 wt.% iodine exhibits the highest room temperature ionic conductivity of  $5.27 \times 10^{-3} \text{ S cm}^{-1}$ . The dye-sensitized solar cell (DSSC) fabricated with this electrolyte exhibits an efficiency of 3.5% with  $J_{\text{SC}}$  of  $7.38 \text{ mA cm}^{-2}$ ,  $V_{\text{OC}}$  of 0.72 V, and fill factor of 0.66. When various amounts of lithium iodide (LiI) were added to the optimized gel electrolyte, the overall conductivity is observed to decrease. However, the efficiency of the DSSC increases to a maximum value of 3.71% when salt ratio of Pr<sub>4</sub>NI : LiI is 2 : 1. This cell has  $J_{\text{SC}}$ ,  $V_{\text{OC}}$  and fill factor of  $7.25 \text{ mA cm}^{-2}$ , 0.77 V and 0.67, respectively.

## 1. Introduction

A solar cell is a device that directly converts light energy into electrical energy through the photovoltaic process. The solar cells currently produced are generally divided into several types according to their material composition and operating mechanism, such as photoelectrochemical solar cells and thin film junction devices. Photoelectrochemical solar cells have become attractive devices since Gratzel and O' Regan first reported the prototype dye-sensitized solar cell (DSSC) using wide band gap TiO<sub>2</sub> semiconductor in 1991 [1]. The DSSC has gained a great deal of attention due to its relatively high energy conversion efficiency and low production cost [2]. DSSCs are also semitransparent and can be produced in various colours, making it possible for them to be applied in building integrated photovoltaic (BIPV) applications [3]. A typical DSSC consists of a nanocrystalline semiconductor coated photoactive electrode, an iodide based liquid electrolyte, and a counter electrode (normally platinum or

carbon-based coating on a conducting glass substrate). When the DSSC is irradiated with light, photoexcited electrons of the dye are transferred to the conduction band of TiO<sub>2</sub>, and the oxidized dye cations are regenerated by the I<sup>-</sup> in the electrolyte. The I<sub>3</sub><sup>-</sup> formed in this process is reduced at the counter electrode, thus completing the cycle and generating the photocurrent [4]. I<sup>-</sup>/I<sub>3</sub><sup>-</sup> redox mediator shuttles between the two electrodes.

In the determination of high efficiency and long time stability of the DSSCs, electrolytes play an important role [5]. A gel polymer electrolyte has been used in this work in order to replace liquid electrolytes that may cause some practical limitations of physical and chemical stability at higher temperatures [5, 6]. The conductivity of gel type electrolytes is usually high compared to that of solid polymer electrolytes and it can be improved to be almost comparable to that of the conventional electrolyte solutions in case of high solution fraction [7]. Since the solvent is entrapped in the polymer network structure in gel electrolytes, leakage problems can

be avoided. The solvents entrapped in the polymer matrix not only improve the conductivity of electrolytes but also improve the contacts between interfaces of the electrolyte and the dye covered nanocrystalline TiO<sub>2</sub> surface and electrolyte-counter electrode leading to improved efficiency of DSSCs [5, 7].

Many host polymers have been used to prepare electrolytes for use in DSSCs [8–11]. In this work, chitosan has been chosen as the host polymer for the electrolyte since this polysaccharide is nontoxic and biocompatible. Chitosan is also being explored intensively for applications in pharmaceutical, cosmetics, biomedical, biotechnological, agricultural, food, and nonfood industries [12–15]. Chitosan is the deacetylated form of the chitin polysaccharide and contains the  $\beta$ -(1-4) linked 2-amino-2-deoxy-D-glucopyranose repeating structure [16, 17]. Chitosan is generally insoluble under normal conditions due to the presence of  $\beta$ -1, 4'-glycosidic linkages that gives chitosan its structural rigidity and crystalline structure besides promoting the formation of intramolecular hydrogen bonds. This limits its usage and further investigation for the biological activities and development has been restricted [18]. Since chitosan and its derivatives are favourable for many applications, chitosan should be effectively modified to fully explore its ability. The chemical modification of chitosan can provide functional groups as primary amine as well as secondary hydroxyl groups in its monomers [12].

In order to improve the solubility of chitosan in general organic solvents, *N*-phthaloylation is found to be one of the convenient methods. Kurita et al. have applied *N*-phthaloylchitosan as an organosoluble key intermediate for a series of controlled modification reactions [19–21]. Chemical introduction of some functional groups of hydrophobic nature will result in disruption of the formation of specific hydrogen bond interactions between its amino and hydroxyl groups with the solvents [22]. *N*-Phthaloylchitosan exhibits high affinity for organic solvents, namely, dimethylsulfoxide (DMSO), dimethylacetamide (DMAc), dimethylformamide (DMF), and pyridine [23]. In this work, we aim at developing a best performing DSSC using a *N*-phthaloylchitosan-based gel polymer electrolyte. Therefore, gel polymer electrolytes were prepared with various amounts of tetrapropylammonium iodide, Pr<sub>4</sub>NI, as the salt and investigated in order to find the best composition for high conductivity. Pr<sub>4</sub>NI has been chosen as the primary iodide salt for the electrolyte as it has been shown to produce good efficiencies in DSSCs by enhancing the iodide conductivity in the electrolyte [24, 25]. The performances of the electrolytes were tested in DSSCs based on mesoporous TiO<sub>2</sub> sensitized with N719 dye as the sensitizer. The performance of the best DSSC was improved further with the addition of a second iodide salt, LiI.

## 2. Experimental

**2.1. Phthaloylation of Chitosan.** The synthesis procedure used in this work is similar to that reported by Nishimura et al. [22]. Chitosan (Aldrich) and phthalic anhydride (Aldrich) were refluxed between 100°C and 120°C under nitrogen atmosphere for 6 h in dimethylformamide (DMF) purchased

TABLE 1: Pr<sub>4</sub>NI content of different electrolyte samples.

Samples	PhCh/g	Pr <sub>4</sub> NI/g
1	0.1	0.02
2	0.1	0.04
3	0.1	0.06
4	0.1	0.08
5	0.1	0.10
6	0.1	0.12
7	0.1	0.14
8	0.1	0.16

TABLE 2: Composition of the salts in binary salt electrolytes.

Samples	Pr <sub>4</sub> NI/g	LiI/g
A	0.12	0.00
B	0.10	0.02
C	0.08	0.04
D	0.06	0.06
E	0.04	0.08

from R & M Chemicals. The temperature was then reduced to 60°C, and the mixture was left overnight. The product of reaction between chitosan and phthalic anhydride dissolved in DMF is a yellowish solution. This solution was poured into ice water to precipitate the product, *N*-phthaloylchitosan. The precipitate was collected and washed with distilled ethanol (from J. T. Baker) in a soxhlet extractor for 8 h. The final product was dried in vacuum at 60°C for about 6 h.

**2.2. Preparation of Gel Polymer Electrolyte (GPE).** Fixed amounts of ethylene carbonate (0.2 g) and propylene carbonate (0.2 g) from Aldrich were stirred well in a closed glass container with the relevant weights of Pr<sub>4</sub>NI (see Table 1). 0.1 g of phthaloylchitosan was then added to each salt solution. The mixture was heated to 150°C and stirred until the mixture becomes a homogeneous gel. Then heater was stopped and the solution was allowed to cool down to room temperature. Iodine (10 wt.% of salt) was then added to the gel polymer electrolyte and stirred until the solution becomes homogeneous. The impedance of the resulting gel polymer electrolyte was then measured.

To the most conducting gel polymer electrolyte (Sample 6), lithium iodide, LiI, was added in such a way that the total weight of the iodide salts remains the same (0.12 g) in all the electrolytes. The salt compositions used in the electrolytes are shown in Table 2.

**2.3. Device Assembly.** Fluorine tin oxide (FTO) glasses (from Solaronix SA), which were used as the substrates, were rinsed with distilled water and ethanol before use. For preparing TiO<sub>2</sub> layer on the substrate, TiO<sub>2</sub> colloidal suspension was prepared by grinding 0.5 g powder of TiO<sub>2</sub> with 2 mL of HNO<sub>3</sub>, 0.1 g of carbowax, and few drops of surfactant octylphenol ethylene oxide condensate (Triton X-100) in an agate mortar. The TiO<sub>2</sub> colloidal suspension was spread on

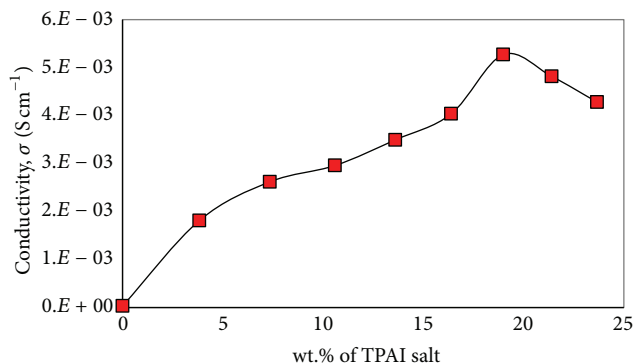


FIGURE 1: Effect of  $\text{Pr}_4\text{NI}$  concentration on the conductivity at  $25^\circ\text{C}$ .

the clean (FTO) glass by applying the doctor blade technique. The  $\text{TiO}_2$  electrode was sintered in a furnace at  $450^\circ\text{C}$  for 45 minutes. The  $\text{TiO}_2$  electrode was cooled down to about  $60^\circ\text{C}$  and then dipped in a warm ethanol solution of Ruthenium dye (N719) for 24 hours for dye adsorption.

The photovoltaic performance of DSSCs was investigated using a LOT-Oriel solar simulator ( $1.5\text{ AM}$ ,  $1000\text{ W m}^{-2}$ ) and a computer controlled eDAQ Potentiostat. From the  $J$ - $V$  (current density-cell potential) characteristic curves, the short-circuit current ( $J_{\text{SC}}$ ) and open circuit voltage ( $V_{\text{OC}}$ ) were obtained and the fill factor (FF) and energy conversion efficiency ( $\eta$ ) were calculated from the following equations:

$$\text{FF} = \frac{J_{\text{max}} \times V_{\text{max}}}{J_{\text{SC}} \times V_{\text{OC}}}, \quad (1)$$

$$\eta = \frac{P_{\text{out}}}{P_{\text{in}}} \times 100 = \frac{J_{\text{SC}} \times V_{\text{OC}} \times \text{FF}}{P_{\text{in}}} \times 100,$$

where  $J_{\text{max}}$  is the current density at maximum power output,  $V_{\text{max}}$  is the voltage at maximum power output, and  $P_{\text{in}}$  is the power of the incident light.

### 3. Results and Discussion

Figure 1 shows the variation of conductivity at room temperature for the phthaloylchitosan-based gel polymer electrolytes with various  $\text{Pr}_4\text{NI}$  salt compositions. The conductivity of the electrolyte with the lowest  $\text{Pr}_4\text{NI}$  concentration, 3.8 wt.%, is  $1.81 \times 10^{-3}\text{ S cm}^{-1}$  at  $25^\circ\text{C}$ . With increasing amount of  $\text{Pr}_4\text{NI}$  salt up to 19.0 wt.% in gel polymer host, the ionic conductivity increases until a maximum conductivity of  $5.27 \times 10^{-3}\text{ S cm}^{-1}$  at  $25^\circ\text{C}$ . On increasing the  $\text{Pr}_4\text{NI}$  concentration further, the conductivity is observed to decrease.

This behavior of the conductivity can be attributed to the change in the amount of mobile ions in the gel electrolytes [26]. The increase in number of mobile ions due to the increased salt dissociation with the increasing amount of salt in the electrolyte can result in the conductivity increase. The  $\text{Pr}_4\text{NI}$  salt molecules are expected to dissociate into  $\text{Pr}_4\text{N}^+$  cations and  $\text{I}^-$  anions in the GPE. As the  $\text{Pr}_4\text{N}^+$  cations are bulky they are expected to have sluggish movement or get trapped in the polymer matrix and therefore ionic

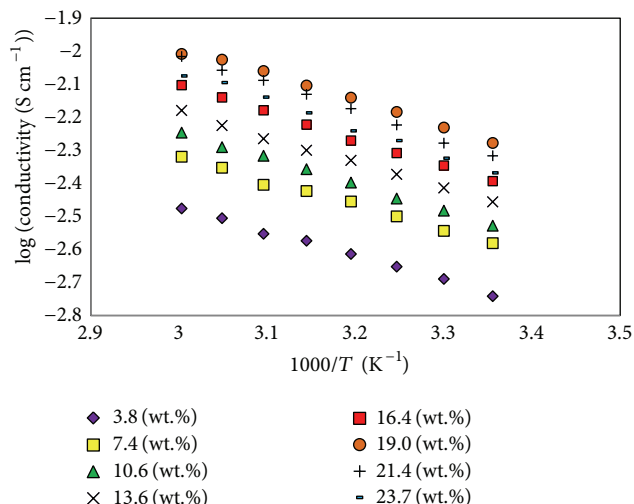


FIGURE 2: Temperature dependence of conductivity for phthaloylchitosan doped with different wt.% of  $\text{Pr}_4\text{NI}$  salt.

conductivity mainly comes from the  $\text{I}^-$  ions. Initially as the salt concentration increases, since dissociated ions are less, both  $\text{I}^-$  ions and  $\text{Pr}_4\text{N}^+$  ions can be expected to be mobile and contribute to ionic conduction and the conductivity rises sharply. On further increase of salt content, the number of both  $\text{Pr}_4\text{N}^+$  ions and  $\text{I}^-$  ions increases but the mobility of  $\text{Pr}_4\text{N}^+$  ions is hindered due to entanglement in the polymer matrix and  $\text{I}^-$  ions may be main contributor to the conductivity. Therefore, the conductivity increases only slightly with further increase in salt content up to about 16.4 wt.% of salt. Beyond this concentration of the salt the conductivity again rises sharply due to the increase in iodide ions coming from increased salt dissociation and increased added iodine amount, which is 10 wt.% of iodide salt, giving the maximum conductivity at 19 wt.% of salt content. At 21.4 wt.% and 23.7 wt.% of  $\text{Pr}_4\text{NI}$ , ion association may have taken place in the system as the conductivity begins to decrease. In addition, conductivity can drop due to blocking effects imposed by the undissociated salt or due to higher ion aggregates present in the electrolyte at high salt concentrations.

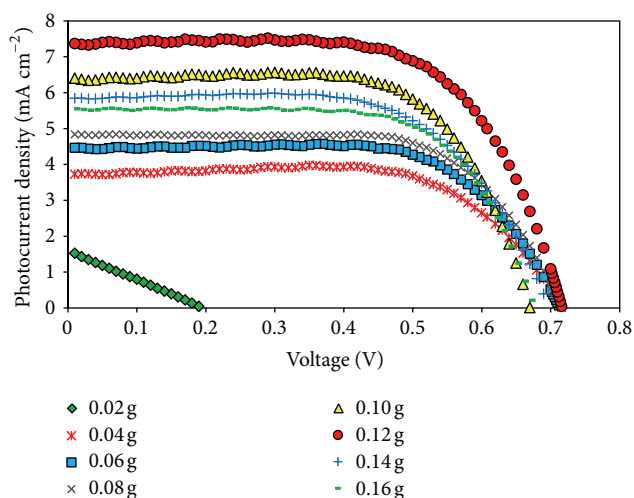
The conductivity-temperature relationship of phthaloylchitosan-EC-PC electrolytes with different amounts of  $\text{Pr}_4\text{NI}$  is exhibited in a plot of  $\log \sigma$  versus  $1000/T$  shown in Figure 2. It is observed that the conductivity of each electrolyte increases as the temperature is increased from  $25^\circ\text{C}$  to  $60^\circ\text{C}$ . The variations of ionic conductivity with temperature for the polymer electrolytes obey Arrhenius law, suggesting that the conductivity is thermally activated. The Arrhenius model employed in describing the temperature dependence of conductivity is as follows:

$$\log \sigma = \log \sigma_o - \frac{0.4342E_a}{kT}, \quad (2)$$

where  $\sigma_o$  is the preexponential factor,  $E_a$  is the activation energy of ionic conduction,  $k$  is the Boltzmann constant, and  $T$  is temperature in Kelvin.

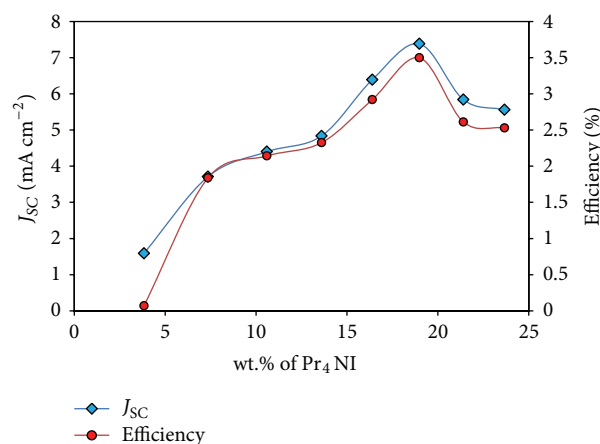
TABLE 3: Performance parameters of DSSCs with phthaloylchitosan-based electrolytes containing various salt contents.

wt.% of Pr <sub>4</sub> NI	V <sub>max</sub> /V	J <sub>max</sub> /mA cm <sup>-2</sup>	V <sub>oc</sub> /V	J <sub>sc</sub> /mA cm <sup>-2</sup>	FF	η/%
3.8	0.10	0.78	0.19	1.59	0.26	0.07
7.4	0.51	3.54	0.68	3.24	0.69	1.79
10.6	0.53	4.04	0.71	4.40	0.69	2.14
13.6	0.52	4.44	0.71	4.84	0.67	2.32
16.4	0.48	6.08	0.67	6.39	0.68	2.92
19.0	0.52	6.70	0.72	7.38	0.66	3.50
21.4	0.50	5.20	0.70	5.84	0.64	2.61
23.7	0.51	4.94	0.67	5.56	0.68	2.53

FIGURE 3: Photocurrent density variation with cell potential for dye-sensitized solar cells having phthaloylchitosan-based electrolyte with various Pr<sub>4</sub>NI/I<sub>2</sub> contents.

The electrolytes with various amounts of Pr<sub>4</sub>NI were employed in DSSCs sensitized with N719 dye and the photocurrent density versus cell potential ( $J$ - $V$ ) characteristics were obtained under light irradiation of  $100 \text{ mW cm}^{-2}$  at room temperature. The  $J$ - $V$  curves for the DSSCs are shown in Figure 3. Very poor solar cell performance is shown by the DSSC with the electrolyte containing 3.8 wt.% of Pr<sub>4</sub>NI. This can be due to the poor conductivity and the low density of redox mediators in the electrolyte. However with increasing amount of iodide salt together with increasing iodine content in the electrolyte, better solar cell performance is observed as can be seen from the  $J$ - $V$  characteristic curves. The performance parameters for the DSSCs obtained from the  $J$ - $V$  curves shown in Figure 3 are given in Table 3. The cell with electrolyte having 19.0 wt.% of Pr<sub>4</sub>NI shows both the highest values of  $V_{OC} = 0.72 \text{ V}$  and  $J_{SC} = 7.38 \text{ mA cm}^{-2}$ . Electrolyte with the lowest salt content of 3.8 wt.% shows the lowest values of  $V_{OC}$  and  $J_{SC}$  of about  $0.19 \text{ V}$  and  $1.59 \text{ mA cm}^{-2}$ , respectively.

In addition to  $V_{OC}$  and  $J_{SC}$ , the performance of the DSSCs is reflected by the parameters of fill factor (FF) and energy conversion efficiency ( $\eta$ ). The calculated values of FF and  $\eta$  are summarized in Table 3. The DSSC fabricated using

FIGURE 4: Effects of weight percentage of Pr<sub>4</sub>NI salt in the electrolyte on efficiency and short-circuit photocurrent density of DSSCs.

the electrolyte containing 19.0 wt.% of Pr<sub>4</sub>NI with  $\eta$  of 3.50 exhibits fill factor of 0.66. The highest fill factor was obtained for the DSSC that had the electrolyte containing 19.0 wt.% of Pr<sub>4</sub>NI. This can be attributed to the combined effect of series resistance and shunt resistances as reported in [26]. In a DSSC, low shunt resistance provides a substitute path for light generated current and hence lowers the power output which in turn decreases the fill factor. As series resistance in the DSSC is usually lower when compared to conventional solar cells, improved fill factor is expected.

The relationships between Pr<sub>4</sub>NI content in the electrolyte with efficiency and short-circuit current density are shown in Figure 4. Efficiency of the cells is observed to increase with the Pr<sub>4</sub>NI content until 19.0 wt.% of Pr<sub>4</sub>NI and further increase of salt decreases the efficiency. Thus the cell with 19.0 wt.% of Pr<sub>4</sub>NI shows the highest efficiency value of 3.5%, the highest value obtained with the single iodide salt polymer electrolyte system used in this work. The efficiency variation shown in Figure 4 correlates with the conductivity variation shown in Figure 1. Figure 4 also shows that the short-circuit current density of DSSCs increases with increasing concentration of the salt up to 19.0 wt.% of Pr<sub>4</sub>NI. It can be seen that the variation of efficiency of the cells is parallel with variation of short-circuit current density as well as the conductivity of the electrolyte with the salt content. The short-circuit current of the cell is governed by the ionic

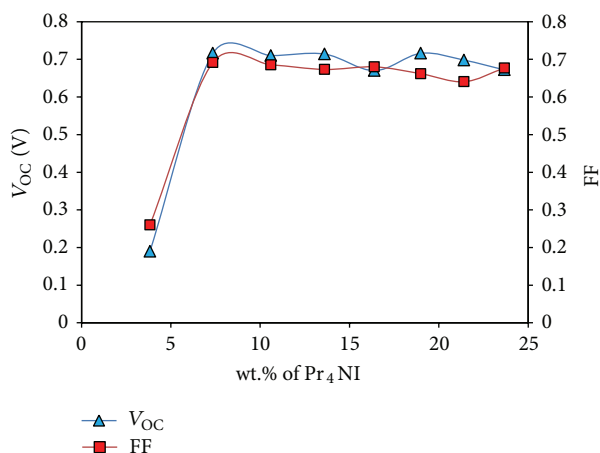


FIGURE 5: Effects of weight percentage of Pr<sub>4</sub>NI salt in the electrolyte on open circuit voltage and fill factor of DSSCs.

conductivity dominated by the transport of I<sup>-</sup>/I<sub>3</sub><sup>-</sup> redox couple as exhibited by a comparable PAN based electrolyte system using the same salt and plasticizers [27]. As explained earlier, the iodide ions are the main contributors to the ionic conductivity in the GPE used. Since iodides (I<sup>-</sup>/I<sub>3</sub><sup>-</sup>) play a major role in determining the current in DSSCs, the J<sub>SC</sub> should follow the variation of free iodide ions content in the electrolyte and therefore must increase sharply as the salt content increases as more and more iodide ions are expected to be produced due to salt dissociation. According to the results in Figure 1, the number of iodide ions increases up to 19 wt.% of salt and the number decreases beyond this salt content due to possible ion association taking place. Hence the J<sub>SC</sub> is expected to follow this trend. But in Figure 4, as the salt content increases, J<sub>SC</sub> increases sharply at the beginning up to 7.4 wt.% of salt and beyond 13.6 wt.% up to 19 wt.% of salt content. The increase becomes less steep for the salt contents between 7.4 and 13.6 wt.%. It should be noted that the current in the DSSC is not only controlled by the iodide conduction in the electrolyte but also controlled by the electron injection rate from the dye molecules to TiO<sub>2</sub> and the recombination rate of injected electrons with the iodide ions in the electrolyte. The injection rate is also affected by the cations as they can stick to the TiO<sub>2</sub> surface and shift the Fermi level. The combined effect of all these processes results in the observed variation of J<sub>SC</sub> with salt content. Further experiments and analysis are needed to explain the exact correlation between ionic conductivity and the J<sub>SC</sub>.

To our best knowledge, the J<sub>SC</sub> and efficiency values obtained in this study for DSSC containing 19.0 wt.% of Pr<sub>4</sub>NI are the highest values reported so far for a quasisolid state DSSC having chitosan host polymer based electrolyte system with a single iodide salt.

The dependence of V<sub>OC</sub> and FF on the weight percentage of Pr<sub>4</sub>NI salt in the electrolyte is shown in Figure 5. The V<sub>OC</sub> and FF show similar variations but different to that shown by J<sub>SC</sub> in Figure 4. These results show that the efficiency variation of the DSSCs is determined mainly by the changes in J<sub>SC</sub>.

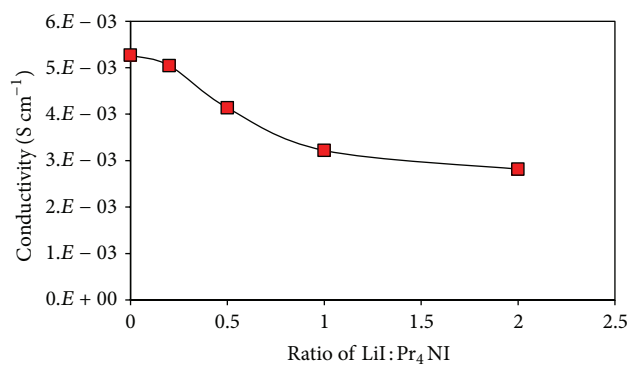


FIGURE 6: Effect of various LiI : Pr<sub>4</sub>NI compositions on the conductivity.

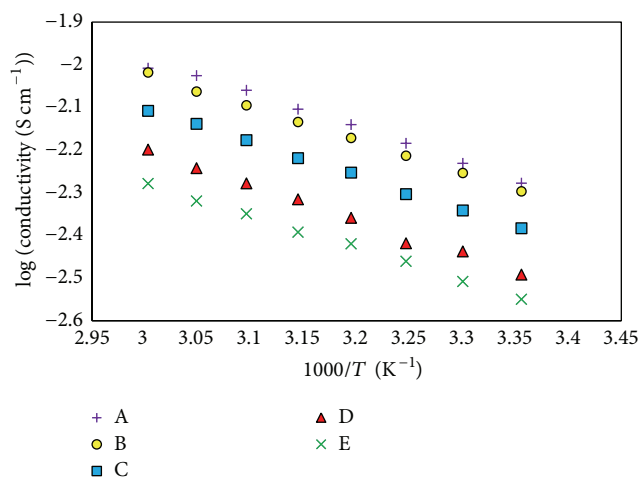
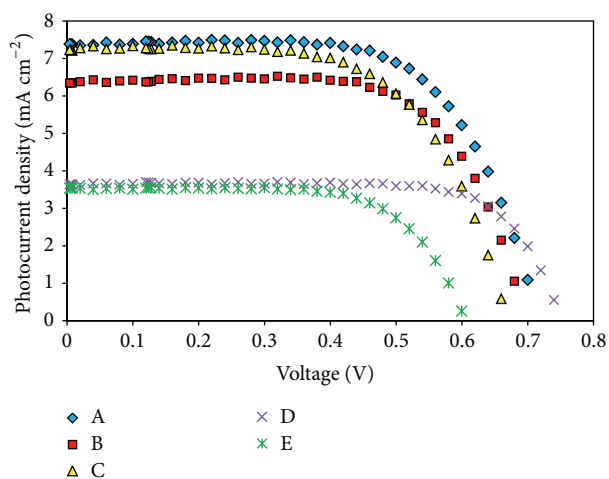


FIGURE 7: Temperature dependence of conductivity for phthaloylchitosan-based electrolyte containing different ratio of LiI : Pr<sub>4</sub>NI binary salt.

It has been reported that the addition of small cations such as Li<sup>+</sup>, K<sup>+</sup>, and Mg<sup>2+</sup> to the gel polymer electrolytes so as to have two mixed cations in the electrolyte improves the solar cell performance [28–30]. In particular these small cations adsorbed onto the TiO<sub>2</sub> surface alter the flat band potentials so as to improve the charge injection rates from excited dye molecules to the TiO<sub>2</sub> enhancing the photocurrent [31]. Hence in order to improve the photocurrent density of the DSSC various amounts of lithium iodide (LiI) have been added to the most conducting polymer electrolyte, that is, phthaloylchitosan with 19.0 wt.% of Pr<sub>4</sub>NI. Figure 6 shows the room temperature ionic conductivity variation of the gel polymer electrolyte for different mass fractions of the LiI and Pr<sub>4</sub>NI. The conductivities of gel polymer electrolytes with various compositions of LiI : Pr<sub>4</sub>NI at different temperatures are shown in Figure 7. With the addition of LiI conductivity drops are observed at all temperatures in the measured temperature range. This conductivity drop can be attributed to the reduction of polymer flexibility due to inter- and intramolecular cross links by Li<sup>+</sup> due to its high charge density. The reduction of polymer flexibility can

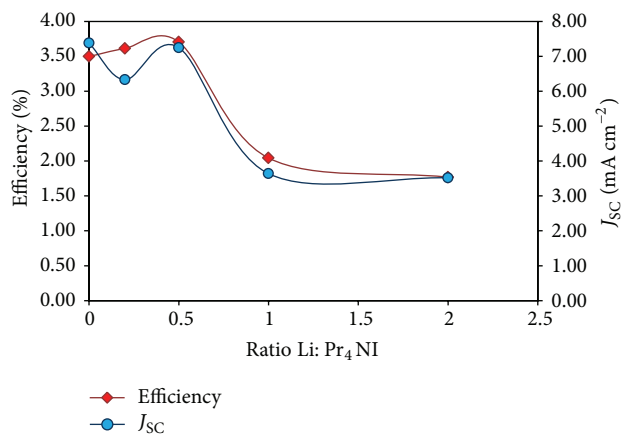
TABLE 4: The performance parameters of DSSCs with different gel polymer electrolytes.

Electrolyte samples	$V_{\max}/V$	$J_{\max}/\text{mA cm}^{-2}$	$V_{\text{oc}}/V$	$J_{\text{sc}}/\text{mA cm}^{-2}$	FF	$\eta/\%$
A	0.52	6.70	0.72	7.38	0.66	3.50
B	0.60	6.02	0.80	6.33	0.72	3.61
C	0.57	6.50	0.77	7.25	0.67	3.71
D	0.61	3.35	0.75	3.64	0.75	2.04
E	0.53	3.35	0.70	3.52	0.71	1.77

FIGURE 8: Photocurrent-voltage curves of DSSCs with phthaloylchitosan based electrolyte different ratio of LiI : Pr<sub>4</sub>NI binary salt.

increase the local viscosity of electrolyte medium hindering mobility of charge carriers. As can be seen from Figure 7, the temperature dependence of conductivity for all electrolytes approximately obeys the Arrhenius relationship as observed in other polymer systems [32].

As expected the incorporation of small amount (less than 0.04 g) of LiI into the electrolyte has improved the solar cell performance (see Figure 8) even though these electrolytes have shown a slight decrease in conductivity as shown in Figure 6. The DSSC parameters for the devices having the binary salt system are tabulated in Table 4. The efficiency reaches a maximum value of 3.71% for a combination of 0.08 g Pr<sub>4</sub>NI and 0.04 g LiI in the electrolyte. This increase in efficiency can be attributed to the mixed cation effect as observed with many binary salt electrolytes [29, 30]. Mixed cation effect is observed when binary iodide salts having smaller and larger cations are present in the gel electrolyte. The smaller cations get adsorbed to the TiO<sub>2</sub> and reduce the Fermi level in such a way to improve the electron injection and, at the same time, the number of iodide ions in the electrolyte increases due to the addition of LiI salt and both these effects increase the current in the DSSC. However, higher amounts of added LiI (more than 0.04 g) have reduced the solar cell efficiency due to the ionic conductivity drop as explained above. Variations of efficiency and photocurrent density with different ratio of Pr<sub>4</sub>NI:LiI are shown in Figure 9. The efficiency variation closely follows that of the current density variation.

FIGURE 9: Dependence of  $J_{\text{SC}}$  and  $\eta$  of DSSCs with different gel polymer electrolytes.

#### 4. Conclusions

In this work, a gel polymer electrolyte has been successfully prepared using phthaloylchitosan as the polymer host and it has been used to produce high performance in a dye-sensitized nanocrystalline solar cell. The most conducting polymer electrolyte containing 19.0 wt.% of Pr<sub>4</sub>NI exhibited the highest efficiency of 3.5% with  $J_{\text{SC}}$  of 7.38 mA cm<sup>-2</sup>,  $V_{\text{OC}}$  of 0.72 V, and FF of 0.66. The efficiency of the DSSC was further improved to 3.7% when part of the Pr<sub>4</sub>NI salt in the electrolyte is replaced with LiI salt (Pr<sub>4</sub>NI:LiI = 2:1) with the value of  $J_{\text{SC}}$ ,  $V_{\text{OC}}$  and fill factor of 7.25 mA cm<sup>-2</sup>, 0.77 V and 0.67, respectively. The presence of the LiI in addition to the Pr<sub>4</sub>NI improves the charge injection rates and increases the iodide contribution to the total conductivity and both factors contribute to the increase in efficiency of the DSSC.

#### Conflict of Interests

The authors declare that there is no conflict of interests regarding the publication of this paper.

#### Acknowledgments

S. N. F. Yusuf, M. F. Aziz, and H. C. Hassan acknowledge travel supports from Centre for Ionics University of Malaya (CIUM) to carry out part of the experimental work at Chalmers University, Sweden. Research support from The National Research Council Sri Lanka (Grant 11-196), the

Swedish Research Council, and University of Malaya (Grant no. RP003-13AFR) is gratefully acknowledged.

## References

- [1] S. Tan, J. Zhai, B. Xue et al., "Property influence of polyanilines on photovoltaic behaviors of dye-sensitized solar cells," *Langmuir*, vol. 20, no. 7, pp. 2934–2937, 2004.
- [2] T. Horieuchi, H. Miura, K. Sumioka, and S. Uchida, "High efficiency of dye-sensitized solar cells based on metal-free indoline dyes," *Journal of the American Chemical Society*, vol. 126, no. 39, pp. 12218–12219, 2004.
- [3] S. J. Park, K. Yoo, J.-Y. Kim et al., "Water-based thixotropic polymer gel electrolyte for dye-sensitized solar cells," *ACS Nano*, vol. 7, no. 5, pp. 4050–4056, 2013.
- [4] L. Wang, H. Zhang, C. Wang, and T. Ma, "Highly stable gel-state dye-sensitized solar cells based on high soluble polyvinyl acetate," *ACS Sustainable Chemistry & Engineering*, vol. 1, no. 1, pp. 205–208, 2012.
- [5] J. Shi, S. Peng, J. Pei, Y. Liang, F. Cheng, and J. Chen, "Quasi-solid-state dye-sensitized solar cells with polymer gel electrolyte and triphenylamine-based organic dyes," *ACS Applied Materials & Interfaces*, vol. 1, no. 4, pp. 944–950, 2009.
- [6] Z. Huo, S. Dai, C. Zhang et al., "Low molecular mass organogelator based gel electrolyte with effective charge transport property for long-term stable quasi-solid-state dye-sensitized solar cells," *The Journal of Physical Chemistry B*, vol. 112, no. 41, pp. 12927–12933, 2008.
- [7] Y. Saito, H. Kataoka, C. Capiglia, and H. Yamamoto, "Ionic conduction properties of PVDF–HFP type gel polymer electrolytes with lithium imide salts," *The Journal of Physical Chemistry B*, vol. 104, no. 9, pp. 2189–2192, 2000.
- [8] T. M. W. J. Bandara, M. A. K. L. Dissanayake, I. Albinsson, and B.-E. Mellander, "Dye-sensitized, nano-porous TiO<sub>2</sub> solar cell with poly(acrylonitrile): MgI<sub>2</sub> plasticized electrolyte," *Journal of Power Sources*, vol. 195, no. 11, pp. 3730–3734, 2010.
- [9] G. P. Kalignan, M.-S. Kang, and Y. S. Kang, "Effects of compositions on properties of PEO-KI-I<sub>2</sub> salts polymer electrolytes for DSSC," *Solid State Ionics*, vol. 177, no. 11-12, pp. 1091–1097, 2006.
- [10] J. Kang, W. Li, X. Wang et al., "Gel polymer electrolytes based on a novel quaternary ammonium salt for dye-sensitized solar cells," *Journal of Applied Electrochemistry*, vol. 34, no. 3, pp. 301–304, 2004.
- [11] S. Y. Bang, K. J. Lee, J. H. Koh, M.-S. Kang, Y. S. Kang, and J. H. Kim, "PEO electrolytes containing dioctyl phthalate (DOP) for dye-sensitized nanocrystalline TiO<sub>2</sub> solar cells," *Ionics*, vol. 14, no. 2, pp. 143–148, 2008.
- [12] V. K. Mourya and N. N. Inamdar, "Chitosan-modifications and applications: opportunities galore," *Reactive and Functional Polymers*, vol. 68, no. 6, pp. 1013–1051, 2008.
- [13] M. Y. Abdelaal, T. R. Sobahi, and H. F. Al-Shareef, "Modification of chitosan derivatives of environmental and biological interest: a green chemistry approach," *International Journal of Biological Macromolecules*, vol. 55, pp. 231–239, 2013.
- [14] T. R. A. Sobahi, M. Y. Abdelaal, and M. S. I. Makki, "Chemical modification of chitosan for metal ion removal," *Arabian Journal of Chemistry*, 2010.
- [15] A. Binette and J. Gagnon, "Regioselective silylation of *N*-phthaloylchitosan with TBDMS and TBDPS groups," *Biomacromolecules*, vol. 8, no. 6, pp. 1812–1815, 2007.
- [16] X. Liu, X. Zhi, Y. Liu, B. Wu, Z. Sun, and J. Shen, "Effect of chitosan, *O*-carboxymethyl chitosan, and *N*-[(2-hydroxy-3-*N,N*-dimethylhexadecyl ammonium)propyl] chitosan chloride on overweight and insulin resistance in a murine diet-induced obesity," *Journal of Agricultural and Food Chemistry*, vol. 60, no. 13, pp. 3471–3476, 2012.
- [17] M. Bodnar, J. F. Hartmann, and J. Borbely, "Synthesis and study of cross-linked chitosan-*N*-poly(ethylene glycol) nanoparticles," *Biomacromolecules*, vol. 7, no. 11, pp. 3030–3036, 2006.
- [18] M. Morimoto, H. Saimoto, H. Usui, Y. Okamoto, S. Minami, and Y. Shigemasa, "Biological activities of carbohydrate-branched chitosan derivatives," *Biomacromolecules*, vol. 2, no. 4, pp. 1133–1136, 2001.
- [19] K. Kurita, H. Ikeda, Y. Yoshida, M. Shimojoh, and M. Harata, "Chemospecific protection of the amino groups of chitosan by controlled phthaloylation: facile preparation of a precursor useful for chemical modifications," *Biomacromolecules*, vol. 3, no. 1, pp. 1–4, 2002.
- [20] K. Kurita, H. Akao, J. Yang, and M. Shimojoh, "Nonnatural branched polysaccharides: synthesis and properties of chitin and chitosan having disaccharide maltose branches," *Biomacromolecules*, vol. 4, no. 5, pp. 1264–1268, 2003.
- [21] K. Kurita, K. Sugita, N. Kodaira, M. Hirakawa, and J. Yang, "Preparation and evaluation of trimethylsilylated chitin as a versatile precursor for facile chemical modifications," *Biomacromolecules*, vol. 6, no. 3, pp. 1414–1418, 2005.
- [22] S. Nishimura, O. Kohgo, K. Kurita, and H. Kuzuhara, "Chemo-specific manipulations of a rigid polysaccharide: syntheses of novel chitosan derivatives with excellent solubility in common organic solvents by regioselective chemical modifications," *Macromolecules*, vol. 24, no. 17, pp. 4745–4748, 1991.
- [23] R. Yoksan, M. Akashi, S. Biramontri, and S. Chirachanchai, "Hydrophobic chain conjugation at hydroxyl group onto  $\gamma$ -ray irradiated chitosan," *Biomacromolecules*, vol. 2, no. 3, pp. 1038–1044, 2001.
- [24] T. M. W. J. Bandara, W. J. M. J. S. R. Jayasundara, M. A. K. L. Dissanayake, M. Furlani, I. Albinsson, and B.-E. Mellander, "Effect of cation size on the performance of dye sensitized nanocrystalline TiO<sub>2</sub> solar cells based on quasi-solid state PAN electrolytes containing quaternary ammonium iodides," *Electrochimica Acta*, vol. 109, pp. 609–616, 2013.
- [25] O. A. Ileperuma, G. R. A. Kumara, and K. Murakami, "Quasi-solid polymer electrolytes based on polyacrylonitrile and plasticizers for indoline dye sensitized solar cells of efficiency 5.3%," *Chemistry Letters*, vol. 37, no. 1, pp. 36–37, 2008.
- [26] M. Z. A. Yahya and A. K. Arof, "Studies on lithium acetate doped chitosan conducting polymer system," *European Polymer Journal*, vol. 38, no. 6, pp. 1191–1197, 2002.
- [27] M. A. K. L. Dissanayake, L. R. A. K. Bandara, R. S. P. Bokalawala, P. A. R. D. Jayathilaka, O. A. Ileperuma, and S. Somasundaram, "A novel gel polymer electrolyte based on polyacrylonitrile (PAN) and its application in a solar cell," *Materials Research Bulletin*, vol. 37, no. 5, pp. 867–874, 2002.
- [28] Q. Yu, Y. Wang, Z. Yi et al., "High-efficiency dye-sensitized solar cells: the influence of lithium ions on exciton dissociation, charge recombination, and surface states," *ACS Nano*, vol. 4, no. 10, pp. 6032–6038, 2010.
- [29] O. A. Ileperuma, M. A. K. L. Dissanayake, S. Somasunderam, and L. R. A. K. Bandara, "Photoelectrochemical solar cells with polyacrylonitrile-based and polyethylene oxide-based polymer electrolytes," *Solar Energy Materials and Solar Cells*, vol. 84, no. 1–4, pp. 117–124, 2004.

- [30] M. A. K. L. Dissanayake, C. A. Thotawatthage, G. K. R. Senadeera, T. M. W. J. Bandara, W. J. M. J. S. R. Jayasundera, and B.-E. Mellander, "Efficiency enhancement by mixed cation effect in dye-sensitized solar cells with PAN based gel polymer electrolyte," *Journal of Photochemistry and Photobiology A: Chemistry*, vol. 246, pp. 29–35, 2012.
- [31] A. K. Arof, M. F. Aziz, M. M. Noor et al., "Efficiency enhancement by mixed cation effect in dye-sensitized solar cells with a PVdF based gel polymer electrolyte," *International Journal of Hydrogen Energy*, vol. 39, no. 6, pp. 2929–2935, 2013.
- [32] M. H. Buraidah, L. P. Teo, S. R. Majid, and A. K. Arof, "Ionic conductivity by correlated barrier hopping in  $\text{NH}_4\text{I}$  doped chitosan solid electrolyte," *Physica B: Condensed Matter*, vol. 404, no. 8–11, pp. 1373–1379, 2009.

## Research Article

# Production of Biologically Activated Carbon from Orange Peel and Landfill Leachate Subsequent Treatment Technology

Zhigang Xie, Wei Guan, Fangying Ji, Zhongrong Song, and Yanling Zhao

Chongqing Key Laboratory of Environmental Materials & Remediation Technologies,  
Chongqing University of Arts and Sciences, Chongqing 402160, China

Correspondence should be addressed to Wei Guan; [guanwei951030@126.com](mailto:guanwei951030@126.com)

Received 28 April 2014; Revised 20 May 2014; Accepted 20 May 2014; Published 23 June 2014

Academic Editor: Fan Dong

Copyright © 2014 Zhigang Xie et al. This is an open access article distributed under the Creative Commons Attribution License, which permits unrestricted use, distribution, and reproduction in any medium, provided the original work is properly cited.

In order to improve adsorption of macromolecular contaminants and promote the growth of microorganisms, active carbon for biological wastewater treatment or follow-up processing requires abundant mesopore and good biophile ability. In this experiment, biophile mesopore active carbon is produced in one-step activation with orange peel as raw material, and zinc chloride as activator, and the adsorption characteristics of orange peel active carbon is studied by static adsorption method. BET specific surface area and pore volume reached  $1477 \text{ m}^2/\text{g}$  and  $2.090 \text{ m}^3/\text{g}$ , respectively. The surface functional groups were examined by Fourier transform infrared spectroscopy (FT-IR). The surface of the as-prepared activated carbon contained hydroxyl group, carbonyl group, and methoxy group. The analysis based on X-ray diffraction spectrogram (XRD) and three-dimensional fluorescence spectrum indicated that the as-prepared activated carbon, with smaller microcrystalline diameter and microcrystalline thickness and enhanced reactivity, exhibited enhanced adsorption performance. This research has a deep influence in effectively controlling water pollution, improving area water quality, easing orange peel waste pollution, and promoting coordinated development among society, economy, and environment.

## 1. Introduction

There is still no economic and applicable treatment method to deal with the wastewater after biochemical process with high residual concentration of COD and BOD [1–3]. Especially, the concentration of COD and  $\text{NH}_3\text{-N}$  of landfill leachate reached 419–622 mg/L and 12.4–174.0 mg/L, respectively [4]. Moreover,  $\text{BOD}_5/\text{COD}$  is less than 0.012 [5]. This result leads to a serious imbalance ratio of C : N : P. Thus, the wastewater is difficult to be further biodegradation. In addition, the landfill leachate after biochemical treatment still contains a lot of naphthenic hydrocarbons, esters, carboxylic acids, phenol, and other toxic substances [6, 7]. Therefore, developing an efficient, stable, and advanced treatment of wastewater is of great technological and scientific significance.

Biological activated carbon (BAC) has great advantages in low concentration and refractory organic wastewater degradation [8–10]. The advantages of BAC include several aspects as follows. (1) The adsorption function of active carbon [11,

12]: organic matter is enriched in carbon particles, increasing contact time of organic matter and microorganisms and providing favorable conditions for microbial acclimation, so that the refractory material can be removed [13, 14]. (2) Adsorption of active carbon increases organic matter concentration around carbon particles, which is favorable to biological degradation [15, 16]. (3) The rough surface with cracks and honeycomb pits provides residential area for dominant bacteria to evade fluid shear stress [17, 18]. (4) The active carbon with strong adsorption capacity can absorb dissolved organic matters (DOMs). These DOMs provide food for the dominant bacteria [19, 20]. (5) Intense microbial activity accelerated the removal of organic matter. Even in the condition of low organic content, microorganisms still grow actively and decompose organic matter constantly due to the accumulation of carbon surface. And then the concentration of organics in the effluent decreased [21, 22]. (6) Active carbon reduces the effect of harmful substances to microorganism in water [23, 24]. This is mainly because the

adherent microorganism can resist poison of biodegradable organic compounds.

Orange peel with porous structure possesses hydrophilic surface group [25]. This is a cheap adsorbent. The adsorption can be enhanced by carbonization and activation [26]. During the activation process, activator can get into the interface due to the natural pore of orange peel [27]. Thus, the activation reaction can be in progress under a mild condition. The as-prepared active carbon with loose pore structure and large specific surface area and massive surface functional groups possesses favorable biophile characteristic and adsorption performance.

In this study, biophile mesopore active carbon was prepared by waste orange peel as raw material to deal with effluent of landfill leachate after biochemical treatment. Based on experiments, peel biological activated carbon technology for wastewater treatment was developed. Furthermore, a subsequent processing method for refractory organic leachate was investigated.

## 2. Materials and Methods

**2.1. Raw Materials.** The raw materials of producing active carbon are the processed orange pomace obtained from Chongqing Three Gorges Fruit Group. This citrus pericarp was dried and crushed sieving through 60-mesh sieve. The specifications and production units of reagents and materials used in this experiment are KBr, ZnCl<sub>2</sub>, I<sub>2</sub>, KI, HCl, N<sub>2</sub>, and H<sub>2</sub>O, respectively.

**2.2. Preparation of Orange Peel Activated Carbon.** Prior to the preparation experiment, orange peel was cleaned, cut, dried, and then crushed. 10 g samples were immersed into 100 mL zinc chloride solution. After 36 h, these samples were centrifuged from the solution and dried. And then, we added proper amount of coal tar and mixed with samples. The samples with partial size of 5~8 mm were formed by extrusion.

The heating process was under the protection of nitrogen. The flow of nitrogen was 0.2 mL/min. The reaction temperature increased to 150°C with 3°C/min, and the reaction time is 30 min when the temperature reached 150°C. Then, we increased the temperature to 300°C continuously to carbonize for 30 min. Solid samples were taken out when the temperature decreased to 20°C and were cleaned by 10% HCl and deionized water successively. The as-prepared citrus peel granular activated carbon was obtained after being dried at 105°C. The preparation process is shown in Figure 1.

The proper preparation condition of activated carbon is as follows: reaction temperature of 550°C; impregnation ratio of 3 : 1; and reaction time of 1 h.

**2.3. Experimental Installation.** Biological active carbon reactor (BAC) and process chart are shown in Figure 2. Biological active carbon pool was made of organic glass, which is a column reactor. The height of carbon pool is 2 m. Inside diameter is 63 mm. The filling height is 1800 mm. The carbon layer height is 1500 mm. The sand filters height is 300 mm.

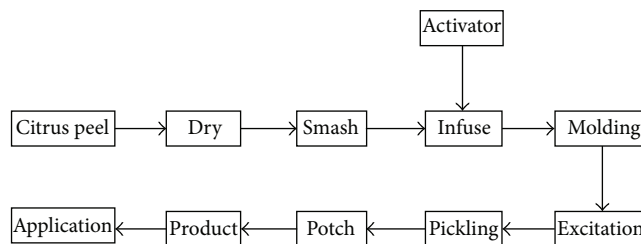


FIGURE 1: Preparing process of activated carbon from orange peel.

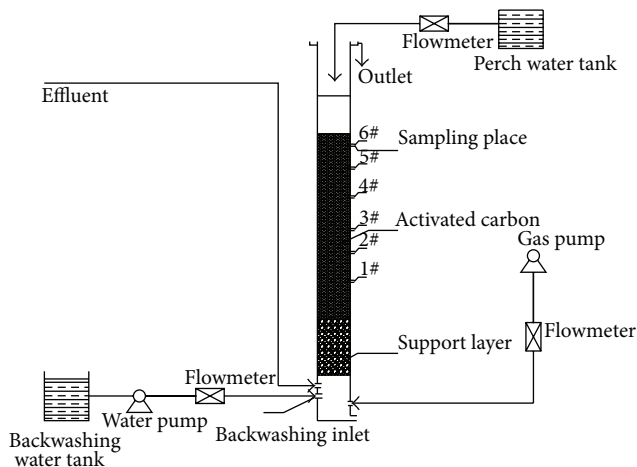


FIGURE 2: Biological activated carbon reactor.

The effective reaction volume is 4.7 L. There are 5 water sampling ports along with carbon pool. And there are aerators in the bottom and overflow weir in the top of carbon pool. The indicator of water quality analysis is UV<sub>254</sub> (ultraviolet spectrophotometry and ultraviolet spectrophotometer).

**2.4. Characterization Instruments.** The crystal phases of the sample were analyzed by X-ray diffraction using Cu K $\alpha$  radiation (XRD, model XD-2 instrument, Persee, China). Nitrogen adsorption-desorption isotherms were obtained on a nitrogen adsorption apparatus (ASAP-2010, USA). All the samples were degassed at 200°C prior to measurements. Fourier transformed infrared spectroscopy (FT-IR, IR Prestige-21FT-infrared spectrometer, Shimadzu, Japan) was measured on FT-IR spectrometer on the transmission mode in the KBr pellet technique: resolution is 4 cm<sup>-1</sup> and scan is 40 times. The morphology was observed by transmission electron microscope (TEM, JEOL JEM-2010, Japan). 3DEEM of examined water was obtained by F-7000 fluorescence spectrophotometer (Hitachi, USA).

## 3. Results and Discussion

**3.1. FT-IR Analysis.** The orange peel mesoporous active carbon and commercial active carbon were analyzed by FT-IR spectra (Figure 3). As shown in Figure 3, orange peel shows 4 strong absorption peaks in the region of 3500~1000 cm<sup>-1</sup>.

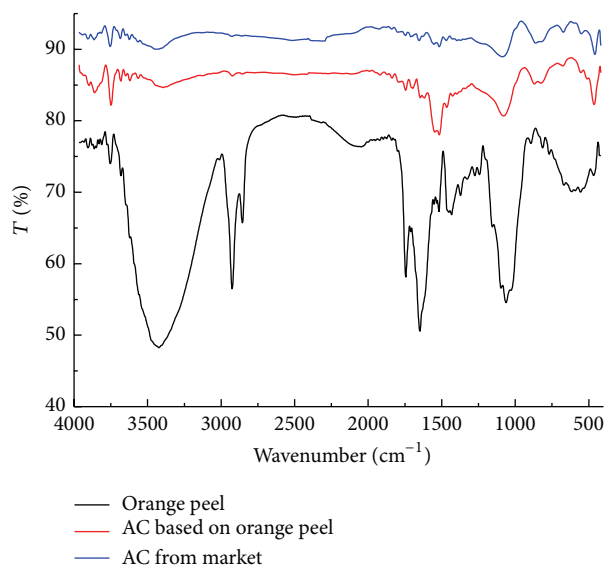


FIGURE 3: FT-IR spectrum of orange peel and activated carbon samples.

These peaks could be attributed to the antisymmetric stretching vibration of  $-\text{OH}$  (at  $3435.07\text{ cm}^{-1}$ ),  $-\text{CH}_3$  and  $-\text{CH}_2$  (at  $2924.31\text{ cm}^{-1}$ ), and  $\text{C}=\text{O}$  (at  $1646.40\text{ cm}^{-1}$ ), respectively [28]. The peak at  $1068.77\text{ cm}^{-1}$  was attributed to the vibration absorption of  $\text{C}-\text{O}$ . These peaks indicated that the orange peel contains a lot of cellulose and hemicelluloses. After being carbonized, the absorption peaks at  $3500\sim 1700\text{ cm}^{-1}$  disappeared. This indicated that the crystal structure of cellulose molecular chain has been destructed.

After being carbonized, the as-prepared mesoporous active carbon and commercial active carbon show the stretch vibration absorption spectra of  $-\text{OH}$  at  $3750\text{ cm}^{-1}$  and  $3420\text{ cm}^{-1}$ . The peak at  $1840\text{ cm}^{-1}$  belongs to the nonsymmetric vibration absorption of  $\text{C}=\text{O}$ , and peak at  $1750\sim 1640\text{ cm}^{-1}$  is the stretching vibration absorption of  $\text{C}=\text{O}$ . This indicated that the mesoporous active carbon and commercial carbon contain hydroxyl, carbonyl products, methoxy, and lactones. In comparison, the adsorption peak of mesoporous active carbon is stronger than the other. Strong absorption peak of mesoporous active carbon in  $1630\sim 1520\text{ cm}^{-1}$  is stretching vibration of benzene ring skeleton. In addition, there is a  $\text{C}-\text{H}$  symmetric stretching vibration peak at  $2820\text{ cm}^{-1}$ . The adsorption peak of commercial carbon at  $1630\sim 1520\text{ cm}^{-1}$  is weak, indicating the mesoporous active carbon containing more orange. Natural groups of citrus peel active carbon were retained to hydrophilic groups, which have strong biophile characteristics.

**3.2. Microstructure of Citrus Peel Active Carbon.** The microstructure of citrus peel active carbon was observed using TEM (Figure 4). TEM shows that citrus peel active carbon has rich mesoporous with a few large pores. The developed pore structure of active carbon is useful for attachment of microorganisms.

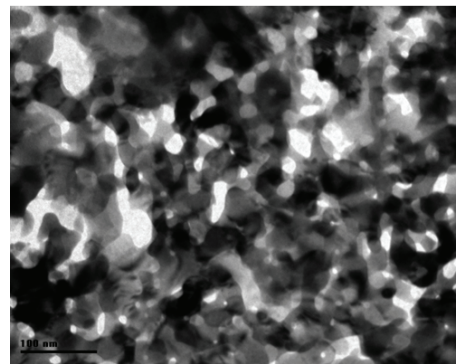


FIGURE 4: TEM image of orange peel activated carbon.

### 3.3. The Pore Size Distribution of Citrus Peel Active Carbon.

Figure 5 shows  $\text{N}_2$  adsorption-desorption isotherms and pore-size distribution curves of citrus peel mesoporous active carbon and commercial active carbon. As seen in Figure 5, according to analyzing adsorption characteristics of activated carbon from the orange peel, it was found that it had the characteristics of type I adsorption isotherm. The specific surface area of biological activated carbon and commercial activated carbon is  $1477\text{ m}^2/\text{g}$  and  $977\text{ m}^2/\text{g}$ , respectively. The pore structure of orange peel active carbon is mesoporous with  $2.0\text{ nm}\sim 4.0\text{ nm}$ . Mesoporosity reached 68.9%. The average pore size of citrus peel active carbon is  $2.0\sim 4.0\text{ nm}$ . This pore structure is beneficial to microbial nutrient matrix and the growth of the microorganisms.

### 3.4. The XRD Analysis of Citrus Peel Active Carbon.

Figure 6 is the XRD patterns of citrus peel active carbon and commercial active carbon. As shown in Figure 6, the strong and weak diffraction peaks emerged at  $2\theta = 25^\circ$  and  $2\theta = 45^\circ$ , respectively. This result indicates the existence of graphite crystallite in citrus peel active carbon and commercial active carbon. The diffraction peaks of commercial active carbon are sharper than those of citrus peel active carbon, indicating that crystallite size of citrus peel active carbon is smaller. This result can be proven by the data of Table 1.

The whole wall of activated carbon is composed of graphite crystallite scale decreases, which can lead to widening or internal structure disordered, so as to form a larger specific surface area. The activated carbon is comprised of ultrafine particles possesses porous structure. The lower the crystallinity, the larger the specific surface area.

There is a close relationship between the degree of graphitization and the interplanar spacing  $D_{002}$  of carbon materials. The smaller the value of carbon crystallites  $D_{002}$  is, the higher the degree of graphitization might be. As shown in Figure 6, compared with commercial activated carbon, the diffraction angle of citrus peels active carbon decreased, indicating that the degree of graphitization of citrus peels active carbon is higher than that of commercial active carbon. The decrease of microcrystalline strength leads to the stronger activity of active carbon. This result indicates that the orange peel active carbon substratum graphite trend is obvious.

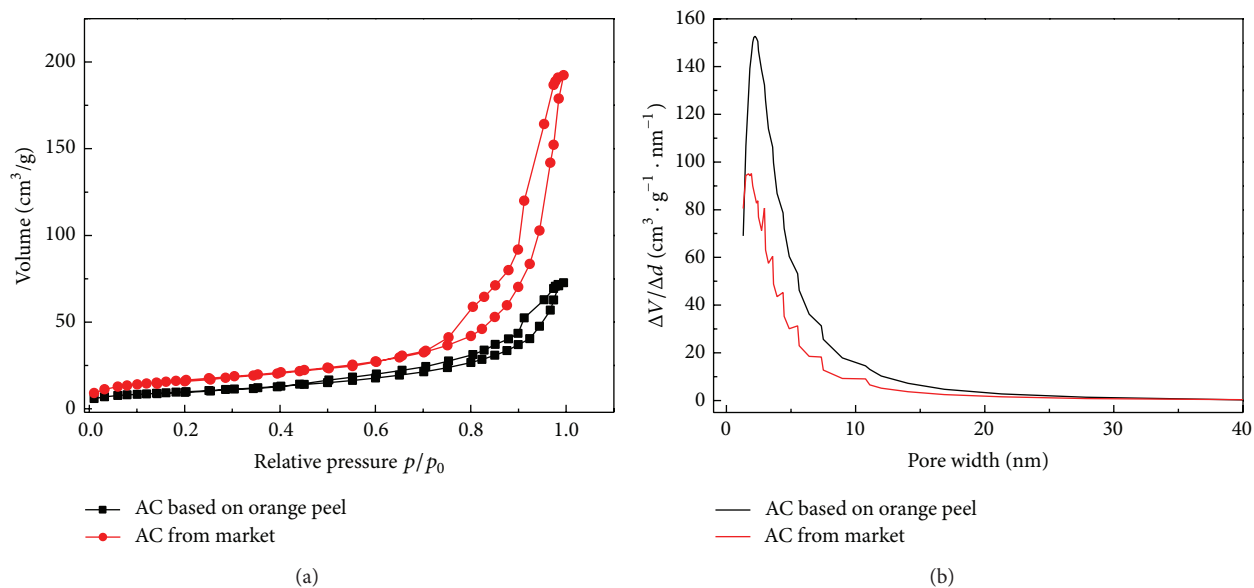


FIGURE 5: N<sub>2</sub> adsorption-desorption isotherms (a) and pore-size distribution curves (b) of citrus peel mesoporous active carbon and commercial active carbon.

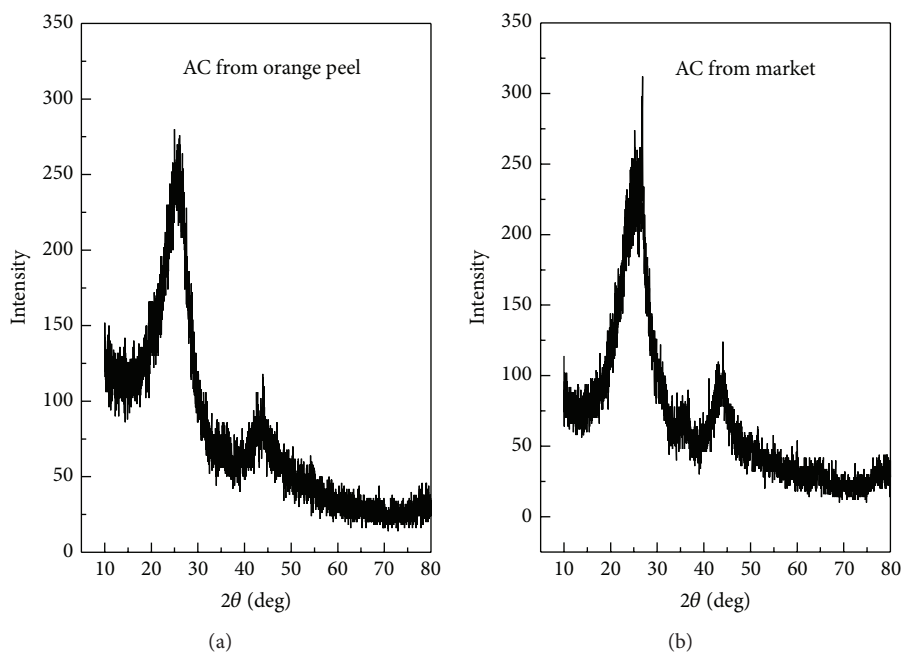


FIGURE 6: XRD pattern of activated carbon.

TABLE 1: Crystalline parameters of activated carbon.

Samples	Microcrystalline diameter	Microcrystalline thickness	$d_{002}/\text{nm}$	$d_{100}/\text{nm}$
	La/nm	Lc/nm		
Orange peel Active Carbon	2.7831	0.7541	0.3485	0.2059
Commercial Active Carbon	3.7914	0.9832	0.3331	0.2153

TABLE 2: The main performance parameters of activated carbon in experiment.

Index	Orange peel active carbon	Commercial active carbon
Grain size/mm	3.0	2.0
Specific surface area/(m <sup>2</sup> /g)	1477	960
Average pore size/mm	3.87	2.02
Micropore volume/(cm <sup>3</sup> /g)	0.532	0.201
Mesopore volume/(cm <sup>3</sup> /g)	1.440	0.616
Total pore volume/(cm <sup>3</sup> /g)	2.090	0.900

3.5. *Adsorption Properties of Orange Peel Active Carbon.* Table 2 is the structure parameters of orange peel active carbon and commercial active carbon. Figure 7 is the static adsorption curve of orange peel active carbon and commercial active carbon. Dosage of active carbon is 0.2 g, and the volume of biochemical water is 50 mL. Figure 8 is the TEM photographs of orange peel active carbon after absorbing biochemical water. Figure 9 is 3DEEM of biochemical water before and after being absorbed by orange peel active carbon.

According to Figure 7, orange peel active carbon exhibited good properties to adsorb biochemical water. The concentration of UV<sub>254</sub> and TOC has a similar change trend. The removal efficiency of UV<sub>254</sub> and TOC is 63.0% and 59.7%, respectively. The adsorption property of commercial active carbon is weak. The removal efficiency of UV<sub>254</sub> and TOC is only 52.9% and 24.8%. According to Table 2, the pore volume of commercial active carbon is smaller than that of orange peel active carbon. There were two stages in the UV<sub>254</sub> removal curves by citrus peel AC in Figure 7; they corresponded to the film diffusion and particle diffusion, respectively.

According to the TEM photographs in Figure 8, the pore structure of orange peel active carbon filled with the amount of organic matter, which means that the pores of active carbon can effectively absorb pollutants in leachate tail water.

As seen in Figure 9, biochemical leachate tail water DOM has two obvious fluorescence peaks: UV fulvic-like fluorescence (Ex/Em = 255/455 nm, Peak, A) and visible fulvic-like fluorescence (Ex/Em = 330/405 nm, Peak, C), containing carboxyl and carbonyl groups. After being adsorbed by orange peel active carbon, ultraviolet water fulvic-like fluorescence intensity (IA) drops from 2222 to 1132, reduced by 49.1%. Visible fulvic-like fluorescence intensity (IC) drops from 1840 to 338.8, reduced by 81.6%. Ex of peak A shift to 250 nm after adsorption. The blue shift of absorption bands for Ex and Em of peak C was observed (Ex/Em = 315/400 nm), and the fluorescence peak center disappears and only the long band exists. This shows that orange peel active carbon has good adsorption properties for water class fulvic acids and other organic matters.

3.6. *Adsorption Kinetics of Citrus Peel Active Carbon.* Based on adsorption kinetics, the adsorption law of orange peel

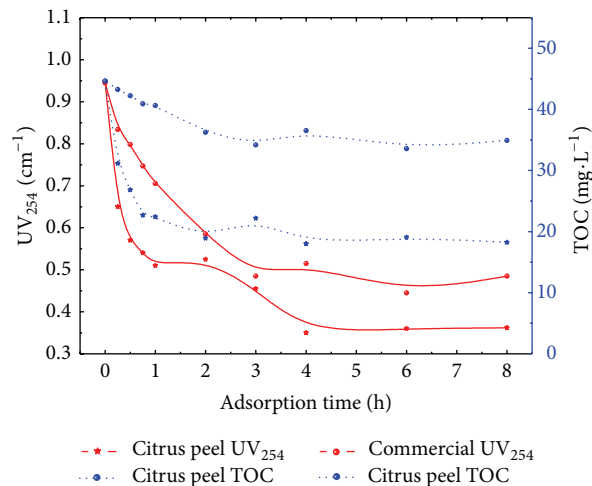


FIGURE 7: Adsorption property of activated carbon.

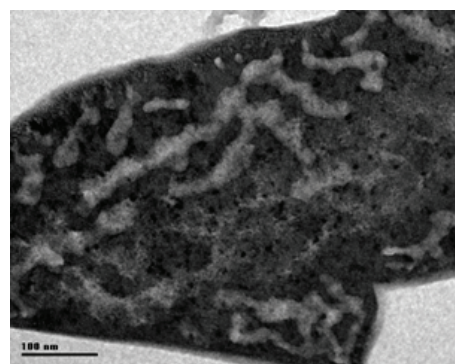


FIGURE 8: TEM image of activated carbon from orange peel after adsorbing organic matters.

active carbon was studied at 25°C, 35°C, and 45°C, respectively. The absorptivity of active carbon can be calculated by

$$q = V \times \frac{(c_0 - c)}{(1000m)}, \quad (1)$$

where  $q$  is adsorption, mg/g,  $V$  is adsorbed solution volume, mL,  $c_0$  and  $c$  are the concentration of TOC in water, respectively, mg/L, and  $m$  is the quality of active carbon.

According to Figure 10, under different temperature conditions, the absorbance of TOC increased quickly in the initial 1h and reached adsorption equilibrium after 4h. The absorbance decreased with the increase of temperature. This indicates that lower temperature is beneficial to the adsorption process of active carbon.

The Lagergren equation (pseudo-first-order kinetic equation) adsorption mechanism and pseudo-two-order kinetics equation are suitable for the expression of the solid adsorption mechanism in aqueous solution [29]. Lagergren kinetic equation can be expressed as follows:

$$\frac{dq}{dt} = k_1 (q_e - q), \quad (2)$$

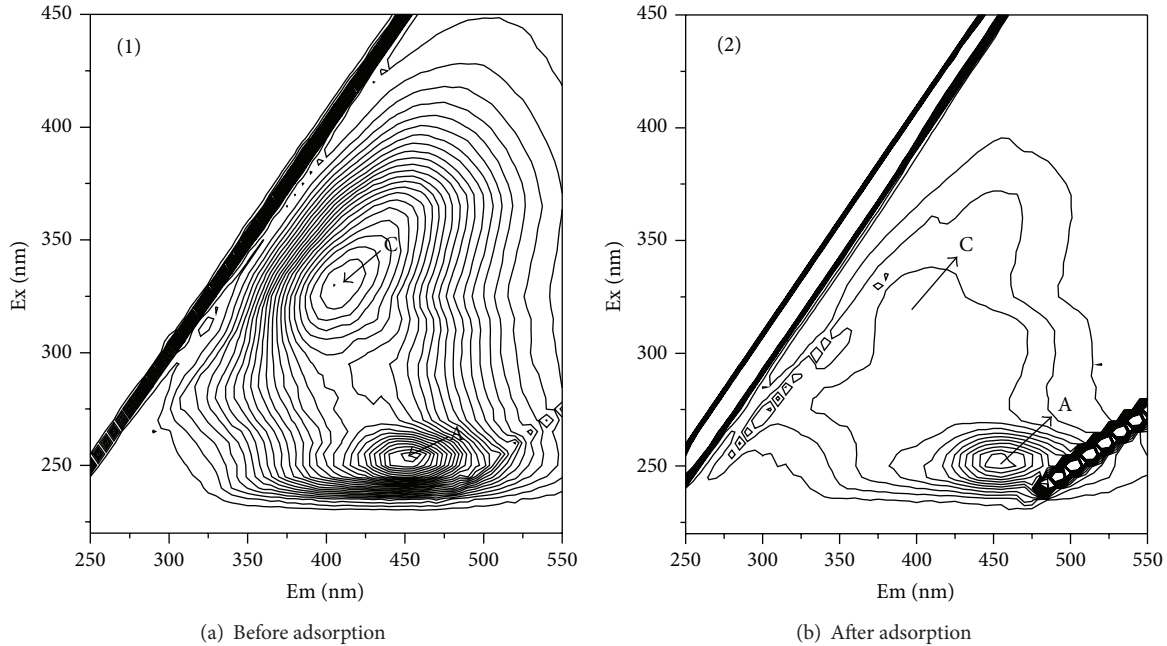


FIGURE 9: 3DEEM for dissolved organic matters of leachate biochemical treatment effluent.

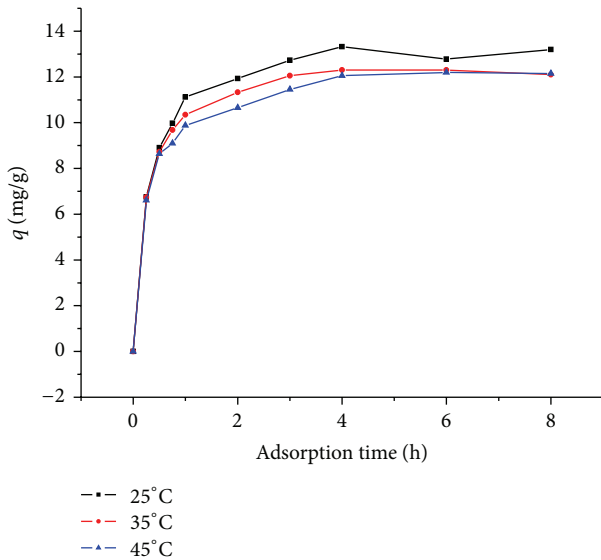


FIGURE 10: Effect of contact time on TOC adsorption of activated carbon.

where  $q_e$  is the equilibrium adsorption capacity (mg/g);  $q$  is adsorption quantity at a time (mg/g); and  $k_1$  is adsorption kinetics rate constant ( $\text{min}^{-1}$ ). Equation (1) can be integral as follows:

$$\lg(q_e - q) = \lg q_e - \frac{k_1 t}{2.303}. \quad (3)$$

The pseudo-second-order model provided by Ho has been widely used to describe the various adsorption systems. The pseudo-second-order model can be expressed as

$$\frac{dq}{dt} = k_1(q_e - q)^2, \quad (4)$$

where  $k$  is the adsorption rate constant [ $\text{g}(\text{mg} \cdot \text{h})^{-1}$ ]. The integral linear can be expressed as follows:

$$\frac{t}{q} = \frac{1}{k_2 q_e^2} + \frac{t}{q_e}. \quad (5)$$

Intraparticle diffusion model can be expressed as follows:

$$q_t = k_p t^{0.5}, \quad (6)$$

where  $k_p$  is the diffusion rate constant [ $\text{mg}/(\text{g} \cdot \text{min})$ ].

Liquid film diffusion model can be expressed as follows:

$$\ln\left(\frac{c_t}{c_0}\right) = \frac{-k_f A t}{V}, \quad (7)$$

where  $c_0$ ,  $c_t$ ,  $A/V$ , and  $t$  are the initial concentration, the concentration at  $t$  min, the adsorption area, the ratio of volume of solution, and adsorption time, respectively, and  $k_f$  is the diffusion coefficient.

The experiment data of the adsorption process can be fitted by (3) and (4), respectively (Figures 11(a) and 11(b)). According to Figures 11(a) and 11(b), the adsorption data of citrus peel activated carbon on TOC can be fitted by Lagergren kinetic equation (proposed a kinetic equation) and proposed two kinetic equations. The correlation coefficient

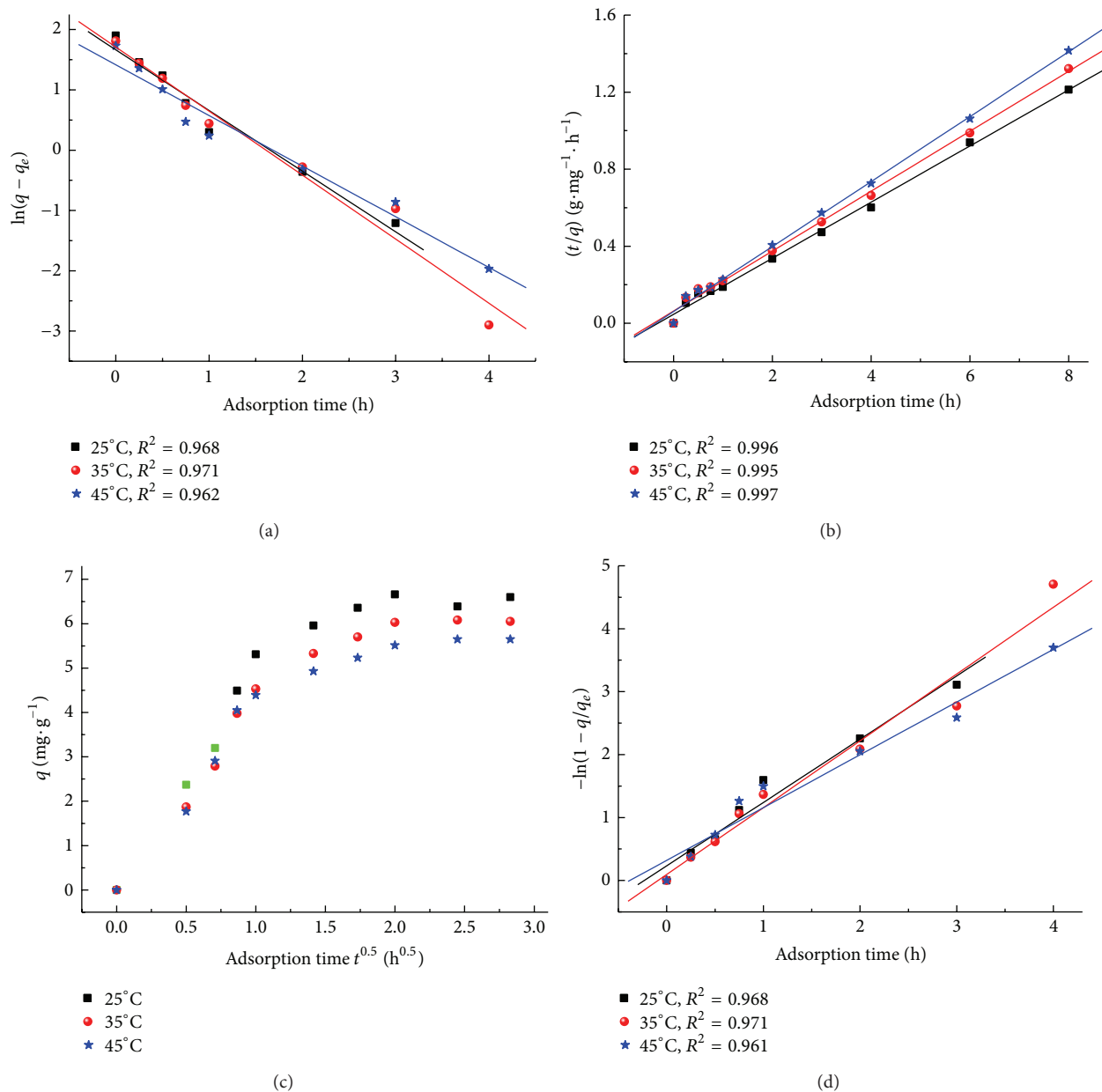


FIGURE 11: Adsorption kinetics models of activated carbon, (a) Lagergren model, (b) pseudo-second-order model, (c) intraparticle diffusion model, and (d) liquid film diffusion model.

$R^2$  of Lagergren kinetic equation is 0.961~0.969, and the correlation coefficient  $R^2$  of proposed two kinetic equations is 0.961~0.969. Higher correlation coefficient indicating the second-order equation is proper to describe the adsorption mechanism of active carbon to deal with biochemical leachate tail water.

The diffusion rate of absorbent in the interface of active carbon increased with the increasing temperature. Thus, the adsorption rate constant increased with the increasing adsorption rate. The adsorption process of active carbon includes three steps, such as film diffusion, the particle diffusion, and adsorption reaction. Adsorption reaction is the

fast step. The plot  $q$  to  $t^{0.5}$  in Figure 11(c) and the plot  $\ln(1 - q/q_e)$  to  $t$  are shown in Figure 11(d). According to Figure 11(c), there is an inflection point between 1.0~1.5 h, indicating that the influencing factors include particle internal diffusion and liquid membrane diffusion. As seen in Figure 11(d), there is a straight line deviating from the origin, indicating that film diffusion is the main rate control step in the early adsorption. The absorbate can be absorbed only through the film arriving carbon surface. Organic molecules through the film are a few in the early adsorption and can be absorbed in carbon surface quickly. Therefore, film diffusion is rate control step. When organic molecules arrived, carbon surface increased

to a certain extent; the particle diffusion is adsorption rate control step.

#### 4. Conclusion

Based on the analysis of characteristics of orange peel, this study provides an innovative idea that the natural pore structure of orange peel is beneficial for the formation of mesoporous active carbon. In this paper, orange peel activated carbon with biophile characteristic has been prepared by one-step method. The yield of the as-prepared biological activated carbon is 50.9%. Orange peel active carbon has hydroxyl, carbonyl, methoxy, and lactones hydrophilic functional group. XRD analysis indicates that the substratum trend of orange peel active carbon is obvious. The orange peel active carbon exhibited enhanced reactivity due to small crystallite size and crystallite thickness. The static adsorption experiment indicated that orange peel active carbon has a good adsorption to deal with leachate biochemical tail water. The removal rate of  $UV_{254}$  is 63.0% and TOC is 59.7%, respectively. Three-dimensional fluorescence spectroscopy has been used to follow the adsorption process. Orange peel active carbon exhibited enhanced ability to adsorb fulvic acids in leachate biochemical water. This research has a deep positive influence in effectively controlling water pollution, improving area water quality, easing orange peel waste pollution, and promoting coordinated development among society, economy, and environment.

#### Conflict of Interests

The authors declare that they have no conflict of interests regarding the publication of this paper.

#### Acknowledgments

This work was supported by the Municipal Education Commission Funded Project of Chongqing, China (KJ111203), and the Construction Science and Technology Project of Chongqing (2011-2-115).

#### References

- [1] D. A. Jones, T. P. Lelyveld, S. D. Mavrofidis, S. W. Kingman, and N. J. Miles, "Microwave heating applications in environmental engineering—a review," *Resources, Conservation and Recycling*, vol. 34, no. 2, pp. 75–90, 2002.
- [2] F. R. Kolb and P. A. Wilder, "Activated carbon adsorption couple with biodegradation to treat problematic wastewater," in *Proceedings of the 1st IAWQ Specialized Conference on Adsorption in Water Environment and Treatment Process*, pp. 191–199, Wadayama, Japan, 1996.
- [3] K. Mochizuki and Y. Takeuchi, "The effects of some inhibitory components on biological activated carbon processes," *Water Research*, vol. 33, no. 11, pp. 2609–2616, 1999.
- [4] M. Cháfer, C. González-Martínez, A. Chiralt, and P. Fito, "Microstructure and vacuum impregnation response of citrus peels," *Food Research International*, vol. 36, no. 1, pp. 35–41, 2003.
- [5] K. N. Ghimire, K. Inoue, H. Yamaguchi, K. Makino, and T. Miyajima, "Adsorptive separation of arsenate and arsenite anions from aqueous medium by using orange waste," *Water Research*, vol. 37, no. 20, pp. 4945–4953, 2003.
- [6] M. Ajmal, R. A. K. Rao, R. Ahmad, and J. Ahmad, "Adsorption studies on *Citrus reticulata* (fruit peel of orange): removal and recovery of Ni(II) from electroplating wastewater," *Journal of Hazardous Materials*, vol. 79, no. 1-2, pp. 117–131, 2000.
- [7] A. B. Pérez-Marín, V. M. Zapata, J. F. Ortuño, M. Aguilar, J. Sáez, and M. Lloréns, "Removal of cadmium from aqueous solutions by adsorption onto orange waste," *Journal of Hazardous Materials*, vol. 139, no. 1, pp. 122–131, 2007.
- [8] Z. Xuan, Y. Tang, X. Li, Y. Liu, and F. Luo, "Study on the equilibrium, kinetics and isotherm of biosorption of lead ions onto pretreated chemically modified orange peel," *Biochemical Engineering Journal*, vol. 31, no. 2, pp. 160–164, 2006.
- [9] C. Namasivayam, N. Muniasamy, K. Gayatri, M. Rani, and K. Ranganathan, "Removal of dyes from aqueous solutions by cellulosic waste orange peel," *Bioresource Technology*, vol. 57, no. 1, pp. 37–43, 1996.
- [10] R. Sivaraj, C. Namasivayam, and K. Kadirvelu, "Orange peel as an adsorbent in the removal of Acid violet 17 (acid dye) from aqueous solutions," *Waste Management*, vol. 21, no. 1, pp. 105–110, 2001.
- [11] K. V. Kumar and K. Porkodi, "Batch adsorber design for different solution volume/adsorbent mass ratios using the experimental equilibrium data with fixed solution volume/adsorbent mass ratio of malachite green onto orange peel," *Dyes and Pigments*, vol. 74, no. 3, pp. 590–594, 2007.
- [12] M. Arami, N. Y. Limaee, N. M. Mahmoodi, and N. S. Tabrizi, "Removal of dyes from colored textile wastewater by orange peel adsorbent: Equilibrium and kinetic studies," *Journal of Colloid and Interface Science*, vol. 288, no. 2, pp. 371–376, 2005.
- [13] G. Annadurai, R. S. Juang, and D. J. Lee, "Use of cellulose-based wastes for adsorption of dyes from aqueous solutions," *Journal of Hazardous Materials*, vol. 92, no. 3, pp. 263–274, 2002.
- [14] B. Ozkaya, "Chlorophenols in leachates originating from different landfills and aerobic composting plants," *Journal of Hazardous Materials*, vol. 124, no. 1-3, pp. 107–112, 2005.
- [15] P. J. He, L. M. Shao, X. Qu, G. J. Li, and D. J. Lee, "Effects of feed solutions on refuse hydrolysis and landfill leachate characteristics," *Chemosphere*, vol. 59, no. 6, pp. 837–844, 2005.
- [16] R. J. Slack, J. R. Gronow, and N. Voulvoulis, "Household hazardous waste in municipal landfills: contaminants in leachate," *Science of the Total Environment*, vol. 337, no. 1-3, pp. 119–137, 2005.
- [17] A. A. Bakare, A. A. Mosuro, and O. Osibanjo, "An in vivo evaluation of induction of abnormal sperm morphology in mice by landfill leachates," *Mutation Research*, vol. 582, no. 1-2, pp. 28–34, 2005.
- [18] L. N. Huang, S. Zhu, H. Zhou, and L. H. Qu, "Molecular phylogenetic diversity of bacteria associated with the leachate of a closed municipal solid waste landfill," *FEMS Microbiology Letters*, vol. 242, no. 2, pp. 297–303, 2005.
- [19] N. Sang and G. Li, "Chromosomal aberrations induced in mouse bone marrow cells by municipal landfill leachate," *Environmental Toxicology and Pharmacology*, vol. 20, no. 1, pp. 219–224, 2005.
- [20] G. Gupta and W. Gardner, "Use of clay mineral (montmorillonite) for reducing poultry litter leachate toxicity (EC50)," *Journal of Hazardous Materials*, vol. 118, no. 1-3, pp. 81–83, 2005.

- [21] C. Visvanathan, M. K. Choudhary, M. T. Montalbo, and V. Jegatheesan, "Landfill leachate treatment using thermophilic membrane bioreactor," *Desalination*, vol. 204, no. 1–3, pp. 8–16, 2007.
- [22] E. Noaksson, M. Linderöth, B. Gustavsson, Y. Zebühr, and L. Balk, "Reproductive status in female perch (*Perca fluviatilis*) outside a sewage treatment plant processing leachate from a refuse dump," *Science of the Total Environment*, vol. 340, no. 1–3, pp. 97–112, 2005.
- [23] H. D. Robinson, K. Knox, B. D. Bone, and A. Picken, "Leachate quality from landfilled MBT waste," *Waste Management*, vol. 25, no. 4, pp. 383–391, 2005.
- [24] M. Mavros, N. P. Xekoukoulotakis, D. Mantzavinos, and E. Diamadopoulos, "Complete treatment of olive pomace leachate by coagulation, activated-carbon adsorption and electrochemical oxidation," *Water Research*, vol. 42, no. 12, pp. 2883–2888, 2008.
- [25] M. C. Mittelmeijer-Hazeleger and J. M. Martín-Martínez, "Microporosity development by CO<sub>2</sub> activation of an anthracite studied by physical adsorption of gases, mercury porosimetry, and scanning electron microscopy," *Carbon*, vol. 30, no. 4, pp. 695–709, 1992.
- [26] K. Tomków, T. Siemienińska, F. Czechowski, and A. Jankowska, "Formation of porous structures in activated brown-coal chars using O<sub>2</sub>, CO<sub>2</sub> and H<sub>2</sub>O as activating agents," *Fuel*, vol. 56, no. 2, pp. 121–124, 1977.
- [27] M. Jagtoyen, M. Thwaites, J. Stencel, B. McEnaney, and F. Derbyshire, "Adsorbent carbon synthesis from coals by phosphoric acid activation," *Carbon*, vol. 30, no. 7, pp. 1089–1096, 1992.
- [28] W. Jiang, J. A. Joens, D. D. Dionysiou, and K. E. O'Shea, "Optimization of photocatalytic performance of TiO<sub>2</sub> coated glass microspheres using response surface methodology and the application for degradation of dimethyl phthalate," *Journal of Photochemistry and Photobiology A: Chemistry*, vol. 262, pp. 7–13, 2013.
- [29] B. S. Girgis, L. B. Khalil, and T. A. M. Tawfik, "Activated carbon from sugar cane bagasse by carbonization in the presence of inorganic acids," *Journal of Chemical Technology and Biotechnology*, vol. 61, no. 1, pp. 87–92, 1994.

## Research Article

# Removing and Recovering Phosphate from Poultry Wastewater Using Amorphous Ceramics

**Youhui Xie, Qin Li, Xianzhi Zhao, Yi Luo, Yangming Wang, Xiangwei Peng, Qigui Wang, Jian Su, and Yin Lu**

*Chongqing Academy of Animal Science, Chongqing 402460, China*

Correspondence should be addressed to Yangming Wang; [cqwym@126.com](mailto:cqwym@126.com)

Received 20 February 2014; Revised 22 April 2014; Accepted 22 April 2014; Published 21 May 2014

Academic Editor: Fan Dong

Copyright © 2014 Youhui Xie et al. This is an open access article distributed under the Creative Commons Attribution License, which permits unrestricted use, distribution, and reproduction in any medium, provided the original work is properly cited.

A novel and effective technique for phosphate from poultry wastewater was developed using amorphous ceramics. Amorphous ceramics, which showed high performance for phosphate removal and recovery from poultry wastewater, were synthesized using unlimitedly available, inexpensive materials such as silica fume and lime. Dissolved phosphate in poultry wastewater can be deposited as a solid on the surface of amorphous ceramics. Phosphate content on the surface of amorphous ceramics could reach 14.20%. The phosphate removal and recovery process and mechanism was revealed by a series of characterizations, such as XRD, FESEM, BET, and so on. The present study demonstrated that amorphous ceramics have great potential as a novel, beneficial material for removing and recovering phosphate from poultry wastewater.

## 1. Introduction

The pollution caused by livestock and poultry breeding is not only a local environmental problem, but also a big basin environmental issue [1, 2]. Especially, high concentration of phosphate discharged from poultry wastewater was one of the main incentives of eutrophication [3, 4]. Therefore, removing phosphate from poultry wastewater has been the present research hotspot [5–7].

According to the supersaturation theory, when the concentration of  $\text{Ca}^{2+}$ ,  $\text{OH}^-$ , and phosphate ion reaches saturation state, phosphate can be deposited in the form of calcium orthophosphate on the surface of crystal seed [8, 9]. Previous studies showed that calcium silicate hydrate can be used as the crystal seed [10–13]. And the phosphate recovery efficiency of calcium silicate hydrate was about 13% according to the existing research [14, 15]. The crystallization process could remove phosphate in wastewater by producing calcium orthophosphate on the surface of granular seed crystal [16–18]. This process possesses the advantages of easy dewatering and potential phosphate recycling for the product. Due to the unique chemical composition of amorphous ceramics, it could ensure the efficient removal and the recovery of

soluble phosphate [19]. From a theoretical and practical point of view, micromorphology of amorphous ceramics was also important for increasing reaction rate of phosphate recovery [20]. This critical issue has not yet been sufficiently solved so far. Overall, the goal of this study was to define the micromorphology properties and to optimize the influence conditions for amorphous ceramics to remove and recover phosphate.

Laboratory experiments were carried out to investigate the key features of the removing and recovering process. Theoretical analysis and experimental evidences were also provided to demonstrate the underlying principles of crystallization and mechanism of the process. The originality and importance that can be drawn from this study are summarized, such as examining the effects of pH value, stirring intensity and dosage of amorphous ceramics on the phosphate removal and recovery efficiency. Then, cycling phosphate removal experiments were performed to evaluate the phosphate recovery performance of amorphous ceramics. The applicability of the phosphate recovery system using amorphous ceramics as a seed crystal was also examined. At last, by using Avrami kinetics equation, the capacity of  $\text{Ca}^{2+}$  release and the pore structure of amorphous ceramics

TABLE 1: Chemical components of silica fume and lime.

	Chemical components (contents)/%								
	CaO	SiO <sub>2</sub>	Al <sub>2</sub> O <sub>3</sub>	SO <sub>2</sub>	MgO	Fe <sub>2</sub> O <sub>3</sub>	NaOH	CuO	H <sub>2</sub> O
Lime	79.60	3.35	2.36	1.18	0.66	0.17	—	—	12.68
Silica fume	0.04	97.50	0.15	1.83	—	0.02	0.30	0.01	0.15

were determined. The mechanism of phosphate recovery by amorphous ceramics as seed crystal on the condition of weak alkaline was also revealed.

## 2. Materials and Methods

**2.1. Materials.** Amorphous ceramics were synthesized using silica fume as the silicon oxide materials and lime as calcium oxide materials, respectively. Lime (calcareous, hoar and powdery, Chongqing Changshou Chemical Co., Ltd.) was calcined at 700°C for 2 h. The chemical constituents of silica fume (Particles present spherical with homogeneous diameter, Chongqing Jianfeng chemical Co., Ltd.) and lime are in Table 1. The phosphate solution was poultry wastewater. The phosphate concentration of poultry wastewater was 40 mg/L, and pH value was 7.0~7.5. The above materials and chemicals were placed into sealed bottles for storage.

**2.2. Preparation of Amorphous Ceramics.** Amorphous ceramics were prepared with lime (providing CaO) and silica fume (providing SiO<sub>2</sub>). Lime and silica fume were mixed with a molar ratio of 1.5~1.6. The mixture was then added to prepared slurries. The slurry was hydrothermal reacted at 165~170°C for 6 h and taken out when the temperature was reduced to the natural conditions. The hydrothermal reaction was carried out with a liquid/solid ratio of 29~30. The obtained products were dried at 105°C for 2 h and then were ground through a sieve of 200 meshes.

**2.3. Phosphate Removal and Recovery Using Amorphous Ceramics.** The pH values of phosphate-content solution were in the range of 7.0~7.5 before the amorphous ceramics samples were added to this solution. The experiment temperature condition is 20°C. Continuous phosphate removal tests were carried out using amorphous ceramics for the removal of phosphate from poultry wastewater. Amorphous ceramics samples (dosage of samples 0.5, 1.0, 2.0, 3.0, and 4.0 g/L, resp.) were added to a series of bottles and stirring (40, 60, 80, 100, and 120 r/min, resp.) under controlled temperature conditions (20°C). Phosphate concentration of supernatant was measured according to the molybdenum blue ascorbic acid method (the relative error of data is 0.3%) with a spectrophotometer (UV-2012PCS, Shanghai Unico Instruments Co., Ltd., China). The solid samples were then separated from the removed synthetic solution with the addition of samples after reaction. Finally, the produced sediments were separated from removed synthetic solution, dried, and weighted. Phosphate is contented by (1), where  $C_t$  is the restrained phosphate concentration in synthetic solution (mg/L),  $v$  is the volume of the solution (L),  $w$  is the mass of produced sediment after

phosphate recovery (mg), and  $C_0$  is the initial phosphate concentration (mg/L):

$$P = \frac{(c_0 - c_t) \times v}{w} \times 100\%. \quad (1)$$

**2.4. Ca<sup>2+</sup> Release Experimental of Amorphous Ceramics.** 1g of amorphous ceramics samples was immersed in 1L of demonized water contained in a glass bottle, generating samples with a solution concentration of 1g/L. The bottle was placed on an agitation table and shaken at 40 r/min under controlled temperature conditions (20°C). Samples of solution were taken after 5, 10, 15, 20, 40, and 60 min of agitation. Ca<sup>2+</sup> concentration of samples was determined by EDTA titration (the relative error of data is 0.05%).

**2.5. Characterization Methods.** X-ray diffraction (XRD) patterns were collected in an XD-2 instrument (Persee, China) using Cu K $\alpha$  radiation.

Field emission scanning electron microscopy (FESEM) images were collected on an S-4800 field emission scanning electron microscope (Hitachi, Japan).

Brunauer-Emmett-Teller (BET) surface areas were measured by nitrogen adsorption at 77.35 K on an ASAP-2010 adsorption apparatus (Micromeritics, USA).

## 3. Results and Discussion

**3.1. Phase Structure of Amorphous Ceramics.** The XRD patterns of amorphous ceramics before phosphate removal, phosphate removal for the first time, and phosphate removal for 6 times were compared (Figure 1). The main phase of amorphous ceramics was Jennite (PDF card 18-1206, chemical formula Ca<sub>9</sub>Si<sub>6</sub>O<sub>18</sub>(OH)<sub>6</sub>·8H<sub>2</sub>O). After phosphate removal for the first time, the dominant peaks of Jennite were obviously weakened, and the weak peaks of calcium orthophosphate (PDF card 09-0432, chemical formula Ca<sub>5</sub>(PO<sub>4</sub>)<sub>3</sub>(OH)) emerged at 25.88°, 31.76°, and 53.26°. The sharp dominant peaks of calcium orthophosphate appeared after phosphate removal for 6 times instead of the dominant peaks of Jennite. This phenomenon indicated that original property of amorphous ceramics seed crystal disappeared and transformed to calcium orthophosphate during the phosphate recovery process.

**3.2. BET Surface Areas and Pore Structure of Amorphous Ceramics.** Nitrogen adsorption-desorption isotherms of amorphous ceramics before and after phosphate removal are shown in Figure 2. The specific surface areas of these

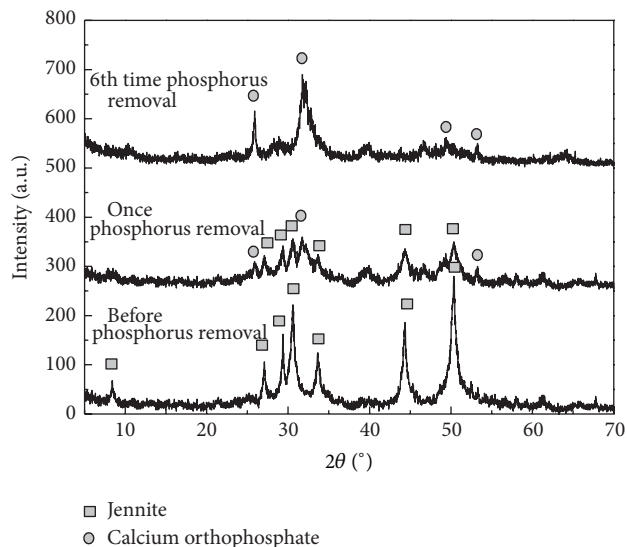


FIGURE 1: XRD patterns of samples.

samples were 114.14, 57.38, 34.25, 23.74, and 7.55 m<sup>2</sup>/g, respectively. Pore volumes of these samples were 0.52, 0.31, 0.12, 0.09, and 0.04 cm<sup>3</sup>/g, respectively. These results indicated that the specific surface areas and pore volumes decreased with the increase of phosphate removal times. Figure 2 shows the phenomenon of adsorption hysteresis loop. This implies that mesopore or narrow gap pore exists in the samples. Adsorption in mesopore occurred mainly in medium pressure region (0.4 < P/P<sub>0</sub> < 0.9) [21, 22]. The phenomenon of adsorption hysteresis loop disappeared gradually with the increased phosphate removal times. The FESEM photographs of amorphous ceramics before and after removing phosphate are shown in Figure 3. Before phosphate removal, amorphous ceramics possess obvious porous structure with a large number of mesopores (Figure 3(a)). The micrograph in Figure 3(b) reveals that amorphous ceramics are covered with finely distributed crystalline substances, which was calcium orthophosphate as indicated in XRD result.

**3.3. Kinetic of Ca<sup>2+</sup> Release.** The effect of phosphate removal for the first 4 times on the Ca<sup>2+</sup> release capacity of amorphous ceramics was investigated (Figure 4). Ca<sup>2+</sup> concentration released from amorphous ceramics decreased with the increase of phosphate removal times. The maximum Ca<sup>2+</sup> concentration released from amorphous ceramics was 3.02 mg/g before phosphate removal. This concentration decreased to 1 mg/g after phosphate removal for 4 times. Avrami kinetic equation could describe how the solid change from one phase state to another (that means phase transition), which could also describe the chemical reaction rate [23]. So, the experimental capacities of Ca<sup>2+</sup> release could be fitted by Avrami kinetic equation; the model is as follows:

$$-\ln(1-x) = kt^n, \quad (2)$$

where  $k$  is the kinetic constant,  $n$  is the characteristic constant of solid,  $t$  is the reaction time (min), and  $x$  ( $x = C_t/C_{\max}$ ,  $C_t$  is concentration of time  $t$  (mg/L), and  $C_{\max}$  is concentration

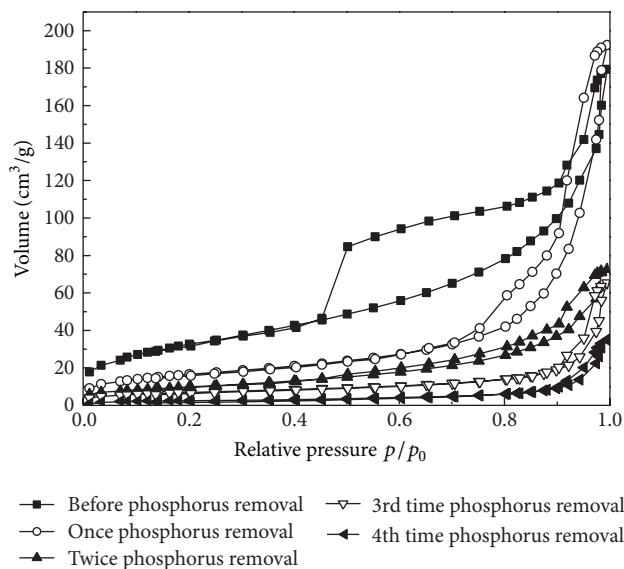


FIGURE 2: Nitrogen adsorption-desorption isotherms of amorphous ceramics before and after removing phosphate.

TABLE 2: The correlate constants for the Avrami kinetic equation describing Ca<sup>2+</sup> release.

Samples	$n$	$k$	$R^2$
Before phosphate removal	0.9156	0.0758	0.9893
Once phosphate removal	0.9204	0.0682	0.9752
Twice phosphate removal	0.9182	0.0602	0.9790
3rd time phosphate removal	0.8687	0.0564	0.9548
4th time phosphate removal	0.9913	0.0301	0.9836

of the maximum (mg/L)) is the fraction conversion. The characteristic constant  $n$  was 0.9156. The kinetic constants were determined by fitting the Avrami kinetic equation to the experimental data obtained (Table 2).

The high correlation coefficients ( $R^2 > 0.9$ ) indicated that this model could well describe the law of Ca<sup>2+</sup> release. Combined with specific surface area ( $S$ ) of samples, a relationship between  $k$  and  $S$  could be established:

$$k = 0.1502S^{0.3695} \quad R^2 = 0.9232. \quad (3)$$

According to (3), the larger surface area of amorphous ceramics could result in faster Ca<sup>2+</sup> release. Subsequently, the concentration of Ca<sup>2+</sup> release increased.

#### 3.4. Phosphate Removal with Amorphous Ceramics

**3.4.1. Effect of pH Values.** The effect of pH values on the phosphate ions removal performance was investigated with the initial phosphate concentration 40 mg/L (Figure 5). The results in Figure 5 show that pH value has an obvious effect on the residual phosphate concentration. The residual phosphate concentration was up to 7.7~9.1 mg/L when the pH values were in the range of 4.0~7.0. In this range of pH values, the solution has not reached supersaturation with Ca<sup>2+</sup>, OH<sup>-</sup>, and phosphate ions coexisted. Under this condition, amorphous ceramics did not possess phosphate

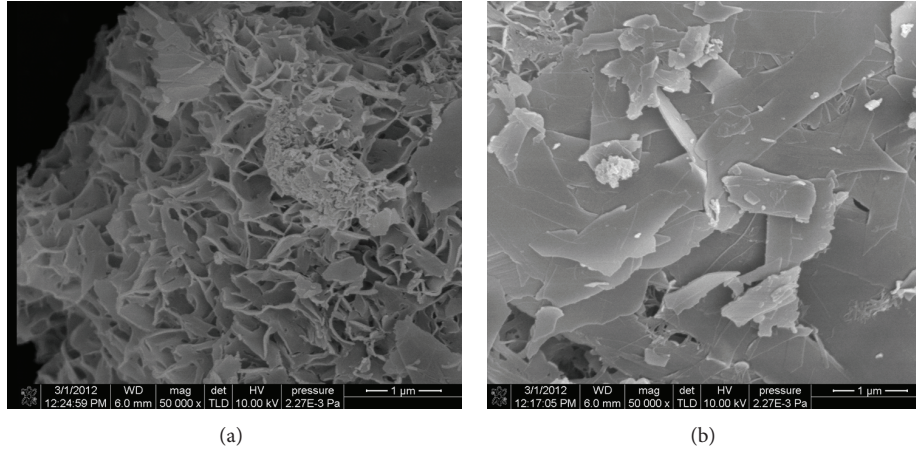


FIGURE 3: FESEM photographs of amorphous ceramics before and at the 6th time phosphate removal. (a) Amorphous ceramics before phosphate removal. (b) Amorphous ceramics of the 6th time phosphate removal.

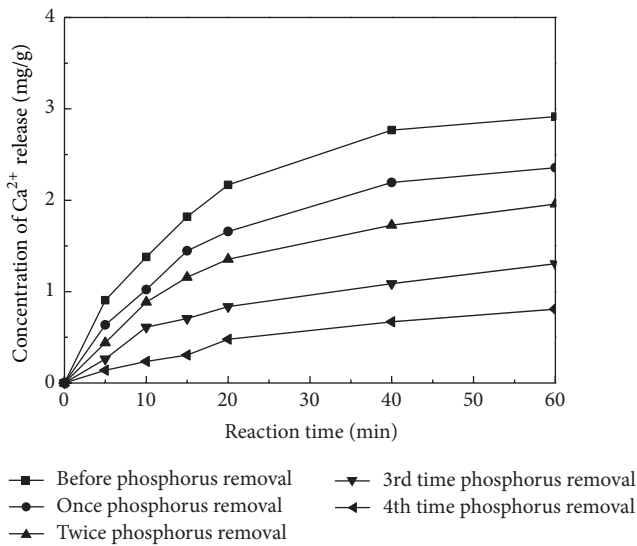


FIGURE 4: Concentration of Ca<sup>2+</sup> released from samples.

removal performance. At the pH value of 8.0, the residual phosphate concentration declined to 4.34 mg/L. When the pH value reached to 9.0, the phosphate removal performance of amorphous ceramics increased obviously, and the residual phosphate concentration declined to the minimum of 0.82 mg/L. Phosphate existed in the form of  $\text{HPO}_4^{2-}$  in the range of 8.0~9.0 [24]. The residual phosphate concentration increased with the pH values increasing continuously. So, the kinetic models of phosphate removal were established at pH value of 9.0. This reaction is accorded with the tendency of second order reaction kinetics, and the kinetic equation could be established:

$$\frac{dC}{dt} = -kC^2 \quad (4)$$

or

$$\frac{1}{C_t} - \frac{1}{C_0} = kt, \quad (5)$$

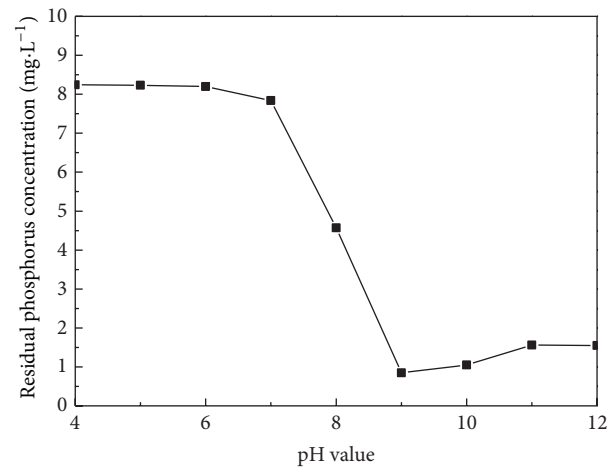


FIGURE 5: Influence of pH value on residual phosphate concentration.

where  $C_t$  is the concentration of time  $t$  (mg/L),  $C_0$  is the initial time, and  $k$  is the kinetic constant.

3.4.2. *Kinetic of Phosphate Removal.* With the pH value unchanged, initial phosphate concentration, stirring intensity, and amorphous ceramics dosage have been predicted as the major factors influencing the phosphate removal rate by calcium orthophosphate crystallization. Hence, the overall rate constant  $k$  in (6) is likely to be a function of stirring intensity and amorphous ceramics dosage,

$$k = f(M, I) = aM^b I^c, \quad (6)$$

where  $b$ ,  $c$ , and  $d$  were constants and  $M$  and  $I$  were amorphous ceramics dosage and stirring intensity, respectively.

The effect of amorphous ceramics dosage on the removal of phosphate was investigated at amorphous ceramics dosages range of 0.5, 1, 2, 3, and 4 g/L, respectively (Figure 6). As shown in Figure 6, when the dosages were in the range of 1~4 g/L, the residue phosphate concentration kept unchanged with 4~5 mg/L. The residue phosphate concentration rose to

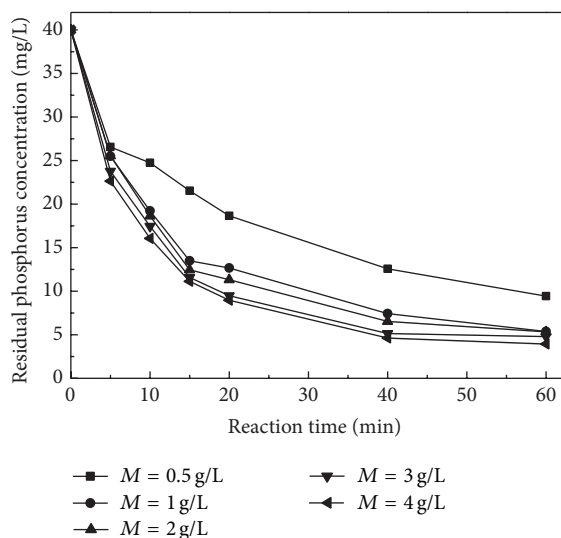


FIGURE 6: Influence of dosage of amorphous ceramics.

9.45 mg/L when the dosage was as low as 0.5 g/L. This result was inconsistent with the conclusion of traditional coagulation precipitation experiment. In the traditional experiment, the removal of phosphate could be better with the increase of dosages of calcium. This is because the removal efficiency of phosphate was much dependent on the alkalinity caused by excess calcium, and the malpractice of this traditional method is reducing the utilization efficiency of calcium. Considering the effective utilization rate from seed, 1 g/L is the proper dosages. The reaction rate of phosphate removal increased with the increase of dosage, and the relationship could be fitted as follows:

$$k = 0.0003M^{1.3865} \quad R^2 = 0.9453. \quad (7)$$

Under pH value of 9.0, amorphous ceramics dosage of 1 g/L, the results showed that the residual phosphate concentration declined with the increase of stirring intensity when the stirring intensity was lower than 80 r/min. When the stirring intensity reached 80 r/min, the residual phosphate concentration declined to minimum (Figure 7). According to Figure 7, stirring intensity has an obvious influence on the phosphate removal performance of amorphous ceramics. The reaction rate of phosphate removal increased with the increase of stirring intensity. The relationship could be fitted as follows:

$$k = 0.0004I^{0.4712} \quad R^2 = 0.9247. \quad (8)$$

By comprehensive analysis of initial, amorphous ceramics dosage and stirring intensity, (4) could be expressed as follows:

$$k = aM^{1.3865}I^{0.4712}. \quad (9)$$

According to (7) and (9), the parameter  $a$  can be determined to be 0.0034. The kinetic model of phosphate removal could be established by taking the coefficient  $a$  into (5):

$$\frac{1}{C_t} = \frac{1}{C_0} + (0.0046M^{1.3865}I^{0.4712})t. \quad (10)$$

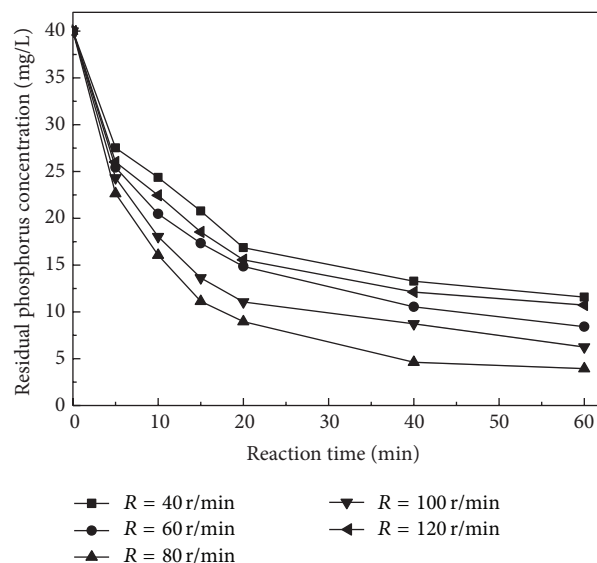


FIGURE 7: Influence of stirring intensity on residual phosphate concentration.

The phosphate recovery process is the calcium orthophosphate crystallization process on the surface of amorphous ceramics. When the stirring intensity is too low, amorphous ceramics cannot touch phosphate wastewater adequately. When the stirring intensity is too high, the calcium orthophosphate crystal cannot be formed due to the strong shearing force.

**3.5. The Phosphate Recovery Performance of Amorphous Ceramics.** According to (1) and (10), the kinetic model verified the experimental result of phosphate removal. Analysis from the view of phosphate recovery showed that the conditions such as the improvement of initial phosphate concentration, stirring intensity, and the decrease of dosage were beneficial for the improvement of phosphate content of solid segment. But the value of  $k$  was only 0.00007 when the amorphous ceramics dosage was 0.5 g/L. This reaction rate was too low to the engineering application. Thus, the proper dosage should be 1 g/L, and the reaction rate  $k$  was 0.0005. So, the proper process condition for phosphate recovery using amorphous ceramics is as follows: amorphous ceramics dosage of 1 g/L and stirring intensity of 80 r/min. To obtain the maximum efficiency of phosphate recovery continuous experiments were carried out using amorphous ceramics calculated for the removal of phosphate. Changes of residual phosphate concentration by circulation of phosphate removal were shown in Figure 8. For the first 4 times of phosphate removal, the restrained phosphate concentration was changed greatly. The restrained phosphate concentration almost remained stable when phosphate removal circulated for 6 times. The quality of solid segment was 1.08 g and the phosphate content of solid segment was 14.20% after the circulation of phosphate removal. The changes of pH values showed that amorphous ceramics could maintain the pH value between 8.0 and 9.0 at the first 4 times phosphate removal. Calcium phosphate had been crystallized on the surface of amorphous ceramics

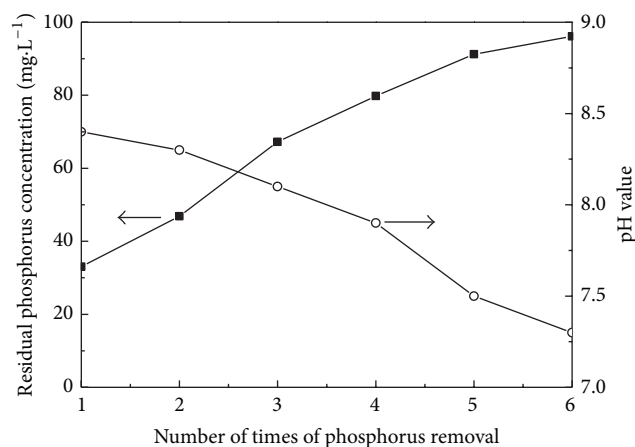


FIGURE 8: Changes of residual phosphate concentration and pH values.

during the 6 times phosphate recovery process. Thus, BET surface areas and pore volume decreased. Due to the large BET surface areas and pore volume of amorphous ceramics,  $\text{Ca}^{2+}$  and  $\text{OH}^-$  can be released continuously, and pH values increased. During the phosphate recovery process, phosphate sedimentation produced on the surface of amorphous ceramics to block the pore structure to restrain the release of  $\text{Ca}^{2+}$  and  $\text{OH}^-$ . The pH values declined with the increased circulate times of phosphate removal. Subsequently, the phosphate removal performance of amorphous ceramics decreased. The pH value declined to 7.5 after the circulation of phosphate removal for 6 times. At this time, the restrained phosphate concentration was up to 95.47 mg/L, which indicated that amorphous ceramics did not possess phosphate removal capacity in neutral condition.

Indeed, the phosphate recovery process is the form process of calcium orthophosphate, which is also different from the traditional chemical phosphate removal process. Because the traditional chemical phosphate removal process needs a high alkalinity (pH = 10.5~12.5) condition to make  $\text{Ca}^{2+}$ ,  $\text{OH}^-$ , and  $\text{PO}_4^{3-}$  reach supersaturated, the phosphate sedimentation precipitated would be produced. Under the proper process condition, amorphous ceramics could release a suitable concentration of  $\text{Ca}^{2+}$  and  $\text{OH}^-$  to maintain the pH value during 8.0~9.0. Phosphate existed in the form of  $\text{HPO}_4^{2-}$  in the range of these pH values.  $\text{Ca}^{2+}$ ,  $\text{OH}^-$ , and  $\text{HPO}_4^{2-}$  formed a local condition with high concentration. This condition was beneficial to the formation of calcium orthophosphate with pH = 8.0~9.0.

#### 4. Conclusion

The present work demonstrated that phosphate in poultry wastewater was dropped as the pH value increased during 8.0~9.0 at a proper  $\text{Ca}^{2+}$  and  $\text{OH}^-$  concentration during calcium orthophosphate crystallization. The design factors for calcium orthophosphate crystallization process were investigated systematically using the model proposed in this study. The calcium orthophosphate crystallization was affected by pH value, stirring intensity, and amorphous ceramics dosage.

The phosphate content of regenerated product obtained by amorphous ceramics reached 14.20%, exceeding that of the regenerated product obtained by tobermorite (13%) and xonotlite (10%). Experiments have also demonstrated the applicability of the phosphate crystallization process as a phosphate recovery system for recycling phosphates in poultry wastewater using amorphous ceramics as seed crystal.

#### Conflict of Interests

The authors declare that there is no conflict of interests regarding the publication of this paper.

#### Acknowledgments

This work was supported by the National Waterfowl Industry Technology System Chongqing Comprehensive Test Station (CARS-43-43) and one project of Science and Technology Committee in Chongqing named New Variety Breeding of Wulong Black Chicken (CSTC, 2011AC1180, 11301).

#### References

- [1] L. H. Peng and Y. Bai, "Numerical study of regional environmental carrying capacity for livestock and poultry farming based on planting-breeding balance," *Journal of Environmental Science*, vol. 25, no. 9, pp. 1882–1889, 2013.
- [2] K. Yetilmzsoy and S. Sakar, "Improvement of COD and color removal from UASB treated poultry manure wastewater using Fenton's oxidation," *Journal of Hazardous Materials*, vol. 151, no. 2-3, pp. 547–558, 2008.
- [3] K. Yetilmzsoy, "Integration of kinetic modeling and desirability function approach for multi-objective optimization of UASB reactor treating poultry manure wastewater," *Bioresource Technology*, vol. 118, pp. 89–101, 2012.
- [4] R. Rajakumar, T. Meenambal, P. M. Saravanan, and P. Ananthanarayanan, "Treatment of poultry slaughterhouse wastewater in hybrid upflow anaerobic sludge blanket reactor packed with pleated poly vinyl chloride rings," *Bioresource Technology*, vol. 103, no. 1, pp. 116–122, 2012.
- [5] M. G. Hajaya and S. G. Pavlostathis, "Fate and effect of benzalkonium chlorides in a continuous-flow biological nitrogen removal system treating poultry processing wastewater," *Bioresource Technology*, no. 118, pp. 73–81, 2012.
- [6] M. G. Hajaya and S. G. Pavlostathis, "Modeling the fate and effect of benzalkonium chlorides in a continuous-flow biological nitrogen removal system treating poultry processing wastewater," *Bioresource Technology*, no. 130, pp. 278–287, 2013.
- [7] K. Yetilmzsoy and Z. Sapci-Zengin, "Recovery of ammonium nitrogen from the effluent of UASB treating poultry manure wastewater by MAP precipitation as a slow release fertilizer," *Journal of Hazardous Materials*, vol. 166, no. 1, pp. 260–269, 2009.
- [8] E. V. Munch and K. Barr, "Controlled struvite crystallisation for removing phosphorus from anaerobic digester sidestreams," *Water Research*, vol. 35, no. 1, pp. 151–159, 2001.
- [9] C. Guo, V. Stabnikov, S. Kuang, and V. Ivanov, "The removal of phosphate from wastewater using anoxic reduction of iron ore in the rotating reactor," *Biochemical Engineering Journal*, vol. 46, no. 2, pp. 223–226, 2009.

- [10] W. Guan, F. Y. Ji, Q. K. chen, P. Yan, and L. Pei, "Synthesis and enhanced phosphate recovery property of porous calcium silicate hydrate using polyethyleneglycol as pore-generation agent," *Materials*, vol. 6, no. 7, pp. 2846–2861, 2013.
- [11] W. Guan, F. Y. Ji, Q. K. Chen, P. Yan, and Q. Zhang, "Preparation and phosphorus recovery performance of porous calcium-silicate-hydrate," *Ceramics International*, vol. 39, no. 2, pp. 1385–1391, 2013.
- [12] W. Guan, F. Y. Ji, D. X. Fang et al., "Porosity formation and enhanced solubility of calcium silicate hydrate in hydrothermal synthesis," *Ceramics International*, vol. 40, no. 1, pp. 1667–1675, 2014.
- [13] W. Guan, F. Y. Ji, Q. K. Chen, P. Yan, and W. W. Zhou, "Influence of hydrothermal temperature on phosphorus recovery efficiency of porous calcium silicate hydrate," *Journal of Nanomaterials*, vol. 2013, Article ID 451984, 6 pages, 2013.
- [14] Y.-H. Song, D. Donnert, U. Berg, P. G. Weidler, and R. Nueesch, "Seed selections for crystallization of calcium phosphate for phosphorus recovery," *Journal of Environmental Sciences*, vol. 19, no. 5, pp. 591–595, 2007.
- [15] W. Guan, F. Y. Ji, Y. Cheng et al., "A novel synthesis method of porous calcium silicate hydrate based on the calcium oxide/polyethylene glycol composites," *Journal of Nanomaterials*, vol. 2013, Article ID 542109, 7 pages, 2013.
- [16] M. Özen, M. Mertens, J. Luyten, F. Snijkers, H. D'Hondt, and P. Cool, "Hydrothermal synthesis of carbonate-free submicron-sized barium titanate from an amorphous precursor: synthesis and characterization," *Ceramics International*, vol. 38, no. 1, pp. 619–625, 2012.
- [17] W. Cai, B. G. Zhang, Y. X. Jin et al., "Behavior of total phosphorus removal in an intelligent controlled sequencing batch biofilm reactor for municipal wastewater treatment," *Bioresource Technology*, vol. 132, pp. 190–196, 2013.
- [18] D. Seyhan, "Country-scale phosphorus balancing as a base for resources conservation," *Resources, Conservation and Recycling*, vol. 53, no. 12, pp. 698–709, 2009.
- [19] E.-H. Kim, S.-B. Yim, H.-C. Jung, and E.-J. Lee, "Hydroxyapatite crystallization from a highly concentrated phosphate solution using powdered converter slag as a seed material," *Journal of Hazardous Materials*, vol. 136, no. 3, pp. 690–697, 2006.
- [20] K. Suzuki, Y. Tanaka, K. Kuroda et al., "Removal and recovery of phosphorous from swine wastewater by demonstration crystallization reactor and struvite accumulation device," *Bioresource Technology*, vol. 98, no. 8, pp. 1573–1578, 2007.
- [21] F. Dong, Y. J. Sun, M. Fu, Z. B. Wu, and S. C. Lee, "Room temperature synthesis and highly enhanced visible light photocatalytic activity of porous BiOI/BiOCl composites nanoplates microflowers," *Journal of Hazardous Materials*, vol. 219–220, pp. 26–34, 2012.
- [22] F. Dong, Y. J. Sun, M. Fu, W. K. Ho, S. C. Lee, and Z. B. Wu, "Novel in situ n-doped (BiO)<sub>2</sub>CO<sub>3</sub> hierarchical microspheres self-assembled by nnosheets as efficient and durable visible light driven photocatalyst," *Langmuir*, vol. 28, no. 1, pp. 766–773, 2012.
- [23] N. Demirkiran and A. Künkül, "Dissolution kinetics of ulexite in perchloric acid solutions," *International Journal of Mineral Processing*, vol. 83, no. 1-2, pp. 76–80, 2007.
- [24] Y. Liu, X. Sheng, Y. H. Dong, and Y. J. Ma, "Removal of high-concentration phosphate by calcite: effect of sulfate and pH," *Desalination*, vol. 289, pp. 66–71, 2012.

## Research Article

# A Quaternized Polysulfone Membrane for Zinc-Bromine Redox Flow Battery

Mingqiang Li, Hang Su, Qinggang Qiu, Guang Zhao, Yu Sun, and Wenjun Song

School of Energy and Power Engineering, Dalian University of Technology, Dalian 116023, China

Correspondence should be addressed to Mingqiang Li; [limingqiang918@sohu.com](mailto:limingqiang918@sohu.com)

Received 13 February 2014; Revised 25 April 2014; Accepted 30 April 2014; Published 15 May 2014

Academic Editor: Ying Zhou

Copyright © 2014 Mingqiang Li et al. This is an open access article distributed under the Creative Commons Attribution License, which permits unrestricted use, distribution, and reproduction in any medium, provided the original work is properly cited.

A quaternized polysulfone (QNPSU) composite membrane is fabricated for zinc-bromine redox flow battery. The structure of the membrane is examined by FT-IR spectra and SEM. The conductivity of the membrane is tested by electrochemical analyzer. After a zinc-bromine battery with this composite membrane is operated at different voltage while charging and at different current while discharging to examine the performance of the membrane, it is found that the discharge voltage was 0.9672 V and the power density was 6 mW/cm<sup>2</sup> at a current of 0.1 A, which indicated that the novel composite membrane is a promising material for the flow battery.

## 1. Introduction

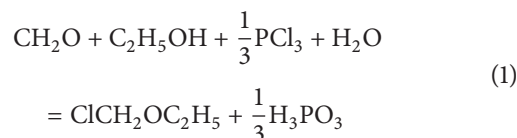
Recently, many people have focused on the zinc-bromine redox flow battery because it is considered highly fascinating for energy storage. Because Zn-Br flow battery has an advantage in cost [1], the cost of electrolyte, to a great extent, determines the overall cost of the battery. Zinc, as a very common metal, is of low cost and abundant. And the bromine can be extracted in sewage and swamp. Moreover, zinc-bromine battery is of high energy density and power density, as well as good charge and discharge properties [2–5]. Although, up to now, too many experiments have been carried out, there are still a few technical problems unresolved [6, 7]. The problems are the fact that bromine diffusion towards the zinc electrode could not be completely worked out so far. In the zinc-bromine redox flow battery, the membrane with good properties in ionic conductivity, mechanical strength, and chemical stability is required [8–12]. However, up to now, the fabrication of this kind of membrane is very challenging.

In this paper, we prepared a thin quaternized polysulfone (QNPSU) composite membrane for zinc-bromine redox flow battery, which, to our knowledge, has not been reported previously. QNPSU composite membrane provides good mechanical strengths with low cost. The initial results indicate that the new membrane is a promising material for zinc-bromine redox flow battery.

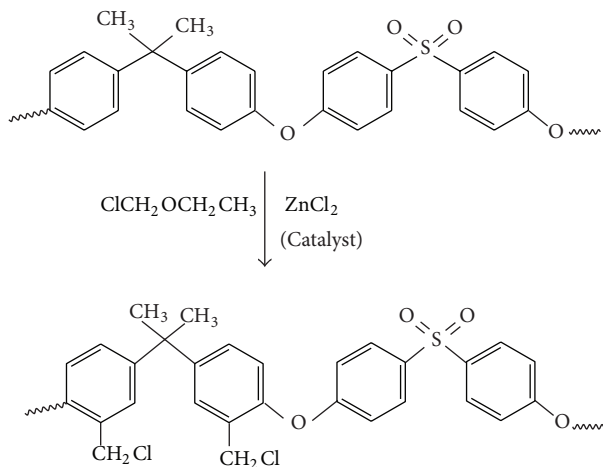
## 2. Experimental

**2.1. The Composition of Chloromethyl Ethyl Ether.** The procedure for chloromethyl ethyl ether preparation was as follows. Formaldehyde solution (50 g) was dissolved in the alcohol with a volume of 30 mL in a reaction kettle equipped with mixer, dropping funnel, and then thermometer. 52.5 g phosphorus trichloride was added to the solution with magnetic stirring in ice bath. Temperature was controlled ranging from 30°C to 35°C and stirring continued for one hour. Keeping still for 10 minutes, the solution was separated into two layers. Upper solution was chloromethyl ethyl ether which is what we need.

The equation is given as follows:



**2.2. Chloromethylated Polysulfone Preparation.** The synthesis of Chloromethylated polysulfone (CMPFS) was prepared according to a modification of a published procedure [13]. First, 7 g polysulfone was dissolved in 100 cm<sup>3</sup> (mL) 1,2-dichloroethane with magnetic stirring at room temperature. 0.5 g zinc chloride anhydrous was added to the above-mentioned 10 mL chloromethyl ethyl ether. This solution was



SCHEME 1: Preparation of the chloromethylation of polysulfone.

added dropwise into the reaction kettle and the reaction proceeded for 8 h at 70°C. The final reaction solution was light red. The white product was precipitated in hot water. The resulted step was dried in high vacuum to remove any residual solvent and kept in a vacuum before further use.

The preparation of the chloromethylation of polysulfone is as shown in Scheme 1.

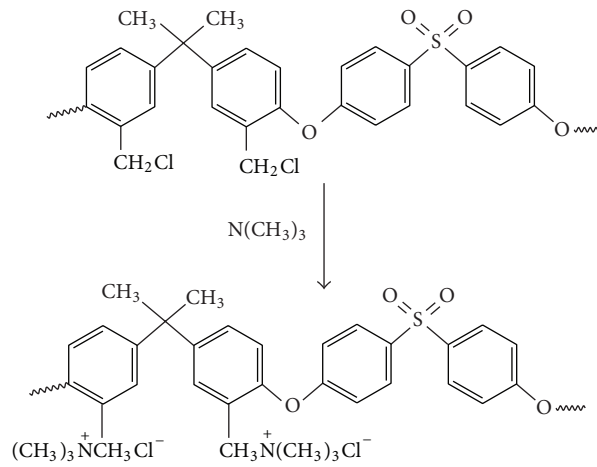
**2.3. Preparation of CMPFS Composite Membrane.** 5 g CMPFS was dissolved in 30 cm<sup>3</sup> (mL) N-methyl-2-pyrrolidone (NMP) and then the mixture was stirred at 60°C. Composite membranes of CMPFS were prepared by CMPFS-NMP solution evenly spreading on the glass for 30 min at 60°C and then dried at 100°C.

**2.4. Preparation of the Quaternized Polysulfone Membrane.** The procedure for the preparation of the quaternized polysulfone membrane was as follows. The composite membranes of CMPFS were bathed in 100 cm<sup>3</sup> (mL) trimethylamine (TMA) till the membranes softened. Then the membrane was rinsed with copious amounts of deionised (DI) water, immersed in aqueous NaOH (1.0 mol/dm<sup>3</sup>) solution for 12 h at 25°C, and then dried.

The preparation of the quaternized polysulfone membrane is as shown in Scheme 2.

**2.5. Conductivity Measurement.** Membrane conductivity was measured with a four-point probe and frequency response electrochemical analyzer CHI604D (Shanghai Chenhua Instrument Co., Ltd.). The polymer membranes were held at the desired temperature and humidity for 0.5 h, to ensure that a steady state was achieved, and measurements were taken at 1 min intervals.

**2.6. Battery Tests.** The membranes were cut into 4 cm × 4 cm. High-density graphite plates are used directly as framework components and electrodes. There is a 5 mm depth slot on one side of graphite plates to make solution circulate smoothly.



SCHEME 2: The preparation of the quaternized polysulfone membrane.

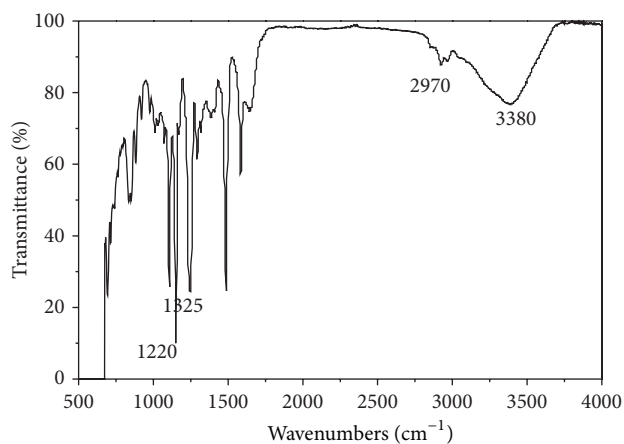


FIGURE 1: FT-IR spectra of quaternized polysulfone membrane.

The molarities of zinc-bromine solution are about 4 mol/L so that the amount is nearly half of the optimal value not only for the conductivity but also for the bromine solubility [14–17]. The anode and cathode electrodes were filled with electrolyte through constant pumping.

This research carried out the battery charging and discharging tests through battery testing system 7.5.X (Neware Co., Ltd.). The charge was conducted by a designated current, while the discharge was at a constant current.

### 3. Results and Discussion

**3.1. FT-IR Analysis.** Figure 1 shows the infrared spectra of quaternized polysulfone membrane. We can find that S=O vibration peaks are at 1220 and 1325 cm<sup>-1</sup> [18]. The broad peak at around 3380 cm<sup>-1</sup> was attributed by O–H and residual water. The quaternary ammonium group stretching vibration peaks are at 2970 cm<sup>-1</sup> [19]. The data suggests that there was a successful synthesis of quaternized polysulfone composite membrane.

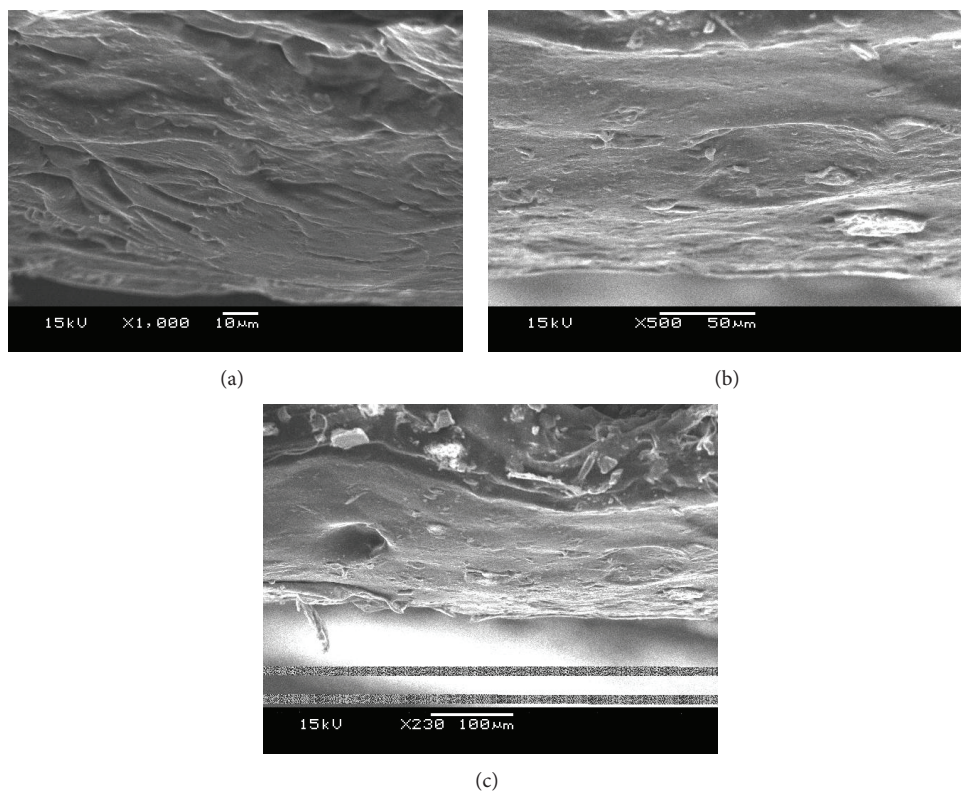


FIGURE 2: SEM image of the cross-sectional quaternized polysulfone membrane.

**3.2. Morphology of QNPSU Composite Membrane.** Figure 2 shows an image of the microporous structure of the composite membrane. From the dense structure of composite membrane cross-section in different magnification, we can see that the membrane cross-section was comparatively dense and no holes were produced.

**3.3. Proton Conductivity of the Quaternized Polysulfone.** AC impedance diagram includes frequency, real part, and imaginary part. The real parts of impedance serve as the horizontal axis and the imaginary parts serve as the vertical axis; namely,  $Z = Z' + jZ''$ . The AC impedance curve is as shown in Figure 3. Internal resistance of the battery is about  $0.5 \Omega$  and the conductivity of the membrane is about  $0.01 \text{ S/cm}$  in  $25^\circ\text{C}$  with 100 RH%.

**3.4. Ions Permeability Experiments.** Two different kinds of membranes are prepared for the permeability experiments, namely, commercial Nafion membrane and quaternized polysulfone composite membrane. Experimental procedure is as follows. 20 mL bromine water with a certain molar concentration is contained in a sealed container and the bottom of the container is quaternized polysulfone composite membrane which is pasted onto the container to let ions cross through it. Then we put the container into a bottle and seal the bottle. After some time of nine days, we find some red liquid in the bottle and collect it; subsequently, we measure the volume of the collected liquid and the measurement result is 15.8 mL. In the same way, we change the commercial Nafion membrane

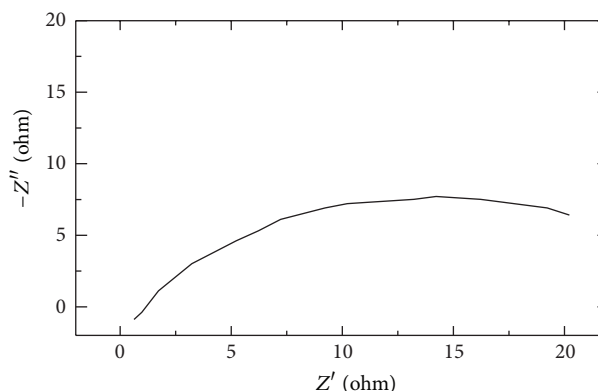


FIGURE 3: The AC impedance diagram of the quaternized polysulfone membrane. High freq. (Hz) =  $1e + 5$ ; low freq. (Hz) = 1; amplitude (V) = 0.005.

instead of quaternized polysulfone composite membrane and repeat the above steps and another measurement data of the collected liquid is obtained, namely, 9 mL.

Compared with the two different measured volumes, we find that quaternized polysulfone membrane is more useful to let the solution pass through it than the commercial Nafion membrane. So quaternized polysulfone membrane is more suitable for zinc-bromine redox flow battery.

**3.5. Battery Performance.** Figure 4 shows polarization curves of the battery with quaternized polysulfone membranes at

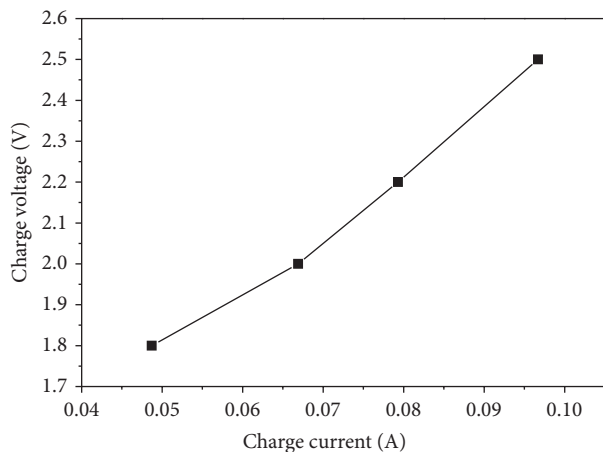


FIGURE 4: Polarization curves of the battery with quaternized polysulfone membranes at different charge voltage.

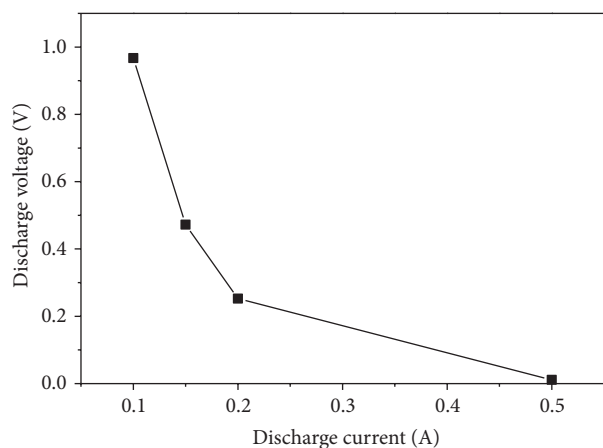


FIGURE 5: Polarization curves of the battery with quaternized polysulfone membranes at different discharge voltage.

different charge voltage. Because the theoretical open circuit potentials for the battery were 1.82 V, the present charge test was carried out with a voltage slightly higher than 1.8 V. From the data, we see that the battery performance increased with the voltage increasing at the same temperature and pressure.

This indicates that there was still a small degree of porosity in the membrane. This factor would need to be investigated in more detail in subsequent development of the membrane for redox flow battery applications.

Figure 5 shows polarization curves of the battery with quaternized polysulfone at different discharge voltage. As expected, battery voltage declined with current density increasing while discharging. For example, at a cell current of 0.1 A, the discharge voltage was 0.9672 V and the power density was 6 mW/cm<sup>2</sup>, while, at 0.15 A current, the voltage was 0.4724 V and the power density was 4.4 mW/cm<sup>2</sup>. The relatively good performance was mainly attributed to the high proton conductivity of the composite membrane. The major cause for voltage loss of the battery was associated with the performance of the electrode layers and solution. This

indicates that the improvement of the zinc-bromine battery performance can be made through further development of the electrodes and solution.

#### 4. Conclusions

A quaternized polysulfone (QNPSU) composite membrane has been fabricated for zinc-bromine redox flow battery. The structure of the membrane is examined by FT-IR spectra and SEM. The successful synthesis of membrane was comparatively dense and no holes were produced. Tested by electrochemical analyzer, the conductivity of the membrane is about 0.01 S/cm in 25°C with 100 RH%. A zinc-bromine battery with this composite membrane is operated at different voltage while charging and at different current while discharging. The battery performance of the membrane shows that the discharge voltage was 0.9672 V and the power density was 6 mW/cm<sup>2</sup> at a 0.1 A current. This result indicates that the novel composite membrane is a promising material for the flow battery.

#### Conflict of Interests

The authors declare that there is no conflict of interests regarding the publication of this paper.

#### Acknowledgment

This work was supported by the Fundamental Research Funds for the Central Universities.

#### References

- [1] P. Singh and B. Jonshagen, "Zincbromine battery for energy storage," *Journal of Power Sources*, vol. 35, no. 4, pp. 405–410, 1991.
- [2] E. D. Woumfo and O. Vittori, "Electrochemical behaviour of a zinc electrode in 8 M KOH under pulsed potential loading," *Journal of Applied Electrochemistry*, vol. 21, no. 1, pp. 77–83, 1991.
- [3] P. Singh, K. White, and A. J. Parker, "Application of non-aqueous solvents to batteries part I. Physicochemical properties of propionitrile/water two-phase solvent relevant to zinc-bromine," *Journal of Power Sources*, vol. 10, no. 4, pp. 309–318, 1983.
- [4] G. Bauer, J. Drobits, C. Fabian, H. Mikosch, and P. Schuster, "Raman spectroscopic study of the bromine storing complex phase in a zinc-flow battery," *Journal of Electroanalytical Chemistry*, vol. 427, no. 1-2, pp. 123–128, 1997.
- [5] Y. Ito, M. Nyce, R. Plivelich, M. Klein, D. Steingart, and S. Banerjee, "Zinc morphology in zinc-nickel flow assisted batteries and impact on performance," *Journal of Power Sources*, vol. 196, no. 4, pp. 2340–2345, 2011.
- [6] M. Mastragostino and S. Valcher, "Polymeric salt as bromine complexing agent in a Zn-Br<sub>2</sub> model battery," *Electrochimica Acta*, vol. 28, no. 4, pp. 501–505, 1983.
- [7] D. J. Eustace, "Bromine complexation in zinc-bromine circulating batteries," *Journal of the Electrochemical Society*, vol. 127, no. 3, pp. 528–532, 1980.
- [8] K. Scott, W. M. Taama, and P. Argyropoulos, "Performance of the direct methanol fuel cell with radiation-grafted polymer

- membranes," *Journal of Membrane Science*, vol. 171, no. 1, pp. 119–130, 2000.
- [9] S. Lu, J. Pan, A. Huang, L. Zhuang, and J. Lu, "Alkaline polymer electrolyte fuel cells completely free from noble metal catalysts," *Proceedings of the National Academy of Sciences of the United States of America*, vol. 105, no. 52, pp. 20611–20614, 2008.
- [10] M. Li, L. Yang, S. Fang, and S. Dong, "Novel polymeric ionic liquid membranes as solid polymer electrolytes with high ionic conductivity at moderate temperature," *Journal of Membrane Science*, vol. 366, no. 1-2, pp. 245–250, 2011.
- [11] J. R. Varcoe and R. C. T. Slade, "Prospects for alkaline anion-exchange membranes in low temperature fuel cells," *Fuel Cells*, vol. 5, no. 2, pp. 187–200, 2005.
- [12] J. R. Varcoe and R. C. T. Slade, "An electron-beam-grafted ETFE alkaline anion-exchange membrane in metal-cation-free solid-state alkaline fuel cells," *Electrochemistry Communications*, vol. 8, no. 5, pp. 839–843, 2006.
- [13] A. Warshawsky and O. Kedem, "Polysulfone-based interpolymer anion exchange membrane," *Journal of Membrane Science*, vol. 53, no. 1-2, pp. 37–44, 1990.
- [14] W. Kautek, A. Conradi, C. Fabjan, and G. Bauer, "In situ FTIR spectroscopy of the Zn-Br battery bromine storage complex at glassy carbon electrodes," *Electrochimica Acta*, vol. 47, no. 5, pp. 815–823, 2001.
- [15] D. Aymé-Perrot, S. Walter, Z. Gabelica, and S. Valange, "Evaluation of carbon cryogels used as cathodes for non-flowing zinc-bromine storage cells," *Journal of Power Sources*, vol. 175, no. 1, pp. 644–650, 2008.
- [16] S. L. Chiu and J. R. Selman, "Determination of electrode kinetics by corrosion potential measurements: zinc corrosion by bromine," *Journal of Applied Electrochemistry*, vol. 22, no. 1, pp. 28–37, 1992.
- [17] P. M. Hoobin, K. J. Cathro, and J. O. Niere, "Stability of zinc/bromine battery electrolytes," *Journal of Applied Electrochemistry*, vol. 19, no. 6, pp. 943–945, 1989.
- [18] B. P. Tripathi, M. Kumar, and V. K. Shahi, "Organic-inorganic hybrid alkaline membranes by epoxide ring opening for direct methanol fuel cell applications," *Journal of Membrane Science*, vol. 360, no. 1-2, pp. 90–101, 2010.
- [19] J. Fang and P. K. Shen, "Quaternized poly(phthalazinone ether sulfone ketone) membrane for anion exchange membrane fuel cells," *Journal of Membrane Science*, vol. 285, no. 1-2, pp. 317–322, 2006.